Karlsruher Institut für Technologie

Reservoir temperature characterization from historical environment to future geothermal applications

Zur Erlangung des akademischen Grades eines

DOKTORS DER NATURWISSENSCHAFTEN (Dr. rer. nat.)

von der KIT Fakultät für

Bauingenieur-, Geo- und Umweltwissenschaften

des Karlsruher Instituts für Technologie (KIT)

genehmigte

DISSERTATION

von

M.Sc. Guoqiang Yan

aus China

Tag der mündlichen Prüfung:

19. Dezember 2024

Referent: Prof. Dr. Thomas Kohl

Korreferent: Jun. Prof. Dr. Haibing Shao

Karlsruhe 2025

Abstract

As the global shift toward sustainable energy intensifies, geothermal resources are increasingly recognized for their potential to contribute to greenhouse gas reductions and fulfill rising energy demands. Unlike other renewable energy sources, geothermal energy offers a continuous, base-load power supply that can be particularly valuable in decarbonizing energy sectors worldwide. However, effective geothermal utilization hinges on accurately characterizing subsurface temperature distributions and gaining an in-depth understanding of complex thermal dynamics within reservoirs. These factors are crucial in assessing geothermal potential, guiding resource extraction, and improving thermal storage capabilities. This research investigates the underlying mechanisms that shape temperature distributions in geothermal reservoirs, focusing on heat transfer and fluid flow processes. By leveraging advanced modeling approaches, the work provides critical insights for geothermal reservoir assessment, optimized extraction, and thermal energy storage design, paving the way for more sustainable geothermal utilization.

This study encompasses three distinct studies, each addressing a core aspect of geothermal reservoir dynamics through numerical modeling techniques. Each study builds upon the idea that a better understanding of subsurface heat and fluid movement is essential to unlocking geothermal energy potential and accurately estimating geothermal resources, especially in complex faulted and fractured reservoirs.

Chapter 3 examines transport mechanisms in a faulted sandstone reservoir that exhibits a kilometer-scale high-temperature anomaly, with recorded temperatures between 270–300°C. This phenomenon, observed in the Piesberg Quarry in northwestern Germany, raises questions about the processes responsible for such significant thermal anomalies at depth. Through numerical simulations, we identify buoyancy-driven convection within the primary fault as a key contributor to elevated reservoir temperatures. This study explores how permeability variations, lateral regional flow (as influenced by topographic features), and anisotropic permeability distributions can impact fluid flow pathways and the dominant heat transfer modes. Our sensitivity analyses reveal that lateral convection

within sandstone and advection through transfer faults contribute significantly to the observed thermal anomalies, raising reservoir temperatures well above the baseline conductive levels (≥ 269°C vs. ≤ 250°C in conduction-dominated settings). The findings emphasize the role of spatial permeability distribution, particularly within faulted geological structures, in influencing temperature profiles. The insights gained from this study offer valuable information for enhancing geothermal exploration workflows and for identifying zones with favorable thermal anomalies that could serve as potential geothermal reservoirs.

Chapters 4 and 5 separately advance geothermal reservoir characterization by introducing single-well and doublet temperature-reporting nanoparticle tracer tests as tools for mapping temperature distributions within fractured geothermal systems. Nanotracer technology has recently emerged as a promising approach for understanding temperature variability across reservoir heterogeneities. Using a detailed numerical model, we evaluate the behavior of temperature-reporting nanotracers under realistic three-dimensional geological conditions, considering fluid flow, heat transfer, tracer transport, and reactions. Our findings show that breakthrough curves generated from multiple nanotracers with different temperature thresholds can effectively indicate the upper and lower bounds of reservoir temperatures. Notably, deviations in tracer peak concentrations correspond to significant thermal and geological heterogeneities, allowing for the mapping of both temperature and structural features across the reservoir. By demonstrating how nanotracer data can provide precise temperature measurements along primary flow paths, this study underscores the potential of nanoparticle tracers to advance geothermal resource assessment by enabling more accurate subsurface temperature profiling in fractured reservoirs.

Chapter 6 investigates the influence of wellbore lateral heat transfer on the performance of high-temperature aquifer thermal energy storage (HT-ATES) systems, which are increasingly utilized to store and retrieve thermal energy from aquifers for use in periods of high demand. Focusing on the Swiss Bern HT-ATES project, this study employs a coupled simulation approach that integrates an in-house wellbore simulator (MOSKIO) with the reservoir simulator PorousFlow in the MOOSE framework to capture wellbore-reservoir interactions in greater detail. Our analysis quantifies the heat loss occurring

along the wellbore and examines how this lateral heat transfer affects overall energy recovery efficiency. Several wellbore configurations and operational parameters, such as wellbore diameter, casing materials, fluid flow rates, and injection temperatures, are evaluated to determine their impact on system performance. Results show that smaller wellbore diameters can enhance energy recovery by increasing fluid extraction rates and reducing lateral heat loss, while low thermal conductivity casing materials can reduce lateral heat losses by over 50%. Further, high fluid flow rates accelerate energy recovery by decreasing residence time and limiting thermal diffusion, although higher injection temperatures increase overall heat loss fractions. The findings from this study highlight the critical role of wellbore heat loss in influencing HT-ATES performance and provide recommendations for optimizing wellbore configurations to enhance the efficiency of thermal energy storage systems.

Together, these studies contribute to a comprehensive understanding of geothermal reservoir temperature characterization, from the historical environment to future geothermal applications. By addressing fundamental challenges in subsurface thermal dynamics, this research provides valuable insights for advancing geothermal resource assessment, enhancing extraction methods, and improving the design of thermal storage systems. These findings offer pathways for more sustainable geothermal utilization and underscore the importance of detailed subsurface characterization in realizing geothermal energy's potential as a foundation stone of a decarbonized energy future.

Kurzfassung

Da der globale Übergang zu nachhaltiger Energie an Dynamik gewinnt, werden geothermische Ressourcen zunehmend für ihr Potenzial anerkannt, Treibhausgasemissionen zu reduzieren und den steigenden Energiebedarf zu decken. Im Gegensatz zu anderen erneuerbaren Energiequellen bietet die Geothermie eine kontinuierliche Grundlaststromversorgung, die besonders wertvoll für die Dekarbonisierung der Energiesektoren weltweit sein kann. Die effektive Nutzung der Geothermie setzt jedoch voraus, dass die Temperaturverteilung in der Tiefe genau charakterisiert und die komplexe thermische Dynamik innerhalb von Reservoiren umfassend verstanden wird. Diese Faktoren sind entscheidend, um das geothermische Potenzial zu bewerten, die Ressourcengewinnung zu leiten und die Wärmespeicherung zu verbessern. Diese Forschung untersucht die grundlegenden Mechanismen, die Temperaturverteilungen in geothermischen Reservoiren prägen, mit einem Fokus auf Wärmeübertragungs- und Fluidströmungsprozesse. Durch den Einsatz fortschrittlicher Modellierungsansätze liefert die Arbeit wichtige Erkenntnisse für die Bewertung geothermischer Reservoirs, die Optimierung der Energiegewinnung und die Gestaltung von Wärmespeichersystemen und ebnet so den Weg für eine nachhaltigere Nutzung der Geothermie.

Diese Arbeit umfasst drei verschiedene Studien, die jeweils einen zentralen Aspekt der geothermischen Reservoirdynamik durch numerische Modellierungstechniken untersuchen. Jede Studie baut auf der Idee auf, dass ein besseres Verständnis des Wärme- und Fluidtransports im Untergrund entscheidend ist, um das Potenzial der Geothermie zu erschließen und geothermische Ressourcen, insbesondere in komplexen gestörten und geklüfteten Reservoiren, genau zu schätzen.

Kapitel 3 untersucht Transportmechanismen in einem gestörten Sandsteinreservoir, das eine kilometerweite Hochtemperaturanomalie mit Temperaturen zwischen 270 und 300°C aufweist. Dieses Phänomen, das im Piesberg-Steinbruch in Nordwestdeutschland beobachtet wurde, wirft Fragen zu den Prozessen auf, die für solche signifikanten thermischen Anomalien in der Tiefe verantwortlich sind. Durch numerische Simulationen

identifizieren wir die auftriebgetriebene Konvektion innerhalb der Hauptverwerfung als einen Schlüsselfaktor für die erhöhten Reservoirtemperaturen. Diese Studie untersucht, wie Variationen der Permeabilität, laterale regionale Strömungen (beeinflusst durch topografische Merkmale) und anisotrope Permeabilitätsverteilungen die Fluidströmungswege und die dominanten Wärmeübertragungsmodi beeinflussen können. Unsere Sensitivitätsanalysen zeigen, dass laterale Konvektion im Sandstein und Advektion durch Transferverwerfungen erheblich zu den beobachteten thermischen Anomalien beitragen und die Reservoirtemperaturen deutlich über das leitungsdominierte Niveau anheben ($\geqslant$ 269°C gegenüber $\leqslant$ 250°C in leitungsdominierten Umgebungen). Die Ergebnisse unterstreichen die Bedeutung der räumlichen Permeabilitätsverteilung, insbesondere in gestörten geologischen Strukturen, für die Beeinflussung von Temperaturprofilen. Die gewonnenen Erkenntnisse bieten wertvolle Informationen zur Verbesserung von Geothermie-Explorationsabläufen und zur Identifizierung von Zonen mit günstigen thermischen Anomalien, die als potenzielle geothermische Reservoirs dienen könnten.

Kapitel 4 und 5 erweitern die Charakterisierung geothermischer Reservoirs, indem temperaturmeldefähige Nanopartikel-Tracer als Werkzeuge zur Kartierung von Temperaturverteilungen in geklüfteten geothermischen Systemen eingeführt werden. Die Nanotracer-Technologie hat sich kürzlich als vielversprechender Ansatz für das Verständnis von Temperaturvariabilitäten in Reservoirheterogenitäten herausgestellt. Mithilfe eines detaillierten numerischen Modells bewerten wir das Verhalten temperaturabhängiger Nanotracer unter realistischen, dreidimensionalen geologischen Bedingungen, wobei Fluidströmung, Wärmeübertragung, Tracertransport und -reaktionen berücksichtigt werden. Unsere Ergebnisse zeigen, dass Durchbruchskurven, die aus mehreren Nanotracern mit unterschiedlichen Temperaturschwellenwerten generiert wurden, effektiv die oberen und unteren Grenzen der Reservoirtemperaturen anzeigen können. Insbesondere weichen Tracer-Spitzenkonzentrationen von bedeutenden thermischen und geologischen Heterogenitäten ab, was eine Kartierung sowohl von Temperatur- als auch von Strukturmerkmalen im gesamten Reservoir ermöglicht. Indem gezeigt wird, wie Nanotracer-Daten präzise Temperaturmessungen entlang primärer Strömungspfade liefern können, unterstreicht diese Studie das Potenzial von

Nanopartikeln, die geothermische Ressourcenbewertung voranzutreiben, indem eine genauere Temperaturprofilierung im Untergrund in geklüfteten Reservoirs ermöglicht wird.

Kapitel 6 untersucht den Einfluss des lateralen Wärmetransports im Bohrloch auf die Effizienz hochtemperaturiger Aquifer-Wärmespeichersysteme (HT-ATES), die zunehmend zur Speicherung und Entnahme von Wärme aus Aquiferen für Zeiten hoher Nachfrage genutzt werden. Mit Schwerpunkt auf das HT-ATES-Projekt in Bern, Schweiz, wird ein gekoppelter Simulationsansatz verwendet, der einen eigenen Bohrlochsensor (MOSKIO) mit dem Reservoir-Simulator PorousFlow im MOOSE-Framework integriert, um die Wechselwirkungen zwischen Bohrloch und Reservoir detailliert zu erfassen. Unsere Analyse quantifiziert den Wärmeaustritt entlang des Bohrlochs und untersucht, wie dieser laterale Wärmetransport die Gesamtenergiegewinnungseffizienz beeinflusst. Verschiedene Bohrlochkonfigurationen und Betriebsparameter wie Bohrlochdurchmesser, Verrohrungsmaterialien, Fluidströmungsraten und Einspritztemperaturen werden bewertet, um ihren Einfluss auf die Systemleistung zu bestimmen. Die Ergebnisse zeigen, dass kleinere Bohrlochdurchmesser die Energiegewinnung durch erhöhte Flüssigkeitsextraktionsraten und reduzierte laterale Wärmeverluste verbessern können, während Verrohrungsmaterialien mit geringer Wärmeleitfähigkeit die lateralen Wärmeverluste um über 50% verringern können. Darüber hinaus beschleunigen hohe Fluidströmungsraten die Energiegewinnung, indem sie die Verweilzeit verkürzen und die thermische Diffusion begrenzen, obwohl höhere Einspritztemperaturen den Gesamtheit Verlustanteil erhöhen. Die Ergebnisse dieser Studie unterstreichen die wichtige Rolle des lateralen Wärmeaustritts im Bohrloch für die HT-ATES-Leistung und liefern Empfehlungen zur Optimierung der Bohrlochkonfiguration zur Verbesserung der Effizienz von Wärmespeichersystemen.

Zusammen tragen diese Studien zu einem umfassenden Verständnis der Temperaturcharakteristik geothermischer Reservoirs bei, von der historischen Umgebung bis hin zu zukünftigen geothermischen Anwendungen. Durch die Untersuchung grundlegender Herausforderungen in der thermischen Dynamik des Untergrunds liefert diese Forschung wertvolle Erkenntnisse für die Verbesserung der geothermischen Ressourcenbewertung, die Optimierung der Gewinnungsmethoden und die Gestaltung

effizienter Wärmespeichersysteme. Diese Ergebnisse bieten Wege für eine nachhaltigere Nutzung der Geothermie und unterstreichen die Bedeutung einer detaillierten Untergrundcharakterisierung, um das Potenzial der Geothermie als Eckpfeiler einer dekarbonisierten Energiezukunft zu realisieren.

Contents

List of figures

List of tables

Nomenclature

A	wellbore cross-sectional area, m^2
B	wellbore sign, -
C	Concentration, $mg \cdot L^{-1}$
c_p	specific heat capacity, $J \cdot m^{-3} \cdot K^{-1}$
d	wellbore diameter, m
$\boldsymbol{D}$	diffusion coefficient, $m^2 \cdot s^{-1}$
E	Energy, J
f	friction factor, -
F	mass or energy flux vector, $kg \cdot m^2 \cdot s^{-1}$ or $W \cdot m^{-2}$
g	gravitational acceleration, $m \cdot s^{-2}$
h	specific enthalpy, $J \cdot kg^{-1}$
k	rock permeability, m^2
K	bulk modulus, m
M	mass or energy density term, $kg \cdot m^{-3}$ or $J \cdot m^{-3}$
n	time step, -
p	pressure, Pa
Pe	Peclet number, -
q	mass or heat source term, $kg \cdot m^{-3} \cdot s^{-1}$ or $W \cdot m^{-3}$
Q	volumetric flow rate, $kg \cdot m^{-3}$
r	wellbore radius, m
Ra	Rayleigh number, -
t	time, s
T	temperature, K
$\boldsymbol{u}$	Darcy velocity, $m \cdot s^{-1}$
u	velocity, $m \cdot s^{-1}$
U	heat transfer coefficient, $W \cdot m^{-1} \cdot K^{-1}$
V	volume, m^3
WI	well index, m^3
x	x-coordinate, m
y	y-coordinate, m
z	z-coordinate (positive upward), m
Z	conversion factor, -

Greek symbols

α	fraction, -
β	convective heat transfer coefficient, -
η	energy recovery efficiency, -
θ	angle between the connection and the vertical, ◦
λ	heat conductivity, $W \cdot m^{-1} \cdot K^{-1}$
μ	dynamic viscosity, Pa·s
ρ	density, $kg \cdot m^{-3}$
ϕ	porosity, -

Δ	grid size, m

Subscripts and superscripts

0	initial
a	conversion constant1
ana	analytical
b	conversion constant2
bh	borehole
BHF	basal heat flux
cas	casing wall
cem	cement
cf	cement/formation interface
ci	inside casing
co	outside casing
con	convective
cp	coupling
crit	critical
e	effective
ext	extraction
EG	energy
fo	formation
fa	far-field
fft	fluid film in tubing and the tubing wall
i	equation type, -
initial	initial state
inj	injection
ins	tubing insulation
ir	reservoir element intersecting with the injection well
iw	injection well
j	wellbore type
l	liquid
los	loss
MF	Main fault
MS	mass
ne	nearest
num	numerical
pr	reservoir element intersecting with the production well
prod	product
pw	production well
r	reservoir
rad	radial
reac	reactant
s	solid
SST	sandstone
TF	transfer fault
thre	temperature threshold
ti	inside tubing

to	outside tubing
updated	updated after time step
w	wellbore
xx	length direction
yy	width direction

1 Introduction

1.1 Research background

Over the past century, the Earth's climate has been warming at an unprecedented rate, driven by the accumulation of greenhouse gases (GHGs) in the atmosphere (EIA, 2009; Ürge-Vorsatz et al., 2015; EU, 2010). This increase is largely attributed to human activities such as fossil fuel combustion, deforestation, and industrial processes, which have intensified since the Industrial Revolution. According to the Intergovernmental Panel on Climate Change (IPCC), global temperatures have already risen by approximately 1.1°C above pre-industrial levels. This temperature rise has brought about a series of profound and widespread impacts on the environment, with projections indicating even more severe consequences if current trends continue (Fig. 1.1). Among these impacts are more frequent and intense weather events, such as hurricanes, droughts, and heatwaves, as well as rising sea levels, which threaten coastal communities and infrastructure. Additionally, ocean acidification, resulting from increased CO_2 absorption by seawater, disrupts marine ecosystems and poses risks to biodiversity (UN, 2015). Terrestrial ecosystems are also affected, as shifting climate zones alter habitats and force species migrations, leading to ecological imbalances and loss of biodiversity.

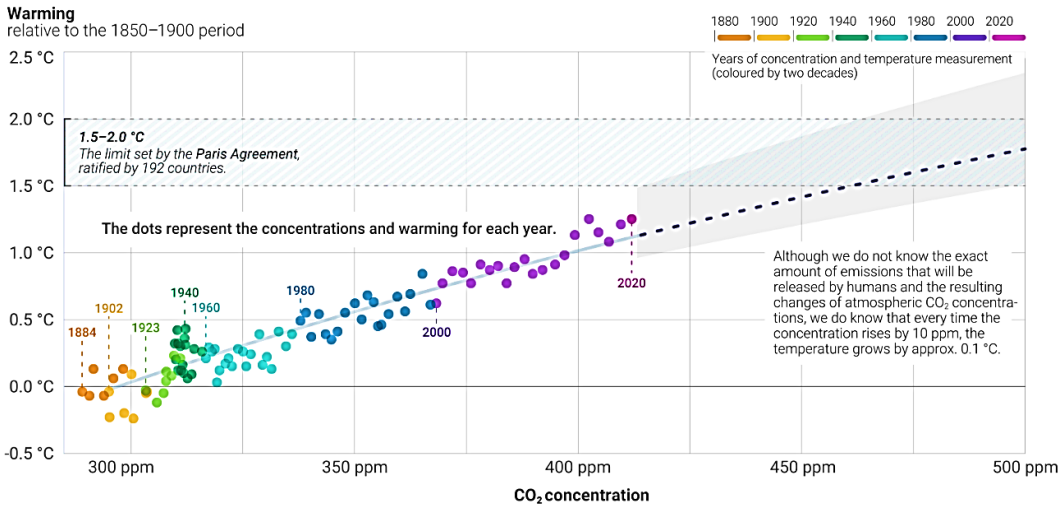

Figure 1.1. The relationship between CO_2 concentration and global warming (IPCC, 2023).

Without immediate and sustained mitigation efforts, scientists project that global temperatures could increase by an additional 1.5°C or more in the coming decades, further exacerbating these negative impacts. This scenario would place unprecedented stress on natural and human systems, intensifying food and water scarcity, health risks, and economic instability worldwide. Addressing global warming, therefore, necessitates a comprehensive transformation of the energy sector, which is currently the largest source of GHG emissions. The global energy demand is continuously rising, propelled by population growth and industrialization, creating an urgent need to shift from reliance on fossil fuels to cleaner, renewable energy sources. Such a transition is essential not only to reduce carbon footprints but also to stabilize climate systems and ensure a sustainable future. Transforming the energy sector through innovation, policy change, and international collaboration can pave the way for achieving climate targets while meeting the increasing global energy demand.

Renewable energy sources (Fig. 1.2), such as wind, solar, biomass, hydropower, and geothermal energy, offer a promising pathway to reducing greenhouse gas (GHG) emissions and limiting global warming (Herzog, 2001). Unlike fossil fuels, renewables are derived from natural processes that are continually replenished, making them sustainable long-term energy solutions. Each renewable energy source possesses unique characteristics that contribute to a balanced, low-carbon energy portfolio and collectively work toward achieving energy security, economic stability, and climate goals.

Geothermal energy stands out among renewable resources for its ability to deliver a stable, continuous energy supply (Moeck 2014). Unlike solar and wind, which are inherently variable, geothermal power can provide a consistent output due to the steady flow of heat from the Earth's interior. This makes geothermal energy particularly valuable in delivering base-load power, comparable to that provided by coal or nuclear energy, yet with minimal GHG emissions. By supplying reliable, low-carbon electricity, geothermal energy can support grid stability and meet demand regardless of weather conditions or time of day.

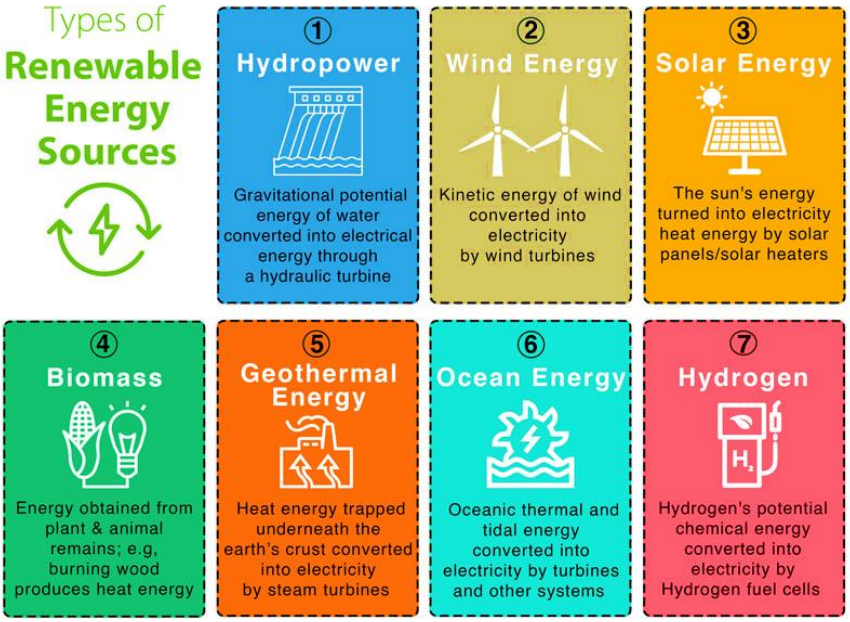

Figure 1.2. Types of renewable energy sources (Elie, 2021).

Geothermal energy is derived from thermal energy stored within the Earth's crust, which originates from two primary sources: residual heat from the planet's formation and the radioactive decay of isotopes in the Earth's mantle. This internal heat continuously flows toward the surface through the high thermal conductivity of rocks and soil, where it can be captured and harnessed for energy production. According to the World Geothermal Congress (2023), a total of 1,476 PJ (410 TWh) of geothermal energy was used globally in 2022, a 44% increase from 2020, with geothermal heating and cooling of buildings accounting for about 79% of the total. Geothermal systems exploit this natural heat through technologies such as geothermal heat pumps, which can provide direct heating, and geothermal power plants, which convert thermal energy into electricity. These plants operate with a high capacity factor, meaning they can produce electricity consistently, unlike other renewable sources that fluctuate in output.

The environmental footprint of geothermal energy is relatively small, particularly in comparison to fossil fuels (Lund et al., 2008; J. W. Tester et al., 1989). While geothermal plants do emit some GHGs, particularly during the drilling and initial production phases, these emissions are minimal and can be further reduced through technological advances. Additionally, geothermal power plants require comparatively little land, allowing them to coexist with other land uses and reducing their impact on surrounding ecosystems.

However, the feasibility of geothermal energy production depends on local geological conditions, as it requires access to sufficient subsurface heat and permeable rock formations. As a result, geothermal resources are often concentrated in regions with volcanic or tectonic activity, though advancements in technology are expanding the range of accessible geothermal resources. Geothermal energy can be harnessed using different methods, depending on the geological characteristics of the site and the application (electricity generation or heating).

1.2 Motivation of this work

Effectively harnessing and storing thermal energy from subsurface environments presents a myriad of scientific and engineering challenges that must be addressed to maximize the potential of geothermal energy resources. One of the primary challenges lies in understanding the intricate and complex interplay of heat and fluid transfer processes occurring within faulted, fractured, and heterogeneous geological formations. These formations often exhibit significant spatial variability in properties such as permeability, porosity, and thermal conductivity, leading to highly heterogeneous temperature distributions within the reservoir. As a result, predicting how heat migrates through these geological structures becomes increasingly complex. The geological complexities inherent in these systems can create unpredictable patterns of heat distribution and fluid flow, further complicating the assessment of geothermal reservoir performance. In faulted and fractured environments, the presence of faults can serve as conduits for fluid flow, resulting in localized zones of elevated temperature due to enhanced heat transfer. Conversely, these same faults can also act as barriers that impede fluid movement, leading to colder regions that significantly impact overall energy extraction efficiency. Therefore, understanding the interactions between different geological features is crucial for developing effective strategies to manage and utilize geothermal resources.

Accurate characterization of subsurface temperature distributions is essential for optimizing resource extraction strategies and ensuring the long-term viability of geothermal projects. Without precise knowledge of temperature profiles within the reservoir, designing effective drilling and extraction methodologies becomes challenging,

potentially leading to inefficient resource use and economic losses. Moreover, in heterogeneous reservoirs, variations in rock properties can result in significant discrepancies in heat transfer mechanisms. Differences in mineral composition and structure can influence both the thermal conductivity of the rock and the movement of fluids, thereby affecting heat retention and transfer rates. This variability necessitates the identification and quantification of these properties through comprehensive modeling and experimental approaches to enhance predictive models.

Understanding the mechanisms behind temperature distribution in these complex environments is crucial for improving the efficiency and reliability of geothermal energy utilization. By elucidating the fundamental processes that govern heat transfer and fluid dynamics in subsurface reservoirs, this research aims to contribute to more effective geothermal system designs. Ultimately, such insights will advance the field of geothermal research and support the broader goals of sustainable energy development and climate change mitigation by maximizing the utilization of renewable energy resources.

This study aims to address these challenges by exploring the mechanisms of reservoir temperature characterization across various geological settings, focusing on three key areas: 1) deciphering the transport mechanisms that drive hydrothermal convection in faulted tight sandstones, 2) evaluating the potential of temperature-reporting nanoparticle tracers to map temperature distributions and characterize fractured geothermal reservoirs, and 3) assessing the impact of wellbore lateral heat transfer on the performance of high-temperature aquifer thermal energy storage (HT-ATES) systems.

1) Revealing the transport mechanisms of hydrothermal convection in faulted tight sandstones

The motivation for this work arises from an observed kilometer-scale high-temperature overprint of 270–300°C at the Piesberg Quarry reservoir outcrop in northwestern Germany, the origins of which remain unclear. Understanding the mechanisms behind such thermal anomalies is critical for advancing geothermal exploration and exploitation, particularly in faulted sandstone reservoirs where complex fluid and heat transfer processes play a dominant role. Previous studies have shown that fault-related

hydrothermal convection can elevate subsurface temperatures, but the contributions of various transport mechanisms—such as buoyancy-driven convection, advective flow along faults, and permeability variations—remain underexplored. This work aims to dissect these mechanisms through numerical simulations, focusing on how lateral and regional flow patterns, along with anisotropic permeability distributions, influence thermal and fluid dynamics within a faulted sandstone reservoir. By clarifying these relationships, we seek to provide a framework for predicting and utilizing positive thermal anomalies in geothermal systems.

2) Studying the working mechanisms of double-well and single-well temperature-reporting nanoparticle tracer tests for fractured geothermal reservoir characterization

Accurate information on subsurface temperature distribution is crucial for efficient geothermal energy development, as it directly influences resource viability and extraction strategies. Traditional methods for temperature mapping often lack precision, particularly in complex geothermal reservoirs where heterogeneity can affect fluid and heat flow. Temperature-reporting nanoparticle tracers have emerged as a promising tool to overcome these limitations, offering a potential means to track in situ temperatures through detectable threshold responses. Despite advancements in the theoretical and experimental study of these nanotracers, most research has been confined to simplified geometries and has not fully accounted for the dynamic interactions of fluid flow, heat transfer, transport, and reaction within realistic three-dimensional systems. This study aims to address these gaps by developing a numerical model to simulate nanotracer behavior in a fractured geothermal reservoir, focusing on the tracers' ability to map temperature distribution and reveal thermal and geological heterogeneities. Through these simulations, we seek to enhance our understanding of nanotracer response mechanisms and explore their potential for accurately delineating subsurface thermal structures, ultimately advancing geothermal resource assessment and management.

3) Investigating the impact of wellbore lateral heat transfer on the performance of aquifer thermal energy storage

The efficient design and optimization of high-temperature aquifer thermal energy storage (HT-ATES) systems are essential for sustainable energy storage solutions, especially as energy demands increase. However, one critical factor that remains underexplored is the impact of wellbore lateral heat transfer, which can significantly influence system performance. Traditional analyses often overlook wellbore heat loss, yet understanding its effects is crucial for accurately predicting energy recovery and efficiency. This study focuses on the Swiss Bern project, aiming to bridge this knowledge gap by investigating the role of wellbore heat transfer within HT-ATES systems. By coupling a wellbore simulator (MOSKIO) with a reservoir simulator (PorousFlow) in the MOOSE framework, we examine the influence of wellbore configurations, materials, and operational parameters on heat loss and energy recovery efficiency. Through this research, we aim to provide valuable insights into optimizing HT-ATES systems, specifically by identifying design strategies that minimize heat loss and maximize energy recovery in large-scale, high-temperature aquifer storage projects.

Overall, this study advances our understanding of the mechanisms of reservoir temperature characterization, bridging the historical environment to future geothermal applications. By addressing the interplay of thermal, fluid, and geological dynamics in faulted and heterogeneous reservoirs, this research offers valuable insights for improving the efficiency and effectiveness of subsurface energy storage and extraction, contributing to a sustainable energy future.

1.3 Thesis structure

This thesis is divided into three main parts. The first part focuses on the transport mechanisms of hydrothermal convection in faulted tight sandstones. The second part explores the working mechanism of temperature-reporting nanoparticle tracers for fractured geothermal reservoir characterization. Lastly, the third part investigates the impact of wellbore lateral heat transfer on the performance of high-temperature aquifer thermal energy storage systems. These investigations comprise four papers that have been published in or submitted to international journals.

Chapter 2 introduces the basic physical phenomena, governing and constitutive equations, and underlying assumptions used in this thesis. Additionally, a brief overview of the finite element method (FEM) and its applications, MOOSE, PorousFlow and MOSKITO, is included. The following four chapters present the papers in accordance with the outline below. Finally, Chapter 7 provides concluding remarks.

Transport mechanisms of hydrothermal convection in faulted tight sandstones

Chapter 3 outlines the research contents aimed at understanding the transport mechanisms of fault-related hydrothermal convection systems, specifically in the context of the high-temperature overprint (270–300 °C) observed at the Piesberg quarry in northwestern Germany. The research objectives are clearly defined, highlighting the importance of investigating buoyancy-driven convection and its role in elevating reservoir temperatures. The methodology section details the numerical simulation framework employed to analyze fluid flow pathways and heat transfer dynamics within the sandstone reservoir, including the interactions between the main fault and embedded transfer faults. The chapter concludes with a discussion of the implications of these findings for geothermal resource exploration and the potential for future research, particularly regarding the fully coupled thermo-hydro-mechanical-chemical processes in faulted tight sandstones. Overall, this chapter aims to provide a holistic understanding of the mechanisms driving temperature anomalies in geothermal systems and their relevance for sustainable energy development.

Single well temperature-reporting nanoparticle tracer test for fractured geothermal reservoir characterization

Chapter 4 investigates the characterization of temperature distributions in fractured geothermal reservoirs using a single-well tracer test, emphasizing the significance of accurate temperature mapping for improving geothermal energy applications. The study develops a comprehensive numerical model to explore single-well tracer tests, where tracers are injected and retrieved from the same well, enabling more detailed and site-specific temperature profiling that accounts for reservoir heterogeneities. The analysis focuses on various factors, including different injection-production configurations, push-pull schemes, and injection methods (single-point and line-source). Ultimately, this

research underscores the potential of single-well nanoparticle tracer tests as advanced diagnostic tools, suggesting that strategic decisions regarding injection configuration and methods can significantly improve the understanding of geothermal reservoir characteristics critical for energy development.

Numerical modeling of temperature-reporting nanoparticle tracer for fractured geothermal reservoir characterization

Chapter 5 presents research focused on the utilization of temperature-reporting nanoparticle tracers for accurately characterizing temperature distribution in subsurface reservoirs, which is crucial for advancing geothermal energy development. A numerical modeling approach is developed to simulate the field implementation of these tracers within a fractured geothermal reservoir, investigating both homogeneous and non-homogeneous scenarios that incorporate various thermal and geological heterogeneities. Key findings from the nanotracer breakthrough curves reveal that deviations in peak concentration values can define upper and lower temperature limits for the reservoir, while peak arrival times accurately estimate the highest temperatures along primary flow paths. Additionally, the research illustrates how geological heterogeneities impact tracer response behavior, demonstrating that variations in conductivity and orientation significantly affect temperature interpretation in the reservoir. Ultimately, the findings emphasize the implications for enhanced geothermal resource assessment and management, while proposing future research directions to improve the understanding of nanoparticle tracer dynamics in complex subsurface environments.

Investigating the impact of wellbore lateral heat transfer on the performance of high-temperature aquifer thermal energy storage system by the coupling of wellbore and reservoir simulators

Chapter 6 delves into the critical examination of wellbore lateral heat transfer and its significant impact on the performance of high-temperature aquifer thermal energy storage (HT-ATES) systems, specifically in the context of the Swiss Bern project. The study employs a coupled approach, integrating an in-house wellbore simulator (MOSKIO) with a reservoir simulator (PorousFlow) under the MOOSE framework to effectively analyze wellbore heat loss. By utilizing both numerical and analytical methods, this research

identifies the effects of wellbore heat loss on HT-ATES performance, highlighting the shortcomings of previous studies that have overlooked this critical factor. A thorough sensitivity analysis is conducted to assess various wellbore configurations and operational parameters, focusing on performance indicators such as extracted energy, wellbore lateral heat loss fraction, and reservoir heat loss fraction. This research underscores the essential role of wellbore lateral heat loss in the evaluation and optimization of HT-ATES systems, offering valuable insights for the design and enhancement of these energy storage solutions.

2 Fundamentals of numerical method

2.1 Numerical equations

2.1.1 Fluid flow and heat transfer in the coupled wellbore-reservoir system

The governing equations (Pan and Oldenburg, 2014; Korzani et al., 2019; Wilkins et al., 2021) for fluid flow and heat transfer-transport in the wellbore and reservoir based on the MOOSE framework are presented in Table 2.1. Note that the conservation law for both mass and energy holds the same format. The differences in equations between the wellbore and the reservoir lie in the definitions of energy flux terms and fluid velocity. In the wellbore, our simulator employs 1D Navier-Stokes equations to realistically simulate pipe flow and study the dynamic processes of fluid flow and heat transfer. Furthermore, kinetic energy and gravitational potential energy are included in the heat equation. In

Table 2.1. The mass, energy and momentum equations solved in the coupled wellbore-reservoir simulator.

Equation and term	1D Wellbore	3D Reservoir
Mass (MS) conservation Energy (EG) conservation	$\frac{\partial M_i}{\partial t} + \nabla \cdot F_i - q_i{}^{cp} = 0$ (i = *MS* or *EG*)	
Mass density: M_{MS}	$\rho_l^w A$	$\phi \rho_l^r$
Mass flux: F_{MS}	$\rho_l^w A u_l^w$	$\rho_l^r \boldsymbol{u}_l^r$
Energy density: M_{EG}	$\rho_l^w A \left[c_{p,l}^w T^w + \frac{(u_l^w)^2}{2} \right]$	$\left[\phi c_{p,l}^r \rho_l^r + (1-\phi) c_{p,s}^r \rho_s^r\right] T^r$
Energy flux: F_{EG}	$\rho_l^w A u_l^w c_{p,l}^w T^w - \lambda_l \nabla(\mathrm{A} T^w) + \rho_l^w A u_l^w \left[\frac{p_l^w}{\rho_l^w} + \frac{(u_l^w)^2}{2} + gz\cos\theta \right]$	$\rho_l^r c_{p,l}^r \boldsymbol{u}_l^r T^r - [\phi \lambda_l^r + (1-\phi)\lambda_s^r] \nabla T^r$
Momentum	$\nabla(p_l^w \mathrm{A}) = \rho_l^w A g \cos\theta \pm \frac{f \rho_l^w A (u_l^w)^2}{2d} \pm \left\{ \frac{\partial}{\partial t}(\rho_l^w A u_l^w) + \nabla[\rho_l^w A (u_l^w)^2] \right\}$	$\boldsymbol{u}_l^r = \frac{k}{\mu_l}(-\nabla p_l^r + \rho_l^r g)$

*The indexes *cp, EG, i, l, MS, r, s and w* represent coupling, energy, equation type, liquid, mass, reservoir, solid and wellbore, respectively.

contrast, in this work, the reservoir equations do, not account for these terms due to the creeping flow in the porous medium. For the momentum equation, fluid flow in the reservoir takes Darcy's law and Navier-Stokes type of equation for the wellbore flow where the inertial forces are considered.

Regarding the mass and energy coupling between the reservoir and wellbore, two regions are considered: the open-hole and the non-open-hole sections. In the open-hole section, there is mass transfer and energy transfer due to fluid flow (convection) and heat conduction driven by the local temperature gradient (Fourier's Law). A Peaceman-type equation (Peaceman, 1983) is employed for calculating the source terms in the mass equations for the open-hole section, which is a function of the pressure difference between the reservoir and the wellbore (see Table 2.2). The well index (*WI*) in the Peaceman-type formula (Chen and Zhang, 2009) accounts for the impact of the reservoir grid size, reservoir permeability and wellbore radius, etc. It reflects the well's ability to inject or produce fluid.

$$WI = 2\pi\sqrt{k_{xx}k_{yy}}\Delta z/\ln(r_e/r_{bh}) \tag{2.1}$$

where k_{xx}, k_{yy}, Δz, r_e, r_{bh} are separately reservoir permeability [m^2] in length direction, reservoir permeability [m^2] in width direction, grid block size [m] in depth direction, wellbore radius [m] and the effective wellbore radius which can be calculated by (Chen and Zhang, 2009):

$$r_e = 0.28\frac{\sqrt{\sqrt{k_{xx}/k_{yy}}(\Delta x)^2+\sqrt{k_{yy}/k_{xx}}(\Delta y)^2}}{(k_{xx}/k_{yy})^{1/4}+(k_{yy}/k_{xx})^{1/4}} \tag{2.2}$$

where Δx is the length [m] and Δy is the width [m] of a grid block.

As for the fluid flow and heat transfer in the radial direction for the non-open-hole section, mass transfer is not considered and only heat exchange exists between the wellbore and surrounding formation. For the non-open-hole section, three calculation approaches for the heat exchange are shown with numerical, analytical and without consideration of wellbore lateral heat transfer, see Table 2.2. In the numerical approach, the heat exchange

is characterized by the temperature difference between the wellbore (i.e., T^w where subscript *w* means wellbore) and the nearest formation (i.e., T_{ne}^f where superscript *f* and

Table 2.2. Comparison of coupling terms at the wellbore-reservoir interface. The heat exchange calculations at the non-open-hole section interface are compared using the numerical and analytical approaches, and the approach without considering wellbore lateral heat transfer.

Region	Coupling term	Numerical approach	Analytical approach	An approach without considering wellbore lateral heat transfer
Non-open-hole	Energy: q_{EG}^{cp}	$2\pi r_{to}U_{to}(T^w - T_{ne}^{fo})$ (Willhite, 1967)	$\frac{2\pi\lambda^{fo}(T^w - T_{fa}^{fo})}{f(t)}$ (Ramey, 1962)	0
Open-hole	Mass: q_{MS}^{cp}	$\rho_l^j \frac{WI}{\mu_l^j}(p_l^w - p_l^r)$ (Peaceman, 1983)		
	Energy: q_{EG}^{cp}	$\rho_l^j \frac{WI}{\mu_l^j}(p_l^w - p_l^r)h_l^j + B\lambda^r \nabla T$		

*1. The indexes *cf, cp, EG, fo, fa, j, l, MS, ne, r, to* and *w* refer to cement/formation interface, coupling, energy, formation, far-field, well type, liquid, mass, nearest, reservoir, overall and wellbore, respectively; 2. well type $j = \begin{cases} w, & injection\ well \\ r, & production\ well \end{cases}$; 3. well sign $B = \begin{cases} 1, & injection\ well \\ -1, & production\ well \end{cases}$; 4. $f(t)$ is dimensionless time function. When time is greater than one week, it can be calculated by $f(t) = ln\frac{2\sqrt{\frac{\lambda^{fo}}{\rho^f c_p^{fo}}t}}{r_{cf}} - 0.29$.

subscript *ne* are formations and nearest node, separately) and an overall heat transfer coefficient (U_{to}). Both formation temperature and temperature at the interface of cement and formation are dynamic. As shown in Equation (2.3), the overall heat transfer coefficient is a combination of several thermal resistances including those of the tubing, annulus fluid, casing and cement, which can be referred to in more detail in Willhite (1967) and Xiong et al. (2016).

$$U_{to} = \frac{1}{\frac{r_{to}}{r_{ti}h_f} + \frac{r_{to}\ln(r_{to}/r_{ti})}{\lambda_t} + \frac{r_{to}\ln(r_{ins}/r_{to})}{\lambda_{ins}} + \frac{r_{to}}{r_{ins}(h_c+h_r)} + \frac{r_{to}\ln(r_{co}/r_{ci})}{\lambda_{cas}} + \frac{r_{to}\ln(r_{cf}/r_{co})}{\lambda_{cem}}} \quad (2.3)$$

where r_{ti}, r_{to}, r_{ins}, r_{ci}, r_{co}, and r_{cf} represent the radii of inside tubing, outside tubing, tubing insulation, inside casing, outside casing, and cement/formation interface, respectively. λ_{t}, λ_{ins}, λ_{cas}, and λ_{cem} are the thermal conductivities of the tubing wall, tubing insulation, casing wall, and cement. h_{f}, h_c, and h_r are the convective heat transfer coefficient between the fluid film in tubing and the tubing wall, and the convective and

radial heat transfer coefficients of fluid inside annulus. Furthermore, the analytical approach ignores the heat transfer within the tubing-casing-cement-formation range and assumes that the temperature (i.e., T_{fa}^{f} where subscript *fa* means far-field) in the far-field is static. However, the third approach (Table 2.2) for calculating the heat exchange in the non-open-hole section just employs the reservoir-wellbore simulator without consideration of wellbore lateral heat transfer.

2.1.2 Fully coupled processes of fluid flow, heat transfer, transport and reaction for temperature-reporting nanoparticle tracers in the formation

1) Reaction process

In the following, we present our numerical approach for simulating the temperature-reporting nanotracers reaction. The relevant reaction can be described as follows:

$$C_{T_{thre.}}^{reac.} \xrightarrow{T>T_{thre.}} C_{T_{thre.}}^{prod.} \tag{2.4}$$

where $C_{T_{thre.}}^{reac.}$ denotes the concentration of reactant and $C_{T_{thre.}}^{prod.}$ is the corresponding product's concentration after the reaction. $T_{thre.}$ refers to the temperature threshold of the reactant.

2) Transport process

Each temperature-reporting nanotracer with a certain temperature threshold has a group of the two advection-diffusion equations (Shan & Pruess, 2005) for both reactant and product:

$$\frac{\partial C_{T_{thre.}}^{reac.}}{\partial t} - \nabla \cdot (\boldsymbol{D} \nabla C_{T_{thre.}}^{reac.}) + \nabla \cdot (\boldsymbol{u_w} C_{T_{thre.}}^{reac.}) - Q_{C_{T_{thre.}}^{reac.}} = 0 \tag{2.5}$$

$$\frac{\partial C_{T_{thre.}}^{prod.}}{\partial t} - \nabla \cdot (\boldsymbol{D} \nabla C_{T_{thre.}}^{prod.}) + \nabla \cdot (\boldsymbol{u_w} C_{T_{thre.}}^{prod.}) - Q_{C_{T_{thre.}}^{prod.}} = 0 \tag{2.6}$$

where $\boldsymbol{D}$ refers to the diffusion coefficient ($m^2 \cdot s^{-1}$), $\boldsymbol{u_w}$ is the Darcy velocity ($m \cdot s^{-1}$), $Q_{C_{T_{thre.}}^{reac.}}$ and $Q_{C_{T_{thre.}}^{prod.}}$ represent the mass source of reactant and product ($kg \cdot m^{-3} \cdot s^{-1}$),

respectively. Here we assume that the nanotracers are well mixed with water as components of the liquid solution and the gravity segregation between water and nanotracer is ignored due to the low mass fraction (<10^{-3}) of nanotracers in the liquid. In addition, for simplicity we do not consider the deposition and aggregation of nanotracers during the flow process.

Equation 4 indicates a sharp conversion process of the injected nanotracers / reactants into products. To release this constraint, we include a conversion factor Z in the following reaction expression for temperature-reporting nanotracers:

$$(C_{T_{thre.}}^{reac.\,n})^{updated} = Z^n \cdot C_{T_{thre.}}^{reac.\,n} \tag{2.7}$$

where $(C_{T_{thre.}}^{reac.\,n})^{updated}$ represents the newly updated concentration of the reactant after reaction (at time step n) and Z is defined as:

$$Z^n = \begin{cases} 1, & T^n < (T_{thre.} - a); \\ \frac{1}{1+e^{b\cdot(T^n - T_{thre.})}}, & (T_{thre.} - a) \le T^n \le (T_{thre.} + a); \\ 0, & T^n > (T_{thre.} + a). \end{cases} \tag{2.8}$$

where a (°C) and b (=6/a, °C^{-1}) are conversion constants that can be controlled such that a smooth conversion between 100% and 0% nanotracer conversion can be achieved when environment temperature T is near the nanotracer temperature threshold $T_{thre.}$.

The product concentration after the reaction at the time step n is updated with:

$$(C_{T_{thre.}}^{prod.\,n})^{updated} = (1 - Z^n) \cdot C_{T_{thre.}}^{reac.\,n} + C_{T_{thre.}}^{prod.\,n} \tag{2.9}$$

where the two parts on the right side separately refer to the concentration increase of the product after the reaction and product concentration at time step n.

The updated results $(C_{T_{thre.}}^{reac.\,n})^{updated}$ and $(C_{T_{thre.}}^{prod.\,n})^{updated}$ at time step *n* are separately used explicitly in the following tracer transport Equations A4 and A5 for the implicit computation of the reactant and product concentrations at time step *n*+1.

$$\frac{C_{T_{thre.}}^{reac.\,n+1} - (C_{T_{thre.}}^{reac.\,n})^{updated}}{\Delta t} - \nabla \cdot \left(\boldsymbol{D} \nabla C_{T_{thre.}}^{reac.\,n+1}\right)$$

$$+\nabla \cdot \left(\boldsymbol{u_w^{n+1}} C_{T_{thre.}}^{reac.\,n+1}\right) - Q_{C_{T_{thre.}}^{reac.\,n+1}} = 0 \tag{2.10}$$

$$\frac{C_{T_{thre.}}^{prod.\,n+1} - (C_{T_{thre.}}^{prod.\,n})^{updated}}{\Delta t} - \nabla \cdot \left(\boldsymbol{D} \nabla C_{T_{thre.}}^{prod.\,n+1}\right)$$

$$+\nabla \cdot \left(\boldsymbol{u_w^{n+1}} C_{T_{thre.}}^{prod.\,n+1}\right) - Q_{C_{T_{thre.}}^{prod.\,n+1}} = 0 \tag{2.11}$$

After obtaining $C_{T_{thre.}}^{reac.\,n+1}$ and $C_{T_{thre.}}^{prod.\,n+1}$, we need to update these two variables at time step *n+1* according to the new conversion factor Z^{n+1} using Equations (2.8).

2.2 Finite element method (FEM)

2.2.1 Fundamentals of FEM

The Finite Element Method (FEM) is a powerful numerical technique used for solving differential equations, especially in engineering and physical sciences. It is widely applied in the modeling of complex systems, including fluid flow, heat transfer, structural mechanics, and multiphysics simulations. The method is based on the discretization of a continuous domain into smaller, finite elements, which simplifies the solving of governing equations over each element. The key steps of FEM include:

1) Discretization of the Domain**:** The continuous problem domain is divided into a finite number of subdomains, called elements, which are connected by nodes. The solution is approximated over these elements by shape functions. The elements can have various geometries such as triangles, quadrilaterals (in 2D), or tetrahedrons and hexahedrons (in 3D).

2) Governing Equations**:** The physical processes are typically described by partial differential equations (PDEs). These PDEs are transformed into a weak form, which involves multiplying the equations by a test function and integrating over the domain. This process ensures the conservation of quantities such as energy, mass, or momentum across the domain.

3) Interpolation Functions**:** Inside each element, the unknown field variables (e.g., temperature, velocity) are approximated using interpolation (or shape) functions that depend on the values of the field variables at the nodes. The most common choices for interpolation are linear, quadratic, or higher-order polynomials.

4) Element stiffness matrix**:** The PDEs are then solved for each element, resulting in element-level matrices (stiffness matrices for structural problems or conductivity matrices for thermal problems). These matrices describe the relationship between the nodal values of the field variables and the governing equations within the element.

5) Assembly**:** The element matrices are assembled into a global system of equations that represents the entire problem domain. The assembly process accounts for the interconnection of elements through their shared nodes.

6) Boundary conditions**:** Appropriate boundary conditions are applied to the global system to ensure a physically realistic solution. These conditions can include Dirichlet (fixed value) or Neumann (flux or derivative) boundary conditions.

7) Solution of the global system**:** Once the global system of equations is assembled, numerical solvers are used to solve the resulting algebraic equations. This step produces an approximate solution to the original problem at the nodes of the elements.

8) Post-processing**:** After solving the system of equations, the results are post-processed to compute quantities of interest, such as stresses, heat fluxes, or fluid velocities. These results can also be interpolated back to the entire domain for visualization and further analysis.

2.2.2 Application of FEM to subsurface processes

The Finite Element Method (FEM) is extensively used to model subsurface processes, particularly in the fields of geothermal energy, petroleum engineering, groundwater flow, and environmental engineering. Subsurface processes typically involve the interaction of multiple physical phenomena, including fluid flow through porous media, heat transfer, and mechanical deformation. The complex geometry and heterogeneity of geological

formations make FEM an ideal choice for such applications due to its flexibility in handling irregular boundaries and material properties.

1) Modeling fluid flow in porous media

FEM is used to solve Darcy's law, which governs fluid flow in porous media. The method discretizes the porous domain into smaller elements and solves for the pressure distribution, which drives fluid movement. The governing equations often take the form of a conservation law, balancing the rate of mass inflow, outflow, and accumulation within each element. This approach can handle complex boundary conditions, including wells, faults, and varying permeability.

2) Heat transfer in geothermal systems

FEM is widely applied to simulate heat transfer in geothermal systems. Heat transport in the subsurface occurs through both conduction and convection, and FEM is used to solve the coupled equations governing these processes. The method captures spatial variations in thermal conductivity and fluid properties, which are critical for accurately predicting temperature distributions and energy extraction in geothermal reservoirs and aquifer thermal energy storage (ATES) systems.

3) Coupled Thermo-Hydro-Mechanical (THM) Processes

Subsurface environments often involve coupled interactions between thermal, hydraulic, and mechanical processes. FEM is particularly suited for simulating these multiphysics phenomena. For example, in geothermal energy extraction, fluid injection and extraction cause pressure changes that affect rock deformation, while heat transfer alters the mechanical properties of the subsurface. FEM allows for the simultaneous solution of the governing equations for fluid flow (hydraulic), heat transfer (thermal), and mechanical stress and strain (mechanical), enabling a comprehensive understanding of the system's behavior under different operational conditions.

4) Reactive transport processes

In environmental and reservoir engineering, FEM is used to model reactive transport, where chemical reactions occur alongside fluid flow and mass transport. FEM handles the advection-diffusion-reaction equations, which describe the transport of solutes and

their interaction with the surrounding media. This is important for predicting the movement of contaminants, mineral precipitation, or dissolution in geothermal systems and groundwater aquifers.

5) Advantages of FEM in subsurface modeling

The use of FEM in subsurface processes offers several advantages: (1) Flexibility in meshing complex geometries, such as faulted formations or variable topographies; (2) Adaptability to heterogeneous material properties and boundary conditions; (3) Accuracy in handling nonlinearities and multiphysics interactions; (4) Scalability to model large, regional-scale domains as well as smaller, site-specific areas. By applying FEM, engineers and researchers can predict the performance of subsurface systems under varying operational conditions, design more efficient geothermal and energy storage systems, and assess the environmental impact of subsurface processes.

2.3 Simulation tools

2.3.1 MOOSE framework

Moose is a Finite Element Method (FEM) solver, a software package for simulating complex physical systems, developed at the Idaho National Laboratory (INL) in the United States. This solver is built using object-oriented C++ which is well-suited for scientific computing. Moose is designed to solve large-scale, multi-physics problems using a modular approach, where users can easily add or modify physical models and numerical methods to suit their needs. It is an open-source software package, meaning it is freely available to anyone to use and modify, and is actively maintained by a team of developers at the INL. Moose is particularly useful in simulating problems in which multiple physical phenomena interact, such as heat transfer, fluid dynamics, and structural mechanics. By using FEM, Moose can accurately model the behavior of these systems, considering geometric complexity and non-linear behavior. The software also includes a variety of numerical methods and algorithms for solving partial differential equations (PDEs), making it a powerful tool for a wide range of applications in engineering, physics, and materials science. The modular architecture of Moose allows users to quickly build

complex simulations by combining pre-existing modules or creating their own. This makes it an efficient and flexible tool for researchers and engineers, who can quickly test and validate their designs or hypotheses. Additionally, Moose includes a graphical user interface (GUI) for creating and visualizing simulations, as well as tools for post-processing and data analysis. These features make Moose a user-friendly and comprehensive package for modeling complex systems in a variety of fields.

2.3.2 Reservoir simulator — PorousFlow

PorousFlow is a robust and versatile simulation tool designed to model fluid flow and heat transfer in porous media, such as geothermal reservoirs or aquifers. It operates within the MOOSE (Multiphysics Object-Oriented Simulation Environment) framework and is well-suited for simulating various physical processes relevant to Aquifer Thermal Energy Storage (ATES) systems. PorousFlow enables the simulation of:

1) Multiphase flow: The movement of multiple fluid phases (e.g., water, steam) through porous media, which is essential for accurately capturing the behavior of injected and extracted fluids in an ATES system.

2) Heat transport: The transfer of thermal energy between the fluids and the surrounding porous rock, a critical component of thermal energy storage.

3) Coupled fluid and heat flow: The ability to couple the effects of fluid dynamics and thermal processes ensures more accurate modeling of subsurface conditions.

4) Geomechanics coupling: Though not directly applied in this study, PorousFlow can be extended to include mechanical stress effects, which might be relevant in other geothermal or subsurface applications.

2.3.3 Wellbore simulator — MOSKITO

MOSKITO is a powerful and user-friendly wellbore simulator initially developed by Dr. Maziar Gholami Korzani. The acronym MOSKITO stands for Multiphysics cOupled Simulator toolKIT for wellbOres. It is an open-source C++ code developed on the MOOSE Framework that can handle transient non-isothermal multi-phase and

multicomponent flows. MOSKITO solves the conservation equations in a fully coupled manner. This numerical tool has been designed to handle the simulation of wellbores with complex configurations, including Multilateral, U-shape, and Coaxial. Additionally, MOSKITO has the unique ability to calculate the thermo-physical properties of two-phase multi-component mixtures, including H_2O, CO_2, CH_4, N_2, H_2S, NaCl, KCl, $CaCl_2$, and $MgCl_2$, using a fast equation of state that has been trained through machine learning. The researchers and engineers can use MOSKITO regardless of their preferred operating system as it can be run on macOS, Linux, and Windows.

2.3.4 Further development in this work

1) Fully coupled processes of fluid flow, heat transfer, transport and reaction for temperature-reporting nanoparticle tracers in the formation

The modeled physical and chemical processes consist of fluid flow, heat transfer, transport and the reaction of temperature-reporting nanotracers in the reservoir. The numerical models for simulating fully coupled processes of fluid flow, heat transfer, transport and reaction for temperature-reporting nanotracer are developed for the first time and implemented in the finite element simulator-PorousFlow module (Wilkins et al., 2021) within the MOOSE framework (Permann et al., 2020). The relevant equations are described in Section 2.1.1. The numerical algorithms of the fully coupled processes of fluid flow, heat transfer, transport and reaction for temperature-reporting nanoparticle tracers are shown in Fig. 2.1. At time step *n*, the fluid flow model, nanotracer transport model together with the heat transfer model are solved implicitly. After obtaining the results, the reactant and product concentrations of tracers are updated using the nanotracer reaction model, which provides the inputs for the tracer computation at the next time step $n+1$.

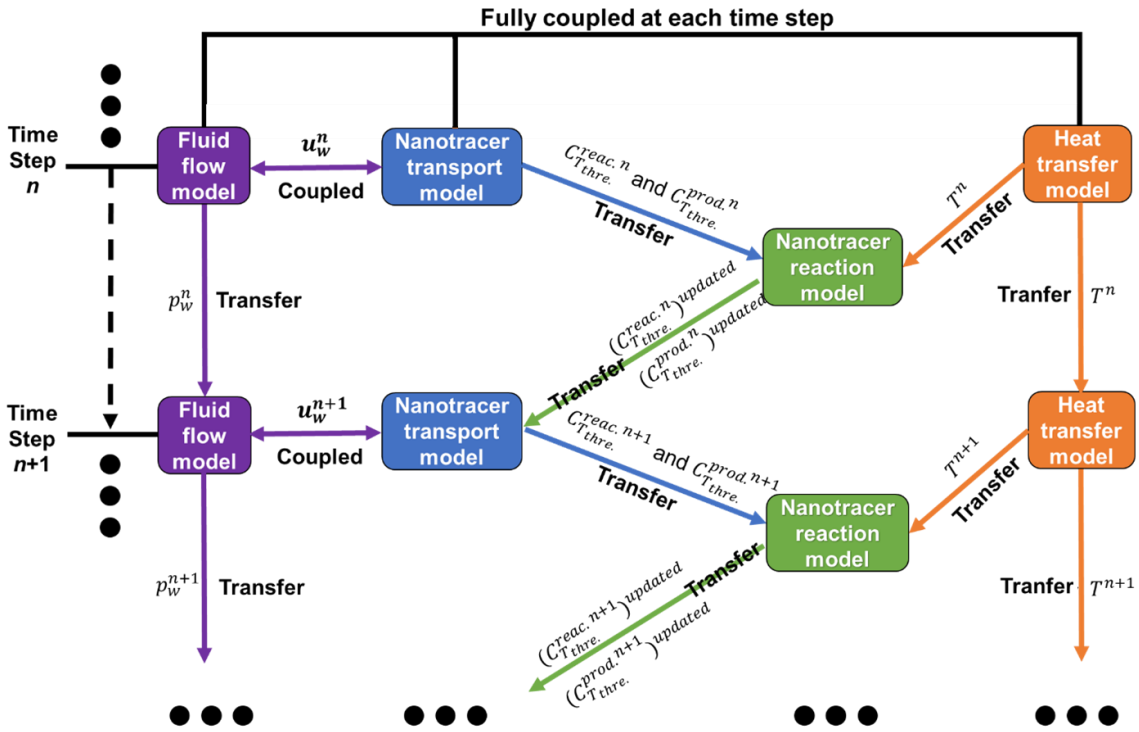

Figure 2.1. Schematic of the fully coupled fluid flow, heat transfer, transport and reaction models of temperature-reporting nanoparticle tracers.

2) Fully coupled wellbore-reservoir system

We have fully coupled the wellbore fluid flow and heat transfer processes, simulated by our in-house developed wellbore simulator MOSKITO (Korzani et al., 2019) together with an existing reservoir simulator PorousFlow (Wilkins et al., 2021) under the MOOSE framework (Permann et al., 2020). The numerical algorithm of how the coupled wellbore-reservoir model being solved is detailed as follows. Taking the open-hole section as an example in Fig. 2.2a, the 1D wellbore intersects the center position of a column of formation grid blocks. The wellbore works as a line source, meaning that fluid and heat can flow out of or into the coupled reservoir grid block along the whole element lines (red dots in Fig. 2.2a). Simultaneously, the corresponding reservoir grids conservatively exchange the mass and energy with the wellbore elements. Space distributions of variables are based on the linear interpolation of their nodal values. The fluid properties in the coupling terms are evaluated based on the upstream method (fluid flow direction), which is only from either the wellbore or reservoir. The numerical algorithm of how the coupled wellbore-reservoir model is being solved is briefly illustrated in Fig. 2.2b.

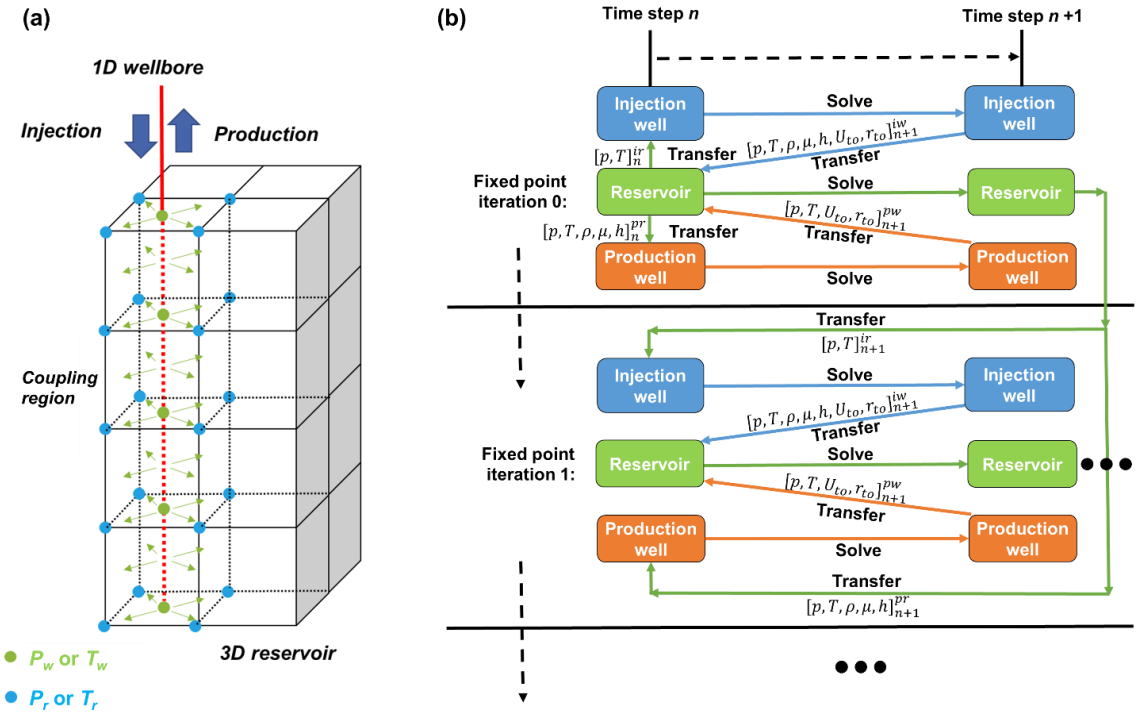

Figure 2.2. Illustration of (a) the full coupling between the 1D wellbore simulator and the 3D reservoir simulator using the FEM; (b) numerical algorithm of the fully coupled simulator at each time interval (i.e., between time step *n* and time step *n*+1).

- **Wellbore modeling**: At the first iteration, given the initial pressure, temperature and fluid properties (i.e., density, viscosity and enthalpy) from the reservoir's coupling grids, the wellbore simulator is employed to simulate the fluid flow and heat transfer processes, implicitly.
- **Reservoir modeling**: Secondly, the corresponding results from the wellbore simulator's coupling grids are transferred into the reservoir simulator, as inputs. The reservoir modeling results are then fed back into the wellbore simulator for the next iteration.
- **Coupling iterations**: There are two iterations for this coupled simulation. One is the inner iteration for solving each simulator (reservoir or wellbore), the convergence criteria should be satisfied with the Newton-Raphson method. Another one is the outer iteration between the wellbore and reservoir simulators by simply transferring coupling data between them. Once this convergence criterion is met, we move to the next time step for new computations.

3 Transport mechanisms of hydrothermal convection in faulted tight sandstones

This part is reproduced from the manuscript that has been published in the peer-reviewed journal ***Solid Earth***.

***Yan, G.**, Busch, B., Egert, R., Esmaeilpour, M., Stricker, K., and Kohl, T.: Transport mechanisms of hydrothermal convection in faulted tight sandstones, **Solid Earth**, 14, 293–310, https://doi.org/10.5194/se-14-293-2023, 2023.*

Abstract

Motivated by the unknown reasons for a kilometer-scale high-temperature overprint of 270 ~ 300 °C in a reservoir outcrop analog (Piesberg Quarry, northwestern Germany), numerical simulations are conducted to identify the transport mechanisms of the fault-related hydrothermal convection system. The system mainly consists of a main fault and a sandstone reservoir in which transfer faults are embedded. The results show that the buoyancy-driven convection in the main fault is the basic requirement for elevated temperatures in the reservoir. We studied the effects of permeability variations and lateral regional flow mimicking the topography conditions on the preferential fluid flow pathways, dominant heat transfer types, and mutual interactions among different convective and advective flow modes. The sensitivity analysis of permeability variations indicates that lateral convection in the sandstone and advection in the transfer faults can efficiently transport fluid and heat, thus causing elevated temperatures (≥ 269 °C) in the reservoir at the depth of 4.4 km compared to purely conduction-dominated heat transfer (≤ 250 °C). Higher-level lateral regional flow interacts with convection and advection and changes the dominant heat transfer from conduction to advection in the transfer faults for

the low permeability cases of sandstone and main fault. Simulations with anisotropic permeabilities detailed the dependence of the onset of convection and advection in the reservoir on the spatial permeability distribution. The depth-dependent permeabilities of the main fault reduce the amount of energy transferred by buoyancy-driven convection. The increased heat and fluid flow resulting from the anisotropic main fault permeability provide the most realistic explanation for the thermal anomalies in the reservoir. Our numerical models can facilitate exploration and exploitation workflows to develop positive thermal anomaly zones as geothermal reservoirs. These preliminary results will stimulate further petroleum and geothermal studies of fully coupled thermo-hydro-mechanical-chemical processes in faulted tight sandstones.

3.1 Introduction

Thermal anomalies in sedimentary basins are common geological phenomena and may affect hydrocarbon reservoir properties and the utilization of subsurface space concerning porosity and permeability due to cementation with temperature-related authigenic cement (Baillieux et al., 2013). Meanwhile, the thermal anomalies in sedimentary basins can be targeted as geothermal resources for heat and electricity production (Moeck, 2014). In general, thermal anomalies may be caused by variations of thermal conductivities around structures such as salt domes (O'Brien and Lerche, 1988; Magri et al., 2008), geological/tectonic activity (Emry et al., 2020), geochemical reactions (Elderfield et al., 1999), or hydrothermal activities in faults and fractures (Cherubini et al., 2013). Indeed, in addition to being a possible cause of thermal anomalies (Zwingmann et al., 1998, 1999; Liewig and Clauer, 2000; Will et al., 2016), the hydrothermal activities in faults and fractures are often invoked to explain natural processes in sedimentary basins, such as hydrothermal mineralization (Kühn and Gessner, 2009; Harcouët-menou et al., 2009). The common driving force for hydrothermal activities in faulted and fractured lithologies is the fluid density difference caused by temperature variations (Nield and Bejan, 2017). The resulting process is called buoyancy-driven convection/flow. Many numerical models imply that buoyancy-driven convection in faulted basins could explain the correlation between faulted zones or adjacent lithologies and thermal anomalies (Bruhn et al., 1994; Andrews et al., 1996; Lampe and Person, 2000). Besides the buoyancy-driven

force, pore pressure gradients or lateral regional flow (LRF) from topography, magmatic, or metamorphic fluid production also cause hydrothermal activities (e.g. controlling the fluid flow and heat transfer) (Wisian and Blackwell, 2004b), while the two flow modes may also coexist (McKenna and Blackwell, 2004). Several studies further reveal that these flow modes generate complex flow patterns within the faults (i.e., convection cells) and/or across the adjacent permeable lithologies (Magri et al., 2016).

Transport mechanisms of hydrothermal convection in faulted zones, including preferential fluid flow pathways, dominant heat transfer types (i.e., conduction, advection, and convection), and the mutual interactions of different flow modes, are crucial for interpreting related diagenetic, petrophysical, and thermal phenomena in sedimentary basins. Therefore, it is necessary to understand the transport mechanisms of hydrothermal convection in faulted zones, which are mainly controlled by the permeability distributions of the fault systems and the surrounding lithologies, pore pressure gradients, and LRF (López and Smith, 1995; Fairley, 2009). The dominant heat transfer types are quantified by analyzing the Peclet number, which in this case represents the ratio of heat transfer by convection/advection to heat transfer by conduction (Jobmann and Clauser, 1994). For Peclet numbers much less than 1 (e.g., < 0.1), the system is conduction-dominated, while for values greater than 1, the system is convection/advection-dominated (Kämmlein et al., 2019). A Peclet number within the range of 0.1 and 1 indicates a convective-conductive system (Beck et al., 1989). Furthermore, rock heterogeneities (e.g. anisotropic and depth-dependent permeabilities), mainly resulting from sedimentary depositional environments, superimposed tectonics, and lithostatic stress, are common phenomena in sedimentary basins (Parry, 1998; Achtziger-Zupančič et al., 2017b; Panja et al., 2021). Affected by the preferential orientation of pore connectivity during deformation, the orientation of maximum permeability of faulted zones commonly lies parallel to the fault plane (i.e., parallel to bedding) (Scibek, 2020). The horizontal permeability of sedimentary rocks generally shows higher values than the vertical (i.e., perpendicular to bedding) permeability due to the effect of bedding, as controlled by the sedimentary depositional environments (Panja et al., 2021). Permeability is generally expected to decrease with increasing lithostatic pressure (Manning and Ingebritsen, 1999; Saar and Manga, 2004). Anisotropic and depth-

dependent permeabilities may change the fluid flow pathways and affect heat transfer (Guillou-Frottier et al., 2020). López and Smith (1995) and Magri et al. (2016) presented 3D numerical investigations involving topography-driven flow and buoyancy-driven flow to infer the transport mechanisms of a hydrothermal convection system. Magri et al.'s hydraulic conditions were isotropic and homogeneous, whereas López and Smith's simulation set partly anisotropic and heterogeneous hydraulic conditions. The effects of thermo-hydraulic conditions, including permeability distributions of fault systems and surrounding lithologies, and LRF, on the transport mechanisms, have not yet been systematically investigated.

A blueprint for complex hydrothermal conditions is the Piesberg Quarry, exposing Upper Carboniferous sandstones in the Lower Saxony Basin (LSB) in northwestern Germany. The quarry is chosen as a reservoir analog because of its similarity to still producing tight sandstone reservoirs in LSB concerning sedimentology, stratigraphy, fault patterns, and average porosity. Tight sandstone, generally referred to low permeability reservoirs that produce mainly dry natural gas, is a common play type of petroleum reservoir (Becker et al., 2019). The Upper Carboniferous sandstone reservoir analog, once located at a maximum depth of about 5 km, was affected by a kilometer-scale thermal anomaly (270 ~ 300 °C), as interpreted from geothermometry data including fluid inclusion, K/Ar-dating, chlorite thermometry, and vitrinite reflectance analyses (Wüstefeld et al., 2017b). The geothermometry data indicated that the chlorite in veins typically reaches temperatures of ~ 300 °C due to fluid flow, whereas the pore-filling chlorite records an average temperature of 270 °C. Furthermore, the Piesberg Quarry is also an experimental study case for the thermal control of a porosity-permeability evolution defined by long-term history matching in this play type (Becker et al., 2019). Thus, revealing the transport mechanisms of the hydrothermal convection system in the Piesberg Quarry is an effective strategy for interpreting related geological phenomena such as kilometer-scale thermal anomalies).

Our study aims to systematically identify the transport mechanisms as inferred from the results of fluid flow and heat transfer in the tight sandstone reservoir. For the first time, the example of the Upper Carboniferous Piesberg Quarry and its geological past is used to numerically investigate the physical processes leading to the kilometer-scale thermal

anomaly in faulted tight sandstones. A 3D model is established based on the geological conditions of the Piesberg Quarry. Firstly, considering complex thermo-hydraulic conditions, numerical modeling is performed, and the influence of the different transport mechanisms is quantified. Then, the transport mechanisms are further assessed and discussed to study the effects of the anisotropic and depth-dependent permeabilities on the transport mechanisms. Possible reasons for the kilometer-scale thermal anomaly in the Piesberg Quarry are inferred. Based on the generalized structural characteristics of the studied domain, the numerical results can be applied to interpret hydrothermal convection-related geological phenomena and to draw implications for future exploration and exploitation of reservoirs in analogous settings.

3.2 Material and methods

3.2.1 The reservoir analog study area

The studied Piesberg Quarry is located at the southwestern margin of the LSB (Fig. 3.1a and b). The reservoir-scale Piesberg study site has dimensions of approximately 1 km in the W-E direction and 0.5 km in the N-S direction, with a depth of roughly 0.1 km (Fig. 3.1c). Within the Piesberg Quarry, two dominant fault systems can be distinguished (Fig. 3.1c). First, the NNW-SSE striking normal fault (at ~ 170° strike angle) is represented in the east of the quarry (not exposed anymore), with a down-dip displacement of up to 600 m (Hinze, 1979; Baldschuhn R. et al., 2001). The second main strike orientation of the normal faults is W-E (at ~ 95° strike angle) to WNW-ESE, with average fault displacements of 10 m (Wuestefeld et al., 2014; Wüstefeld et al., 2017a; Becker et al., 2019). The initial total thickness of Upper Carboniferous sandstones in the region was 1.5 km (David et al., 1990). During the burial, the thickness of the sandstones decreased to nearly 1 km in the Late Jurassic to Early Cretaceous times. The sandstones are overlain by impermeable claystone and Zechstein cap rocks (Becker et al., 2019).

The geothermometry data from the outcrop samples in the Piesberg Quarry show a high-temperature thermal overprint of about 270 ~ 300 °C at about 4.4 km depth around the significant NNW-SSE striking normal fault at about 160 Ma. The NNW-SSE striking normal fault may thus have acted as a conduit for the heat/fluid source of the thermal

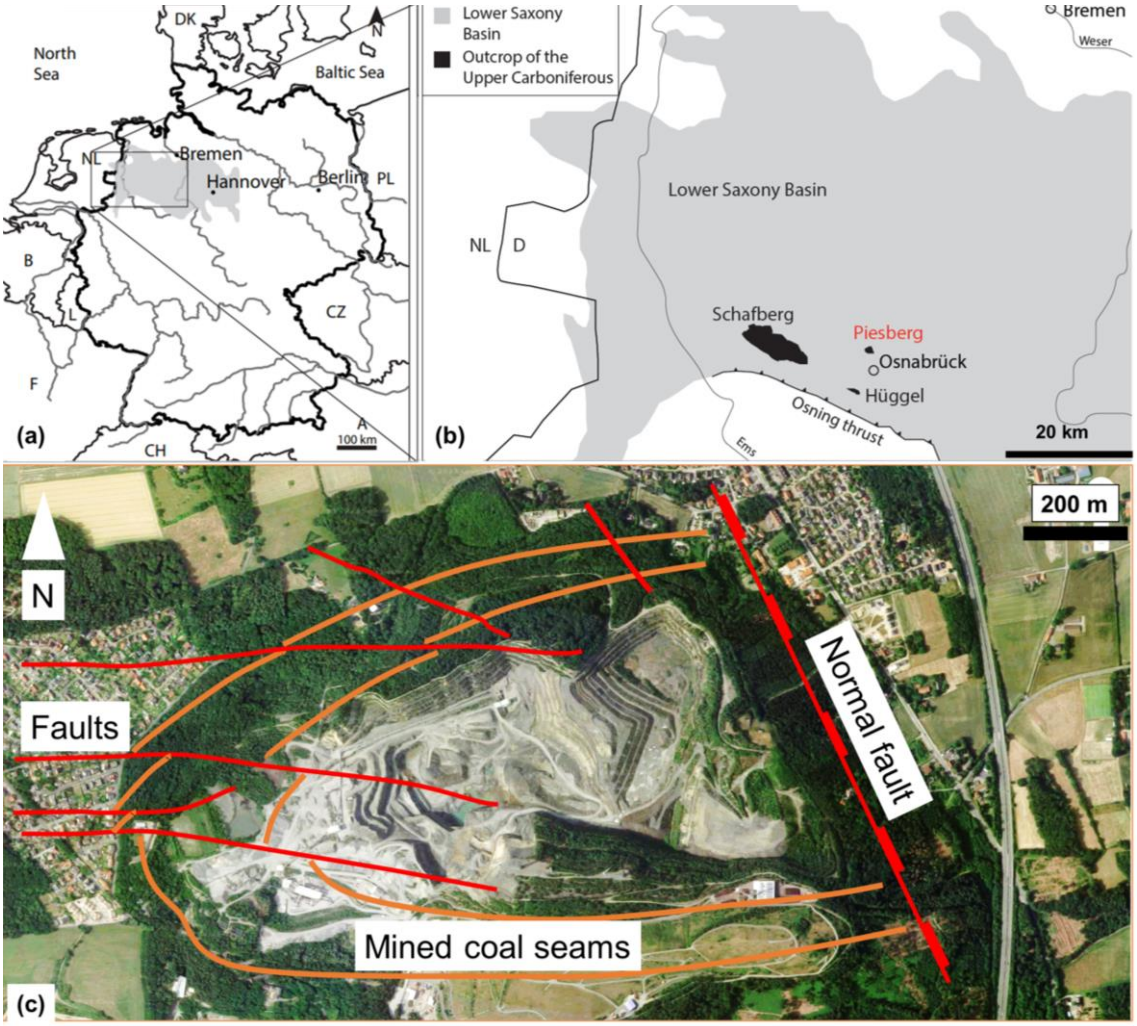

Figure 3.1. (a) Location of the studied area in northwestern Germany. (b) Detailed location of the investigated Piesberg Quarry at the southern rim of the LSB (redrawn from Senglaub et al. (2006) and Busch et al. (2019)). (c) Aerial image of the Piesberg Quarry (© Google Maps, 2023). The coal seams, faults, and the main normal fault in the east are based on historical subsurface mining data (Haarmann, 1909; Wüstefeld et al., 2017b).

overprint. Wüstefeld et al. (2017b) concluded that the local thermal increase of approximately 90 ~ 120 °C was the result of hydrothermal fluids circulating along the fault damage zone of the NNW-SSE striking normal fault, which laterally heated the tight sandstones. Furthermore, it is noteworthy that the W-E striking faults within the tight sandstones may also affect fluid flow and heat transfer processes because of their higher permeability (i.e., 10^{-13} m^2) and intersection with the NNW-SSE striking fault. Even though there are no field observations and evidence, LRF resulting from the topography conditions are hypothesized to investigate the effect of topography conditions on the transport mechanisms of hydrothermal convection. Considering the geological conditions,

especially fault patterns and stratigraphy, the Piesberg Quarry area might be an example of the coexistence of buoyancy-driven convective and lateral regional flows. Thermo-hydraulic numerical simulations are required to investigate and quantify the plausibility of different hypotheses of transport mechanisms that could contribute to the kilometer-scale thermal anomaly.

3.2.2 Numerical workflow

3) Governing equations

Inspired by the Piesberg Quarry, an idealized and synthetic numerical analog is created to characterize geological conditions in faulted tight sandstones and to enable investigation of the transport mechanisms leading to fluid flow and heat transfer. Only single-phase liquid flow is considered in this study. The numerical simulations for coupled fluid flow and heat transfer processes are carried out with a finite element open-source application called TIGER (THMC sImulator for GEoscience Research) (Gholami Korzani et al., 2019; Egert et al., 2020; Egert et al., 2021), which is based on the MOOSE (Multiphysics Object-Oriented Simulation Environment) framework (Permann et al., 2020). TIGER has been developed to tackle thermo-hydraulic-mechanical-chemical problems in petroleum and geothermal reservoirs. The numerical study of thermal convection in permeable and porous media involves coupling fluid flow and heat transfer equations as shown below (Gholami Korzani et al., 2020). The mass transport equation is written as

$$S_m \frac{\partial p}{\partial t} + \nabla \cdot \boldsymbol{q} = 0 \tag{3.1}$$

where the subscript *m* means porous media, S_m is the constrained specific storage of the porous media (Pa^{-1}), p is the pore pressure (Pa), t is time (s), and $\boldsymbol{q}$ is the Darcy velocity in the porous media ($m \cdot s^{-1}$). The S_m comprised a mechanical alteration in response to pressure and is assumed as a constant given by $S_m = (1-n)/K^s + n/K^l$ with porosity n (-), the bulk moduli of solid K^s and of liquid K^l (Pa) (Watanabe et al., 2017). The Darcy velocity is given as

$$\boldsymbol{q} = \frac{k}{\mu}(-\nabla p + \rho^l \boldsymbol{g}) \tag{3.2}$$

where k is the permeability (m^2), μ is the fluid dynamic fluid viscosity (Pa·s), the superscript *l* means liquid phase, ρ^l is the fluid density ($kg \cdot m^{-3}$), and $\boldsymbol{g}$ is the gravitational acceleration vector ($m \cdot s^{-2}$).

The heat transfer equation is written as

$$\left[nc_p^l\rho^l + (1-n)c_p^s\rho^s\right]\frac{\partial T}{\partial t} - \left[n\lambda^l + (1-n)\lambda^s\right]\nabla^2 T + \rho^l {c_p}^l \boldsymbol{q}\nabla T - Q = 0 \tag{3.3}$$

where the superscript *s* means solid phase, c_p^l and ${c_p}^s$ are the specific heat capacity of the liquid and solid phases ($J \cdot m^{-3} \cdot K^{-1}$), ρ^s is the solid density ($kg \cdot m^{-3}$), T is the temperature (K), t is the time (s), λ^l and λ^s are the heat conductivity of the liquid and solid phases ($W \cdot m^{-1} \cdot K^{-1}$), $\boldsymbol{q}$ is the Darcy velocity in the porous media ($m \cdot s^{-1}$), and Q is the heat source ($W \cdot m^{-3}$).

4) Numerical model

The numerical model represents the stratigraphic distributions of the Piesberg Quarry region (belonging to the sandstone reservoir) at about 160 Ma. The model geometry extends 5 km along the W-E direction (i.e., X-axis), 12 km along the N-S direction (i.e., Y-axis), and over a depth of 12 km (i.e., Z-axis). The NNW-SSE striking fault ("main fault" in Fig. 3.2a) has a damage zone width of 400 m based on damage zone scaling relations to the fault displacement (Shipton et al., 2006; Torabi and Berg, 2011), a length of 12 km, and a height of 7 km (ranging from -11 km to -4 km on the Z-axis (Schultz et al., 2006)). In addition, three W-E striking faults ("transfer faults") with 10 m width (along Y-axis) and 100 m height (along Z-axis) are embedded in the sandstone (Fig. 3.2b). To the west of the main fault, the sandstone is located at 3.9 ~ 4.9 km depth; to the east of the main fault, it is located at 4.5 ~ 5.5 km depth due to the 600 m displacement of the main fault. Lithologies that have similar permeability and heat conductivity are merged into a single lithological unit. Basement layers mainly consist of shale, limestone, and sandstone. The claystone and Zechstein are lumped into caprock at the top of the model. The model consists of 174,675 nodes connecting 827,610 tetrahedra, with mesh sizes of

1000 m for low permeability zones and mesh sizes of 100 m for high permeability zones. Preliminary mesh sensitivity analyses were performed to avoid any mesh dependency on the results.

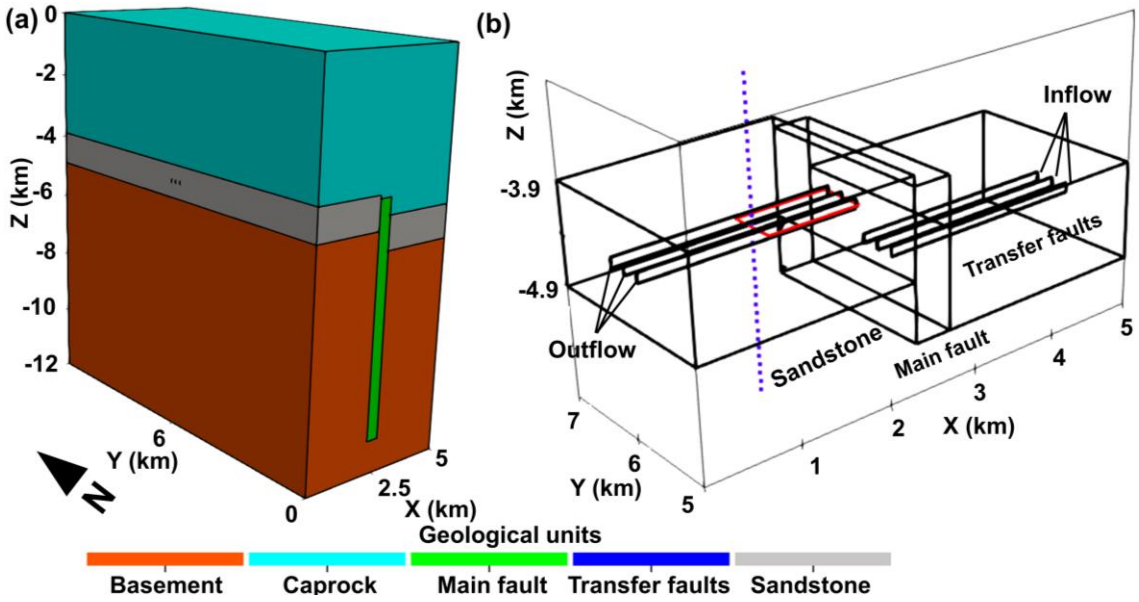

Figure 3.2. Model geometry of (a) the total model; (b) zoomed part of the sandstone reservoir where the transfer faults are embedded. The red rectangle, which is perpendicular to the main fault, represents the outline of the Piesberg Quarry. The dashed purple line shown in (b) is used to illustrate the extent of the temperature-depth profile.

The physical properties of each lithological unit are summarized in Table 3.1. The typical parameterization of main fault permeability (κ_{MF}) and sandstone permeability (κ_{SST}) are 10^{-13} m^2 and 10^{-15} m^2, respectively. The transfer faults permeability (κ_{TF}) is constant at 10^{-13} m^2.

Table 3.1. Parameters of the lithological units (Bruns et al., 2013; Wüstefeld et al., 2017a; Becker et al., 2019; Busch et al., 2019).

Properties	Symbols	Units	Caprock	Main Fault	Sandstone	Transfer faults	Basement
Porosity	n	-	0.01	0.26	0.07	0.26	0.01
Bulk modulus	K_s	Pa	10^{10}	10^{10}	10^{10}	10^{10}	10^{10}
Permeability	k	m^2	$5\cdot10^{-18}$	$10^{-15} \sim 10^{-13}$	$10^{-16} \sim 10^{-14}$	10^{-13}	10^{-20}
Density	ρ^s	kg·m^{-3}	1800	2000	2642	2000	2650
Specific heat capacity	c_p^s	J·kg^{-1}·K^{-1}	1000	1000	1000	1000	1000
Heat conductivity	λ^s	W·m^{-1}·K^{-1}	3	2	2.5	2	2

*The main fault and sandstone permeabilities are abbreviated as κ_{MF} and κ_{SST}, respectively. The subscript MF means the main fault and the subscript SST represents sandstone.

Fluid properties are summarized in Table 3.2. The fluid density is a temperature/pore pressure-dependent variable. The following polynomial function fitting experimental data for pure water in the liquid phase is used to compute fluid density over temperature and pore pressure ranges of 273.15 ~ 1273.15 K and 0 ~ 500 MPa (Linstrom and Mallard, 2001).

$$\rho^l = 1006 - 3.922 \cdot 10^{-1} \cdot (T - 273.15) - 3.774 \cdot 10^{-3} \cdot (T - 273.15)^2 + 2.955 \cdot 10^{-6} \cdot (T - 273.15)^3 + 7.424 \cdot 10^{-7} \cdot p + 4.547 \cdot 10^{-9} \cdot p \cdot (T - 273.15) + 5.698 \cdot 10^{-11} \cdot (T - 273.15)^4 + 7.485 \cdot 10^{-12} \cdot p \cdot (T - 273.15)^2 - 4.441 \cdot 10^{-15} \cdot p^2 + 7.372 \cdot 10^{-15} \cdot p \cdot (T - 273.15)^3 - 1.793 \cdot 10^{-17} \cdot P^2 \cdot (T - 273.15) + 4.018 \cdot 10^{-21} \cdot p^2 \cdot (T - 273.15)^2 + 1.451 \cdot 10^{-23} \cdot p^3 + 1.361 \cdot 10^{-26} \cdot p^3 \cdot (T - 273.15) - 1.463 \cdot 10^{-32} \cdot p^4 \quad (3.4)$$

The dynamic viscosity of the fluid is temperature-dependent and follows the equation (Smith and Chapman (1983)):

$$\mu = 2.414 \cdot 10^{\left(\frac{247.8}{T-144.15} - 5\right)} \quad (3.5)$$

Table 3.2. Fluid properties (Smith and Chapman, 1983; Linstrom and Mallard, 2001; Watanabe et al., 2017)

Properties	Symbols	Units	Value
Coefficient of thermal expansion	β	K^{-1}	$2.14 \cdot 10^{-4}$
Bulk modulus	K_l	Pa	$2 \cdot 10^9$
Density	ρ^l	$kg \cdot m^{-3}$	Eq. (3.4)
Viscosity	μ	Pa·s	Eq. (3.5)
Specific heat capacity	c_p^l	$J \cdot kg^{-1} \cdot K^{-1}$	4194
Heat conductivity	λ^l	$W \cdot m^{-1} \cdot K^{-1}$	0.6

The boundary and initial conditions are set as follows. An air surface pore pressure of 10^5 Pa is fixed at the top of the model as a Dirichlet boundary condition. The initial condition of the hydraulic field corresponds to a hydrostatic gradient. The lateral sides of the model are assigned to no-flow boundary conditions in terms of pore pressure and temperature. The temperature at the top of the model is fixed at 20 °C as a Dirichlet boundary condition. A basal heat flux (BHF) of 0.1 $W \cdot m^{-2}$ represents the sum of the mantle heat flow and the heat emitted by the decay of radioactive elements in the crust (Wisian and Blackwell, 2004b), and is set at the bottom of the model as a Neumann boundary condition. The International Heat Flow database (Lucazeau, 2019) showed two

available surface heat flow data of 0.058 $W \cdot m^{-2}$ and 0.084 $W \cdot m^{-2}$ near the Piesberg Quarry. These data were measured at 60 km southwest and 42 km north of the Piesberg Quarry, respectively. The preliminary tests reveal that a BHF of 0.1 $W \cdot m^{-2}$ is close to the minimum requirement for reproducing the kilometer-scale thermal anomaly of 270 ~ 300 °C in the Piesberg Quarry. A typical threshold of BHF of 0.1 $W \cdot m^{-2}$ for geothermal development is assumed here (e.g., Blackwell et al., 2006; Cloetingh et al., 2010; Erkan, 2015) even though there is no evidence for the high BHF of 0.1 $W \cdot m^{-2}$ near the Piesberg Quarry areas during the Late Jurassic to Early Cretaceous times and at the current time. It must be noted that the magnitudes of these physical characteristics are not significant because the transport mechanism of hydrothermal convection is mostly controlled by permeability distributions of the main fault and sandstone, which can vary by many orders of magnitude. The initial condition of the thermal field is derived from the steady-state simulation of pure heat conduction to avoid the effects of initial temperature perturbation on mass transport and heat transfer. The solution of the initial condition of temperature in our model is shown as follows:

$$T_{\text{initial}}(z) = T_{\text{top}} + \left(\frac{Q_{\text{BHF}}}{n\lambda^{l}+(1-n)\lambda^{s}}\right) \cdot z \tag{3.6}$$

where $T_{\text{initial}}(z)$ is the initial temperature at z (m) position, T_{top} is the imposed surface temperature (°C), and Q_{BHF} is the imposed BHF ($W \cdot m^{-2}$).

Under the coexistence of buoyancy-driven convection, lateral convection, and LRF, Neumann boundary conditions are superimposed on the eastern (as “inflow zones”) and western (as “outflow zones”) boundaries of the transfer faults, respectively (Fig. 3.2b). The transient simulations are run up to 1 Myr, which allows the simulations to reach an approximate thermo-hydraulic equilibrium to compare the results of different transport mechanisms of hydrothermal convection.

5) Simulation cases

Based on the permeability distributions in the reservoir and LRF boundary conditions, the following simulations have been carried out to identify the different fluid flow pathways (Fig. 3.3) and to understand how the reservoir parametrization impacts fluid flow and heat

transport. Rayleigh number (Ra) is a dimensionless number to characterize the fluid's flow regime and is defined as the ratio of buoyancy and viscosity forces multiplied by the ratio of momentum and thermal diffusivities (e.g. Nield and Bejan, 2006):

$$Ra = \frac{k(\rho^l)^2 c_p^l g \beta \Delta T H}{\mu[n\lambda^l + (1-n)\lambda^s]} \tag{3.7}$$

where β is the coefficient of fluid thermal expansion (K^{-1}), ΔT is the temperature variation (K) over the porous media height H (m). The initial temperature and pore pressure of the main fault range from 152.5 °C to 502.3 °C and 39.3 MPa to 108 MPa over its 7 km height, respectively. Thus, according to Eq. (3.4), the density and viscosity of the fluid are 921.5 $kg \cdot m^{-3}$ and $1.8 \cdot 10^{-4}$ Pa·s at the lowest temperature and pore pressure conditions leading to

$$Ra_{\mathrm{MF}} = \frac{10^{-15} \cdot (921.5)^2 \cdot 4200 \cdot 9.81 \cdot 2.14 \cdot 10^{-4} \cdot (502.3\text{-}152.5) \cdot 7000}{1.8 \cdot 10^{-4} \cdot [0.263 \cdot 0.6 + (1\text{-}0.263) \cdot 2]} \approx 63$$

for the lowest permeability (i.e., 10^{-15} m^2) of the main fault in Fig. 3.2a. The *Ra* is proportional to the permeability of the porous media. Buoyancy-driven convection in the main fault (Fig. 3.3, red dashed ovals) is triggered when its *Ra* exceeds the critical Rayleigh number (Ra^{crit}). Furthermore, an analytical solution to calculate Ra^{crit} values for the case of a porous media with dynamic fluid viscosity are shown as follows (Malkovsky and Magri, 2016):

$$Ra^{crit} = 0.25\left[\left(\frac{6.428}{\Delta}\right)^{1.165} + (27.1)^{1.165}\right]^{0.8584} \tag{3.8}$$

with half of the aspect ratio $\Delta = \frac{d}{2H} < 0.1$ where *d* is the thickness of the porous media. In this studied case (Fig. 3.2a), the half aspect ratio of the main fault $\Delta_{MF} \approx 400/(2\ 7000) = 2.9 \cdot 10^{-2}$ leads to the $Ra_{MF}^{crit} \approx 60$ for a temperature-dependent viscous fluid. This estimation suggests that the buoyancy-driven convection likely develops within the main fault even at the lowest permeability and temperature conditions. Furthermore, the presented model on the scale of faulted hydrothermal systems has been successfully validated against the results of the study conducted by Malkovsky and Magri (2016) and Guillou-Frottier et al. (2020). Lateral convection in the sandstone (Fig. 3.3, yellow arrows)

can be enhanced if the pore pressure difference between the sandstone and the main fault decreases (McKenna and Blackwell, 2004). Natural advective flow in the transfer faults (Fig. 3.3, blue vectors) is getting significant when the transfer fault is more permeable than the main fault. Apart from the natural advective flow, forced advection in the transfer faults (Fig. 3.3, green vectors) gets significant if an LRF boundary condition is applied.

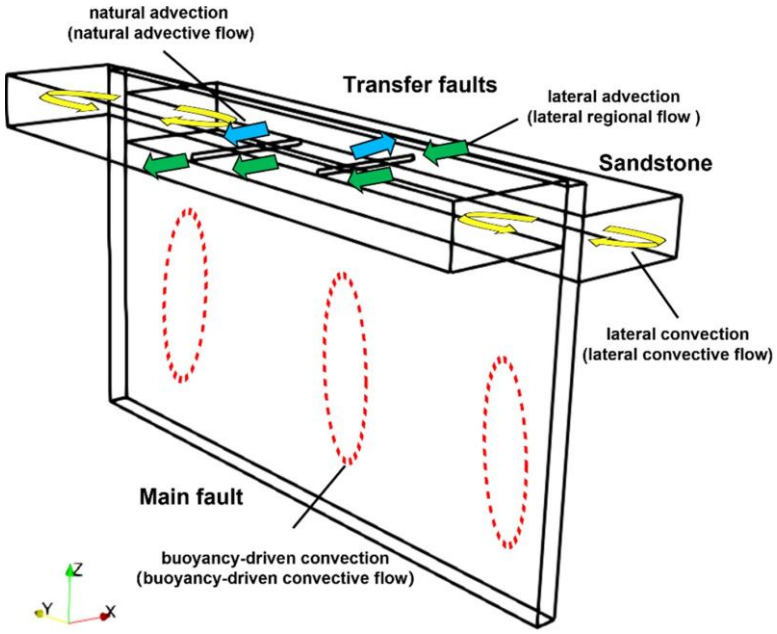

Figure 3.3. Schematic representation of the modeled 3D main fault. Four different types of fluid flow pathways involving the lithological units are illustrated. The 3D main fault account for the relative displacement (i.e., 600 m) of the surrounding lithological units. Only one transfer fault is shown on both sides of the main fault for simplicity.

Herein, a reference case with typical play type parameterization (Table 3.1) has been selected to demonstrate the general behavior of fluid flow pathways and heat transfer types in the hydrothermal convection system. Then a sensitivity analysis is conducted on the κ_{MF} (ranging from 10^{-15} m^2 to 10^{-13} m^2) and κ_{SST} (between 10^{-16} m^2 and 10^{-14} m^2) to identify their effects on the preferential fluid flow pathways and dominant heat transfer types. Then, these above-described permeability cases are superimposed by three representative LRFs. The LRFs range from 10^{-8} m·s^{-1} to $5 \cdot 10^{-7}$ m·s^{-1} (LRF_{max}). Besides the preferential fluid flow pathways and heat transfer types, the mutual interactions between the LRF and convective/advective flows are studied.

Furthermore, the effects of anisotropic and depth-dependent permeabilities on the transport mechanism are discussed. Many researchers show that the degree of

permeability heterogeneity greatly varies even within the meter scale of the lithological unit (Ingebritsen and Manning, 1999; Saar and Manga, 2004). However, our discussion only focuses on the effects of the anisotropic and depth-dependent permeabilities of the main fault on the transport mechanisms. This is because the variation in lithostatic stress and sandstone properties is smaller than that of the main fault, and the low value of median κ_{SST} (i.e. 10^{-15} m^2). Farrell et al. (2014) shown the degree of anisotropy (i.e., horizontal permeability ($\kappa_{MF\_vertical}$)/vertical permeability ($\kappa_{MF\_horzontial}$)) of the fault ranges from one to three orders of magnitude. Thus, the $\kappa_{MF\_horizontal}$ is set at one to three magnitudes (i.e., $10^{-16} \sim 10^{-14}$ m^2) lower than $\kappa_{MF\_vertical}$ (i.e., 10^{-13} m^2), in which the anisotropic κ_{MF} is investigated. Influenced by the in situ lithostatic pressure distribution in the LSB (Manning and Ingebritsen, 1999; Saar and Manga, 2004), the κ_{MF} is exponentially decreased by one to three orders of magnitudes from its top locations (i.e., 10^{-13} m^2 at z = -4 km location) to its bottom locations (i.e., $10^{-16} \sim 10^{-14}$ m^2 at z = - 11 km location). The above anisotropic and depth-dependent variations lie in the inferred ranges by Kuang and Jiao (2014) and Achtziger-Zupančič et al. (2017a).

In this study, the "thermal anomaly" is defined by the computed temperature minus the initial temperature distribution conditions. The maximum temperature at the western boundary of the Piesberg Quarry (T_{max}) is employed to compare with the geothermometer data. The temperature-depth profile following the western boundary of the Piesberg Quarry (Fig. 3.2b) and the Peclet number of the lithological units are used to reveal the temperature distribution with depth and to identify the dominant heat transfer types, respectively. The Peclet number is calculated as the ratio of the heat flow rate by convection to the heat flow rate by conduction for a uniform temperature gradient (Jobmann and Clauser, 1994), as follows:

$$Pe = \frac{\rho^l c_p^l \boldsymbol{q} L}{n\lambda^l + (1-n)\lambda^s} \tag{3.9}$$

where Pe is the Peclet number (-) and L is the length scale of the fluid flow (m). The Peclet numbers are not uniform across lithological units, therefore the statistically median value of the Peclet numbers rather than the Peclet number at a specific location (e.g., geometric center) is used to assess the general heat transfer types within the lithological

units. The statistically median Peclet number of the main fault, transfer faults, and sandstone are abbreviated to Pe_{MF}, Pe_{TF}, and Pe_{SST}, respectively.

3.3 Results

3.3.1 Reference case

A reference case is developed to demonstrate the general behavior of fluid flow pathways and heat transfer types in the hydrothermal convection system, as shown in Fig. 3.4. In the initial state (t = 0 s), the temperature and its gradient increase with depth depending on the thermal conductivities of deep lithological units (black line in Fig. 3.4a). At 1 Myr, the buoyancy-driven convection in the main fault with Pe_{MF} = 9.0 results in thirteen convective cells which consist of seven downflows and upflows in each at the maximum Darcy velocity of $1.1 \cdot 10^{-7}$ m·s^{-1} (Fig. 3.4b). The buoyancy-driven convection is triggered by fluid density variations resulting from the temperature difference. The mentioned upward and downward flows of fluids generate six full and one-half thermal plumes, as shown in Fig. 3.4c. The convective flow transports heat upwards inside the main fault. Thus, compared to the initial temperature distribution (black line in Fig. 3.4a), the buoyancy-driven convection results in positive thermal anomalies ranging between 0 °C and 86 °C in the shallow part of the main fault (i.e., z = - 6 ~ - 4 km locations in Fig. 3.4d).

Initiated by the same permeability of the main fault and transfer faults (i.e., 10^{-13} m^2), the lateral convection in the transfer faults with Pe_{TF} = 0.5 includes fluid recharge and discharge processes at the maximum Darcy velocity of $4.6 \cdot 10^{-8}$ m·s^{-1} as shown in Fig. 3.4b. The heated fluid recharges from the main fault into the shallow part of the transfer faults (i.e., z = - 4.4 ~ - 4.35 km locations) and discharges from the deep part of the transfer faults (i.e., z = - 4.45 ~ - 4.4 km locations) into the main fault, respectively. However, the temperature-depth profile of the reference case (i.e., the red line in Fig. 3.4a) shows that the lateral convection has a negligible effect on increasing the temperature in the transfer faults because of the narrow (i.e., width 10 m) and thin (i.e., thickness 100 m) geometry conditions of the transfer faults and the low permeability of the surrounding sandstone (i.e., 10^{-15} m^2).

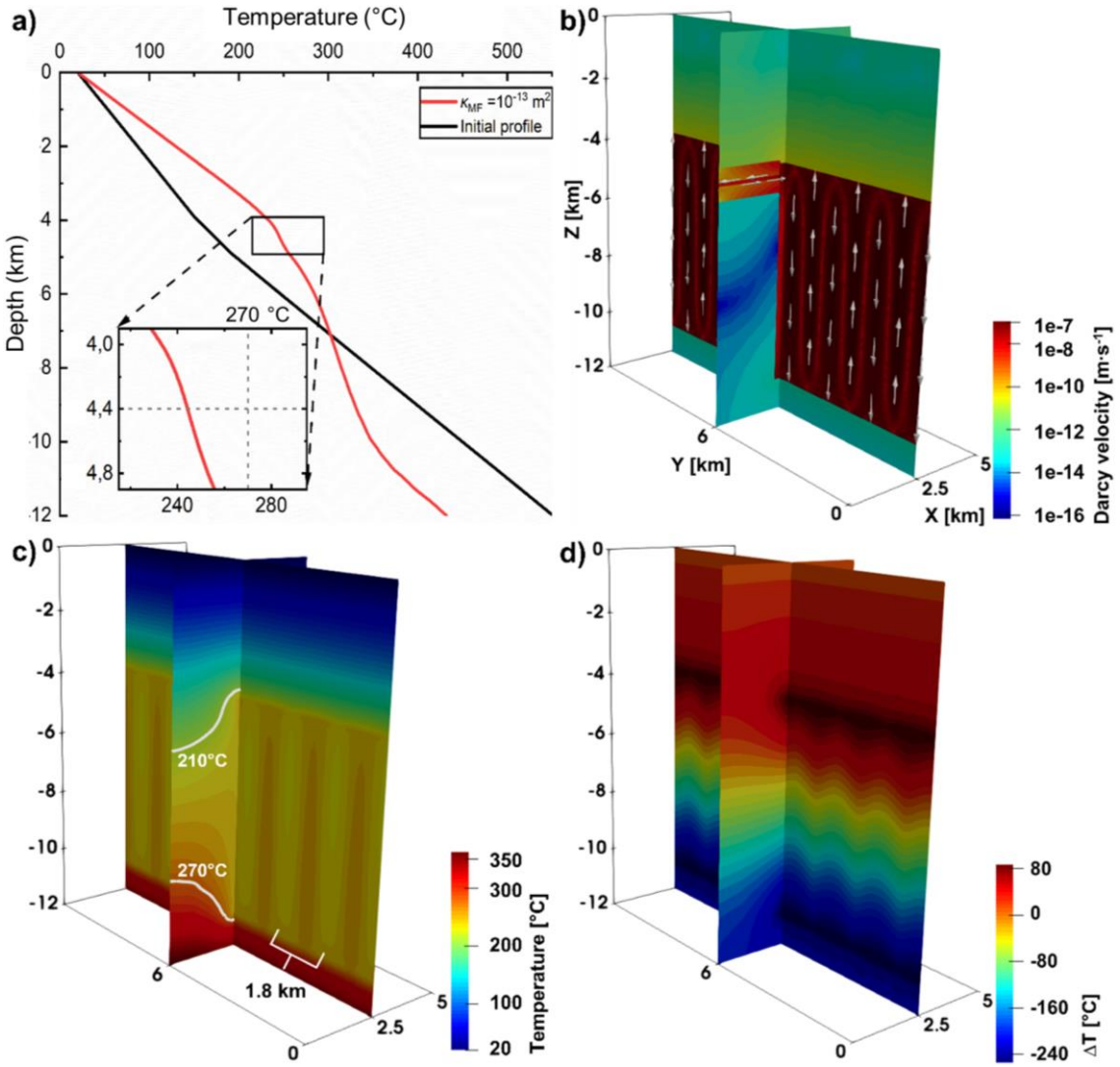

Figure 3.4. Fluid flow and temperature fields of the reference case. (a) Temperature-depth profiles that follow the western boundary of the Piesberg Quarry (Fig. 3.2b) at the initial time and when T_{max} is reached, respectively. At 1 Myr, cross-sectional views of the (b) flow field with arrows representing the preferential fluid flow pathways; (c) resulting temperature distributions. The 210 °C and 270 °C isotherms are highlighted to indicate the dominant heat transfer types; (d) temperature differences compared to the initial conductive temperature distribution.

Figure 3.4b shows that the reference case yields weak fluid flow with Darcy velocity $\leq 5 \cdot 10^{-9}$ m·s^{-1} in the sandstone, caprock, and basement units ("off-faults domains") owing to their relatively low permeabilities (i.e., $\leq 10^{-15}$ m^2). The temperature distribution in the off-fault domains (e.g., Pe < 0.1) is mainly dominated by heat conduction, as shown in Fig. 3.4a and c. Influenced by the thermal anomalies inside the main fault, heat conduction leads to upward-convex isotherms in the units located near the shallow region of the main fault (i.e., z = - 7.5 ~ - 4 km locations in Fig. 3.4c).

However, heat conduction causes downward-convex isotherms in the units located near the deep region of the main fault (i.e., z = - 11 ~ - 7.5 km locations in Fig. 3.4c). The resulting upward- and downward-convex isotherms agree with an increase and decrease in temperature above and below 7 km depth (red line in Fig. 3.4a) compared to the initial temperature profile (black line in Fig. 3.4a), respectively. Additionally, impacted by the convective mass flow, a pore pressure perturbation (~ -2.8 MPa) around the main fault extends ~ 0.3 km in the sandstone and transfer faults at a depth of 4.4 km.

3.3.2 Effects of permeability distributions

1) Main fault

We evaluate how the κ_{MF} variations affect the fluid flow pathways and heat transfer types in the hydrothermal convection system. Their differences compared to the reference case are described as follows. The $\kappa_{MF} = 10^{-14}$ m^2 case results in eight buoyancy-convection cells in the main fault with $Pe\_{MF} = 2.6$ and three times lower maximum Darcy velocity of the convective flow than in the reference case with $\kappa_{MF} = 10^{-13}$ m^2. In addition to the above differences, the $\kappa_{MF} = 10^{-14}$ m^2 case has a similar focused flow in the faults and conduction-dominated heat transfer in the sandstone to the reference case. Results of fluid flow, temperature, and pore pressure change 1 Myr are illustrated in Fig. 3.5 for the $\kappa_{MF} = 10^{-15}$ m^2 case. It is observed in Fig. 3.5a that the $\kappa_{MF} = 10^{-15}$ m^2 case leads to two buoyancy-driven convection cells in the main fault with $Pe\_{MF} = 0.7$ and eight times lower maximum Darcy velocity of the convective flow than in the reference case. Figure 3.5b and c show that the temperature increases in the center of the main fault (~ y = 6 km), associated with the upward flow of fluid, and decreases along the main fault's lateral sides (~ y = 0 and 12 km).

From Fig. 3.5a, it is observed that the lateral convection can be enhanced in the sandstone, especially in the part (i.e., $Pe\_{SST} \geq 0.9$) near the main fault, by the equal κ_{MF} and κ_{SST} (i.e., 10^{-15} m^2). The lateral convection consists of fluid recharge and discharge processes at a maximum Darcy velocity of 10^{-8} m·s^{-1}, slightly lower than the buoyancy-driven convection. The heated fluid recharges from the central part of the main fault into the sandstone and discharges from the sandstone into the main fault's margins, respectively.

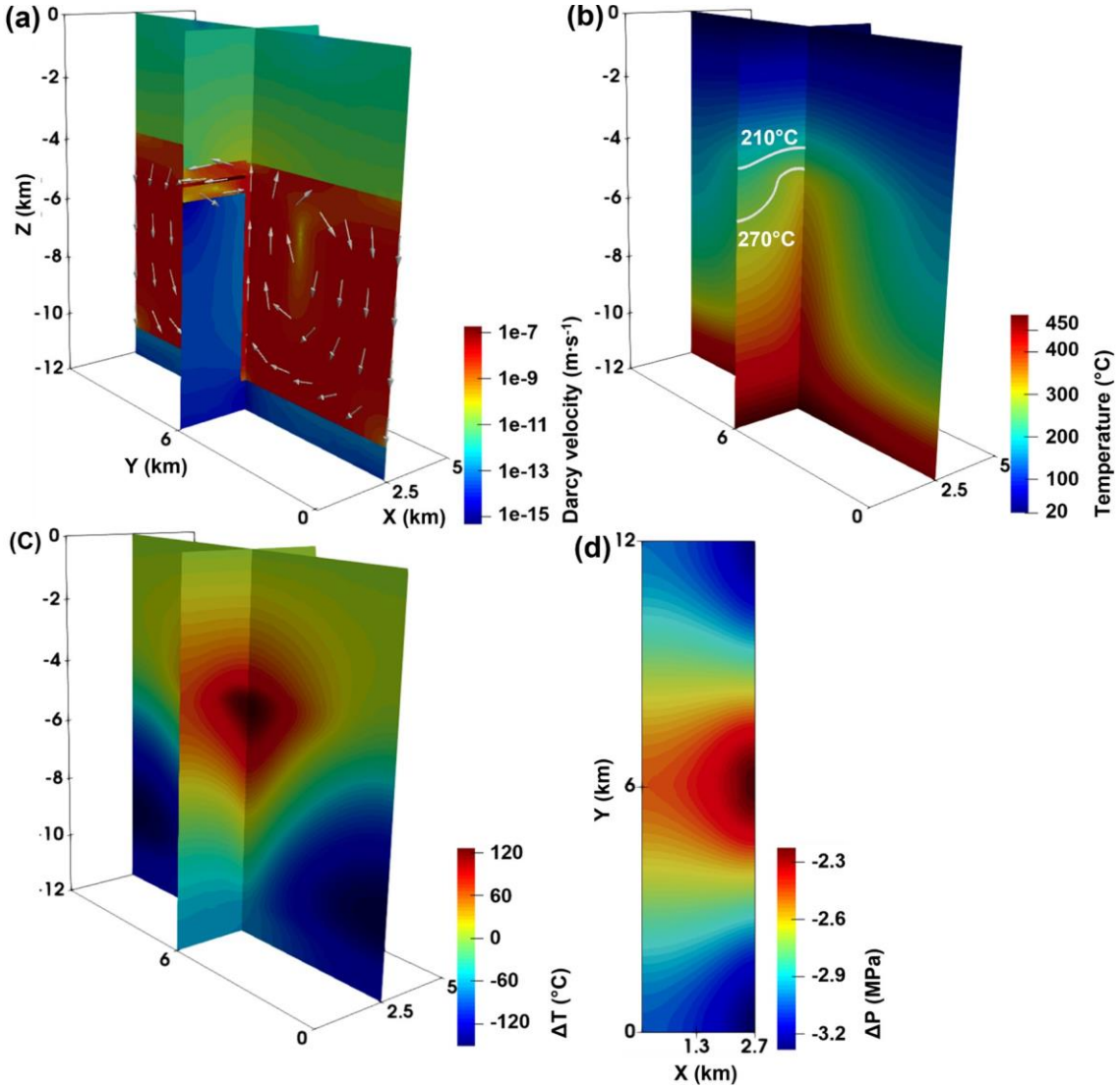

Figure 3.5. Fluid flow, temperature, and pore pressure change fields of the $\kappa_{MF} = 10^{-15}$ m^2 case at 1 Myr. Cross-sectional view of the (a) flow field with arrows representing the preferential fluid flow pathways; (b) resulting temperature field. The 210 °C and 270 °C are highlighted to indicate the dominant heat transfer types; (c) temperature differences compared to the initial conductive temperature distribution; (d) top view of the pore pressure change compared to the initial hydrostatic pore pressure (43.3 MPa) in the western sandstone, transfer faults, and main fault at a depth of 4.4 km. The 1.3 km and 2.7 km along the X-axis follow the west boundary of the Piesberg Quarry and the eastern boundary of the main fault, respectively.

Furthermore, caused by the large permeability contrast between the transfer faults and the main fault (i.e., $\kappa_{TF}/\kappa_{MF} = 100$), the natural advective flow in the transfer faults with $Pe\_{TF} = 3.9$ propagates towards the lateral boundaries of the model as shown in Fig. 3.5a. The maximum Darcy velocity of the natural advective flow reaches $1.7 \cdot 10^{-7}$ m·s^{-1}, which is one order higher than the buoyancy-driven convection. Figure 3.5b and c demonstrate that, compared to the reference case, the increased mass flow involved in the lateral

convection and natural advection effectively causes elevated temperatures in the sandstone and transfer faults near the center of the main fault. Affected by the increased mass flow, the convective/advective flow processes in the main fault, sandstone, and transfer faults result in a larger (~ -3.2 MPa) and more extensive (0 ~ 5 km) pore pressure perturbation than in the reference case as shown in Fig. 3.5d.

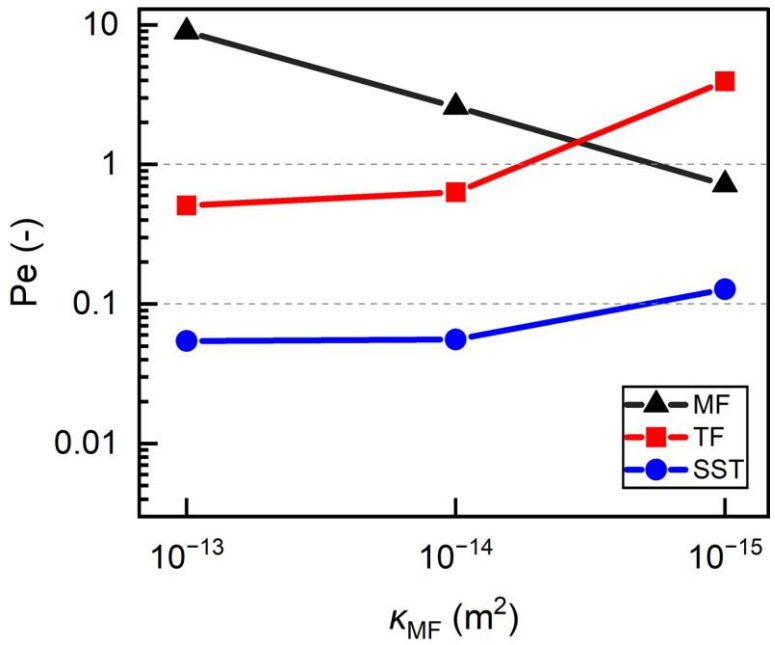

Figure 3.6. Effects of the main fault permeability (κ_{MF}) on the Pe (median Peclet numbers) of the main fault (MF), transfer faults (TF), and sandstone (SST).

In the following, we study how κ_{MF} variations affect the dominant heat transfer types and temperature distribution with depth. With the κ_{MF} decreased from 10^{-13} m^2 to 10^{-15} m^2, the number of convection cells is reduced from thirteen to two, and the maximum Darcy velocity of the buoyancy-driven convective flow is decreased from $1.1 \cdot 10^{-7}$ $m \cdot s^{-1}$ to $1.4 \cdot 10^{-8}$ $m \cdot s^{-1}$ (Figs. 3.4b and 3.5b). These variations show that the intensity of the buoyancy-driven convection within the main fault becomes relatively weak and correspondingly, the $Pe_{\_MF}$ is also decreased from 9.0 to 0.7 as shown in Fig. 3.6. Thus, the upward energy transfer by the buoyancy-driven convection within the main fault is reduced. Conversely, the energy stored at the bottom of the model increases as the κ_{MF} is decreased. This is illustrated by the increase in bottom temperature from 432 °C to 519 °C, as shown in Fig. 3.7.

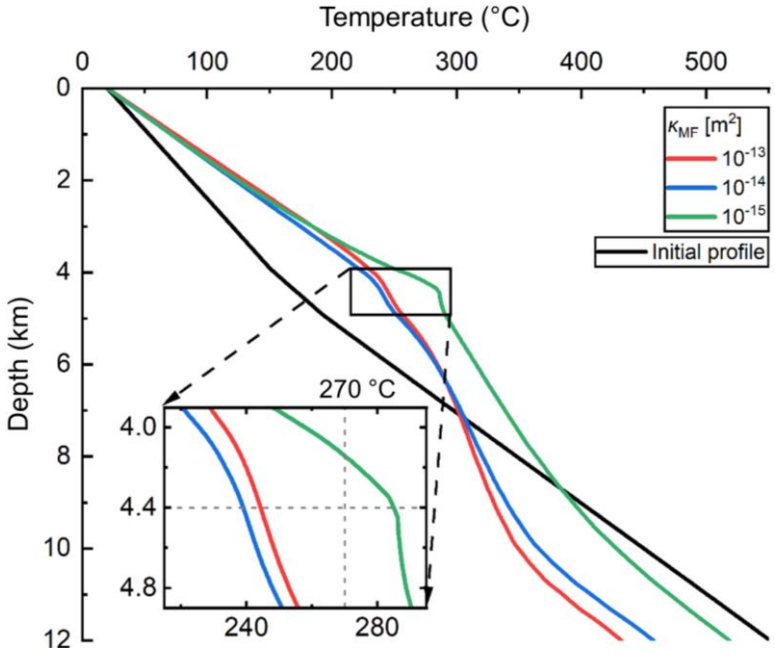

Figure 3.7. Effects of the main fault permeability (κ_{MF}) on the temperature-depth profiles. The $\kappa_{MF} = 10^{-13}$ m^2 case represents the reference case.

Figure 3.6 shows that for the $\kappa_{MF} = 10^{-14}$ m^2 case, fluid flow is mainly confined in the faults and the heat transfer is dominated by conduction in the sandstone with $Pe_{SST} < 0.1$, in agreement with the reference case. Thus, the energy conducted from the main fault and basement into the sandstone is decreased when the κ_{MF} is reduced from 10^{-13} m^2 to 10^{-14} m^2. This is evidenced by the decrease in T_{max} from 244 °C to 239 °C as shown by their temperature-depth profiles (i.e., the red and blue lines in Fig. 3.7). The $\kappa_{MF} = 10^{-15}$ m^2 case (i.e., the green line in Fig. 3.7) results in higher temperature in the range of z = - 12 ~ -3.5 km than the other two cases. This is due to the larger depth extent (i.e., z = - 9 ~ - 4 km locations) and maximum magnitude (i.e., 130 °C) of the positive thermal anomaly (Fig. 3.4d) near the central part of the main fault compared to the reference case (Fig. 3.5c). Furthermore, in the case with $\kappa_{MF} = 10^{-15}$ m^2, the upward energy transfer within the main fault is less than in the other two cases (i.e., $\kappa_{MF} = 10^{-13}$ m^2 and 10^{-14} m^2 cases). However, the enhanced lateral convection and natural advection efficiently increase the fluid and heat flows from the main fault to the sandstone (with $Pe_{SST} = 0.13$) and transfer faults (with $Pe_{TF} = 3.9$), higher than the conduction-dominated heat transfer. Consequently, the temperature increases significantly in the sandstone range of z = - 4.9 ~ - 3.9 km as shown by its temperature-depth profile (blue line in Fig. 3.7),

unlike in the other two cases. $\kappa_{MF} = 10^{-15}$ m^2 results in a higher T_{max} of 285 °C (green line in Fig. 3.7), which is 41 °C higher than the reference case.

2) Sandstone

We investigate the effects of the κ_{SST} variations on the transport mechanisms of the hydrothermal convection system. The $\kappa_{SST} = 10^{-16}$ m^2 case results in eleven buoyancy-convection cells in the main fault with $Pe\_{MF} = 9.1$ and a similar maximum Darcy velocity of the convective flow to the reference case with $\kappa_{SST} = 10^{-15}$ m^2. It has a similar concentrated flow in the faults and conduction-dominated heat transfer in the sandstone to the reference case. Results of fluid flow, temperature, and pore pressure change at 1 Myr are shown in Fig. 3.8 for the $\kappa_{SST} = 10^{-14}$ m^2 case. Focusing on Fig. 3.8b, it is observed in the $\kappa_{MF} = 10^{-14}$ m^2 case leads to fourteen convective cells in the main fault with $Pe\_{MF} = 8.3$ and similar maximum Darcy velocity of the convective flow to the reference case due to their nearly same Pe_{MF} (Fig. 3.9).

Initiated by the high κ_{MF} and κ_{TF}, the lateral convection in the sandstone (i.e., $Pe\_{SST} = 0.5$) and transfer faults (i.e., $Pe\_{TF} = 1.0$) is limited and consists of fluid recharge and discharge processes as shown in Fig. 3.8a. The heated fluid recharges from the main fault into the shallow part (i.e., z = -4.4 ~ -3.9 km locations) of the sandstone and transfer faults and discharges from the deep part (i.e., z = - 4.9 ~ - 4.4 km locations) of the sandstone and transfer faults into the main fault, respectively. The maximum Darcy velocity of the recharge and discharge processes reaches $4.6 \cdot 10^{-8}$ m·s^{-1}, which is ten times higher than in the reference case (Fig. 3.8a). Figure 3.8b and c show that the increased mass flow involved in the lateral convection raises the temperature in the sandstone and transfer faults compared to the reference case. The isotherms of mixed concave-convex shapes in the sandstone range demonstrate that the lateral convection results in a higher temperature rise in the shallow part than the deep part of the sandstone and transfer faults. This is due to the energy and fluid losses in the discharge process. From Fig. 3.8d, it is observed that the lateral convection causes larger (~ -2.9 MPa) and more extensive (~ 1.8 km) pore pressure disturbances in the sandstone and transfer faults at a depth of 4.4 km than in the reference case.

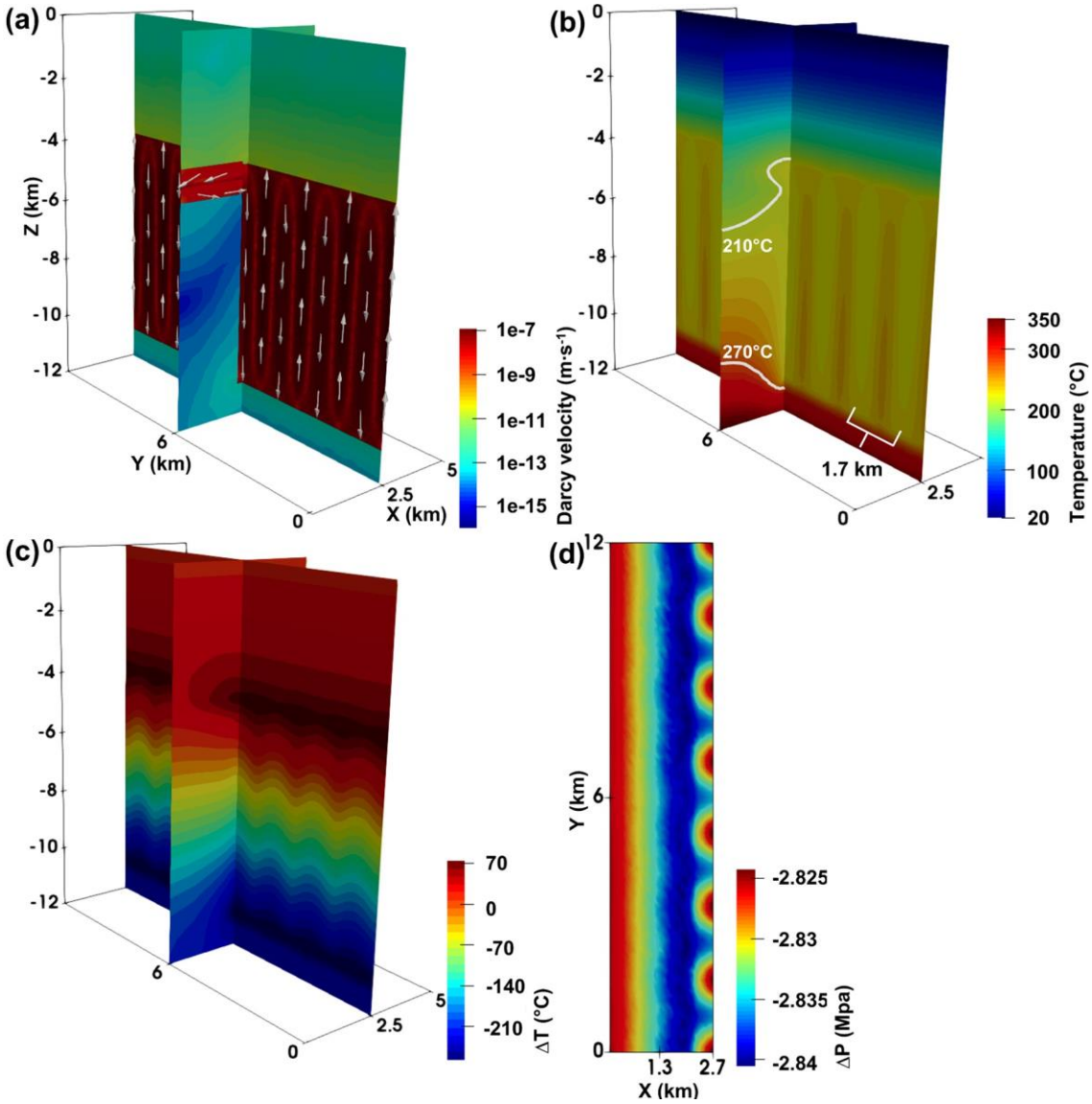

Figure 3.8. Fluid flow, temperature, and pore pressure change fields of the $\kappa_{SST} = 10^{-14}$ case at 1 Myr. Cross-sectional view of the (a) flow field with arrows representing the preferential fluid flow pathways; (b) resulting temperature field. The 210 °C and 270 °C isotherms are highlighted to indicate the dominant heat transfer types; (c) temperature differences compared to the initial conductive temperature distribution; (d) top view of the pore pressure change compared to the initial hydrostatic pore pressure (43.3 MPa) in the western sandstone, transfer faults, and main fault at a depth of 4.4 km. The 1.3 km and 2.7 km along the X-axis follow the west boundary of the Piesberg Quarry and the eastern boundary of the main fault, respectively.

Next, we illustrate how the κ_{SST} variations affect the dominant heat transfer types and temperature distribution with depth. With the κ_{SST} increased from 10^{-16} m^2 to 10^{-14} m^2, the lateral convection in the sandstone and transfer faults is gradually enhanced which is evidenced by the increased Pe_$_{SST}$ from ~ 0 to 0.5 (Fig. 3.9). This is caused by the reduced

pore pressure difference between the main fault and the sandstone due to their decreased permeability contrasts.

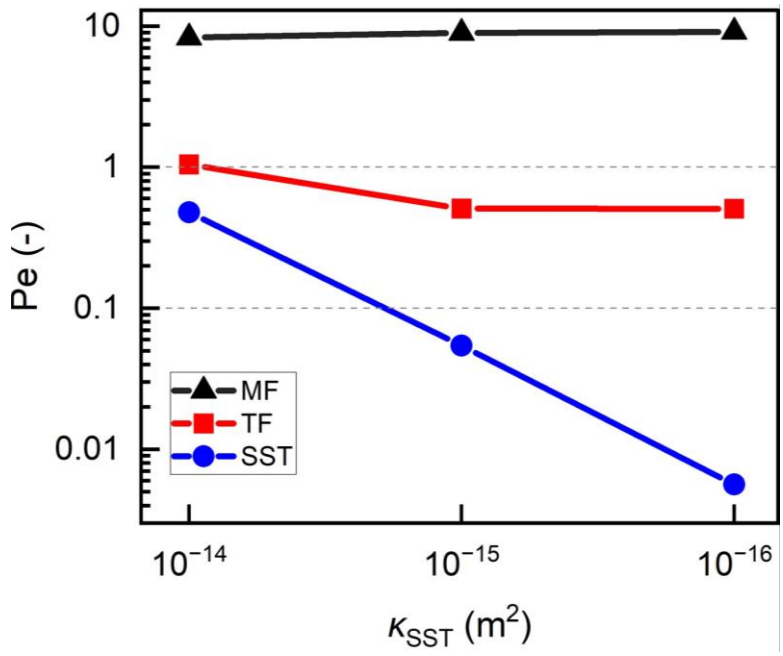

Figure 3.9. Effects of the sandstone permeability (κ_{SST}) on the Pe (median Peclet numbers) of the main fault (MF), transfer faults (TF), and sandstone (SST).

Figure 3.10 illustrates divergent temperature distributions within the 2 km to 5 km depth for all three κ_{SST} cases. The $\kappa_{SST} = 10^{-16}$ m^2 case yields a continuous rise of temperature down to 5 km depth due to conduction-dominated heat transfer in the sandstone ($Pe_{\_SST} \approx 0$) as shown by its temperature-depth profile (i.e., the green line in Fig. 3.10). A slightly decreased T_{max} (i.e., 244 °C) is observed in the reference case (Fig. 3.10, red line) compared to the $\kappa_{SST} = 10^{-16}$ m^2 case (i.e., 248 °C) (Fig. 3.10, green line). The reason is that weak lateral convection ($Pe_{\_SST} = 0.1$) transfers energy into the sandstone away from the main fault and decreases the temperature of the sandstone near the main fault. However, a higher temperature increase within the 2 km to 4.8 km depth is shown for the $\kappa_{SST} = 10^{-14}$ m^2 case (Fig. 3.10, blue line). The T_{max} in the $\kappa_{SST} = 10^{-14}$ m^2 case is 269 °C, which is 25 °C higher than in the reference case. This is due to the increased mass flow involved in the enhanced lateral convection (i.e., $Pe_{\_SST} = 0.5$), which transfers the energy from the main fault into the sandstone, transfer faults, and caprock. The energy and fluid losses in the discharge process cause lower temperature rises than the recharge process in lateral convection. Compared to linear temperature distribution at the initial time, the

mixed concave-convex shapes of the temperature profile (Fig. 3.10, blue line) agree with the isotherms and fluid flow pathways of the lateral convection within the sandstone (Fig. 3.8a and b).

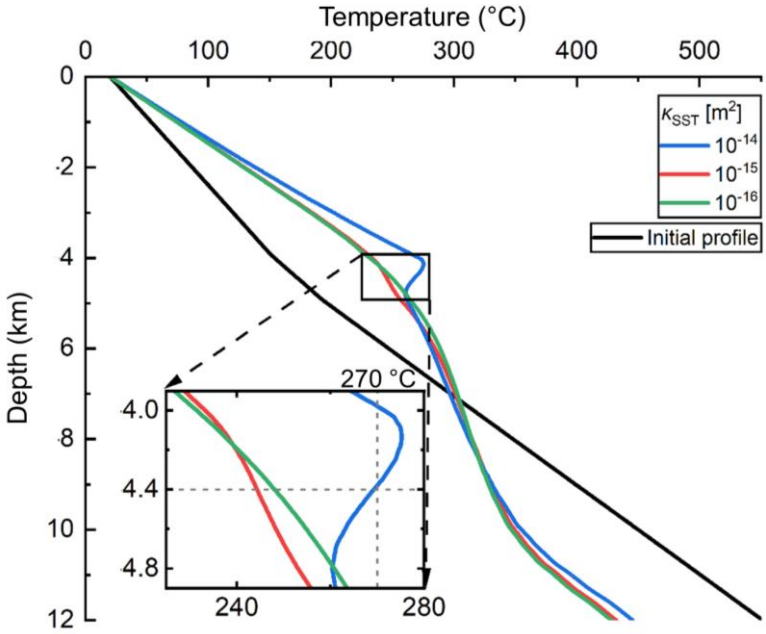

Figure 3.10. Effects of the sandstone permeability (κ_{SST}) on the temperature-depth profiles. The $\kappa_{SST} = 10^{-15}$ m^2 case represents the reference case.

3.3.3 Effects of lateral regional flow

Here we study whether a superimposed LRF changes the fluid flow pathways and types of heat transfer in the hydrothermal convection system. The mutual interaction between LRF and convective/advective flows is also studied. The reference case superimposed by LRFs is used to investigate whether an LRF enhances heat extraction and transfer from the buoyancy-driven convection within the main fault. The results show that forced advection is initiated in the transfer faults only when the LRF exceeds the buoyancy-driven convective flow in the reference case. The dominant heat transfer type in the transfer faults changes from conduction to advection, as proven by the increased $Pe_{\_SST}$ from 0.5 to 2.3 (Schilling et al., 2013). The LRF of $5 \cdot 10^{-7}$ m·s^{-1} superimposed on the reference case increases the T_{max} by 8 °C compared to the reference case without LRF (Table 3.3).

Table 3.3. The effect of maximum lateral regional flow ($LRF_{max}=5\cdot10^{-7}$ m·s^{-1}) on the maximum temperature at the western boundary of the Piesberg Quarry (T_{max}) under different permeability distributions of the main fault (κ_{MF}) and sandstone (κ_{SST}).

Permeability distributions (m^2)		T_{max} (°C)		Effect of LRF_{max} on elevating the T_{max} (°C)
		no LRF	superimposed by LRF_{max}	
κ_{MF}	10^{-13}	244	252	8
	10^{-14}	239	249	10
	10^{-15}	285	314	29
κ_{SST}	10^{-14}	269	271	2
	10^{-15}	244	252	8
	10^{-16}	248	261	13

The interactions between the LRF, buoyancy-driven convective flow, and natural advective flow are shown in the κ_{MF} variation cases in Tale 3.3. As mentioned in '1) Main fault' in Section 3.3.2, the maximum Darcy velocity of the buoyancy-driven convective flow is reduced when κ_{MF} is decreased from 10^{-13} m^2 to 10^{-15} m^2. Therefore, the extent to which the LRF_{max} overwhelms the buoyancy-driven convective flow increases. This is evidenced by the increased Pe_{TF} ranging from 2.3 to 6.7. In contrast, the natural advective flow in the transfer faults gets significant when κ_{MF} is decreased to 10^{-15} m^2. Figure 3.5a shows that the natural advective flow in the western part propagates towards the western boundaries of the model, which is the same as the LRF. Thus, the LRF_{max} can enhance the heat and mass flow in the transfer faults, leading to a larger increase in T_{max} (ranging from 8 °C to 29 °C) compared to the cases without LRF.

The κ_{SST} variation cases in Table 3.3 illustrate the interactions between the LRF, buoyancy-driven convective flow, and lateral convective flow. '2) Sandstone' in Section 3.3.2 shows that the lateral convective flow is gradually weakened (Figs. 3.4b and 3.8a) when κ_{SST} is decreased from 10^{-14} m^2 to 10^{-16} m^2. The maximum Darcy velocity of the buoyancy-driven convective flow is $\sim 1\cdot10^{-7}$ m·s^{-1}, nearly the same in all κ_{SST} cases. Thus, the LRF_{max} can also enhance the heat and mass flows in the sandstone and transfer faults when the κ_{SST} is decreased, causing larger T_{max} (from 2 °C to 13 °C) and increased Pe_{TF} ranging from 2 to 5.4.

According to the above results, the impact of LRF on enhancing the mass and heat flows within the sandstone and transfer faults is reduced for higher κ_{MF} and κ_{SST} cases (López and Smith, 1996; Sheldon et al., 2012). The reason is that the higher κ_{MF} (i.e., 10^{-13} m^2)

and κ_{SST} (i.e., 10^{-14} m^2) lead to a stronger fluid flow and heat transfer in the buoyancy-driven convection and lateral convection, respectively. Thus, the fluid mass fraction that can be impacted by LRF is decreased, resulting in less effect on the increased T_{max} compared to the lower κ_{MF} and κ_{SST} cases.

3.4 Discussions

3.4.1 Effects of the anisotropic and depth-dependent permeabilities

We consider the anisotropic κ_{MF} cases described in Sect. 3.2.3 to study how the anisotropic permeability affects the transport mechanisms. Preliminary tests show that the cases with the one and three orders degree of anisotropy in the κ_{MF} have similar concentrated flow in the faults and conduction-dominated heat transfer in the sandstone to the reference case. They result in a T_{max} of ~ 240 °C, which is 4 °C lower than the reference case. This suggests that the anisotropic main fault acts as a complex pipe-barrier system that favors vertical fluid migration and impedes horizontal fluid migration. In contrast, the κ_{MF} case with two orders of magnitude of anisotropy leads to an elevated temperature in the z = - 7 ~ -3 km range, especially in the sandstone range of z = -4.9 ~ -3.9 km, as shown by its temperature-depth profile (i.e., the blue line in Fig. 3.11). The T_{max} is elevated to 280 °C, which is 36 °C higher than in the reference case. This is caused by the enhanced lateral convection in the sandstone (Pe_{SST} = 0.1) and natural advection in the transfer faults (Pe_{TF} = 4.6) that transfer energy more efficiently than the conduction-dominated heat transfer. The lateral convection and natural advection are initiated by the decreased horizontal permeability contrast between the sandstone and main fault, and the increased horizontal permeability contrast between the transfer faults and main fault, respectively.

The depth-dependent κ_{MF} cases are used to study depth-dependent permeability effects on transport mechanisms. All the depth-dependent κ_{MF} cases have similar focused flow in the faults and conduction-dominated heat transfer in the sandstone to the reference case. However, the number of upward flows within the main fault is decreased in all three cases. When the degree of depth-dependent κ_{MF} is reduced from one to three orders of

magnitudes, the amount of upward transported energy by the buoyancy-driven convection within the main fault is gradually decreased, resulting in a decreased Pe_{MF}, ranging between 6.7 and 0.9. The T_{max} is decreased from 217 °C to 195 °C with the decreased degree of depth-dependent κ_{MF}. Inferred from the in situ lithostatic pressure distribution in the LSB (Manning and Ingebritsen, 1999; Saar and Manga, 2004), the κ_{MF} is exponentially decreased by two orders of magnitudes from its top locations to its bottom locations. Its equation is shown as

$$\kappa_{MF}(z) = 10^{-13} \cdot e^{\frac{z+4000}{1520}} \tag{3.10}$$

where z is the location (m) and $\kappa_{MF}(z)$ is the main fault permeability (m^2) at the z (m) location. The resulting temperature profile is shown by its temperature-depth profile (i.e., the green line in Fig. 3.11) with a T_{max} of 207 °C.

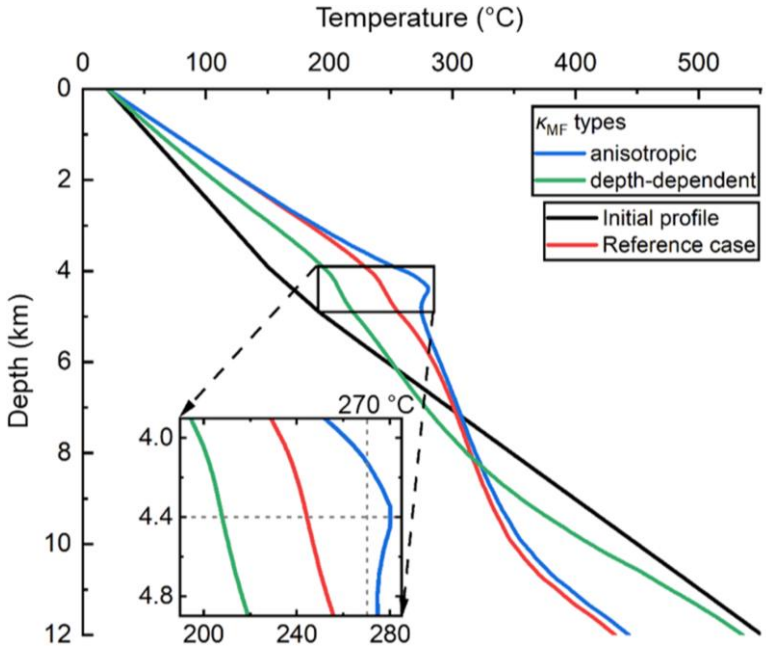

Figure 3.11. Effects of the anisotropic and depth-dependent permeabilities of the main fault (κ_{MF}) on the temperature-depth profiles.

The anisotropic permeability cases prove that the onset of lateral convection and natural advection relies on the horizontal permeability contrast between the sandstone and main fault, and the horizontal permeability contrast between the transfer faults and main fault, respectively. Influenced by the increasing lithostatic pressure with depth, the mass flow and heat transfer of the buoyancy-driven convection is gradually weakened in the main

fault. Thus, the main controlling parameter of the transport mechanism is detailed from the idealized permeability distributions into the spatial permeability distributions of the main fault and sandstone.

3.4.2 Implications for the kilometer-scale thermal anomaly in the Piesberg Quarry and comparable reservoirs

Our study performs the first numerical investigation of possible reasons for the kilometer-scale thermal anomaly (270 ~ 300 °C) in the Piesberg Quarry. Since only the geothermometry data from the outcrop samples in the Piesberg Quarry are available, our discussion will be limited to the thermal profiles at 4.4 km depth where the Piesberg Quarry was located during Late Jurassic-Early Cretaceous. The relation between temperatures and mass flows within the sandstone and transfer faults (shown in Figs. 3.4, 3.5, 3.8, 3.11 and Table 3.3) suggests that the thermal anomaly results from the coexisting of the buoyancy-driven convection in the main fault, lateral convection in the sandstone rather than from conduction-dominated heat transfer. Both buoyancy-driven convection in the main fault and lateral convection are indispensable to reproducing the measured thermal anomaly. Therein, the buoyancy-driven convection in the main fault is an essential prerequisite for the formation of high temperatures in relatively shallow depths because it can transport heat from deeper to shallow depths (Kohl et al., 2000; Bächler et al., 2003). Moreover, the main role played by lateral convection in the sandstone is to redistribute both heat and fluid mass within the sandstone (Wisian and Blackwell, 2004a), as shown in Fig. 3.3 and the results obtained in Sect. 3.3. However, the hypothetical LRF mimicking the effect of topography on the transport mechanisms behave less important than buoyancy-driven convection and lateral convection according to the elevating the T_{max} by LRF (Table 3.3). Favorable permeability distributions for reproducing the measured thermal anomaly include moderately permeable sandstone (i.e., 10^{-14} m^2), same permeabilities (i.e., 10^{-15} m^2) in the main fault and sandstone, and the anisotropic case of the main fault (i.e., $\kappa_{MF\_vertical}/\kappa_{MF\_horizontal}$ = 10^{-13} $m^2/10^{-15}$ m^2). The T_{max} obtained from the simulations for these three cases are 269 °C, 285 °C, and 280 °C, respectively. These results show that the measured thermal anomaly can be reproduced only if the κ_{MF} is equal to or greater than 10^{-15} m^2, meanwhile, the ratio of $\kappa_{SST\_horizontal}$ to $\kappa_{MF\ horizontal}$ is equal to or greater than 1. Thus, the magnitude of the κ_{MF} and the ratio of $\kappa_{SST\_horizontal}$ to κ_{MF}

horizontal are the determinative factors of the formation of the kilometer-scale thermal anomaly (270 ~ 300 °C) in the Piesberg Quarry, rather than the LRF. Wuestefeld et al. (2014) and Becker et al. (2019) study the permeability heterogeneity properties in the Piesberg Quarry. Based on the in situ geological and petrophysical properties (i.e., mean permeability distribution, heterogeneities) around Piesberg Quarry and within the LSB (Wuestefeld et al., 2014; Wüstefeld et al., 2017a; Becker et al., 2019), the increased mass flows involved in the coexisting flow modes resulting from the anisotropic case of the main fault (i.e., $\kappa_{MF\_vertical}/\kappa_{MF\_horizontal} = 10^{-13}\ m^2/10^{-15}\ m^2$), provide the most realistic permeability distribution case to explain the thermal anomaly in the Piesberg Quarry.

In order to make geothermal projects more economically attractive, especially in sedimentary basins (e.g., LSB) with constraint conditions (e.g., low permeability and temperature gradient), fractured/faulted zones are preferentially targeted as valuable geothermal reservoirs (Bruns et al., 2013). As shown in the reference case (Fig. 3.4), the upward fluid flow within the main fault leads to positive thermal anomalies (i.e., at a maximum of 86 °C) in a relatively shallow depth (~ 4 km). The relatively shallow locations of geothermal reservoirs greatly decrease the investments (i.e., the costs of drilling and completions) for developing geothermal energy in the sedimentary basin (Huenges and Ledru, 2010). The processes within geothermal reservoirs have important consequences for their successful exploration since the interesting scale at which thermal anomalies could be exploited greatly depend on the heat transfer types and fluid flow pathways (Huenges and Ledru, 2010; Przybycin et al., 2017). If the temperature anomaly is assumed to persist to the present and geologic conditions are constant, for the given reference case geothermal drilling should target the kilometer-scale elevated temperatures (i.e., 2.8 km on the x-axis; 12 km on the y-axis; 2.8 km on the z-axis) around the depth of 4 km (Fig. 3.4). Our 3D numerical model allows for a better understanding of the processes within geothermal reservoirs (e.g., the role of different selected parameters in the origin, location, scale, and magnitude of thermal anomalies), thus providing tools for predicting and targeting geothermal exploration (Clauser and Villinger, 1990; Guillou-Frottier et al., 2013).

3.5 Conclusions

Inspired by the Piesberg Quarry in northwestern Germany and its established thermal anomaly, we created an idealized numerical model to derive parameters and processes that cause the onset of thermal anomalies in comparable geological settings. The study focused on the developments and mutual interactions of predominant heat transfer types and preferential fluid flow pathways in faulted tight sandstones. The hydraulic parameterizations of the main fault and sandstone are crucial for inferring the mechanisms causing the transport of fluid and heat. Buoyancy-driven convection transports energy upward inside the main fault. Induced by favorable hydraulic conditions (e.g., high sandstone permeability of 10^{-14} m^2; equal permeability of 10^{-15} m^2 of the main fault and sandstone), convective flow in the sandstone and advective flow in the transfer faults redistribute both heat and fluid within the reservoir, causing elevated temperatures ($\geq$ 269 °C) and thermal gradients in the sandstones compared to conduction-dominated heat transfer ($\leq$ 250 °C). Lateral regional flow can interact with convective/advective flows in the sandstone and transfer faults and changes the dominant heat transfer from conduction to advection in the transfer faults when it overwhelms the magnitude of the convective flows in the main fault and sandstone. However, its influence is limited by the geometric and hydraulic constraints of the transfer faults and, therefore, significantly reduced compared to the influence of the local permeability distribution. The anisotropic and depth-dependent permeability cases detail the main controlling parameter of the transport mechanism into the spatial permeability distributions of the main fault and sandstone.

The magnitude of the main fault permeability and the ratio of the horizontal permeability of the sandstone to the horizontal permeability of the main fault are the determining factors in the formation of the thermal anomaly at the Piesberg quarry, rather than topographic conditions. The increased mass flows involved in the coexisting flow modes resulting from the anisotropic case of the main fault (i.e., $\kappa_{MF\_vertical}/\kappa_{MF\_horizontal} = 10^{-13}$ $m^2/10^{-15}$ m^2), provide the most realistic explanation for the kilometer-scale elevated temperature of 270 ~ 300 °C in the Piesberg Quarry. Our study proves that fractured/faulted zones in tight sandstone reservoirs (a common petroleum reservoir play type) and associated thermal anomalies may be preferred geothermal reservoirs in

sedimentary basins worldwide (e.g., LSB). Our 3D numerical model also provides predictive tools for the origin, location, scale, and magnitude of exploitable geothermal reservoirs. More processes (i.e., chemistry and (geo-)mechanics) should be investigated in the further step for the fully coupled transport mechanisms in faulted tight sandstones.

4 Single well temperature-reporting nanoparticle tracer test for fractured geothermal reservoir characterization

This part is reproduced from the manuscript that is prepared for the submission to a peer-reviewed journal.

***Yan, G.**, P. Ø., Qiao & Kohl, T. (2024). Single well temperature-reporting nanoparticle tracer test for fractured geothermal reservoir characterization. (in preparation)*

Abstract

Characterizing temperature distributions within fractured geothermal reservoirs is essential for advancing geothermal energy applications. Temperature-reporting nanoparticle tracers present a valuable technique for mapping reservoir temperatures, yet previous studies have emphasized doublet tracer tests, which can obscure localized variations due to the fixed distance between separate injection and production wells. In contrast, single-well tracer tests, where tracers are both injected and retrieved from a single well, provide a means to capture detailed, site-specific temperature profiles, especially when optimized for reservoir heterogeneities. This study applies a comprehensive numerical model to explore single-well nanoparticle tracer tests within fractured geothermal reservoirs, examining how varying injection-production positions and wellbore open-hole length affect tracer response and temperature sensitivity. In the numerical model, water circulation within the reservoir lasts for 1 year, whereas nanotracer injection are only injected in the first four hours. The injection process lasts for 30 days, after which production begins. Our simulations reveal that the spatial positioning of injection and production points within a single well allows for targeted

probing of temperature gradients, while adjusted push-pull durations increase the temporal resolution of tracer responses. Additionally, different injection methods provide unique insights: single-point injection excel at detecting localized temperature anomalies, while line-source injections help reveal patterns within the broader temperature range. Findings from tracer breakthrough curves and peak concentration deviations demonstrate that well-optimized single-well tracer tests can accurately delineate both the thermal profile and geological heterogeneities within geothermal reservoirs. This work underscores the potential of single-well nanoparticle tracer tests as advanced, high-resolution diagnostic tools, where strategic choices in injection configuration, timing, and method can maximize information on reservoir characteristics essential for geothermal energy development.

4.1 Introduction

Geothermal energy which is the heat stored within the earth's subsurface has emerged as a clean, renewable, and sustainable alternative to traditional energy sources of fossil fuels for direct utilization and electricity generation (Moeck, 2014). Most of the geothermal energy that can be utilized by conventional technologies is located in dry and impermeable rocks, which are not sufficient to extract the energy (Lund, 2008). To move away from the limitations of the conventional hydrothermal geothermal energy system, which is heavily dependent on sufficient water, heat, and permeability in the rocks, enhanced geothermal system (EGS) technology has been proposed to expand the availability of geothermal resources in dry and impermeable rocks (Duchane, 2002). EGS refers to geothermal systems that improve reservoir permeability through stimulation methods, creating new fractures by injecting pressurized fluids into the target reservoir and extending natural fractures by breaking up the rock (Kumari, 2019). The reservoir characteristics of the EGS (e.g., temperature, well-to-well connectivity, volume of fractured zone, heat-transfer surface area, fluid composition, and saturation, etc.) are improved to extract sufficient geothermal energy after stimulation operations.

Thus, evaluating the effectiveness of stimulation operations in improving reservoir properties and providing feedback for guiding next-step stimulation operations needs to

be determined before and after stimulation operations (Xu et.al., 2012). Furthermore, reservoir characterization is needed both for assessing the potential of underground usage in terms of geothermal power generation and for the management and maintenance of operational plants (Domra Kana et al., 2015; Lu, 2018).

However, the inaccessibility of subsurface reservoirs, buried kilometers underground and located in dense lithologies make reservoir characterization a complicated task. Tracer tests are widely used to evaluate variations in reservoir characteristics including inter-well connectivity, fracture volume, and heat transfer surface areas during the drilling, fracturing, and producing processes of hydrocarbon or geothermal reservoirs (Hawkins et al., 2018; Wu et al., 2021; Ren et al., 2023). The break-through curves (BTCs) of tracers can provide a variety of useful, quantitative data depending on the type of tracer used (conservative or reactive types). Meanwhile, this data can be used to give an advanced warning of projected thermal drawdown in the reservoir or thermal breakthrough of re-injected fluids and may therefore improve the reservoir operation and reduce financial risk (e.g. Pruess and Bodvarsson, 1984; Axelsson et al., 2001). Among all reservoir characteristics of the EGS, reservoir temperature is critical for assessing the potential for geothermal energy extraction. It helps determine the viability of geothermal power generation and provides insights into fluid behavior within the reservoir.

Reactive tracers have long been investigated as a means to measure geothermal temperature profiles, but this method has only been used in practice to estimate an effective (or average) reservoir temperature (Robinson et al., 1984). This means that spatial information about the temperature profile is lost. Functional temperature-sensitive tracers in response to temperature variations have emerged as effective tools for characterizing the response behavior of geothermal reservoirs, offering the potential to extend above limited information. By injecting these tracers into the reservoir and monitoring their behavior over time, valuable insights can be obtained regarding the complex flow dynamics, heat transfer mechanisms, and reservoir heterogeneity within a 3D geothermal system (Ames et al., 2015). Williams et al. (2010) proposed a dye-release mechanism, in which encapsulated dyes are released once a threshold temperature is reached. Maier et al., (2015a, b) showed the application of tracers with thermo-sensitive properties to track the thermal state of a geothermal reservoir has been demonstrated as a

promising tool in the laboratory. Ames et al. (2015) used one-dimensional analytical models to separately calculate temperature distribution and tracer return curves, illustrating the potential utility of threshold reactive tracers as geothermal temperature sensors. Alaskar et al. (2015) demonstrated the potential of irreversible thermochromic microspheres and dye-attached silica nanoparticles as temperature sensors to measure the temperature of subsurface reservoirs. Rudolph et al. (2020) developed thermo-reporting nanoparticles with threshold temperature that triggered the irreversible release of the outer dye for accurate sensing of geothermal reservoir conditions. Reimus et al. (2020) successfully estimated the seepage and heat-transfer characteristics of geothermal reservoirs using conservative tracers, thermal degradation tracers, and adsorption tracers.

However, the released works lacks of three-dimensional (3D) reservoir-scale numerical tests and analysis on functional temperature-reporting nanotracers in EGS, which was only focusing on theoretical and laboratory research in previous studies. Yan et al. (2024) predicted reservoir temperature distributions and characterized geological heterogeneities by modeling nanotracer flow in doublet geothermal reservoirs. While general tracers have been extensively studied in various applications, including hydrology and oil and gas reservoir engineering, temperature-reporting tracers' utilization and response behavior in 3D geothermal reservoirs remains relatively underexplored in the single-well tracer test. The complex interplay between thermal gradients, fluid flow pathways, and reservoir heterogeneity poses unique challenges and necessitates a specialized investigation. It is challenging to infer the in-situ temperature distribution, existence, and geometry of the permeable or impermeable zones in the geothermal reservoir based on the produced temperature-reporting tracer data. In addition, effective design and implementation of temperature-reporting tracer tests for geothermal reservoirs still need scientific verification.

Thus, this work aims to address this knowledge gap by conducting numerical simulations to investigate the transport mechanisms of temperature-reporting nanotracer in 3D single-well geothermal reservoir models for the sustainable utilization of this valuable energy source. In this study, we first present the methodology employed in our study, including the reaction mechanism of temperature-reporting tracers and numerical modeling approaches; then, the potential of temperature-reporting temperature-reporting tracers in

single well tracer test and the effect of well placement on the temperature-reporting tracers responses are quantified in a 3D EGS model.

4.2 Materials and methods

In this work, a liquid solution is injected into the EGS reservoir through the single well for a short period, following which water injection and then production. This solution contains a mixture of water and temperature-reporting tracers with different temperature thresholds. The tracer breakthrough data are monitored in the single wellhead during the production process.

During above operation, the physical and chemical processes consist of fluid and tracer flow, heat transfer and reaction of temperature-reporting tracers in the reservoir. The numerical simulations for such processes are carried out using our in-house codes which are built on the finite element simulator-PorousFlow module (Wilkins et al., 2021) within the MOOSE framework (Permann et al., 2020). The relevant equations are described in detail below.

4.2.1 Governing equations

1) Fluid flow and heat transfer

Firstly, the fluid transport equation for slightly compressible and single-phase liquid flow in the porous media is written as:

$$S_m \frac{\partial p}{\partial t} + \nabla \cdot \boldsymbol{q} = 0 \tag{4.1}$$

where the subscript *m* refers to porous media, S_m is the constrained specific storage of the porous media (Pa^{-1}), p is the pore pressure (Pa), t represents time (s) and $\boldsymbol{q}$ is the Darcy velocity ($m \cdot s^{-1}$). S_m is assumed a constant expressed by:

$$S_m = (1 - \phi)/K^s + n/K^l \tag{4.2}$$

with porosity ϕ (-), the bulk moduli of solid K^s and liquid K^l (Pa). The Darcy velocity $\boldsymbol{q}$ is given as:

$$\boldsymbol{q} = \frac{k}{\mu}(-\nabla p + \rho^l \boldsymbol{g}) \tag{4.3}$$

where k is the permeability (m^2), μ refers to the fluid viscosity (Pa·s), superscript l denotes the liquid phase, ρ^l is the fluid density ($kg \cdot m^{-3}$) and $\boldsymbol{g}$ is the gravitational acceleration ($m \cdot s^{-2}$).

Secondly, the heat transfer equation for both solid and fluid in the porous media is written as:

$$\left[\phi c_p^l \rho^l + (1-\phi) c_p^s \rho^s\right] \frac{\partial T}{\partial t} - \left[\phi \lambda^l + (1-\phi)\lambda^s\right] \nabla^2 T + \rho^l c_p{}^l \mathbf{q} \nabla T - Q_T = 0 \tag{4.4}$$

where the four terms on the left side individually represent a transient variation of temperature, heat conduction, heat convection and heat source term. The superscript s represents solid, c_p^l and c_p^s are separately the specific heat capacity of liquid and solid ($J \cdot m^{-3} \cdot K^{-1}$), ρ^s denotes the solid density ($kg \cdot m^{-3}$), T is the temperature (K), λ^l and λ^s refers to the heat conductivity of the liquid and solid ($W \cdot m^{-1} \cdot K^{-1}$) and Q_T is the heat source ($W \cdot m^{-3}$).

2) General tracer transport

The advection-diffusion equation governing the spatial and temporal changes of the tracer concentration in porous media is as follows:

$$\frac{\partial C}{\partial t} - \nabla \cdot (\boldsymbol{D} \nabla C) + \nabla \cdot (\boldsymbol{q} C) - Q_C = 0 \tag{4.5}$$

where C is the tracer concentration ($kg \cdot m^{-3}$), $\boldsymbol{D}$ refers to its diffusion coefficient ($m^2 \cdot s^{-1}$) and Q_C represents the mass source of tracer ($kg \cdot m^{-3} \cdot s^{-1}$).

3) Temperature-reporting tracer reaction and flow

(1) Temperature-reporting tracer reaction

Figure 4.1 illustrates the working mechanism of the temperature-reporting tracer. Specifically, the hull melts/degrades, dye is released and the structure of the developed developed tracer (reactant) are changes when the environment temperature exceeds the temperature threshold of the temperature-reporting tracer. The product resulting from

such a reaction is the target of our detection. The reaction rate of a temperature-reporting tracer is dependent on conversion within it but independent of the concentration present nearby. Thus, in this work, the diffusion of the temperature-reporting tracer is not considered by setting $\boldsymbol{D}$=**0** in Eq. (4.5). We refer to Rudolph et al. (2020) for more details.

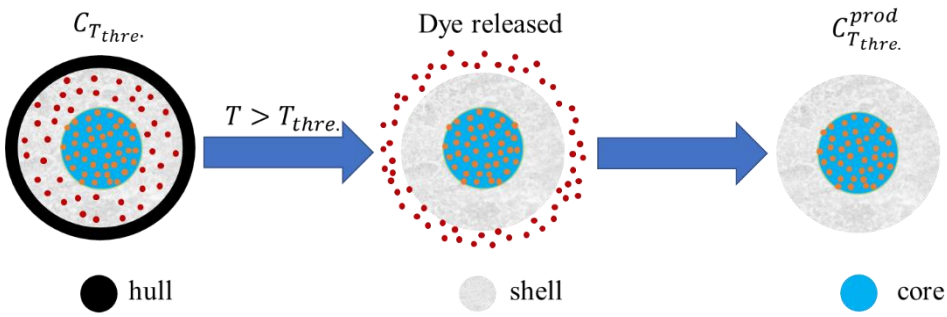

Figure 4.1. Schematic representation of the working mechanism of temperature-reporting tracers: the dye released from the shell of the nanoparticles upon exceeding the temperature threshold (reproduced from Rudolph et al. (2020)).

We present our numerical approach for simulating the temperature-reporting tracers' reaction in the following. Referring to Fig. 4.1, the relevant reaction can be described as follows:

$$C^{reac.\,n}_{T_{thre.}} \xrightarrow{T>T_{thre.}} C^{prod.^n}_{T_{thre.}} \tag{4.6}$$

where n represents the current time step, $C^{reac.}_{T_{thre.}}$ denotes the concentration of reactant and $C^{prod.}_{T_{thre.}}$ is the corresponding product's concentration after the reaction. $T_{thre.}$ refers to the temperature threshold of reactant.

Equation (4.6) indicates a sharp conversion process of the injected tracers/reactants. To release this constraint, we include a transition factor Z in the following reaction expression for temperature-reporting tracers:

$$(C^{reac.\,n}_{T_{thre.}})^{updated} = Z^n \cdot C^{reac.\,n}_{T_{thre.}} \tag{4.7}$$

where $(C^{reac.\,n}_{T_{thre.}})^{updated}$ represents the newly updated concentration of the reactant after reaction (at time step n) and Z is defined below:

$$Z = \begin{cases} 1, & T < (T_{thre.} - a); \\ \frac{1}{1+e^{b\cdot(T-T_{thre.})}}, & (T_{thre.} - a) \le T \le (T_{thre.} + a); \\ 0, & T > (T_{thre.} + a). \end{cases} \tag{4.8}$$

where a and b are two constants that can be controlled such that a smooth transition between 100% and 0% tracer conversion can be achieved when environment temperature T is nearby the tracer temperature threshold $T_{thre.}$. In our work, this transition temperature range is set to be very narrow by choosing a=0.01 and b=50, respectively. Clearly, when the temperature is higher than the tracer's threshold ($Z = 0$), the remaining reactant concentration becomes zero in Eq. (4.7), meaning a 100% conversion.

The product concentration after reaction at the time step n is updated with:

$$(C_{T_{thre.}}^{prod.^n})^{updated} = (1 - Z^n) \cdot C_{T_{thre.}}^{reac.^n} + C_{T_{thre.}}^{prod.^n} \tag{4.9}$$

where the two parts on the right side separately refer to the concentration increase of the product after the reaction and product concentration at time step n.

(2) Temperature-reporting tracer transport

According to updated concentration expressions of reactant and product in Eqs. (4.7) and (4.9), the resulting transport equations of temperature-reporting reactants and products based on Eq. (4.5) are shown as follows.

$$\frac{C_{T_{thre.}}^{reac.\ n} - Z^{n-1} C_{T_{thre.}}^{reac.\ n-1}}{\Delta t} + \nabla \cdot \left(\boldsymbol{q}^n C_{T_{thre.}}^{reac.^n}\right) - Q_{C_{T_{thre.}}^{reac.\ n}} = 0 \tag{4.10}$$

$$\frac{C_{T_{thre.}}^{prod.\ n} - \left[(1 - Z^{n-1}) C_{T_{thre.}}^{reac.\ n-1} + C_{T_{thre.}}^{prod.\ n-1}\right]}{\Delta t} + \nabla \cdot \left(\boldsymbol{q}^n C_{T_{thre.}}^{prod.^n}\right) - Q_{C_{T_{thre.}}^{prod.\ n}} = 0 \tag{4.11}$$

Note that in this work: 1) each temperature-reporting tracer with one temperature threshold has a group of the above two equations for both reactant and product; 2) we assume the tracers are well mixture with water and the segregation between water and tracer is ignored.

4.2.2 Model settings

Our model is inspired by a typical fractured reservoir setting such as Soultz-sous-Forêts EGS (Egert et al., 2020) which contains several irregularly distributed fractures. A highly permeable and thin reservoir is used to mimic a fracture in this study (parametrization of individual models, see below). We use the model settings illustrated in Fig. 4.2a. The reservoir model consists of two 600 m thick types, an inner stimulated (called 'inner reservoir') and an outer non-stimulated reservoir (called 'outer reservoir'). We assume wellbore has three different points for injection (i.e., I) and production (i.e., P) operations. The reservoir depth is between -2.5 km to -3.1 km and extending -0.5 km to 0.5 km in horizontally. The fluid injection process lasts for 30 days, after which fluid production begins. Tracer injection (conservative and temperature-reporting tracers of different temperature thresholds) are only injected on the first four hours. The physical properties of rock and fluid are summarized in Table 4.1 and Table 4.2, respectively.

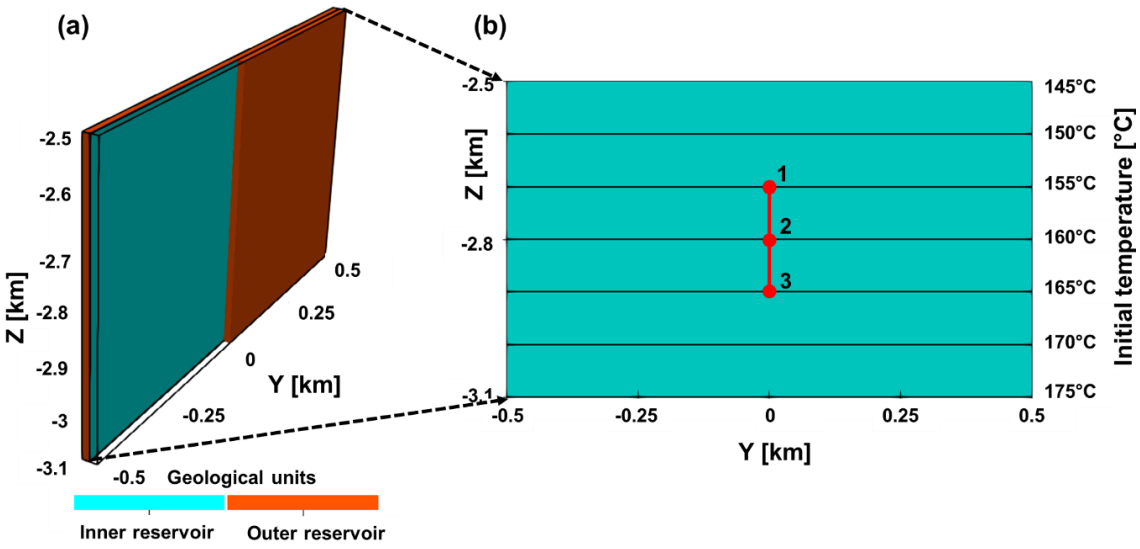

Figure 4.2. The reservoir model was used in this study. (a): A thin and homogeneous reservoir (permeability=$5 \cdot 10^{-11}$ m^2) located within a 3D model. (b): Three injection/production (1, 2, 3) well positions embedded in the simplified reservoir model. The dimensions of the inner reservoir are (1 km·0.6 km·1 m) with the initial reservoir temperature distribution ranging from 145°C to 175°C.

The detailed data are listed in the following: water injection/production flow rates are constant at 40 $L \cdot s^{-1}$ and the injection/production volumetric rate of each tracer is 6 $g \cdot s^{-1}$. The water is injected at a constant temperature of 70°C. The inner reservoir has a thickness of 1 m in the X direction and has a permeability of $5 \cdot 10^{-11}$ m^2. For the initial

temperature condition, the ground surface temperature is assumed to be 20°C, and the subsurface temperature follows the general geothermal gradient 0.05°C·m^{-1}. Therefore, in Fig. 4.2b the temperature range is 145°C to 180°C for a reservoir depth interval of 0.6 km. Three alternative injection/production points 1 (i.e., I1P1), 2 (i.e., I2P2) and 3 (i.e., I3P3) have depth positions of -2.7 km, -2.8 km and -2.9 km, respectively. The initial pressure distribution takes the hydrostatic gradient $9.81 \cdot 10^3$ Pa·m^{-1}. Regarding the reservoir boundary conditions, the top and the bottom of the model are set with closed boundaries for both heat transfer and fluid flow, while a constrained temperature and pressure distributions (same as initial) are applied at the four lateral sides (including the front, back, left and right sides).

Table 4.1. Properties of the rock (Bächler et al., 2003; Baillieux et al., 2013)

Properties	Symbols	Units	Outer reservoir	Inner reservoir
Porosity	ϕ	-	0.1	1
Permeability	k	m^2	$5 \cdot 10^{-16}$	$5 \cdot 10^{-11}$
Density	ρ^s	kg·m^{-3}	2600	2600
Specific heat capacity	c_p^s	J·kg^{-1}·K^{-1}	850	850
Heat conductivity	λ^s	W·m^{-1}·K^{-1}	2	2

Table 4.2. Fluid properties (L. Smith & Chapman, 1983).

Properties	Symbols	Units	Value
Water			
Bulk modulus	K_w	Pa	$2 \cdot 10^{10}$
Density	ρ_w	kg·m^{-3}	$\rho_w = 1000 \cdot e^{\frac{p_w}{K_w}}$
Viscosity	μ_w	Pa·s	10^{-3}
Specific heat capacity	$C_{p,w}$	J·kg^{-1}·K^{-1}	4000
Heat conductivity	λ_w	W·m^{-1}·K^{-1}	0.6
Nanotracer			
Diffusion coefficient	D	m^2·s^{-1}	$4 \cdot 10^{-12}$

4.2.3 Numerical mechanism and model validation

The numerical algorithms of the fully coupled processes of fluid flow, heat transfer, transport and reaction for temperature-reporting nanoparticle tracers are shown in Fig. 4.3. At time step *n*, the fluid flow model, nanotracer transport model together with heat transfer model are solved implicitly. After obtaining the results, the reactant and product concentrations of tracers are updated using the nanotracer reaction model, which provides

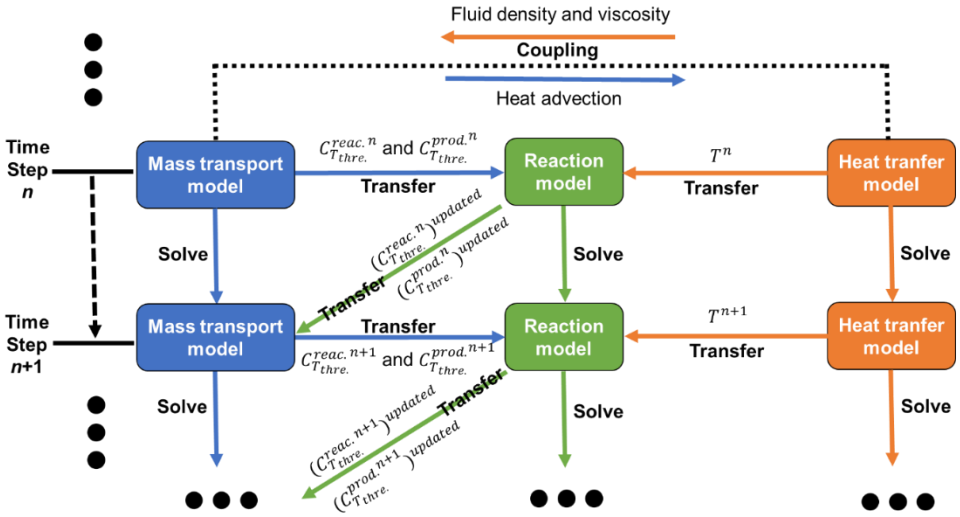

Figure 4.3. Schematic of the fully coupled fluid flow, heat transfer, transport and reaction models of temperature-reporting nanoparticle tracers.

the inputs for the tracer computation at next time step n+1.

Furthermore, A one-dimensional (1D) simulation is run to validate the numerical model with coupled fluid flow, heat transfer, transport and reaction for temperature-reporting nanoparticle tracers, shown in Fig. 4.4. The numerical results produced by the PorousFlow module (Wilkins et al., 2021) within the MOOSE framework (Permann et al., 2020) are validated against an analytical solution. The analytical solution is simply a stepwise function, which totally satisfies the mass conservation and chemical conversion laws. As shown in Fig. 4.4a(1), incompressible fluid is injected with a nanotracer reactant (threshold 2.5°C) into a 100-meter horizontal system. The Darcy velocity is $5 \cdot 10^{-4}$ m·s^{-1} and the injected nanotracer reactant concentration is 0.1 mg·L^{-1}. The porosity is assumed 1 and fluid properties are set constant (density 1000 kg·m^{-3}, viscosity 10^{-3} Pa·s and thermal conductivity 0.6 W·m^{-1}·k^{-1}). The system temperature (0°C~5°C) and pressure (1.1 MPa~0.1 MPa) distributions are constrained following a linear relation from inlet to outlet, during the whole process. The temperature distribution and the corresponding conversion factor Z along the model are shown in Fig. 4.4a(2). The comparisons between the analytical and numerical solutions show agreement for both reactant and product at the two selected times $5 \cdot 10^4$ s and $1.5 \cdot 10^5$ s.

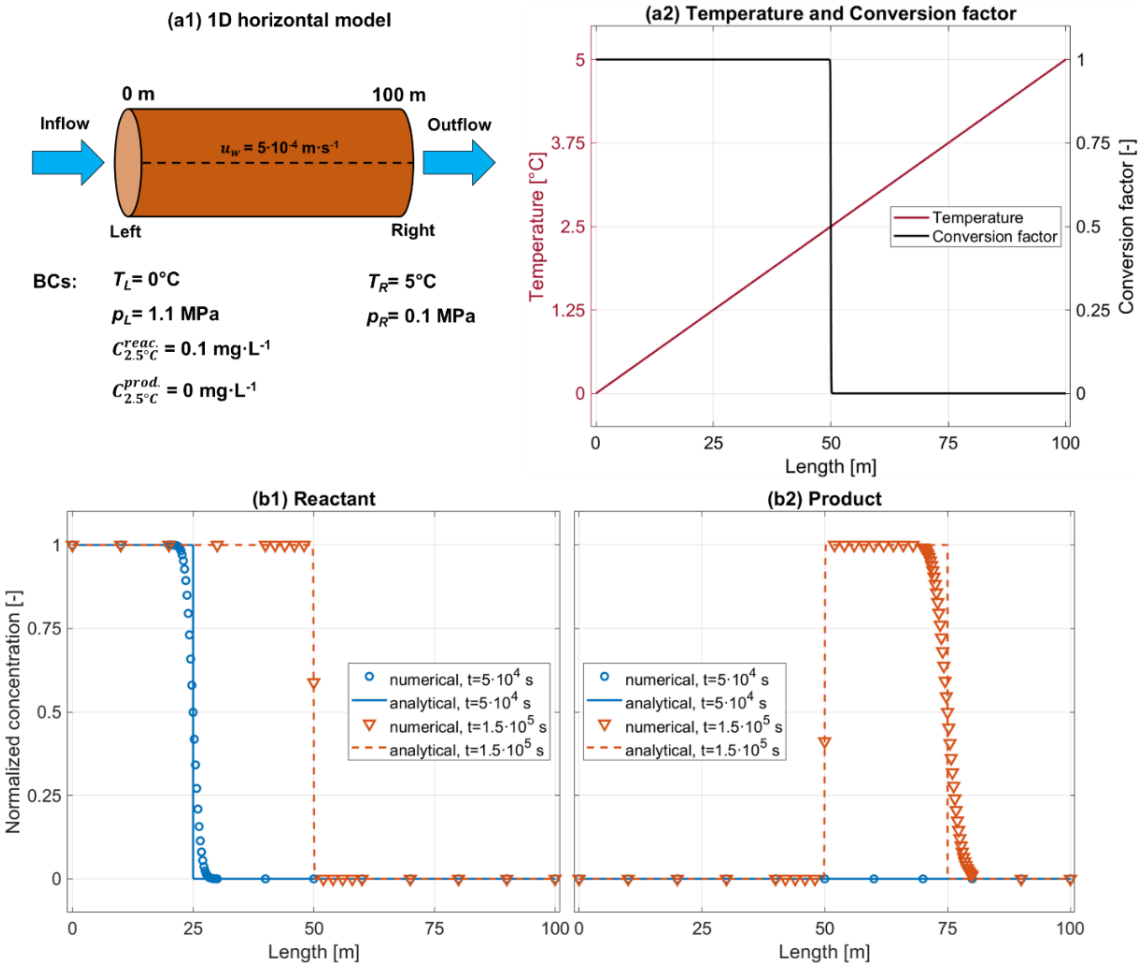

Figure 4.4. Validation on the fully coupled processes of fluid flow, heat transfer, transport and reaction for temperature-reporting nanoparticle tracers: (a1) 1D model with boundary conditions; (a2) temperature and conversion factor profiles; (b1, b2) comparison of numerical and analytical results for reactant $C^{reac.}_{T_{2.5°C}}$ and product $C^{prod.}_{T_{2.5°C}}$ at $5{\cdot}10^4$ s and $1.5{\cdot}10^5$ s.

4.3 Results and discussion

Several numerical simulations are conducted to illustrate the working mechanisms of temperature-reporting tracers by analyzing the response behavior from the data collected during the production process. First, a basic EGS case with homogeneous permeability of the inner reservoir is tested with the main purpose of understanding the velocity field affected by the well positions and discerning how temperature-reporting tracers may respond differently to the temperature field in the EGS. The breakthrough concentrations of these tracers are analyzed by extracting the peak information (i.e., peak value and peak arrival time) from their breakthrough concentration curves. Then, different open-hole

section lengths are then added to the original homogeneous reservoir to investigate the effect of wellbore open-hole section settings.

4.3.1 Reference case

We refer to the EGS system with homogeneous permeability of the inner reservoir as the reference case and the corresponding results including temperature and fluid velocity distributions and tracer response behavior from the production well are illustrated in the figure sequence from Fig. 4.5 to Fig. 4.8. The temperature-reporting tracers we use in this study have different temperature thresholds such as 145°C, 150°C, …, 175°C and 180°C with variations of 5°C. It is assumed that conserved tracers with ultra-high temperature thresholds (e.g., 300°C) are co-injected for comparison. As mentioned, three scenarios of injection/production position setup are simulated with the same well operating conditions, injected materials and volumetric rates.

4.3.2 Interdependency among fluid flow, heat transfer, transport and reaction of temperature-reporting nanoparticle tracers

To clearly illustrate the temperature distribution in the EGS and associated hydraulic flow regimes related to the temperature-reporting tracer testing process, we select typical well position of I1P1, see Fig. 4.3. As scheduled, all tested tracers will be co-injected with water during the first four hours followed by water injection and then production. The results obtained for this case are depicted in Fig. 4.5 at the ending time (i.e., 30 days) of injection operation and when the conservative tracer concentration reaches its peak value at the production well. The tracer is transported within the reservoir, following the displayed flow directions. For the case I1P1 (Fig. 4.5a) peak tracer concentration reaches the production well at 60 days. From the temperature distribution fields in Fig. 4.5a(1) and b(1), since the injected water has a lower temperature than that of the reservoir, the rock volume around the injection point cools down. The temperature field is asymmetrical due to the flow direction of the driven water not being aligned with the initial temperature gradient. The fluid flow direction is shown in both the temperature plots (Fig. 4.5(1)) and fluid velocity magnitude plots (Fig.4.5(2)). The water velocity distribution fields in Fig. 4.5(2) show that the fluid sweeps the reservoir in the main flowing region. Although there

can be temperature-induced fluid-density differences, the results indicate that the gravitational effect on the velocity field is almost negligible under our hypothetical system conditions. The water cannot leave the shown area in Fig. 4.5(1).

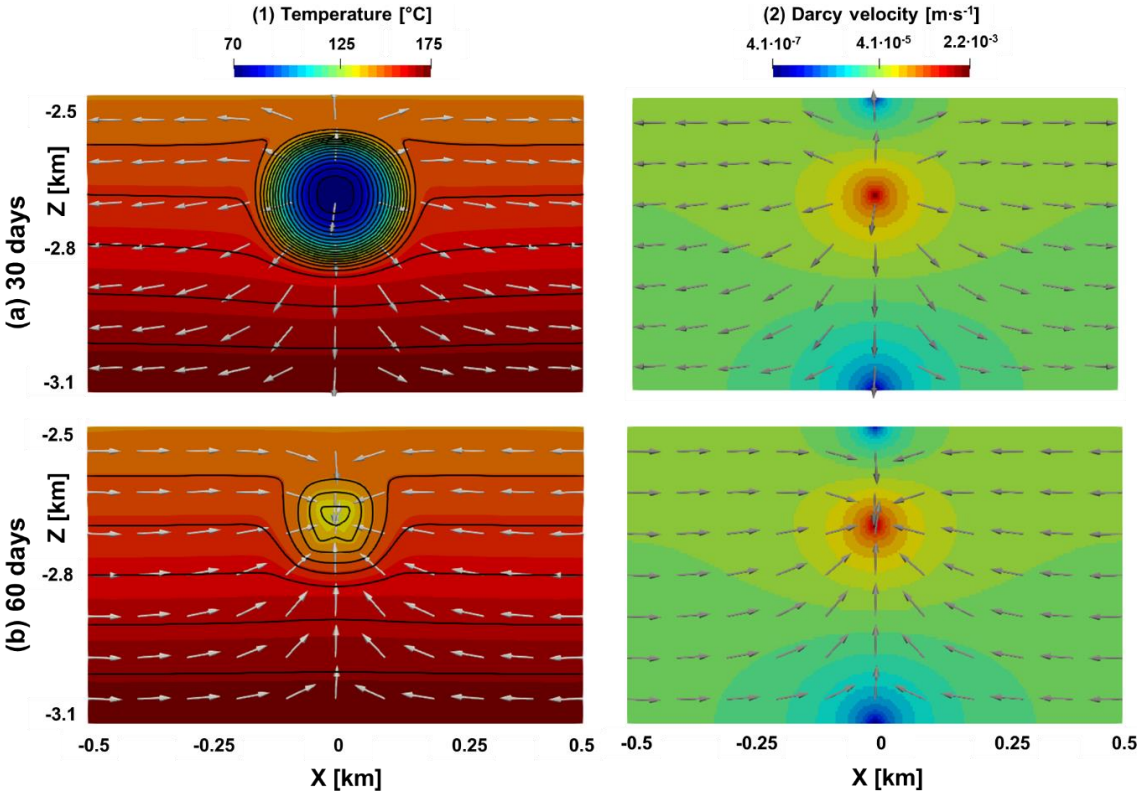

Figure 4.5. Temperature and hydraulic states of the reservoir (depth range 2.5~3.1 km): (1) temperature and fluid flow direction distribution and (2) velocity fields at 30 days and 90 days which correspond to end of injection phase and concentration peaks of the conservative nanotracer collected during the production phase when the injection-production points (a) I1P1 is chosen, respectively. The black lines in (1) is the reservoir temperature contour.

Figure 4.6 illustrates the tracer concentration distribution for the three types of tracers considered: one conservative tracer ($C_{cons.}$) and two temperature-reporting tracers ($C^{prod.}_{T_{160°C}}$ and $C^{prod.}_{T_{165°C}}$) with temperature threshold 160°C and 165°C, respectively. We are interested in the converted temperature-reporting tracers ($C^{prod.}_{T_{thre.}}$), not the non-converted ones ($C^{reac.}_{T_{thre.}}$) which have not exceeded the temperature threshold, see Eq. (4.6). Injection-production position setups are still based on I1P1. In each case two groups of times are selected for plotting: 30 days and 60 days, which individually correspond to the end of injection phase and the peak arrival times of conservative tracer a in the I1P1 case, respectively.

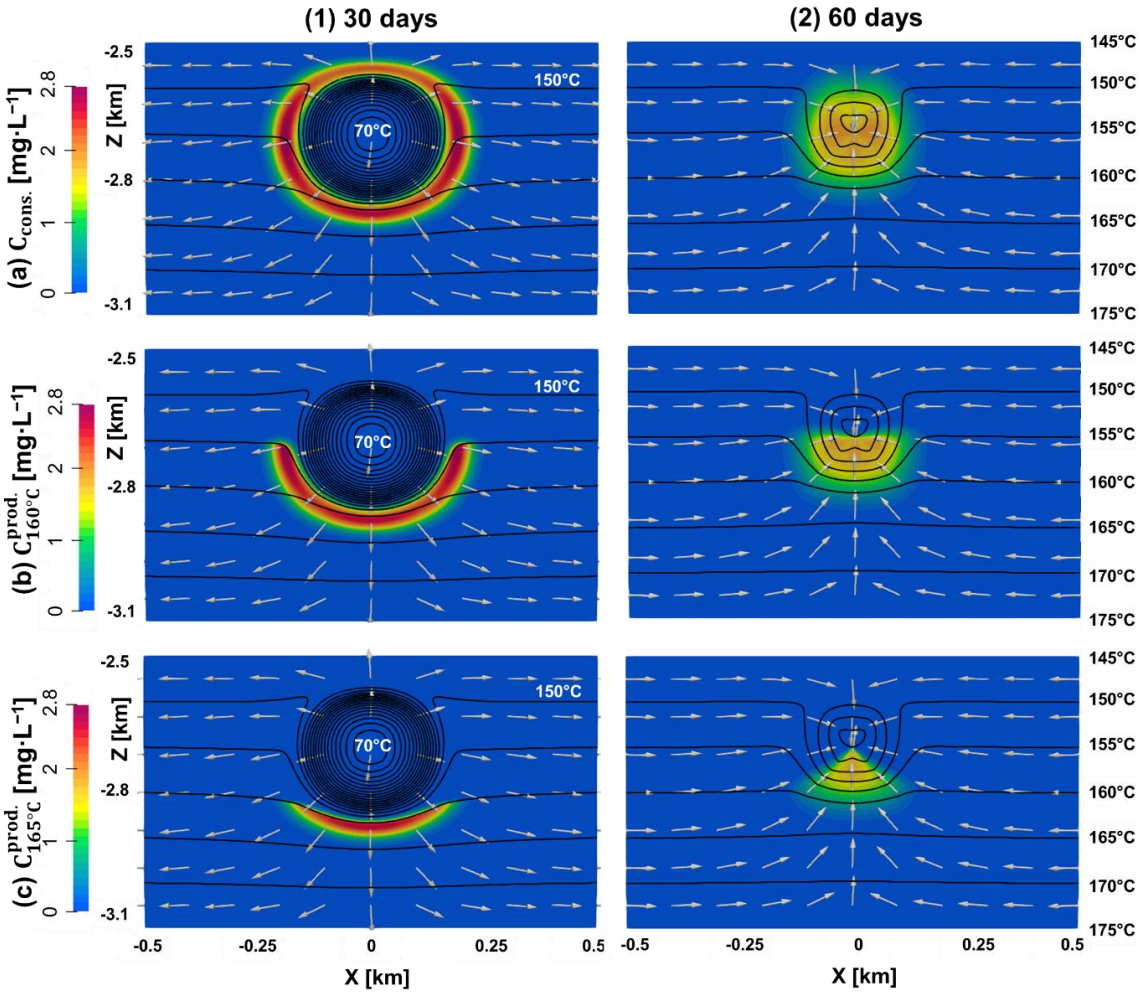

Figure 4.6. Distributions of conservative nanotracer and temperature-reporting nanotracers with $T_{thre.}$ = 160◦C, 165°C in I1P1 case. The black contours with their magnitudes on the right clearly show the reservoir temperature distribution.

In the case of I1P1, the conservative tracer is transported within the reservoir, covering both shallow and deep parts of the reservoir (see Fig. 4.6(1)). The high-concentration part of the conservative tracer is distributed radially. In contrast, the temperature-reporting tracers can react with the temperature above their thresholds thus being converted. Shallow and deep formations with comparatively low and high temperatures have different abilities to convert the temperature-reporting tracers with their corresponding temperature thresholds. As a result, the concentrations of the temperature-reporting tracers are distributed radially and vertically by temperature profile. From Fig. 4.6a and b, there are large proportions of converted temperature-reporting tracers with a threshold of 160°C in the lower half reservoir and only small amounts of converted temperature-reporting tracers with a threshold of 165°C appear in the lower quarter reservoir. This

makes it take a long time for high-threshold temperature-reporting tracers to propagate. Above the middle reservoir, there is no concentration of $C_{T_{160°C}}^{prod.}$ and $C_{T_{165°C}}^{prod.}$, meaning that the corresponding two temperature-reporting tracers are not converted in the upper part of the reservoir. Compared to the results in 60 days, the concentrations of these three tracers become weakened after 60 days due to continuous production.

4.3.3 Well configuration impact on temperature-reporting nanotracer breakthrough curve

As mentioned earlier, there are a total of three injection/production well positions. Figure 4.7 summarizes the results of tracer breakthrough concentrations at the production well, including both conservative tracer and converted temperature-reporting tracers with temperature thresholds varying from 150°C to 180°C.

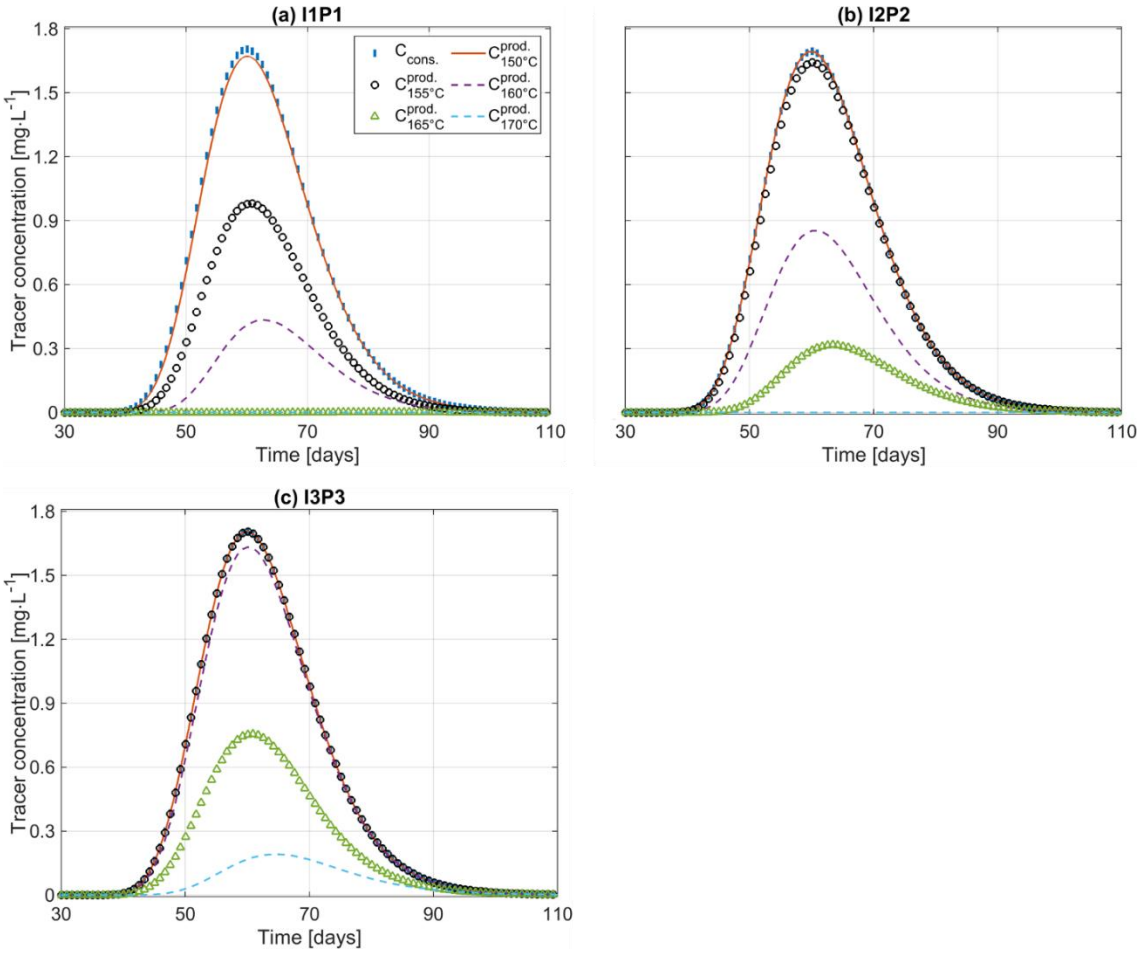

Figure 4.7. Nanotracer breakthrough curves in comparison to the conservative nanotracer (blue points) with a total of three push-pull well configurations.

It can be observed that the conservative tracer always holds the highest magnitude. This is because the tracers are injected with the same concentration, however, the temperature-reporting tracers only react and are converted when their thresholds are met at certain reservoir regions. Referring to Eq. (4.6), the sum of reactant and product equals the conservative tracer concentration. When it is not fully converted, the product is less than the conservative tracer. Therefore, in all subplots of Fig. 4.7, the curves produced by the temperature-reporting tracers with low temperature thresholds, such as 150°C and 155°C, are very close to the conservative one. In addition, high peak values in these tracer breakthrough curves normally correspond to short travel times. On the contrary, the temperature-reporting tracers with high-temperature thresholds such as 170°C actually have lower peak values of concentration and a longer time to reach the peak than those with low temperature thresholds such as 160°C. What causes such differences in breakthrough curves among these temperature-reporting tracers is dependent on the radial flow, temperature profile and boundary interactions.

On this basis, the effects of different injection-production positions are also visible on the tracer breakthrough curves in Fig. 4.7. For example, subplots (a1) I1P1, (b2) I2P2 to (c3) I3P3 show that the overall magnitude of tracer breakthrough curves increases with a deep injection/production position because more tracer is converted at a greater depth / higher temperature. The process to reach their corresponding peaks is also accelerated because the conversion happens along the fastest flow pathway.

4.3.4 Analysis of temperature-reporting nanotracer breakthrough curves for reservoir characterization

To quantify reservoir information from Fig. 4.7, we aim to extract useful information from the tracer breakthrough curves based on which a new analysis method is proposed in our previous work (Yan et al., 2024), including plotting results of concentration peak values and peak arrival times vs. different temperature-reporting tracer temperature thresholds. One example is shown in Fig. 4.8 where subplots (a) are based on peak values and subplots (b) are peak arrival times.

Compared to Fig. 4.7, we also include simulation results of additional temperature-reporting tracers with other temperature thresholds such as 175°C and 180°C in Fig. 4.8.

Nevertheless, no temperature-reporting tracers with thresholds 175°C and 180°C can be converted due to the highest reservoir temperature being limited to 175°C, therefore their peak values in subplot (a) are zero and the peak arrival time in subplot (b) does not exist. The curves of both peak value and peak arrival time vs. different temperature thresholds have their own turning points after a horizontal extension. The horizontal line indicates that the corresponding temperature-reporting tracers are fully converted and reach the same peak value as the conservative one. In the following, the tracer temperature threshold at the turning point of each curve is discussed and compared to the average temperature along the injection/production position. In Fig. 4.2b, the initial temperatures of (I1, P1), (I2, P2) and (I3, P3) are 155°C, 160°C and 165°C. In Fig. 4.8a based on peak concentration values, we see that three curves (with I1P1, I2P2 and I3P3) separately provide 150°C, 155°C and 160°C at their turning points, which underestimates the temperature of wellbore positions to some extent. Concerning the performance of the results based on peak arrival time shown in Fig. 4.6, we observe an accurate estimate of temperatures: 155°C, 160°C and 165°C at the turning points of I1P1, I2P2 and I3P3.

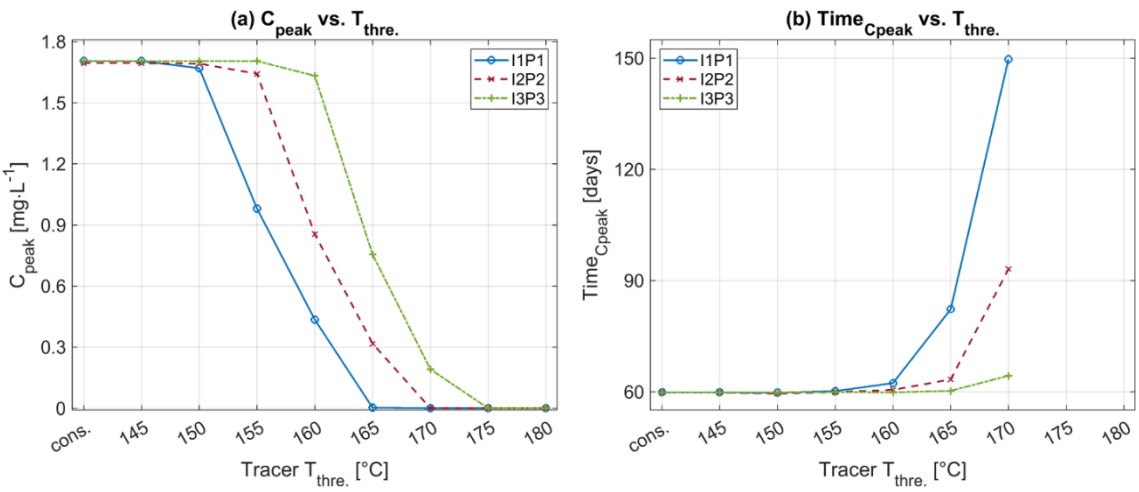

Figure 4.8. Comparison of peak concentration (a) and peak arrival times (b) of the individual nanotracer types from the nanotracer breakthrough curves for different push-pull well configurations. Thresholds from 145°C to 180°C and conservative nanotracers are shown.

To summarize, our results in Fig. 4.6 indicate that it is useful to estimate the average temperature of tested injection/production positions by directly referring to the temperature threshold at the turning points of these curves. More specifically, regarding the estimation of the average temperature of tested positions using two different

approaches based on peak values and peak arrival times, it seems to be useful to choose the peak arrival time approach.

For the estimation of the reservoir temperature range (minimum and maximum values), the temperature at which the peak value approaches zero corresponds to the estimated maximum temperature, and the last stable point (turning point) of the peak value curve gives an estimation of a close value to the minimum reservoir temperature. As shown in Fig. 6a, tracer peak values start to become zero when the temperature threshold approaches 165°C, 170°C and 175°C for three cases I1P1, I2P2 and I3P3, respectively, meaning that the estimated maximum temperature of the overall reservoir is not well estimated for I1P1 and I2P2 cases. At the same time, a shallow injection-production position, such as I1P1 in Fig. 6a and b, can help to detect the low temperature of reservoir (from the turning points) where the temperature-reporting tracer starts to be not fully converted and the approach using peak values in subplot (a) can be a better way to obtain the minimum temperature of the reservoir since it finds a lower value of temperature than the one in subplot (b).

4.3.5 Effects of wellbore open-hole length

We selected cases with open-hole sections of 100 m and 200 m and compared their nanotracer breakthrough curves to a reference case, in which a single-point nanotracer injection and production were conducted. Figs. 4.9 and 4.10 present the comparisons of peak concentration and peak arrival times for each nanotracer type, respectively. As the open-hole section length increases from 100 m to 200 m, the peak concentration decreases, while the peak arrival time increases. This trend is due to the broader distribution of tracer concentration around the wellbore with longer open-hole sections.

In Figs. 4.9 and 4.10, based on peak concentration values, we observe that the three curves (I1P1, I2P2, and I3P3) each reach ~150°C at their turning points, slightly underestimating the actual temperatures at these wellbore positions. However, when examining peak arrival times in Fig. 4.6, we find more accurate temperature estimates, with turning points at 155°C, 160°C, and 165°C for I1P1, I2P2, and I3P3, respectively. Compared to the point source method, the peak arrival time in the open-hole section scheme provides a more

accurate temperature estimate, likely due to its sensitivity to thermal and flow dynamics in the reservoir. This suggests that the peak arrival time effectively captures key processes such as heat advection and conduction, which are influenced by reservoir properties like permeability, thermal diffusivity, and fluid flow patterns. The observed trend highlights the importance of these mechanisms in shaping the thermal response and offers insights into the underlying reservoir conditions.

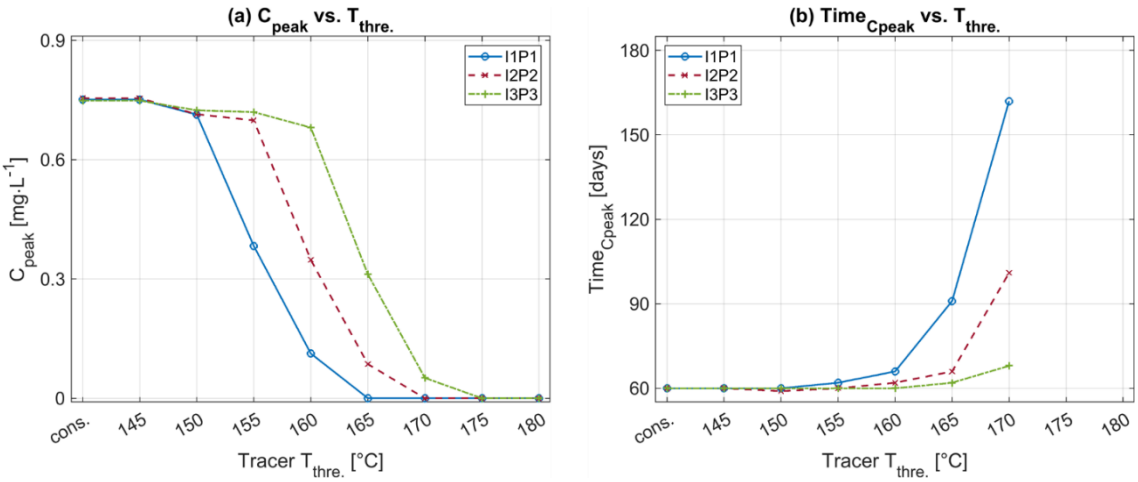

Figure 4.9. Comparison of peak concentration (a) and peak arrival times (b) of the individual nanotracer types from the nanotracer breakthrough curves for different push-pull injection schemes of 100 m open-hole section. Thresholds from 145°C to 180°C and conservative nanotracers are shown.

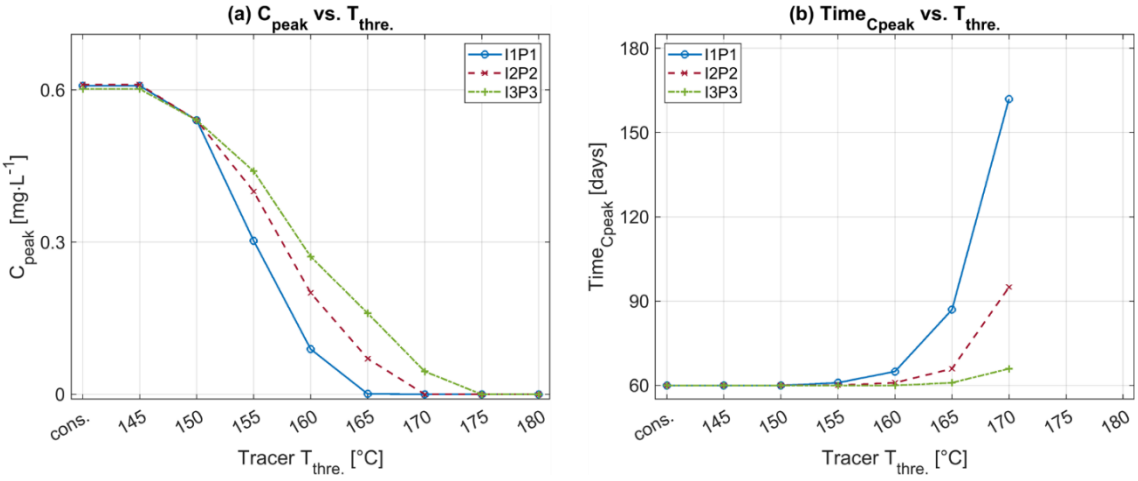

Figure 4.10. Comparison of peak concentration (a) and peak arrival times (b) of the individual nanotracer types from the nanotracer breakthrough curves for different push-pull injection schemes of 200 m open-hole section. Thresholds from 145°C to 180°C and conservative nanotracers are shown.

4.4 Conclusions

The inaccessibility of geothermal formations makes the estimation of reservoir properties and conditions required for reservoir characterization, development and management difficult and costly. Especially, the assessment of geothermal energy extraction capability and viability of geothermal power generation is mainly relying on the formation temperature range and spatial distribution. Temperature-reporting tracers, which can be quickly, fully and irreversibly converted when the environmental temperature reaches a certain threshold, are being studied for characterizing the temperature information of geothermal reservoirs. The potential, utilization and response behavior of temperature-reporting tracers in 3D single-well EGS have not been fully investigated. In this work, we developed a numerical modeling approach to simulate the behavior of temperature-reporting tracers in a thin 3D reservoir with single-well. Various scenarios are considered including homogeneous formation , geothermal reservoirs containing heterogeneities such as inclined zones and thermal anomalies (i.e., different reservoir temperature ranges and regional high temperature) and three injection-production well configurations. The results are analyzed by collecting the peak information (peak values and peak arrival times) from the tracer breakthrough curves at a production well. The temperature at which the peak value approaches zero corresponds to the maximum reservoir temperature. The last stable point (turning point) of the peak value curve gives an estimation of a close value to the minimum reservoir temperature when the injection-production position is in a shallow depth. Based on our work, the following conclusions can be made:

- The coupled physical-chemical processes are complex during the flow of temperature-reporting tracers in geothermal reservoirs. Initial reservoir temperature can be changed due to cold water injection and fluid intrusion from different depths. Therefore, the injected temperature-reporting tracers with various temperature thresholds can be converted into different parts of the reservoir.
- Varying the injection/production positions can influence the main pathways of tracers flowing within the reservoir, therefore impacting the tracer breakthrough and further analysis.

- The peak concentration of a given temperature-reporting tracer is determined by the proportion of the swept reservoir area above its certain temperature threshold and changes in peak arrival times result from alterations in the main flow paths of tracers.
- Regarding the estimation of the average temperature of tested positions using two different approaches based on peak values and peak arrival times, it seems to be useful to choose the peak arrival time approach. Approximation of the reservoir temperature ranges requires shallow injection-production wells' positions using the plotting approach based on peak values.
- Compared to the point source method, only the peak arrival time offers a more accurate temperature estimate in the open-hole section scheme.

To summarize, the conclusions of this work are not limited to the EGS reservoirs but also can be applied to the general geothermal reservoirs. During the whole lifecycle of geothermal reservoir development, temperature-reporting tracer tests can be conducted to detect temperature range and thermal drawdown in the reservoir. More specifically, for the production stage, after the estimation of the present temperature range of the reservoir, the thermal drawdown status of the geothermal reservoir can be periodically quantified by the comparison of the present temperature range to the initial one.

Although forward modeling can provide some useful insights into the effects of geological and thermal heterogeneities on the tracer breakthrough data, a precise prediction of these unknowns in the reservoir generally relies on the inverse modeling method which requires an ensemble of forward modeling results. Regarding the forward modeling, it is clear from our conclusions that it is effective in detecting the temperature information. The inverse modeling approach can optimize the agreement between model-computed and observed field data (i.e., the tracer breakthrough data at the production well in our case) by adjusting the model's inputs, thus giving a precise prediction of temperature information in space.

5 Numerical modeling of temperature-reporting nanoparticle tracer for fractured geothermal reservoir characterization

This part is reproduced from the manuscript that has been published in the peer-reviewed journal ***Geoenergy Science and Engineering***.

***Yan, G.**, Andersen, P. Ø., Qiao, Y., Hatzignatiou, D. G., Nitschke, F., Spitzmüller, L., & Kohl, T. (2024). Numerical modeling of temperature-reporting nanoparticle tracer for fractured geothermal reservoir characterization. **Geoenergy Science and Engineering**, 237, 212787, https://doi.org/10.1016/j.geoen.2024.212787.*

Abstract

Information on the temperature distribution of subsurface reservoirs is essential for geothermal energy development. One of the promising tools to detect the reservoir temperature distribution is temperature-reporting nanoparticle tracers whose functionality has been extensively investigated in both theoretical and experimental ways in the last decade. However, most related studies were limited to simplified geometries and ignored the dynamic interplays of fluid flow, heat transfer, transport and reaction of the temperature-reporting nanoparticle tracer. The response behavior and working mechanisms of such nanotracers in a realistic three-dimensional system still have not been fully revealed through a systematic study. In this work, we develop a numerical modeling approach to simulate field implementation of these nanotracers in a fractured geothermal reservoir. This study aims to evaluate whether the injection of multiple temperature-

reporting nanoparticle tracers with different thresholds can be used to estimate the temperature distribution and provide information on the thermal and geological heterogeneities. Several scenarios have been investigated for the geothermal reservoir including homogeneous and non-homogeneous cases (e.g., thermal and geological heterogeneities). Our obtained results from the nanotracer breakthrough curves show that the deviation temperatures in peak concentration values provide an upper limit of the lowest temperature and precise highest temperature for the reservoir temperature range. The deviation temperature of the peak arrival time curve accurately estimates the highest temperature along the main streamlines between the wells. The proposed analysis curves based on the nanotracer breakthrough data were visibly affected by geological heterogeneities including their conductivities and orientations as well as thermal heterogeneities in the geothermal reservoir.

5.1 Introduction

Geothermal energy is a clean, renewable and sustainable alternative to traditional energy sources of fossil fuels for direct heat utilization and electricity generation (Moeck, 2014). According to the World Geothermal Congress (2023), a total of 1,476 PJ (410 TWh) of geothermal energy was used globally in 2022, a 44% increase from 2020, with geothermal heating and cooling of buildings accounting for about 79% of the total. While major geothermal systems are restricted to structurally dynamic or volcanically active regions (Lund et al., 2008; J. W. Tester et al., 1989), enhanced geothermal system (EGS) technology radically expands the global geothermal potential through hydraulic/thermal/chemical stimulation on target reservoirs to enhance permeability and fluid flow rate, in impermeable and low heat flow regions. Nonetheless, to improve the economic benefits and reduce investment risk in geothermal projects, reservoir characterization is particularly needed to evaluate subsurface heat/energy utilization capabilities in terms of geothermal power generation, as well as the management, maintenance and sustainability of operational plants (Domra Kana et al., 2015; S.-M. Lu, 2018; Olasolo et al., 2016). In general, geothermal reservoir characterization includes assessing reservoir conditions such as estimating temperature profiles (i.e., temperature range and distribution), surveying well-to-well or inter-well connectivity (Dashti et al.,

2023) and extrapolating the volume of the fractured zones (B. Sanjuan et al., 2006). Among all reservoir characteristics, temperature profiles are critical for geothermal energy exploration and assessment in the geothermal reservoir (re-)siting step, as well as for evaluating reservoir thermal performance (e.g., thermal breakthrough prediction due to reinjection of cooled geothermal fluid) and adjusting production strategy in the production step. Nevertheless, the reliable and accurate measurement or estimation of temperature profiles throughout the lifecycle of geothermal energy development has always been a major, complex and difficult challenge for geothermal reservoirs (Frey et al., 2022).

Common methods to measure or estimate temperature profiles include wellbore measurements, geothermometers, analytical/numerical models and tracer tests. Temperature measurements at or near the wellbore do not provide temperature distributions between injection and production wells due to the limited space of the wellbore in the geothermal reservoir. Since the introduction of geothermometers in the 1960s, geothermometer technology has continued to advance in-situ temperature measurements by evaluating sensitive parameters with respect to the chemical equilibrium of fluids and reservoir rocks (e.g., aluminum concentration, pH, vapor loss, etc.) (Fournier & Rowe, 1966; Nitschke et al., 2017; B. Sanjuan et al., 2014; Ystroem et al., 2020). However, the spatial distribution of reservoir temperature is still unknown using geothermometers. Gringarten et al. (1975) presented an analytical solution for temperature determination, based on pure fluid flow and heat transfer in a hot-dry rock reservoir with infinite, equidistant and parallel fractures. Following that, many researchers (P. Cheng, 1979; A. H.-D. Cheng et al., 2001; Fox et al., 2016; Tang et al., 2020; Wilkins et al., 2021) continued to develop analytical solutions and numerical simulators to predict the temperature distribution in fractured geothermal reservoirs. Nevertheless, with the large uncertainties in the geometry of fractures (e.g. aperture, scale, spacing and network) and heat transfer of unfractured zones, their results can only serve as references in practice, although these results are sometimes informative. To compensate for such shortcomings, conservative solute tracers (Erol et al., 2022; Pollack et al., 2021; Robinson, 1985; Robinson & Tester, 1984; Williams et al., 2010; Xu et al., 2022) and adsorbing solute tracers (C. Dean et al., 2012; Hawkins et al., 2018; Leecaster

et al., 2012; Williams et al., 2013) which are able to adhere to the fracture surface were used in field tests to identify key geometry properties (i.e., heat transfer surface area, fracture aperture, etc.) of geothermal reservoirs, assisted by fitting analytical solutions of tracer transportation. Utilizing the obtained geometry properties, the reservoir temperature distribution is roughly estimated by using analytical or numerical models for heat transfer (Robinson, 1985; Williams et al., 2013). In addition, temperature-dependent degrading (Arrhenius reaction kinetics) solute tracers are proposed to infer the average reservoir temperature in fields by analytically fitting the tracers' degradation characteristics (Plummer et al., 2010; Plummer et al., 2011; P. E. Rose, 1994; J. W. Tester et al., 1987). It should be noted that the reaction rates of such kind of tracers vary with the environmental temperature and this method only provides the average reservoir temperatures without spatial temperature information in a single test. Although solute tracers have been used in many fields for temperature estimation in fractured geothermal reservoirs, the combined effects of their diffusion and interaction with reservoir rocks as well as highly mineralized reservoir fluids give rise to less reliable tracer tests due to the high mass loss, low detectability and collectability of the solute tracers (Aydin et al., 2022; Rudolph et al., 2020; Vitorge et al., 2014).

To eliminate deficiencies in solute tracer tests, nanoparticles with controllable size, structure and physical and chemical properties are utilized to measure or estimate temperature profiles in geothermal reservoirs by different transport (e.g., low diffusion) and working mechanisms from solute tracer (Divine & McDonnell, 2005; X.-Z. Kong et al., 2018; Redden et al., 2010). One kind of tracer named 'temperature-sensitive nanotracer' is attractive and utilized to detect thermal drawdown and average temperature by quantifying the extent of tracer degradation. The degradation starts from a certain temperature threshold and its rate is influenced by the environmental temperature (Axelsson et al., 2001; Nottebohm et al., 2012; Robinson et al., 1988)). Many theoretical and experimental studies have been done to investigate the performance behavior of temperature-sensitive nanotracers. For example, theoretically, Ames et al. (2015) used the analytical solution of tracer distribution in the one-dimensional model to inversely predict the thermal drawdown. However, their work does not consider the dynamic interplays of heat transfer, fluid flow, transport and reaction of the nanotracer. In addition, Alaskar et

al. (2015) analytically and experimentally exhibited the prospects of temperature-sensitive nanotracers for forecasting the thermal drawdown. In 2021, a field demonstration of temperature-sensitive nanotracers by Hawkins et al. (2021) showed that the estimated effective inter-well reservoir temperatures have an error of less than 5°C from the true values. However, the above studies have not demonstrated how inter-well test results from temperature-reporting nanotracers are related to geological heterogeneities, temperature distributions and well positioning.

Different from the degradation principle of a temperature-sensitive nanotracer after reaching the temperature threshold, a novel tracer called a 'temperature-reporting nanoparticle tracer' (also 'temperature-reporting nanotracers' for simplicity) can be quickly, fully and irreversibly converted when the environmental temperature reaches a certain threshold, are being studied to characterize the temperature distribution of geothermal reservoirs (Puddu et al., 2016; Rudolph et al., 2020). It was Williams et al. (2010) and Alaskar et al. (2011) who first introduced a dye-release mechanism, wherein encapsulated dyes are released from the nanotracer upon reaching a specific temperature threshold. France et al. studied polymer microcapsules encapsulating dyes that release dyes at a certain temperature threshold. Alaskar et al. (2015) experimentally developed irreversible thermochromic microspheres and dye-attached silica nanoparticles and exhibited their prospect as temperature sensors for forecasting the thermal drawdown analytically and experimentally. Puddu et al. (2016) invented the submicrometer-sized particle, demonstrating for the first time the feasibility of using nucleic acid damage quantitatively to measure temperature. Rudolph et al. (2020) conducted experiments to develop temperature-reporting nanotracers by silica particles synthesized with the core-shell-hull layers. The outer dye in the nanotracer is released irreversibly once the environmental temperature is above its thresholds, giving rise to changes in the structure of the developed nanoparticle tracers. Nevertheless, these works primarily focused on concept development, laboratory research and analytical analysis.

The motivation of this work is to investigate whether temperature-reporting nanotracers can be used for the characterization of 3D geothermal reservoirs related to reservoir temperature distribution prediction, and provide methodologies that when applied enable the development and exploitation of geothermal energy resources. Presently, there have

not been theoretical studies to reveal the working behavior of the temperature-reporting nanotracers, nor have these nanotracers been tested in realistic 3D geothermal reservoirs. The mutual interplay among fluid flow, heat transfer, transport and reaction of the temperature-reporting nanotracers and reservoir heterogeneity necessitates a detailed investigation. In addition, how to design and implement a temperature-reporting nanotracer test in geothermal reservoirs is also questionable. Therefore, numerical simulation can be utilized as a useful approach to shed light on these issues and help us gain insight into the potential of implementing temperature-reporting nanotracers in the field.

The goal of the current work is to study the working mechanisms (i.e., transport, reaction, distribution and resulting concentration breakthrough curves) of temperature-reporting nanotracers in synthetic but typical 3D fractured geothermal reservoirs as well as their performance in the detection of reservoir temperature distributions through analyzing its breakthrough data. To achieve that, a numerical modeling approach is developed for the reaction of temperature-reporting nanotracers. The novelty of this work is the application of a new analysis method based on the peak information of nanotracer breakthrough curves proposed to estimate the temperature along the tested injection-production positions and reservoir temperature range of the fractured geothermal reservoir.

The study is organized as follows. We first present the employed methodology for modeling temperature-reporting nanotracer transport in fractured geothermal reservoirs, including the reaction mechanism of temperature-reporting nanotracers and numerical modeling approaches. Secondly, the potential of temperature-reporting nanotracers in fractured geothermal reservoirs and the effect of well configuration on the temperature-reporting nanotracers' responses are evaluated in a homogeneous model. Finally, the thermal distributions (i.e., different temperature gradients and regional thermal anomalies) and effects of reservoir heterogeneity (i.e., embedded by inclined zones) within the geothermal reservoir are studied.

5.2 Materials and methods

A liquid solution is injected into the fractured geothermal reservoir through the injection well for a short period, followed by pure water injection the rest of the time. The solution is a mixture of water and temperature-reporting nanotracers with different temperature thresholds. The temperature-reporting nanoparticle nanotracers being simulated are representative of silica particles synthesized with core-shell-hull layers developed to characterize temperature distribution when the environmental temperature reaches its threshold (Rudolph et al. (2020)). The nanotracer breakthrough data are monitored in the production well during the injection process.

The modeled physical and chemical processes consist of fluid flow, heat transfer, transport and the reaction of temperature-reporting nanotracers in the reservoir. The numerical models for simulating fully coupled processes of fluid flow, heat transfer, transport and reaction for temperature-reporting nanotracer are developed for the first time and implemented in the finite element simulator-PorousFlow module (Wilkins et al., 2021) within the MOOSE framework (Permann et al., 2020). The relevant equations are described in detail below.

5.2.1 Governing equations

1) Fluid flow and heat transfer

Firstly, the fluid mass balance equation (Cacace & Jacquey, 2017) for compressible and liquid-phase water flow in porous media is written as:

$$\frac{\partial(\phi\rho_w)}{\partial t} + \nabla \cdot (\rho_w \boldsymbol{u_w}) - Q_w = 0 \tag{5.1}$$

where ϕ is the porosity (-) of the porous medium, t represents time (s), the subscript w refers to water, p_w is the pressure (Pa), T is the temperature (K), $\rho_w = \rho_w(p_w, T)$ is the water density (kg·m^{-3}) as a function of pressure and temperature, $\boldsymbol{u_w}$ is the Darcy velocity (m·s^{-1}) and Q_w is the water mass source (kg·m^{-3}·s^{-1}).

The Darcy velocity $\boldsymbol{u_w}$ (Qiao et al., 2018) is given as:

$$\boldsymbol{u_w} = \frac{k}{\mu_w}(-\nabla p_w + \rho_w \boldsymbol{g}) \quad (5.2)$$

where k is the reservoir permeability (m^2), $\mu_w = \mu_w(p_w, T)$ refers to the water viscosity (Pa·s) as a function of pressure and temperature, and $\boldsymbol{g}$ is the gravitational acceleration ($m \cdot s^{-2}$).

Secondly, the heat transfer equation (T. Kohl & Rybach, 1996) for both solid and water in the porous media is written as:

$$\left[\phi c_{p,w}\rho_w + (1-\phi)c_{p,s}\rho_s\right]\frac{\partial T}{\partial t} - \left[\phi\lambda_w + (1-\phi)\lambda_s\right]\nabla^2 T + \rho_w c_{p,w}\mathbf{u_w}\nabla T - Q_T = 0 \quad (5.3)$$

where the four terms on the left side individually represent a transient variation of temperature, heat conduction, heat convection and heat source. The subscript *s* represents the solid phase, $c_{p,w}$ and $c_{p,s}$ are separately the specific heat capacity of water and solid ($J \cdot m^{-3} \cdot K^{-1}$), ρ_s denotes the solid density ($kg \cdot m^{-3}$), T is the temperature (K), λ_w and λ_s refer to the heat conductivity of the water and solid ($W \cdot m^{-1} \cdot K^{-1}$) and Q_T is the heat source ($W \cdot m^{-3}$).

2) Reaction and transport of temperature-reporting nanoparticle tracers

(1) Reaction process

Figure 5.1 illustrates the working mechanism for reporting temperature information of the temperature-reporting nanotracer which are silica particles synthesized with the core-shell-hull layers. Specifically, the hull melts/degrades, dyes are released and the structure of the developed tracer (reactant) changes when the environment temperature exceeds the temperature threshold of the temperature-reporting nanotracer. The product resulting from this temperature-dependent reaction is our research focus. The released dyes only act as indicators of the reaction completion degree in the lab, without directly reflecting temperature changes (Rudolph et al., 2020). In addition, dyes may interact with highly mineralized reservoir fluids and adsorb onto the reservoir rock. Therefore, in this study released dyes are not involved in the temperature reporting mechanism.

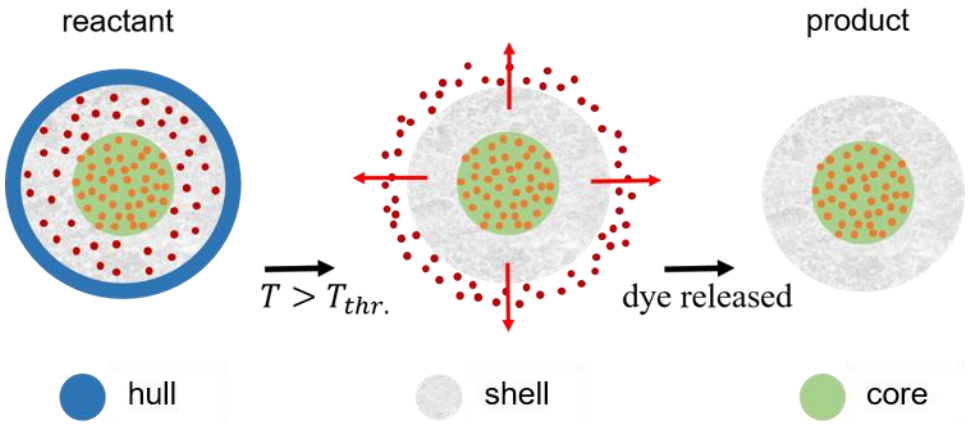

Figure 5.1. Schematic representation of the working mechanism of temperature-reporting nanotracers: the dye released from the shell of the nanoparticles upon exceeding the temperature threshold (reproduced from Rudolph et al. (2020)).

In the following, we present our numerical approach for simulating the temperature-reporting nanotracers reaction. Referring to Fig. 5.1, the relevant reaction can be described as follows:

$$C_{T_{thre.}}^{reac.} \xrightarrow{T>T_{thre.}} C_{T_{thre.}}^{prod.} \tag{5.4}$$

where $C_{T_{thre.}}^{reac.}$ denotes the concentration of reactant and $C_{T_{thre.}}^{prod.}$ is the corresponding product's concentration after the reaction. $T_{thre.}$ refers to the temperature threshold of the reactant.

(2) Transport process

Each temperature-reporting nanotracer with a certain temperature threshold has a group of the two advection-diffusion equations (Shan & Pruess, 2005) for both reactant and product:

$$\frac{\partial C_{T_{thre.}}^{reac.}}{\partial t} - \nabla \cdot (\boldsymbol{D} \nabla C_{T_{thre.}}^{reac.}) + \nabla \cdot (\boldsymbol{u_w} C_{T_{thre.}}^{reac.}) - Q_{C_{T_{thre.}}^{reac.}} = 0 \tag{5.5}$$

$$\frac{\partial C_{T_{thre.}}^{prod.}}{\partial t} - \nabla \cdot (\boldsymbol{D} \nabla C_{T_{thre.}}^{prod.}) + \nabla \cdot (\boldsymbol{u_w} C_{T_{thre.}}^{prod.}) - Q_{C_{T_{thre.}}^{prod.}} = 0 \tag{5.6}$$

where $\boldsymbol{D}$ refers to the diffusion coefficient ($m^2 \cdot s^{-1}$), $\boldsymbol{u_w}$ is the Darcy velocity ($m \cdot s^{-1}$), $Q_{C_{T_{thre.}}^{reac.}}$ and $Q_{C_{T_{thre.}}^{prod.}}$ represent the mass source of reactant and product ($kg \cdot m^{-3} \cdot s^{-1}$),

respectively. Here we assume that the nanotracers are well mixed with water as components of the liquid solution and the gravity segregation between water and nanotracer is ignored due to the low mass fraction (<10^{-3}) of nanotracers in the liquid. In addition, for simplicity we do not consider the deposition and aggregation of nanotracers during the flow process.

5.2.2 Model description and input data

Our model is inspired by a typical fractured reservoir setting such as Soultz-sous-Forêts EGS (Egert et al., 2020) which contains several irregularly distributed fractures. In this study, a highly permeable and thin reservoir is used to mimic a fracture ($\phi = 1$). We use the model settings illustrated in Fig. 5.2a. The reservoir model consists of two types of 600 m thick rocks: an inner stimulated (called 'inner reservoir') and an outer non-stimulated reservoir (called 'outer reservoir'). Both are covered by low permeable caprock and underlain by a low permeable bedrock. The ground surface temperature is assumed to be 20°C and the initial geothermal gradient is 0.05°C·m^{-1}. The initial pressure distribution is based on the hydrostatic gradient. For the model boundary conditions, we use a constrained (initial) pressure and (initial) temperature at the top (2 km depth) and a constant (initial) temperature at the bottom (3.6 km depth). The other facies of the model are set with closed boundaries.

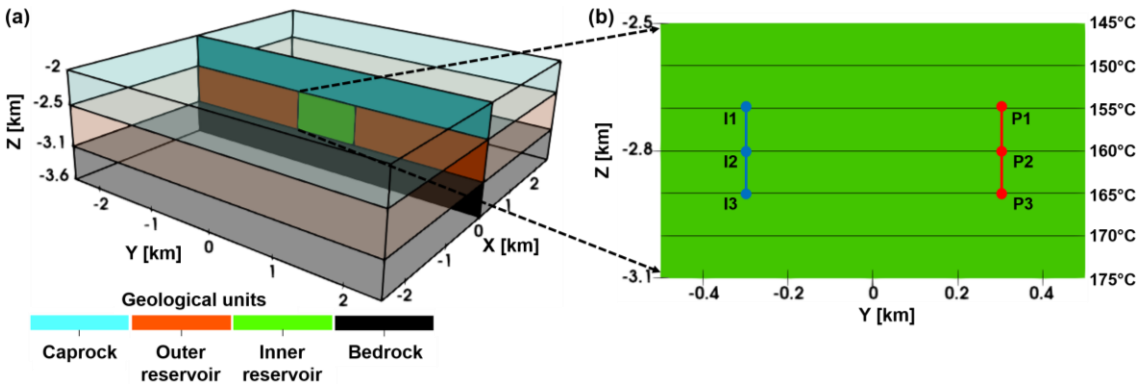

Figure 5.2. The reservoir model was used in this study. (a): A thin and homogeneous reservoir (permeability=5·10^{-11} m^2) located within a 3D model. (b): Three injection (I1, I2, I3) and three production (P1, P2, P3) well positions embedded in the simplified reservoir model. The dimensions of the inner reservoir are (1 km·0.6 km·1 m) and the initial reservoir temperature distribution ranges from 145°C to 175°C.

We assume two wells into the inner reservoir, each having three possible injection/production points, thus leading to nine model configurations with different fluid/tracer schemes. The reservoir depth is between -2.5 km to -3.1 km and extending -0.5 km to 0.5 km horizontally. The unstructured mesh consisting of tetrahedral elements was created by the GMSH software (Geuzaine & Remacle, 2009). The element size differs between 1 m (around the wells) and 400 m (close to the boundaries) with a typical element size of 25 m inside the inner reservoir. The physical properties of rock and fluid are summarized in Table 5.1 and Table 5.2, respectively.

Table 5.1. Properties of the rock (Bächler et al., 2003; Baillieux et al., 2013)

Properties	Symbols	Units	Caprock	Outer reservoir	Inner reservoir	Bedrock
Porosity	ϕ	-	0.01	0.1	1	0.01
Permeability	k	m^2	10^{-18}	$5 \cdot 10^{-16}$	$5 \cdot 10^{-11}$	10^{-20}
Density	ρ^s	$kg \cdot m^{-3}$	2600	2600	2600	2600
Specific heat capacity	c_p^s	$J \cdot kg^{-1} \cdot K^{-1}$	850	850	850	850
Heat conductivity	λ^s	$W \cdot m^{-1} \cdot K^{-1}$	2	2	2	2

Table 5.2. Fluid properties (L. Smith & Chapman, 1983).

Properties	Symbols	Units	Value
Water			
Bulk modulus	K_w	Pa	$2 \cdot 10^{10}$
Density	ρ_w	$kg \cdot m^{-3}$	$\rho_w = 1000 \cdot e^{\frac{p_w}{K_w}}$
Viscosity	μ_w	$Pa \cdot s$	10^{-3}
Specific heat capacity	$C_{p,w}$	$J \cdot kg^{-1} \cdot K^{-1}$	4000
Heat conductivity	λ_w	$W \cdot m^{-1} \cdot K^{-1}$	0.6
Nanotracer			
Diffusion coefficient	D	$m^2 \cdot s^{-1}$	$4 \cdot 10^{-12}$

Tracers (conservative and temperature-reporting nanotracers with different temperature thresholds) are injected only on the first day at a mass rate of 6 $g \cdot s^{-1}$ for each tracer, whereas the injection and production flow rates of water are constant at 40 $L \cdot s^{-1}$ for five years. The water is injected at a constant temperature of 70°C. The inner reservoir has a thickness of 1 m in the X direction and has a permeability of $5 \cdot 10^{-11}$ m^2. As shown in Fig. 5.2b, the initial temperature range is 145°C to 175°C for a reservoir depth interval of 0.6 km. Three alternative injection points I1, I2 and I3 as well as production points P1, P2 and P3 have depth positions of -2.7 km, -2.8 km and -2.9 km, respectively see Fig. 5.2b.

5.3 Results and discussions

Several numerical simulations are conducted to illustrate the working mechanisms of temperature-reporting nanotracers by analyzing the response behavior from the data collected at the production well. Firstly, a case with homogeneous permeability of the inner reservoir is tested. The main purpose is to understand how the velocity field obtained from different well positions affects the breakthrough curve response of the temperature-reporting nanotracers for a given initial temperature distribution. The breakthrough concentrations of these nanotracers are analyzed by extracting the peak information (i.e., peak concentration values and peak arrival time) from their breakthrough concentration curves. Secondly, more complex features are added to the model to investigate the effect of inclined zones (with different permeabilities) embedded within the reservoir and different thermal distributions.

5.3.1 Reference case: homogeneous system

The temperature-reporting nanotracers we use in this example have different temperature thresholds from 145°C to 180°C with variations of 5°C. For specific and detailed investigations, the temperature threshold differences were refined to 1.25°C in part of the temperature range. It should be noted that the selected temperature threshold range of the nanotracers is valid only for our numerical model setting. In future nanotracer field tests, the temperature threshold range can be estimated from a simplified linear relationship between reservoir thickness and temperature data at or near the wellbore from the exploration and well-drilling stages. Conserved nanotracers are co-injected for comparison. Nine scenarios of injection-production position setup are simulated with the same well operating conditions, injected materials and volumetric rates.

1) Interdependency among fluid flow, heat transfer, transport and reaction of temperature-reporting nanoparticle tracers

To illustrate the temperature distribution and associated flow regimes related to the tracer test, consider two well positions: I1P1 and I1P3. The results are depicted in Fig. 5.3 when the conservative nanotracer concentration reaches its peak concentration at the production

well (80 days for I1P1 and 90 days for I1P3). The nanotracer is transported toward the production well, following the displayed fluid flow directions. The fluid (i.e., water well-mixed with nanotracers) flow direction is essentially based on the fluid velocity which is computed from Eq. (5.2). It does not indicate its magnitude. The fluid flow direction together with the velocity field (subplots a2 and b2) reflect the streamlines of fluid flow.

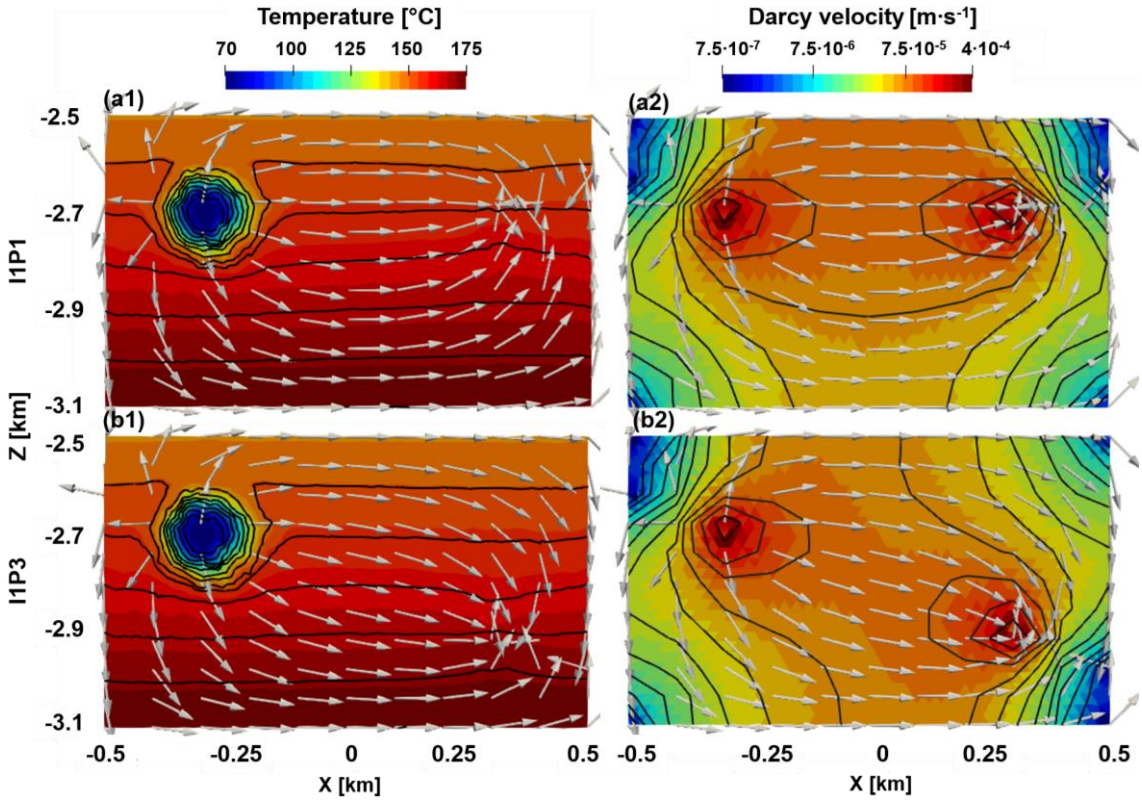

Figure 5.3. Typical thermal and hydraulic states of the reservoir (depth range 2.5~3.1 km): (1) Temperature and fluid flow direction distribution and (2) velocity fields at 80 days and 90 days which correspond to concentration peaks of the conservative nanotracer collected at the production well when the injection-production points (a) I1P1 and (b) I1P3 are chosen, respectively. The black lines in (a) and (b) are the reservoir temperature contour and Darcy velocity distributions, respectively.

The volume around the injection point cools down (Fig. 5.3a(1) and b(1)) since the injected water has a lower temperature. The temperature field is asymmetrical due to the flow field not being aligned with the initial temperature distribution. The injected fluid sweeps the reservoir symmetrically around the main streamline region towards the production point but is affected by the reservoir boundaries. The overall magnitude of fluid velocity for both I1P1 and I1P3 (Fig. 5.3a(2) and b(2), respectively) is similar along the main streamlines since the injection and production rates are the same.

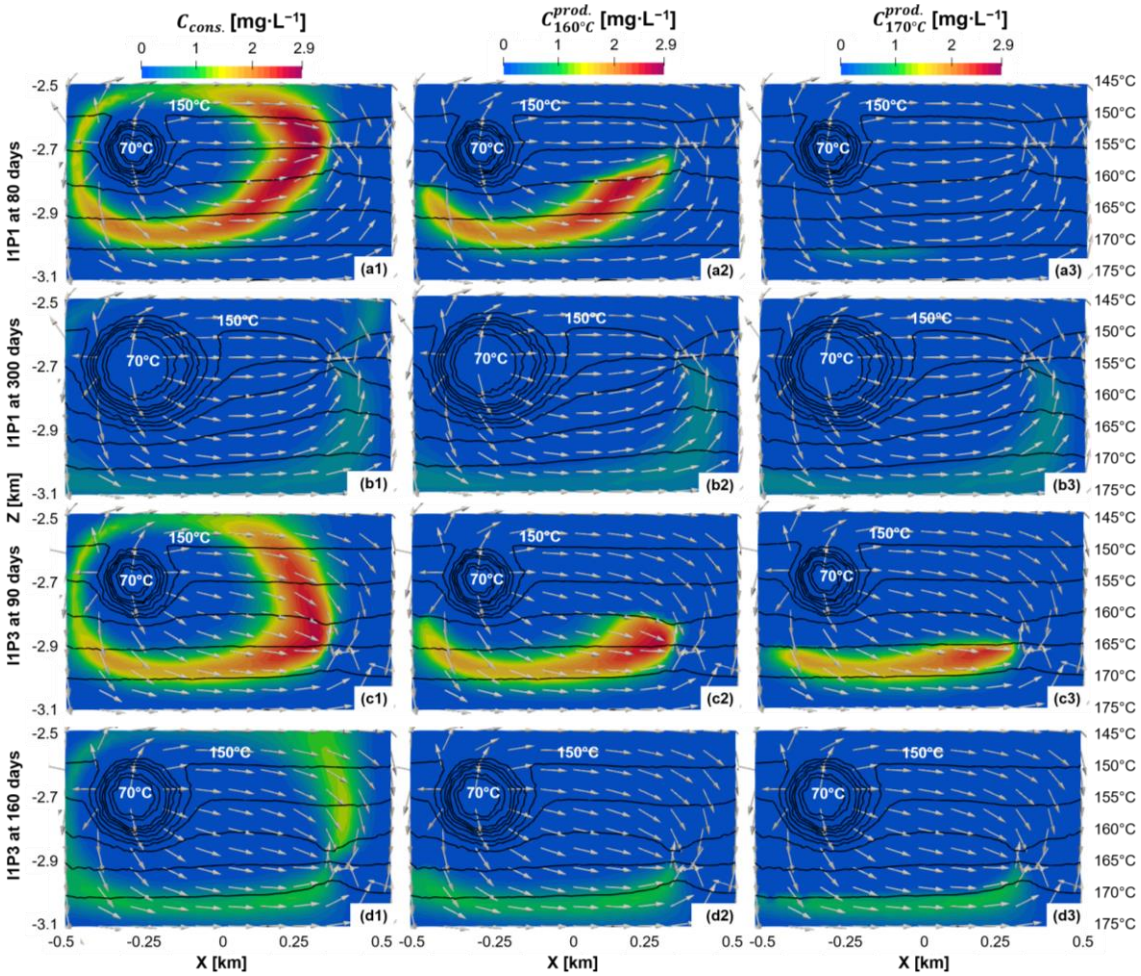

Figure 5.4. Distributions of conservative nanotracer and temperature-reporting nanotracers with $T_{thre.}$=160°C, 170°C. (a, b): I1P1 setup at 80 and 300 days (peak arrival time of conservative nanotracer and nanotracer with $T_{thre.}$=170°C); (c, d): I1P3 setup at 90 days and 160 days (peak arrival time of conservative nanotracer and nanotracer with $T_{thre.}$=170°C). The black contours with their magnitudes on the right clearly show the reservoir temperature distribution.

Figure 5.4 illustrates the nanotracer concentration distribution for three types of nanotracers: one conservative ($C_{cons.}$) and two temperature-reporting nanotracers ($C^{prod.}_{T_{160°C}}$ and $C^{prod.}_{T_{170°C}}$) with temperature threshold 160°C and 170°C, respectively. We track only the converted temperature-reporting nanotracer concentrations ($C^{prod.}_{T_{thre.}}$) as the sum with unconverted nanotracer concentration is preserved (acting as a conservative nanotracer). Injection-production position setups are still I1P1 (Fig. 5.4a and b) and I1P3 (Fig. 5.4c and d). In each case, two groups of times were selected for plotting: the former are 80 days and 300 days and the latter are 90 days and 160 days, which individually correspond

to the peak arrival time of conservative nanotracer and temperature-reporting nanotracer with $T_{thre.}$=170°C in the I1P1 case and the I1P3 case, respectively.

In the case of I1P1, conservative nanotracer flows from the injection point to the production point, covering both shallow and deep parts of the reservoir (Fig. 5.4a(1) and b(1)). The high-concentration part of the conservative nanotracer is best maintained along the main streamline of fluid, while the concentrations are more diffuse in the weak-current region. This is associated with the nanotracer concentrations traveling at different speeds and mixing with low fluid concentrations at neighbouring streamlines. The temperature-reporting nanotracers can react if they reach temperatures above their thresholds thus being converted. As a result, shallow and deep formations with comparatively low and high temperatures have different abilities to convert the temperature-reporting nanotracers with their corresponding temperature thresholds. From Fig. 5.4a(2) and (3), there are large proportions of converted temperature-reporting nanotracers with a threshold of 160°C in the lower half reservoir and only small amounts of converted temperature-reporting nanotracers with a threshold of 170°C appear in the lower quarter reservoir. Above the middle reservoir, there is zero concentration of $C_{T_{160°C}}^{prod.}$ and $C_{T_{170°C}}^{prod.}$ meaning that the corresponding nanotracers are not converted in the upper part of the reservoir. Compared to the conservative nanotracer, the two temperature-reporting nanotracers are just partly converted. Compared to the results in 80 days, the concentrations of the three nanotracers become weakened after 300 days due to continuous production. In addition, the distributions of $C_{T_{160°C}}^{prod.}$ and $C_{T_{170°C}}^{prod.}$ are similar to each other after 300 days, which reflects the slow tail production.

From case I1P1 to I1P3, the fluid flow direction has changed (see Fig. 5.4a(1) and c(1)). The conservative nanotracer in Fig. 5.4a(1) and c(1), flows through a wide region and a slightly longer distance to the production point. The peak arrival time is thus longer with I1P3 than with I1P1. However, when comparing Figures 5.4b(3) and d(3), the peak arrival time of the nanotracer with a 170°C threshold is less with I1P3 (160 days) than with I1P1 (300 days) due to the shorter flow path to cross regions where temperatures reach above 170°C.

2) Well configuration impact on temperature-reporting nanotracer breakthrough curve

As mentioned earlier, there are a total of nine injection-production well positions. Figure 5.5 summarizes the nanotracer breakthrough concentrations at the production well, including both conservative nanotracer and nine converted temperature-reporting nanotracers with temperature thresholds varying from 150°C to 172.5°C.

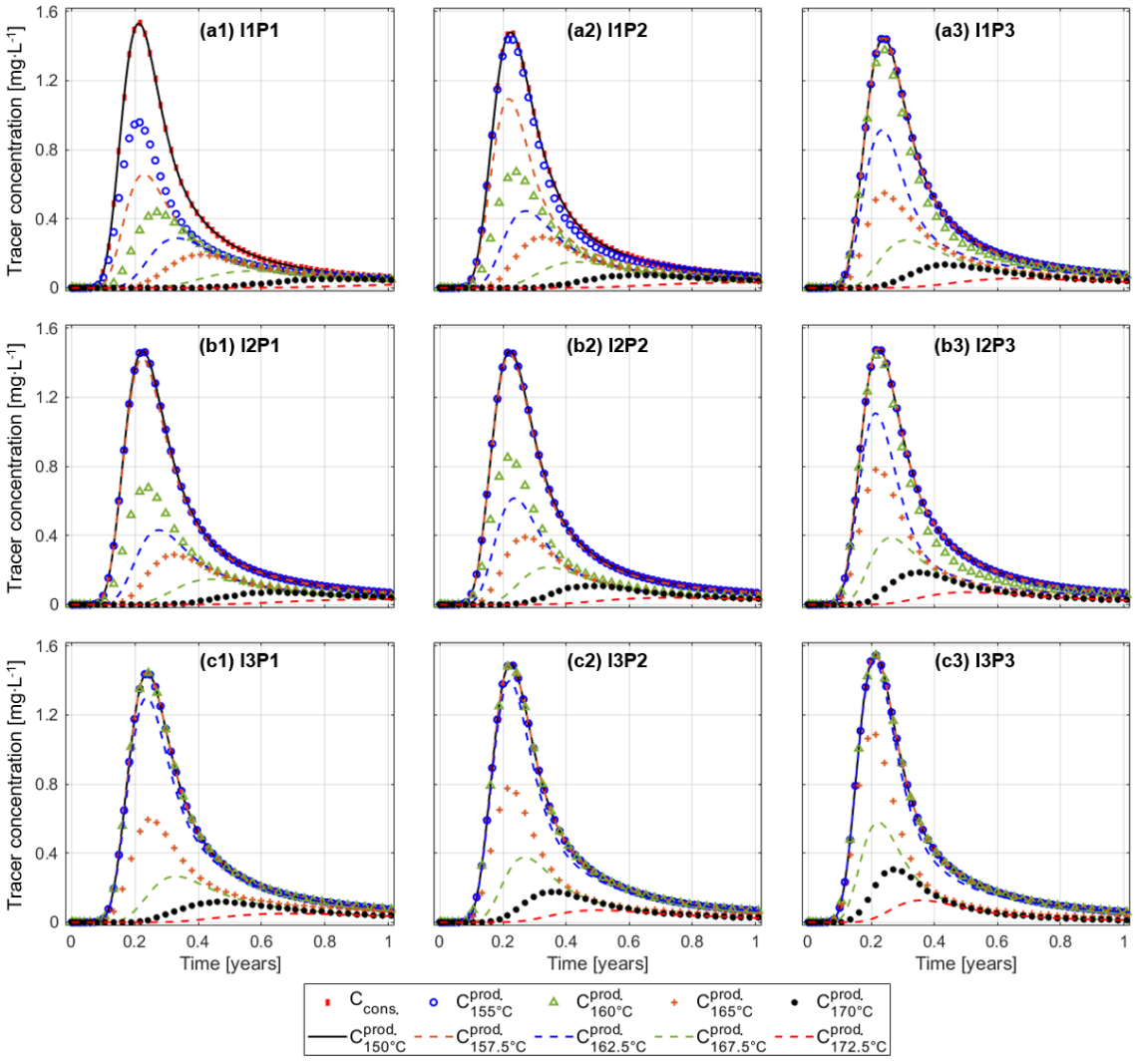

Figure 5.5. Nanotracer breakthrough curves in comparison to the conservative nanotracer (blue points) with a total of nine injection-production well configurations.

The nanotracers are injected with the same concentration and can be directly compared. The conservative nanotracer profile is always above the other nanotracer profiles. The

temperature-reporting nanotracers are converted only when their thresholds are met in certain reservoir regions.

Referring to Eq. (5.4), the sum of reactant and product concentrations equals the conservative nanotracer concentration. When a nanotracer is not fully converted, the product concentration is less than the conservative nanotracer concentration. Therefore, in all subplots of Fig. 5.5, the curves produced by the temperature-reporting nanotracers with low-temperature thresholds, such as 150°C and 155°C, are very close to the conserved one. In addition, high peak concentration values in these nanotracer breakthrough curves normally correspond to short travel time. On the contrary, the temperature-reporting nanotracers with high-temperature thresholds such as 172.5°C are less converted and have lower peak values of concentration. They also take a longer time to reach the peak concentration than those with low-temperature thresholds such as 160°C. Nanotracers with higher thresholds have to be transported further to be converted.

The effects of injection-production positions are visible on the nanotracer breakthrough curves in Fig. 5.5. Subplots (a1) I1P1, (b2) I2P2 to (c3) I3P3 show that the magnitude of temperature-reporting nanotracer breakthrough curves increases towards the conservative curve with deeper injection-production position. More nanotracer is converted at a greater depth with higher temperatures. The process to reach their corresponding peaks is also accelerated because the conversion happens along (or closer to) the fastest streamline. The same trends apply to the cases where well position I or P is constrained but the paired well position P or I moves towards the deep formation, referring to subplots (a1)-(b1)-(c1) in Fig. 5.5.

The results from injection-production positions I1P3 (Fig. 5.5a(3)) and I3P1 (Figure 5.5c(1)) differ, although the geometric settings are symmetrical. The 162.5°C nanotracer curve in subplot (c1) with I3P1 has a higher magnitude than in subplot (a3) with I1P3. This difference is due to the nanotracer starting at a high temperature in the first case, and not meeting that high temperature along all flow lines in the second case.

3) Analysis of temperature-reporting nanotracer breakthrough curves for reservoir characterization

A key factor that can be used to maximize the production of geothermal energy is the knowledge of temperature which is the main streamline of injected water experiences. Since the nanotracers follow the water, the temperature-reporting tracer information can, ideally, reflect the temperature characteristics of the streamlines. Based on that, a new analysis method is proposed to quantify reservoir temperature information from temperature-reporting nanotracer breakthrough curves (such as Fig. 5.5). Peak concentration values and peak arrival time are plotted versus the nanotracer temperature thresholds, see Fig. 5.6. Temperature-reporting nanotracers with thresholds 175°C and 180°C were not converted due to the highest reservoir temperature being 175°C. Therefore, their peak concentrations in subplot (a) are zero and the peak arrival time in subplot (b) does not exist. Here we need to mention that it is important to use a broad range of nanotracer temperature thresholds to cover the reservoir temperatures since the exact temperature distribution is unknown in realistic field tests.

The curves of both peak concentration value and peak arrival time versus threshold temperature have flat sections at low-temperature thresholds, which correspond with the conservative nanotracer, indicating full conversion. The temperature encountered on the flow paths between the wells must therefore be above these thresholds.

When the peak concentration curves deviate from the flat sections, for a nanotracer with a sufficiently high threshold temperature, some of that nanotracer has traveled along a flow path with a temperature below the threshold where it was not converted. In other words, the threshold temperature at the transition from fully converted nanotracers to less converted nanotracers indicates that there are flow paths not exceeding this indicated temperature. This provides an upper limit of the lowest temperature in the flow region. Similarly, when the threshold temperature of the nanotracers becomes sufficiently high, they are not converted (zero peak concentration) indicating no flow paths reach that high temperature. Thus, the threshold temperature where the nanotracers firstly stop being converted is an indication and approximation of the highest temperature in the flow region. As the sum concentration of nanotracer reactant and product acts like a conservative nanotracer, this holds regardless of reservoir properties (this could change if the nanotracer interacted chemically different within the reservoir).

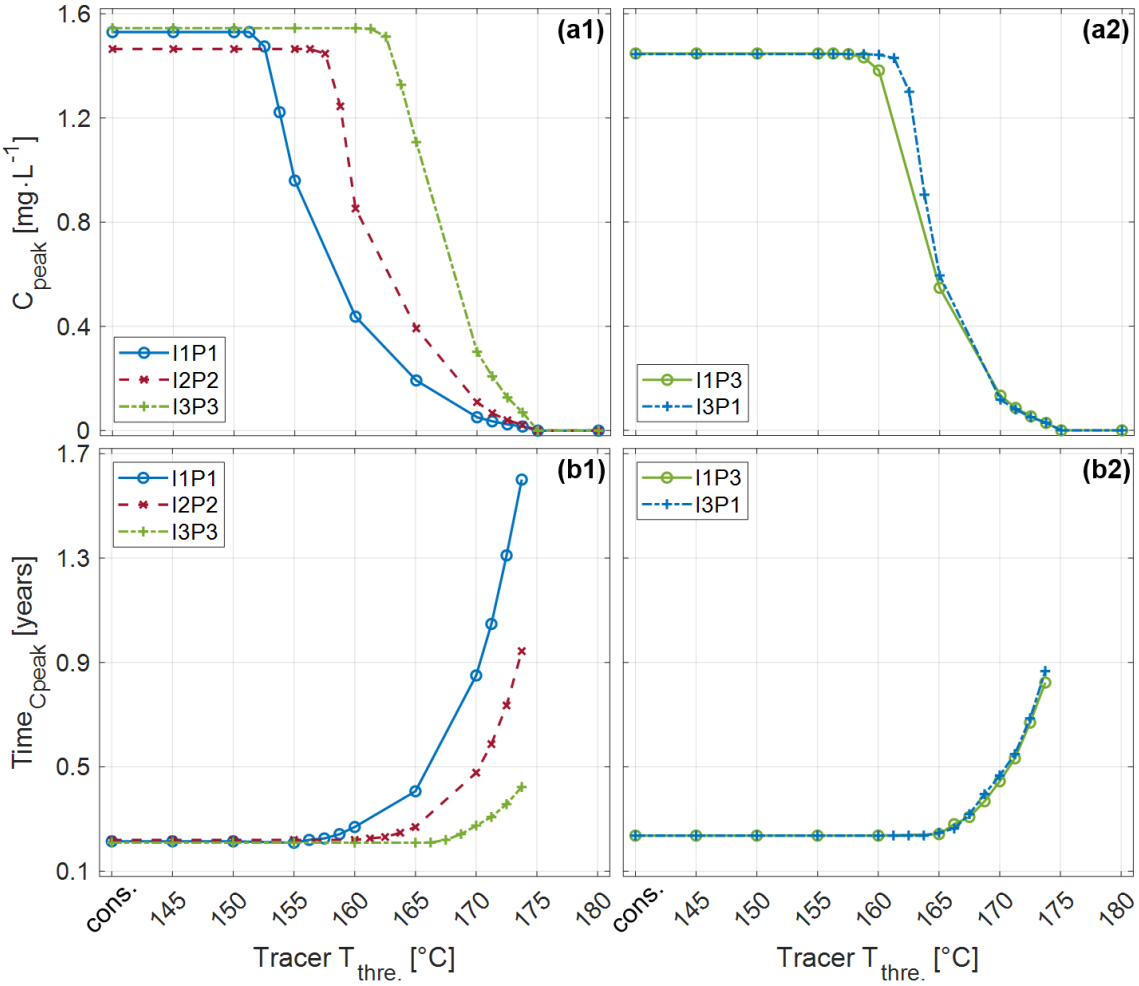

Figure 5.6. Comparison of peak concentration (a) and peak arrival times (b) of the individual nanotracer types from the nanotracer breakthrough curves for different well configurations. Thresholds from 145°C to 180°C and conservative nanotracers are shown.

As indicated, there is an important precaution regarding the history-dependent behavior of the nanotracers. If they have passed through a region above the threshold temperature, they are activated regardless of what happens later. Consider the difference between injection from a deep towards a shallow producer, with injection from a shallow position towards a deep position. (i) In the former case the high temperature is at the injector and the different nanotracers are exposed to high temperature from the start. They might not see much higher temperatures and although there are lower temperatures downstream, they are already activated, yielding a narrow range for the deviation thresholds. Such a case mainly provides reliable information about the highest temperature. (ii) In the latter case the nanotracers are exposed to a low temperature at the injector and take multiple directions having different temperatures towards the producer. The initial high-

temperature fluid at the producer is produced before the nanotracers encounter it, meaning the maximum interpreted temperature may be less than the initial temperature at the producer. Some flow paths can however go deeper to reach even higher temperatures.

In the following, the nanotracer temperature threshold at the turning point of each nanotracer curve is discussed and compared to the temperature along the injection-production positions. Consider first the injector-producer pairs positioned at the same depth. In Fig. 5.2b, the initial temperatures of I1P1, I2P2 and I3P3 are 155°C, 160°C and 165°C, separately. In Fig. 5.6a(1) the peak concentration values deviate at 151.25°C, 156.25°C and 161.25°C, respectively. This means not all the injected nanotracer was converted by the initial temperature surrounding the injector. Keep in mind that the nanotracer mixture (and then water) is injected at 70°C and thus the nanotracer needs some residence time to reach a higher temperature. As seen in Fig. 5.3a(1) there is a low-temperature region near the injector, while the temperature distribution in the rest of the reservoir is less affected. Some nanotracers, particularly the end of the slug, can follow paths that do not reach the high initial temperatures. Concerning the peak arrival time in Fig. 5.6, we observe a deviation from the horizontal section at 155°C, 160°C and 166°C, which corresponds more closely with the initial temperatures at the injectors and producers. In Fig. 5.6a1), nanotracer peak concentrations become zero when the temperature threshold approaches 175°C. This means the maximum temperature of the overall reservoir is below 175°C (as confirmed in Fig. 5.4). While this high temperature was detected in all three cases, the lowest temperature of the reservoir of 145°C (see Fig. 5.4) was not detected by any. Flow lines were passing through temperatures below 150°C for the case I1P1 (Fig. 5.4), thus 145°C might have been expected to be the highest stable point. Likely, each flow line contained a region (close to the well) with a higher temperature that activated the nanotracers, as suggested before. From the above analysis, we conclude that it is generally difficult to estimate the lowest temperatures in the reservoir. However, when the wells, especially the injector, are placed shallower, the threshold temperature where the peak concentrations start to decrease, becomes better, but not reliable, estimates of the minimum temperature.

The results of inclined wellbore positions I1P3 and I3P1 are shown in Fig. 5.6a(2) and b(2). As seen in Fig. 5.4 for I1P3, flow lines pass through both regions below 150°C and

above 170°C and the same is true for I3P1 by symmetry. For both cases, the concentration curves flatten precisely at 175°C, as for the three previous cases, indicating the maximum temperature of 175°C. The peak concentrations of I1P3 and I3P1 cases deviate at 157.5°C and 160°C, respectively, close to the initial temperature of 160°C centrally between the two wells (Fig. 5.2). This reflects that nanotracer needs to flow through regions with this temperature whether it flows from the deep or shallow configuration. Especially in Fig. 5.4, we see that for I1P3 all flow lines cross a temperature of 160°C at the indicated time. The deviation threshold temperature is higher for I3P1, related to the nanotracer encountering higher temperatures from the start. In Fig. 5.6b(2), the peak arrival time deviates for both I1P3 and I3P1 at a temperature threshold of 165°C. This is closer to the deeper wellbore's initial temperature.

It is noticeable that the peak concentrations deviate at lower temperature thresholds than the arrival time. As seen in Fig. 5.6a and b, the peak concentrations reduce while their arrival time stays the same. This is related to where the nanotracers are flowing. The peak of the conservative nanotracer represents the flow from the fastest flow lines between the wells. When the nanotracer is converted along the same lines, we also see the arrival of that nanotracer with the same peak, however, when the nanotracer needs to take a longer path to be converted, the arrival time is increased. Several of the colder streamlines at the top of the reservoir may supply an unconverted nanotracer, yielding less production and a lower peak concentration of the converted nanotracer. But as long as the main flow line between the wells has sufficient temperature the arrival time is similar to the conservative nanotracer. Similarly, we can suggest that the higher peak arrival time represents the time needed for nanotracers with the indicated thresholds to pass through flow lines with those temperatures. In Fig. 5.6b(1) the arrival time of a nanotracer with a given threshold decreases when the horizontally positioned well pair is deeper, because the main flow line has a higher temperature and activates more nanotracers there, and because the nearby flow lines also have a higher temperature. At shallow locations, the nanotracer needs to follow a long flow path to be activated. Considering the inclined positioned wells (Fig. 5.6b(2)), the arrival time profiles are almost identical. They deviate from the flat section when the threshold temperature exceeds the highest temperature of 165°C along the main flow line. Only flowlines deeper than the well pair reach higher temperatures. With the

flow pattern being symmetrical and most of the temperature distribution remaining as the initial, the nanotracers are activated in the same flow lines for the two cases and get the same arrival time.

To summarize the main points, temperature-reporting nanotracer breakthrough curves can be interpreted as follows:

- The nanotracer peak concentrations as a function of threshold temperature:
    - Deviate from full conversion at a threshold temperature which is an upper limit of the lowest temperature encountered along all the flow lines. This is not a reliable estimate of the minimum temperature.
    - First reaches a zero value at a threshold temperature which is a precise estimate of the maximum temperature in the flow region. The estimate is improved by using multiple tracers with small differences in the temperature thresholds.
- The nanotracer arrival time as a function of threshold temperature:
    - Deviates from the arrival time of the conservative nanotracer at a threshold temperature equal to the highest temperature along the fastest/main flow line between the wells. This deviation temperature is usually higher than that from the nanotracer peak concentration curve.
    - Higher arrival time on the curve indicates the time needed to flow along lines reaching the corresponding threshold temperatures.

In the following sections, we utilize the presented analysis method on more complicated reservoir conditions, including **Section 5.3.2** different thermal distributions (varied temperature ranges at certain depths and regional thermal anomalies) within the geothermal reservoir and **Section 5.3.3** inclined zones embedded within the reservoir. The purpose of these investigations is to determine the impact of these thermal and geological uncertainties on the analysis of performance evaluation of temperature-reporting nanotracers in geothermal reservoirs. Schematic illustrations of varied temperature ranges, regional thermal anomalies and inclined zones are shown in Fig. 5.7), respectively.

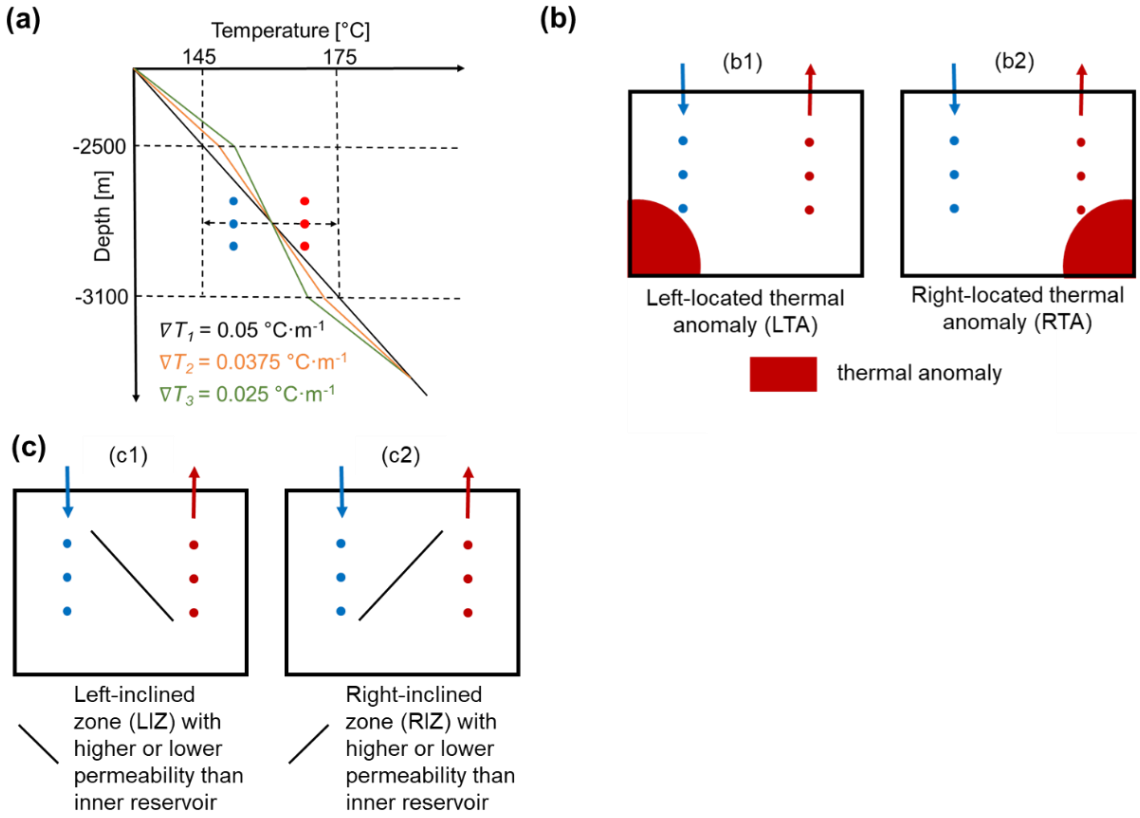

Figure 5.7. Schematic representation of geological heterogeneities and temperature anomalies in a reservoir (a): Different initial temperature ranges with gradients ∇T = 0.05°C·m^{-1}, 0.0375°C·m^{-1} and 0.025°C·m^{-1} along the inner reservoir depth from -2500 m to -3100 m; (b) Lower-left or lower-right located high-temperature regions within the inner reservoir; (c): Left-inclined (LIZ) or right-inclined zones (RIZ) with higher, same, or lower permeabilities compared to the inner reservoir. Note that the inclined zone with dimensions (1000 m·600 m·1 m) is a plane perpendicular to the thin reservoir.

5.3.2 Impact of different thermal distributions in the fractured geothermal reservoir

Temperature distributions and heat flux densities in the subsurface can vary greatly depending on location. Values above average are referred to as positive anomalies. Conversely, a negative anomaly indicates a decrease in temperature or heat flux relative to the surrounding mean. Thermal anomaly in subsurface formations is a common geological phenomenon that can be caused by variations of thermal conductivities around structures such as salt domes, geological and tectonic activity, geochemical reactions, or hydrothermal activities in faults and fractures (Cherubini et al., 2013; Emry et al., 2020; Yan et al., 2023). Subsurface formations with positive thermal anomalies are targeted as areas of geothermal development for heat and electricity production (Moeck, 2014). In

the following, we investigate two scenarios impacted by different local temperature gradients or a positive regional thermal anomaly and whether they are detectable by the nanotracer analysis.

1) Different temperature ranges

We consider three different initial temperature gradients as shown in Fig. 5.7a where the middle of the reservoir is constrained to 160°C. Here, cases 1, 2 and 3 respectively correspond to temperature gradients of 0.05°C·m^{-1}, 0.0375°C·m^{-1}and 0.025°C·m^{-1}, with initial reservoir temperature ranges of 145°C~175°C, 148.25°C~170.75°C and 152.5°C~167.5°C. Note that only the initial reservoir temperature range is varied in the numerical model; the remaining parameters are the same as in the reference case. Case 1 is essentially the reference case studied in **Section 5.3.1**.

The resulting concentration peak and arrival time trends from the nanotracer breakthrough curves are shown in Fig. 5.8a and b for injection-production position setups I1P1 and I1P3. There is an obvious distinction among the curves of the three cases with different initial temperature gradients. In Fig. 5.8c the curve deviation temperatures are compared with initial well temperatures (red markers) and initial reservoir temperature range (grey bars) for additional well setups. Each curve in Fig. 5.8a(1) and (2) flattens at zero concentration at a high temperature. As discussed, this point indicates the maximum temperature, which is confirmed to be accurate by the comparison (top of the grey bar and top green point) in Fig. 5.8c(1) and (2). The lower temperature deviation on the concentration curve, however, does not reliably estimate the minimum reservoir temperature and is in some cases above the lowest initial well temperature and, and some cases below. The deviation temperature of the arrival time curve (blue marker) has been noted to reflect the maximum temperature along the streamline between the wells. As the reservoir is homogenous, this flow line goes directly between the wells and the maximum temperature of this flow line is likely to be approximately the highest initial well temperature. This comparison (blue point and highest red point in Fig. 5.8c is very accurate (0 to 2°C difference) for all 10 cases. We have thus demonstrated accurate prediction of the highest reservoir temperature and main streamline temperature.

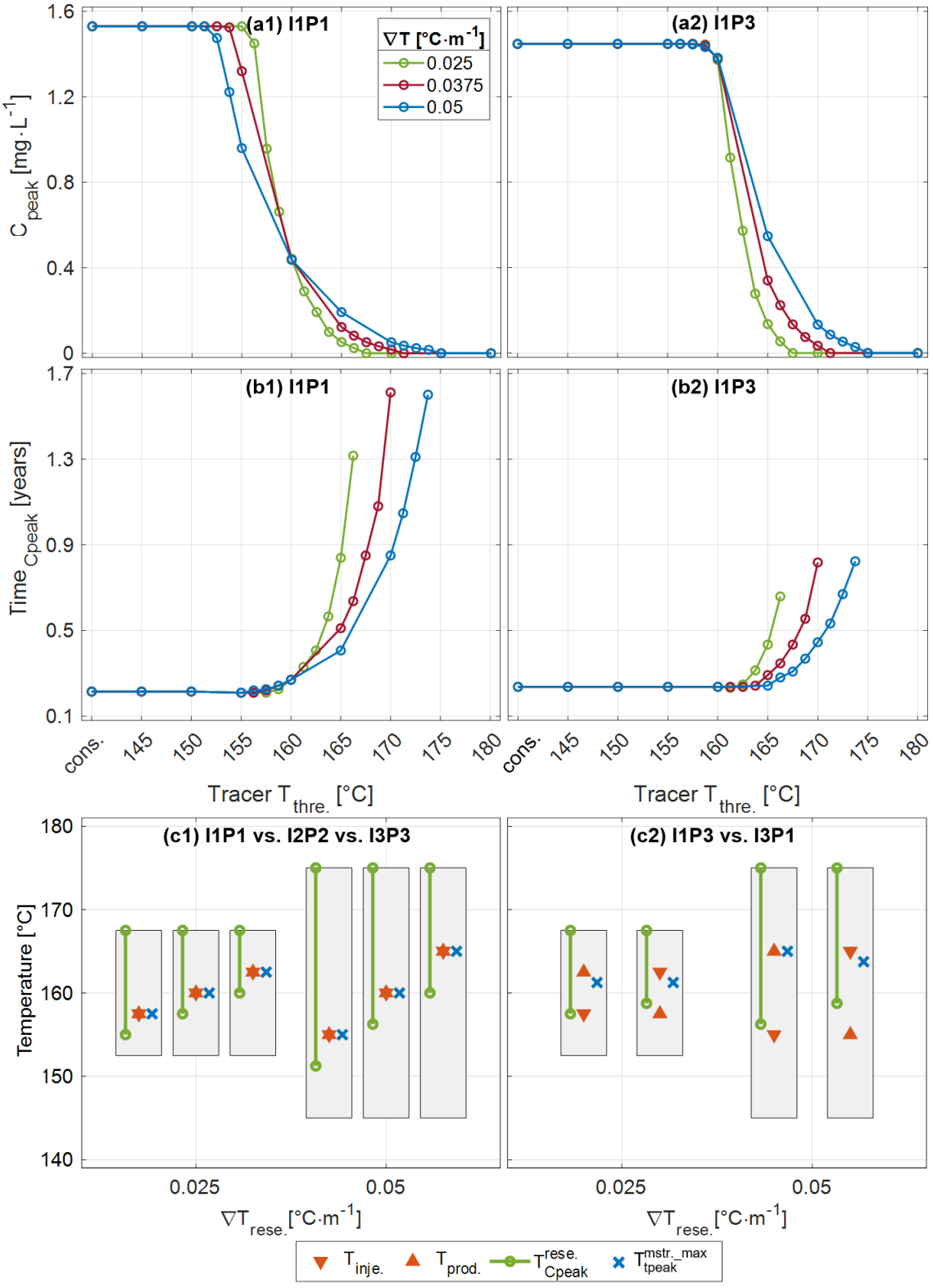

Figure 5.8. Comparison of nanotracer performance for peak concentration (a), peak time (b) and estimated reservoir temperature data (c) for initial temperature gradients ∇T = 0.025 or 0.05°C·m^{-1}. Well configurations are indicated. $T_{inje.}$ and $T_{prod.}$ are initial temperatures at injection and production positions, while grey bars indicate the reservoir's initial temperature range. $T_{C_{peak}}^{rese.}$

show estimated reservoir temperatures based on peak concentration curve deviation. $T_{t_{peak}}^{mstr.\_max}$ is the temperature where the arrival time curve deviates (estimating the highest temperature on the main streamline between the wells).

When the initial temperature range (i.e. local gradient) increases the estimated max temperature increases accordingly. For the horizontally positioned wells, a higher gradient (thus lower min temperature) is reflected in a lower min temperature estimate for I1P1, but when the wells are positioned deeper (I2P2 or I3P3), there is little to no difference with the gradient. The flow lines then start at hotter temperatures (slightly below the initial well temperature) and activate according to higher temperatures than found at the top of the reservoir. Changing the gradient for I1P3 also has little effect on the lower limit temperature estimate, as the flow lines all pass 160°C in the center.

The temperatures between the concentration turning points indicate a possible reservoir temperature range. For a given well positioning the jump of each curve in Fig. 5.8a(1) or a(2) will become sharp when the temperature gradient decreases. Regardless of the initial temperature gradients of the reservoir, subplot (c1) shows that the low reservoir temperature obtained is dependent on the tested positions, the maximum temperature can always be detected, and shallow tested locations such as horizontal I1P1 exhibit more effectiveness in measuring reservoir temperature intervals. Looking at the inclined cases I1P3 and I3P1 in subplot (c2), the estimation performance for reservoir temperature ranges looks pretty generic.

2) Regional Thermal Anomalies

High-temperature regions are artificially added to the reservoir in the lower-left or lower-right positions to mimic regional positive thermal anomalies of up to 200°C from deep radiant heat sources, see Fig. 5.7b. Note that only the high-temperature regions are added to the numerical model, the remaining parameters are the same as in the reference case. The temperature thresholds of the nanotracers have extended from 145°C~180°C to 145°C~205°C with variations of 5°C. For specific and detailed investigation, the temperature threshold difference is refined to 2.5°C in part of temperature ranges. We compare tracer results in Fig. 5.9a and b for a homogeneous case without thermal anomaly

(HOM), a case with left thermal anomaly (LTA), and a case with right thermal anomaly (RTA).

The high-temperature region enhances the conversion of temperature-reporting nanotracers with high thresholds in the deep reservoir, see subplots (a1) and (a2). The cases with LTA and RTA produce nearly the same results for I1P1 in subplot (a1), probably because the streamlines are symmetric in the left-right direction and the cooled-down region due to injection has not affected the high-temperature distribution in the deep reservoir during the given period. Nevertheless, when the injection-production position is changed to the inclined I1P3, the difference between LTA and RTA is clearly distinguishable in subplot (a2) where the case with RTA results in higher peak concentration values than with LTA. The streamlines from I1 to P3 flow through the high-temperature region on the right side (RTA) close to P3 rather than the left one (LTA) which is not close to either well. For I3P1 the resulting behavior between RTA and LTA is opposite.

In subplot (b), the trends of the curve's relative position are similar to those plotted based on peak concentration values in subplot (a). It should be mentioned that a high-temperature region in the reservoir could behave similarly to the one with large temperature gradients when comparing Fig. 5.9a and b to Fig. 5.8a and b. Specifically, the low-temperature gradient case ($0.025°C \cdot m^{-1}$) in Fig. 5.8a and b always gives a narrow threshold temperature range which is also seen in the behavior of the HOM case without high temperature anomaly in Fig. 5.9a and b. Moreover, based on the results presented in Fig. 5.9a(2) and b(2), we are able to distinguish the differences caused by the existence of thermal anomalies as well as the locations of thermal anomalies in the reservoir, when the injection-production well configuration is inclined. A performance evaluation of the nanotracers in the reservoir with thermal anomalies is given according to the breakthrough curve peak analysis (Fig. 5.9a and b) for selected cases. The maximum temperature within the reservoir is estimated accurately, which means the thermal anomaly is detected. Although a shallow injection-production position can help to more accurately estimate the reservoir temperature range as seen in Fig. 5.9c(1), this effect is reduced when a thermal anomaly with high temperature is located in the deep reservoir, including both RTA and LTA. This observation is also valid for inclined well positions, see subplot (c2),

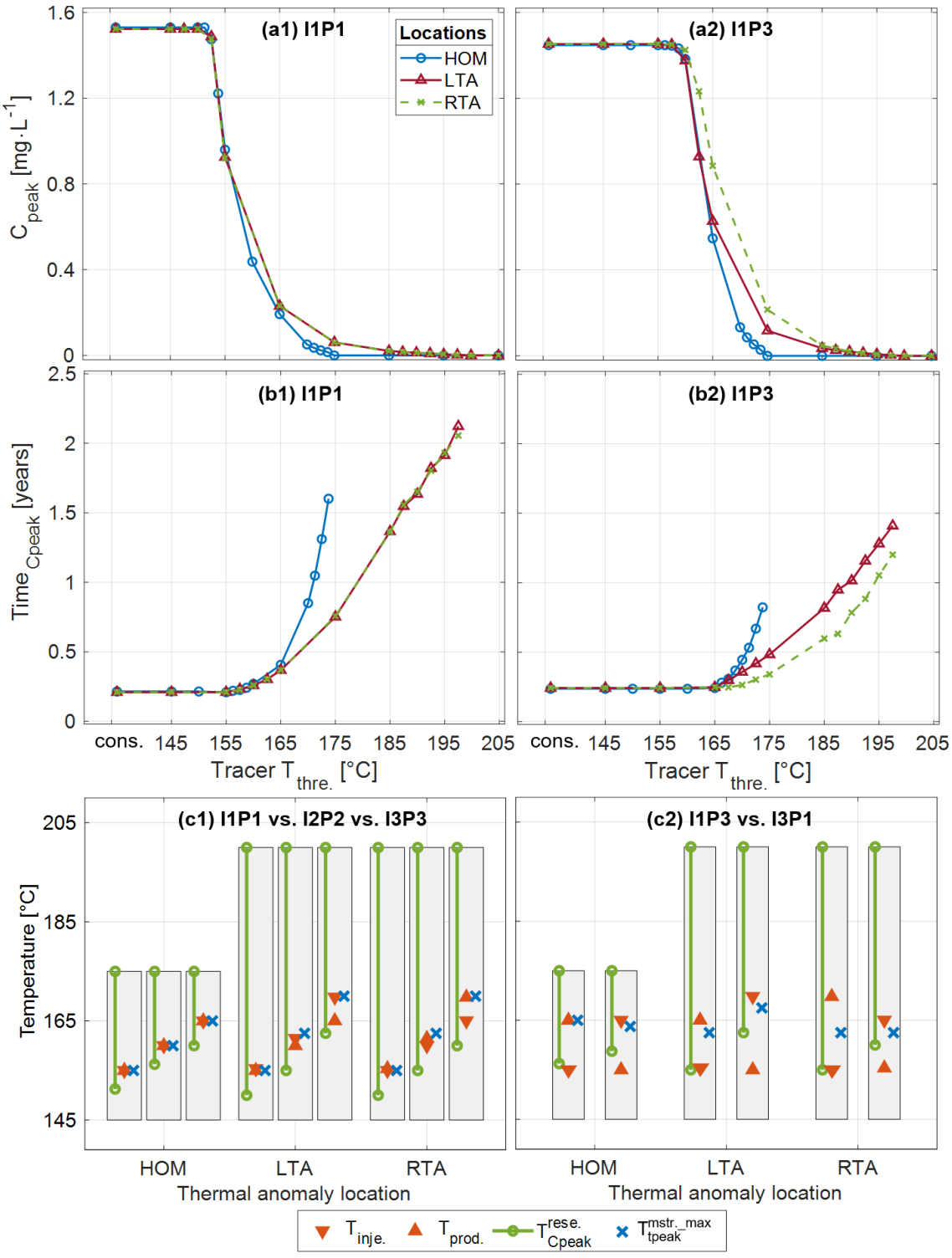

Figure 5.9. Comparison of nanotracer performance for peak concentration (a), peak time (b) and estimated reservoir temperature data (c) in models with no (HOM), left-located (LTA) or right-located (RTA) different thermal anomalies. Well configurations are indicated. $T_{inje.}$ and $T_{prod.}$ are initial temperatures at injection and production positions, while grey bars indicate the reservoir's initial temperature range. $T_{C_{peak}}^{rese.}$ show estimated reservoir temperatures based on peak

concentration curve deviation. $T_{t_{peak}}^{mstr.\_max.}$ is the temperature where the arrival time curve deviates (estimating the highest temperature on the main streamline between the wells).

when comparing the case HOM with the cases LTA and RTA. The temperature where the peak arrival time curve deviates indicates the highest temperature along the main streamlines between the wells and in most cases corresponds well with their highest initial temperature.

5.3.3 Impact of geological heterogeneities resulting from inclined zones

Reservoirs are usually highly heterogeneous and some distinguishing features are large spatial differences in reservoir permeability. In some cases, low permeable zones are encountered, such as faults developed by tectonic movement; high permeability layers exist in other cases, such as thief zones due to possible clay erosion or sand production after a long period of water injection (C. Lu et al., 2021). Tracer testing can identify the properties of fractures or inclined zones, dependent on the shapes of tracer breakthrough curves (J. Li et al., 2016; L. Li et al., 2017). Those studies mainly focused on the conservative tracer, while here we will explore how such geological features affect the performance of temperature-reporting nanotracers in fractured geothermal reservoirs.

Figure 5.7c illustrates a thin inclined zone centrally placed between the wells. The effects of left-inclined and right-inclined zones are studied with permeabilities higher (i.e., $5 \cdot 10^{-10}$ m^2) or much lower (i.e., $5 \cdot 10^{-16}$ m^2) than the inner reservoir permeability (i.e., $5 \cdot 10^{-11}$ m^2). Note that only the inclined zones with different directions and permeabilities are added to the numerical model, the remaining parameters are the same as in the reference case. As illustrated in Fig. 5.10, concentration distributions of a conservative tracer and a temperature-reporting nanotracer with a 160°C threshold are shown with injection-production setup I1P3 at 70 days (when tracers flow through the inclined zone). The results with a low-permeable inclined zone are given in Fig. 5.10a and b), and those with a high-permeable inclined zone are shown in Fig. 5.10c and d. As expected, the temperature-reporting nanotracer with a 160°C threshold mainly exists in the lower part of the reservoir where it is converted whereas the conservative tracer has a large area of distribution in the reservoir.

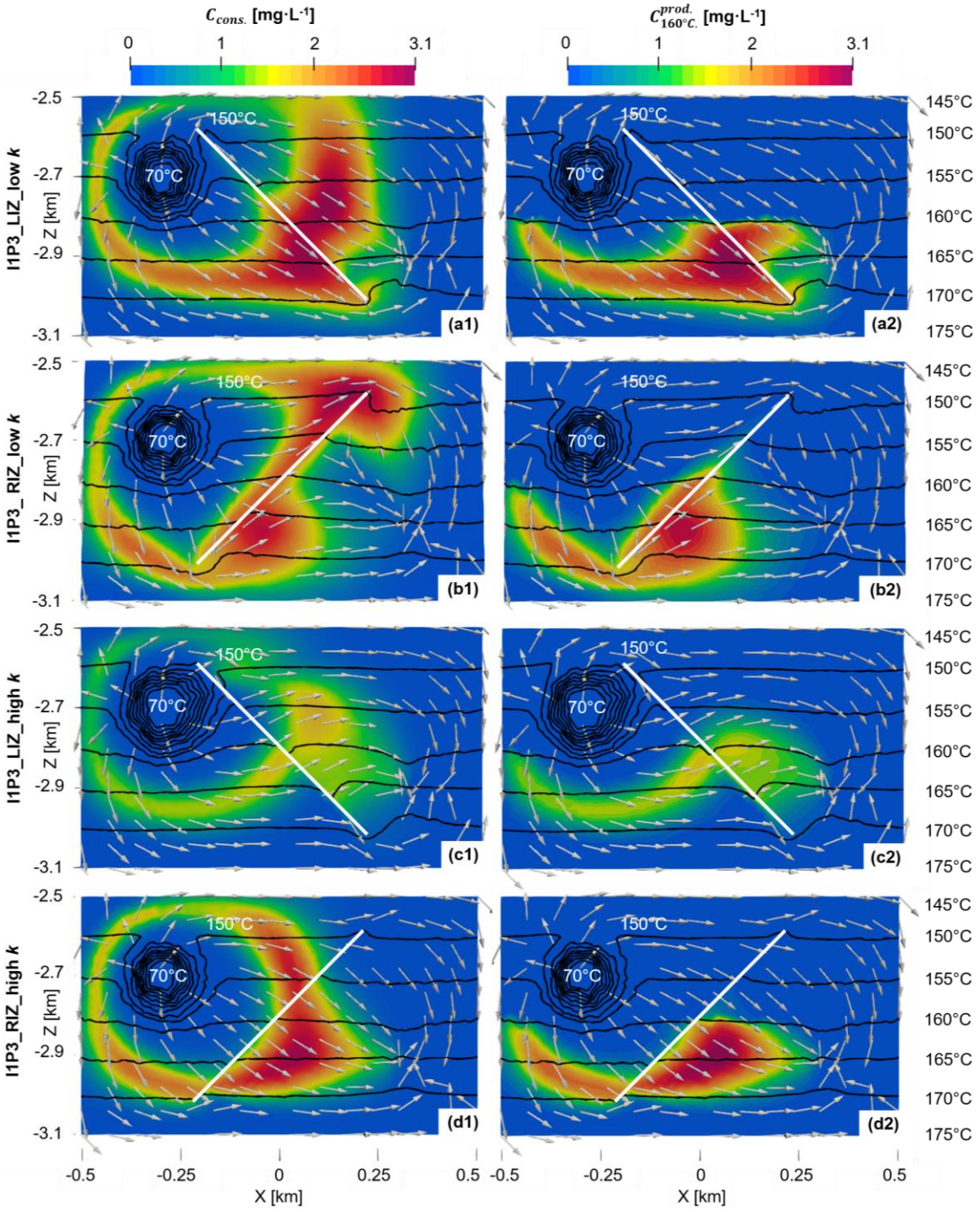

Figure 5.10. Tracer concentration distributions after 70 days for a geological heterogeneous model, i.e. an inclined zone (white line) and configuration I1P3. The difference between a conservative tracer (left column) and a temperature-reporting nanotracer ($T_{thre.}$=160°C, right column) is clearly demonstrated in dependence of the hydraulic setting. Subplot a/b: low-permeable left-/ right-inclined zone (i.e., $5 \cdot 10^{-16}$ m^2); Subplots c and d: high-permeable left and right-inclined zone (i.e., $5 \cdot 10^{-10}$ m^2). Note that the permeability of the inner reservoir is $5 \cdot 10^{-11}$ m^2. The black contours with their magnitudes on the right show the reservoir temperature.

In the cases with a low-permeable inclined zone, the inclined zone behaves as a tight barrier for tracer transport and tracer concentrations are separated. In subplot (a2) there is a region of high-concentration converted tracer above the inclined zone. Temperature-reporting tracer has been transported around the upper region of the reservoir (above the inclined zone) and converted after passing the 160°C isotherm.

In the cases with a high-permeable inclined zone in Fig. 5.10c and d, we notice in subplots (c1) and (c2) that the fluid flow is attracted up towards the high permeability zone giving a more horizontal flow in the reservoir. This flow diversion is less clearly seen in subplots (d1) and (d2) since the direction of I1P3 is perpendicular to the right-inclined zone. The concentration of conservative tracer is less in subplot (c1) than in subplot (d1). The conservative tracer meets the high-permeable zone earlier in subplot (c1) and more tracer transports to the high-permeable zone where the tracer can be accumulated, compared to subplot (d1). Moreover, since the fluid flow is attracted towards a horizontal direction in the upper part of the reservoir in subplot (c2), less temperature-reporting nanotracer transports downward being converted than in subplot (d2).

A comparison of the tracer peak concentration and peak arrival times is shown in Fig. 5.11 for two configurations: I1P1 and I1P3. As seen in Fig. 5.1a(1) and b(1) the results for I1P1 are very similar when comparing whether the inclined zone is left or right-oriented for a given permeability, due to symmetry. For I1P3, left- or right-inclined orientations do not give symmetrical flow and thus the orientation of the inclined zone impacts the tracer profiles, see curves in Fig. 5.11a(2) and b(2). Referring to Fig. 5.10c (1), a high-permeable inclined zone can divert flow towards it and attract tracers to flow in its plane from the reservoir, resulting in low peak concentration values. The separation effect on the tracer transport due to the low-permeable inclined zone can decrease the peak concentration collected in the production point, referring to Fig. 5.10b(1). In Fig. 5.11a(1) the (red) curves of peak concentrations for low-permeable inclined zone take an abrupt turn at 155°C. This is the result of a low permeability zone forcing tracers to flow in the lower part of the reservoir, as we can see in Fig. 5.10a(2). In the I1P1 setup, the fastest streamline will be at the top and stay above 155°C (the initial well temperatures) and not deliver converted tracers with higher thresholds. Streamlines that take the opposite side of the barrier will all have reached 170°C which explains the jump in arrival

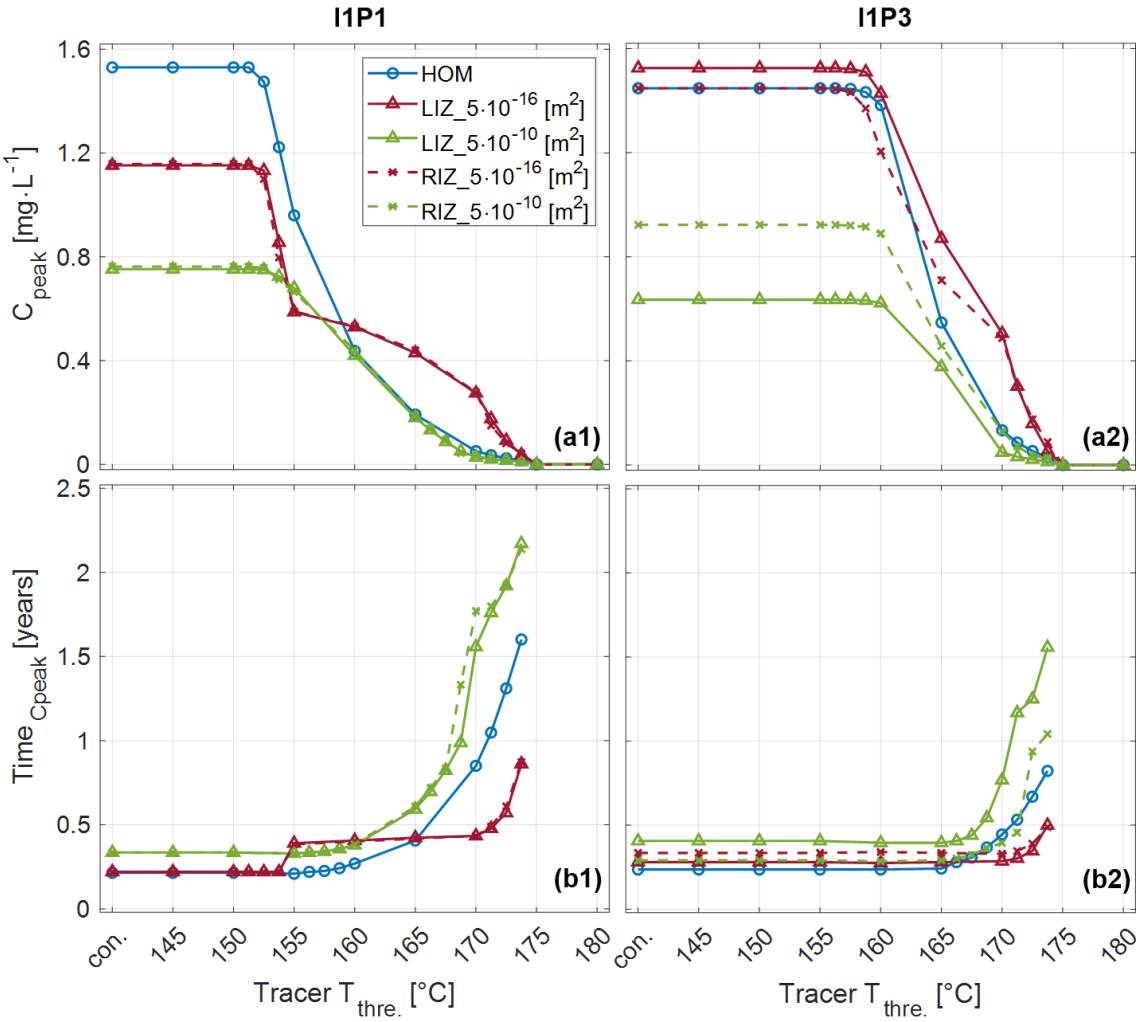

Figure 5.11. Comparison of tracer performance for peak concentration (a) and peak arrival time (b) in homogeneous (HOM) and geological heterogeneous models (LIZ or RIZ) with well configurations of (1) I1P1 and (2) I1I3. The permeability in the left- or right-inclined zone (LIZ or RIZ) is $5 \cdot 10^{-16}$ m^2 or $5 \cdot 10^{-10}$ m^2 while the reservoir permeability is $5 \cdot 10^{-11}$ m^2.

times at 150°C to a higher stable value until 170°C, where only the outermost streamlines can convert the tracers. As the threshold increases gradually less tracer is converted but following a different trend than at first since the tracer is primarily converted at the bottom of the reservoir. Note that the discontinuity in arrival time and the trend of peak concentration happen at the same temperature and are clear indicators of two separate flow line groups. While there were two separate streamlines groups also for I1P3, they arrived at similar times, while the reactive tracer mainly converted in the lower one.

Figure 11(2) gives the results when the injection-production position changes to I1P3 which is exactly the setup shown in Fig. 10. When the inclined zone is low permeable and

the orientation is similar to the injection-production direction, the tracer transport will be efficient and give rise to high peak concentration values of tracer concentration in the production point. That is why it is seen in Fig. 11a(2) that the dashed red line (right-inclined) has a lower magnitude than the solid red line (left-inclined). On the other hand, the green dashed line in Fig. 11a(2) has higher values than the green solid one since the attraction of the high permeable zone plays a more significant role in reducing the tracer concentration in the latter case (solid line, left-inclined), which has been discussed in the above for comparisons between Fig. 10c and d. Therefore, inclined injection-production position I1P3 is useful for the test to differentiate the right- or left-inclined zones. In addition, it is noticeable in Fig. 11a that the curve trends within the high tracer threshold range of 165°C~175°C are similar: top (low permeable zone), middle (homogeneous) and bottom (high permeable zone).

Regarding reservoir temperature estimation using the deviation points of the peak concentration and peak arrival time curves in Fig. 11, we find that the maximum temperature is correctly estimated to be 175°C in all cases. For a given well setup a fairly consistent minimum temperature is estimated as 152°C~153°C for I1P1 and 157°C~158°C for I1P3 although the actual minimum for all cases is 145°C. The highest temperature of the coldest streamline is determined by how deep they go, i.e. the depth of the wells, as explained earlier. The deviation threshold temperature of the arrival time curve shows different trends compared to the homogeneous case. When there is a barrier, the flow is concentrated and it can be diverted from or towards the well, but also from or towards the higher temperatures. In the example of I1P3 with a low permeability RIZ (see Fig. 5.10b(2)) the flow is diverted straight down (increasing the arrival time of the conservative tracer), exceeding 170°C and then straight towards the producer. The deviation of the arrival time (red curve in Fig. 5.11b(2)) correctly indicates that temperatures have exceeded 170°C on the main streamlines.

5.4 Conclusions

Temperature-reporting nanoparticle tracers, which quickly, fully and irreversibly convert when the environmental temperature reaches its threshold value, were studied to

characterize the temperature information of geothermal reservoirs. We developed a numerical modeling approach to illustrate their working mechanisms in a thin 3D reservoir. A mixture of tracers with different temperature thresholds was injected. First, a homogeneous and fractured geothermal reservoir was studied with nine injection-production well configurations. Furthermore, adding heterogeneities such as thermal anomalies and inclined zones were investigated. The following conclusions can be made:

- Reservoir temperature can be changed due to cold water injection and fluid intrusion from different depths. The injected temperature-reporting nanotracers travel along all streamlines but are converted on a streamline only if they reach the temperature threshold of that specific tracer. This happens if the streamline goes sufficiently deep or sufficiently close to a thermal anomaly.
- Injection-production positions and inclined high- or low-permeable zones embedded within the reservoir influence the streamlines, thus impacting the collected tracer breakthrough data. Deeper well positions steer all the streamlines through higher temperatures, while the mentioned zones can spread or deviate streamlines towards or away from the high temperatures.
- The peak concentration of a given temperature-reporting nanotracer is determined by the proportion of the swept reservoir area above its temperature threshold. The changes in tracer peak arrival time result from alterations in the flow paths of its main streamlines. A long flow path generally corresponds to a long peak arrival time of the tracer.
- A new analysis method was proposed, based on plotting the peak concentration and arrival time of each tracer against their temperature threshold.
    - At sufficiently low temperatures, all tracers are fully converted, giving the same peak concentration as the conservative tracer. The temperature where the tracers start to yield lower peak concentrations is an upper limit of the minimum reservoir temperature.
    - At sufficiently high temperatures, no tracer is converted, giving zero peak concentration for higher temperatures. The temperature threshold where the peak concentrations first become zero is identical to the maximum reservoir temperature.

    - The arrival time of the tracer peak is the same as the conservative tracer as long as it is converted on the main (fastest) flowline between the wells. The threshold temperature when the time starts to increase indicates the highest temperature on the main flowline.
- The range in temperature thresholds between the deviations on the peak concentration curve reflects only a part of the reservoir temperature range, but the highest temperature deviation corresponds to the highest reservoir temperature, while the lowest deviation temperature can be near or far away from the lowest reservoir temperature. Changing the reservoir temperature conditions (with other conditions the same), consistently changes the max temperature (actual and estimated) but may not necessarily impact the lower threshold deviation temperature. While a reduced temperature range may be expected to reduce the difference between the thresholds (a sharper peak concentration curve), a sharp curve does not directly imply a narrow reservoir temperature range.
- At a reduced temperature range (and other conditions the same), the flow paths next to the main streamline now have a temperature closer to that of the main streamline. The same streamlines have the same arrival time, but tracers with lower thresholds, corresponding to the streamline max temperature, will dominate. In total, the streamlines with the same arrival times obtain threshold temperatures closer to the main streamline, i.e. a sharper curve.
- The effects of thermal anomalies (existence and locations) and inclined zones (conductivity and orientation) in the reservoir can be more easily observed when the injection-production position is non-horizontal as the tracer data become more sensitive to the orientation and location of such features.

In practice, forward simulations are required to match the breakthrough data from the field tests. Although it provides useful insights into the effects of geological and thermal heterogeneities on the tracer breakthrough data, a precise estimation of these unknowns relies on inverse modelling which uses model sensitivities to update parameters to be more consistent with observations. Our results show clear responses to geological and thermal heterogeneities which are clearly detectable when choosing a non-horizontal injection-production location.

The conclusions of this work are not limited to fractured reservoirs but can also applied to other types of geothermal reservoirs. During the entire lifecycle of geothermal reservoir exploitation, temperature-reporting tracer tests can be conducted to detect temperature range and reservoir thermal drawdown in the reservoir as well as other geological and thermal heterogeneities. At the exploration stage, the initial in-situ reservoir temperature information can be characterized quickly by the tracer curve using high flow rates, especially if shallow injection-production positions are chosen and the tracer can sweep the entire reservoir. For the production stage, the thermal drawdown status can be periodically quantified by comparison of the present temperatures to the initial ones. Potential challenges or limitations that one might be faced with when implementing our proposed approach in a realistic fractured geothermal reservoir scenario include injection-production configurations for inferring the temperature range, and uncertainties in the properties of liquid solution.

In addition to the investigations discussed in this work, the robustness of our proposed analysis approach has also been verified by simulations that consider the variations of communication between the inner reservoir and outer reservoir, injection and production rate and conversion degree of nanotracers. Nevertheless, the following aspects still deserve further studies:

- The impact of complex geometries which may include additional fractures and randomly distributed geological heterogeneities on the temperature-reporting nanotracer’s behaviour in the reservoir and analysis curves.
- Use field test data to validate simulation results to ensure the practical applicability of this research work and its findings.
- Consider the impact of nanotracer properties and mechanisms such as gravity segregation, deposition and aggregation on the results predicted by the proposed numerical model.
- Incorporate the impact of potential fluid source (supply) and/or sink (leakage) from neighbouring geological strata.

6 Investigating the impact of wellbore lateral heat transfer on the performance of high-temperature aquifer thermal energy storage system by the coupling of wellbore and reservoir simulators

This part is reproduced from the manuscript that has been submitted to the peer-reviewed journal ***Geoenergy Science and Engineering***.

Yan, G., *Andersen, P. Ø., Qiao, Y., Hatzignatiou, D. G., Feng, B., & Kohl, T. (2024). Investigating the impact of wellbore lateral heat transfer on the performance of high-temperature aquifer thermal energy storage system by the coupling of wellbore and reservoir simulators.* ***Geoenergy Science and Engineering****. (under review)*

Abstract

This study investigates the often-overlooked impact of wellbore lateral heat transfer on high-temperature aquifer thermal energy storage (HT-ATES) systems, focusing on the Swiss Bern project. We coupled our in-house wellbore simulator (MOSKIO) with the reservoir simulator (PorousFlow) under the MOOSE framework to analyze wellbore heat loss. Utilizing both numerical and analytical approaches, we reveal how wellbore heat loss affects HT-ATES performance compared to previous studies that ignored it. Our sensitivity analysis examines various wellbore configurations and operational parameters, evaluating performance indicators including extracted energy, wellbore lateral heat loss fraction, and reservoir heat loss fraction. Key findings include a more than 10% difference

between the analytical and numerical calculations of wellbore lateral heat loss, with smaller wellbore diameters (e.g., 6.75 inches) improving energy recovery efficiency through larger fluid extraction volumes. Low thermal conductivity wellbore casing materials (e.g., 0.045 $W \cdot m^{-1} \cdot K^{-1}$) reduce wellbore lateral heat loss by 51.4%. Although energy recovery efficiency declines with more supporting wells during the initial storage cycle, three supporting wells yield the best performance in later cycles due to larger extracted fluid volumes. High flow rates (e.g., 25 $L \cdot s^{-1}$) enhance energy recovery efficiency by decreasing heat losses through faster fluid movement, which reduces residence time and thermal diffusion. While high fluid injection temperatures (e.g., 210°C) increase heat losses, overall heat loss fractions decrease due to significant injected energy. This study highlights the critical role of wellbore lateral heat loss in evaluating the performance of the HT-ATES system, providing insights on how to design and optimize these systems.

6.1 Introduction

The intensive use of fossil energy sources over the past few decades has significantly increased atmospheric carbon dioxide concentrations, contributing to various climate change challenges (EIA, 2009; Ürge-Vorsatz et al., 2015; EU, 2010). To achieve the Paris climate agreement (UN, 2015), many countries are actively adopting strategies that include sustainable energy sources based on their strengths and needs (Jäger-Waldau, 2007; Kim et al., 2010; IEA, 2019; Usman et al., 2020; Muhammed and Tekbiyik-Ersoy, 2020). In these strategies, the effective and rational development, and use of geothermal energy sources are key concerns (Barbier 2002; Sharmin et al., 2023). As energy supply does not usually align with demand on a seasonal basis, thermal energy storage methods, such as Aquifer Thermal Energy Storage (ATES), Borehole Thermal Energy Storage (BTES) and Fractured Thermal Energy Storage (FTES) that utilize the subsurface pore space and its geothermal energy are gaining attention (Dincer, 2002; Henry et al., 2020; van der Roest et al., 2021). In particular, as aquifers are large-scale energy storage formations, ATES have a significant capacity to provide large amounts of heating and cooling to reduce total energy imbalance. Specifically, ATES operates on a seasonal basis (Kallesøe et al., 2020; Huang et al., 2021). During the heat storage phase, excess heat

generated from coal- or gas-fired power plants, solar power plants and cogeneration plants is transferred to cold fluid through heat exchangers. The resulting warm fluid transports the heat to the aquifer where it is stored. During the heat extraction phase, the ATES operates oppositely by reversing the direction of fluid flow between the injection and production wells. The stored heat is then recovered from the warm fluid through a heat exchanger and it is used for heating. At the same time, the resulting cold fluid is reinjected into the aquifer (Dickinson et al., 2009).

System performance is the most significant concern for an ATES system (Tsang, 1978; Lee and Lee, 2013; Bloemendal and Hartog 2018). Previous research on the performance in ATES systems has been analyzing standalone reservoir models under various conditions, including the wellbore design and operation parameters, etc. (Doughty et al., 1982; Kangas et al., 1994; Paksoy et al., 2004; Schüppler et al., 2019; Stemmle et al., 2021; Duijff et al., 2023). Among them, Doughty et al. (1982) first introduced a dimensionless factor — energy recovery efficiency — to quantify the thermal performance of a 2D ATES reservoir, defined as the ratio of extracted energy to the injected energy. Using numerical simulation, Sheldon et al. (2021) found that the aquifer thickness and permeability, injection fluid temperature as well as thermal dispersion length dominate the energy recovery efficiency in a single-well 2D ATES system. Sommer et al. (2013) demonstrated that short preferential pathways, short-circuiting and well interference in a heterogeneous 3D doublet ATES system result in the non-full utilization of the aquifer storage capacity and can cause 6%~15% lower energy recovery efficiency compared to the homogeneous case, which highlighted the importance of aquifer heterogeneity in the design and optimization of ATES system. Beernink et al. (2024) examined the impact of heat conduction, heat dispersion and buoyancy-driven convection on the energy loss of the stored heat to the aquifer in a 2D ATES system. Their study considered a broad spectrum of realistic operational storage conditions, including injection fluid temperature and flow rate as well as various hydrogeological factors such as aquifer thickness, hydraulic conductivity and anisotropy. Vidal et al. (2022) proposed a dimensional analysis and 3D finite element reservoir numerical model of the ground surface uplift, heat transport and energy efficiency for the Swiss Bern project (high-temperature ATES (HT-ATES)) with wellbore pattern and investigated the energy

recovery efficiency and system safety risk. To avoid the negative effect of buoyancy-driven convection on the energy recovery efficiency of the ATES system, van Lopik et al. (2022) conducted a numerical study to examine how multiple partially penetrated wells (i.e., only wellbore screen section, not overall wellbore) can improve the energy recovery efficiency, under different conditions of wellbore operation and reservoir conditions. Brown and Gioia (2024) built a simplified 3D ATES reservoir model with only one production well and reservoir to investigate the effects of related factors on the wellbore lateral heat transfer to/from the formation and energy recovery efficiency of the ATES system. A small initial geothermal gradient, low reservoir temperature and high thermal conductivity significantly enhance heat transfer from the wellbore to the surrounding formation. However, the production well was entirely modeled as porous media with a fixed flow rate within the reservoir. The injection wellbore and cooling effect in the reservoir caused by cold fluid re-injection were ignored.

Overall, these works mainly focused on the performance of the ATES system without a detailed study of the 'realistic' wellbore dynamics. The wellbore sections were either simplified as highly permeable porous media or line/point source/sink in the reservoir model. While their approaches greatly simplify the numerical model and speed up the simulation process, the dynamic fluid flow and heat transfer processes within the wellbore part and more importantly the heat transfer between the wellbore and formation are either overlooked or not sufficiently emphasized to quantitatively evaluate the impact of wellbore lateral heat transfer on system performance. Wellbore lateral heat transfer occurs when the fluid temperature in the wellbore differs from that of the surrounding geological formations. The frequent cycling and temperature changes inherent in ATES systems can amplify wellbore lateral heat transfer compared to more stable geothermal systems with more constant thermal conditions. This can lead to significant energy loss during storage and extraction, impacting system performance. Therefore, it is crucial to quantitatively assess wellbore lateral heat transfer to accurately evaluate and optimize ATES systems, requiring a full coupling model between the wellbore and reservoir.

With analytical, semi-analytical or numerical approaches, many researchers have devoted efforts to investigate the dynamic fluid flow and heat transfer (including the wellbore lateral heat transfer) based on the complete wellbore-reservoir system for the general

geothermal development, CO_2 storage, non-typical (i.e., using air or CO_2 as working fluid) energy storage in aquifer (Ramey 1962; Satter, 1965; Pan and Oldenburg, 2014). Ramey (1962) first presented an analytical approach to quantify the temperature distribution around a 1D injection well by assuming steady fluid flow in the wellbore and steady heat transfer in the 2D surrounding formation. Built on Ramey's work, the wellbore lateral heat transfer was further developed (Satter, 1965; Willhite, 1967; Horne and Shinohara, 1979; Wu and Pruess, 1990; Phuoc et al., 2019) for different injection and production conditions. Specifically, to release the assumptions used in Ramey's solution, Wu and Pruess (1990) provided an analytical approach in a 1D wellbore model for heat exchange between the wellbore and the uniform/layered 2D formation, using the dimensionless time and depth on transient lateral heat transfer coefficient. Hasan and Kabir (1991) developed a 1D wellbore lateral heat transfer model at the formation-wellbore interface using Fourier's law and proposed a new time function to predict the 'transient' temperature distribution in the system. Cheng et al. (2011) presented a new analytical model for transient lateral heat conduction in the 1D steam injection wells, incorporating the wellbore's heat capacity to improve the temperature and heat transfer predictions in the wellbore and surrounding formation. As for the semi-analytical approach, Zhang et al. (2011) proposed a time-convolution approach where only the wellbore (i.e., not formation) is fully discretized and semi-analytical solutions of wellbore lateral heat transfer by neglecting vertical conductive heat flow within the formation and thermal resistance between the cased wellbore and the formation. This approach has been implemented and validated in a highly transient and strongly non-isothermal multi-phase wellbore-reservoir system (Pan and Oldenburg, 2014; Ezekiel et al., 2020). Regarding the numerical study, Xiong et al. (2016) developed a 1D thermal wellbore simulator using a finite difference approach and calculated the heat transfer and temperature variation in the steam-assisted gravity drainage system. They employed the overall heat transfer coefficient from Willhite (1967) and temperature at the cement-formation interface from a 2D formation heat transfer equation including Ramey's (1962) approximation approach. Livescu et al. (2008; 2010) developed a series of fully coupled multiphase wellbore-reservoir simulators using the finite volume method. They used the constant overall heat transfer coefficients and transient temperature profiles of the wellbore and reservoir to calculate the wellbore lateral heat transfer based on the formula proposed by Ramey (1962) but the

heat conduction term in the open-hole section was not considered between the reservoir and wellbore. Pan and Oldenburg (2014) developed an integrated simulator T2Well using the finite-difference scheme to solve non-isothermal, multiphase and multi-component fluid flow and heat transfer in the fully coupled 1D wellbore and 3D reservoir system. The T2Well has been widely used to calculate the energy recovery efficiency for compressed air or CO_2 energy storage in aquifers (Li et al., 2023a; Pan and Oldenburg, 2013; Li et al., 2023b; Li et al., 2024) and joint compressed air energy storage and ATES (Guo et al., 2017). To address the limitations of analytical and semi-analytical approaches due to their assumptions, You et al. (2016) developed a fully implicit model that couples a 1D wellbore with a 3D surrounding formation using the finite difference method. This model incorporates radial Fourier heat conduction flux to calculate wellbore lateral heat transfer. The above reviews show that the wellbore lateral heat transfer has been considered in several specific topics including general geothermal development, CO_2 storage and compressed air or CO_2 energy storage in aquifers. However, these approaches have not been applied to typical ATES (i.e., using water as a working fluid for thermal energy storage) and also do not reveal the impacts of related parameters on the wellbore lateral heat transfer.

In this study, our focus is on a HT-ATES system in a shallow reservoir (the Swiss Bern project (Vidal et al., 2022)). The motivation of this work is to reveal the impact of wellbore lateral heat transfer on the HT-ATES performance. We have fully coupled the wellbore fluid flow and heat transfer processes, including lateral heat transfer, simulated by our in-house developed wellbore simulator MOSKITO (Korzani et al., 2019) together with an existing reservoir simulator PorousFlow (Wilkins et al., 2021) under the MOOSE framework (Permann et al., 2020). The coupled model is then used to compute the wellbore lateral heat transfer along the full well trajectory to the surface for quantitative evaluation of the impact of wellbore lateral heat transfer on the HT-ATES performance, specifically for the Bern project. This is done through varying different key wellbore configurations (wellbore diameter, casing thermal conductivity and supporting well number) and operational parameters (injection flow rate and injection temperature at the main well). Such investigations can be helpful to design and optimize the HT-ATES system, regarding the choices of the above parameters. In addition, to achieve a complete

assessment of HT-ATES systems, it is crucial to consider a range of performance indicators. While energy recovery efficiency can tell how effectively the system retrieves the stored energy, it is not enough to reflect either the system's operational capacity or energy loss due to the wellbore lateral heat transfer to the formation (*wellbore lateral heat loss*) and heating reservoir (*reservoir heat loss*). Therefore, it can be worth considering the extracted energy, wellbore lateral heat loss (fraction) and reservoir heat loss (fraction) as additional performance indicators together with the energy recovery efficiency which was generally treated as the only indicator to evaluate the HT-ATES system performance.

The study is organized as follows. Firstly, we present the methodology for fully coupling our in-house developed wellbore simulator and the reservoir simulator under the MOOSE framework. Secondly, the developed coupled simulation tool is used to model a specific HT-ATES case with different scenarios including varying the wellbore configurations and operational parameters. The obtained results are discussed for the impact of the wellbore lateral heat transfer on the HT-ATES performance. Finally, key findings of the design and operation of the HT-ATES system and recommendations for future research are summarized in the conclusion part.

6.2 Material and methods

6.2.1 Equations and coupling methods in wellbore-reservoir system

The governing equations (Pan and Oldenburg, 2014; Korzani et al., 2019; Wilkins et al., 2021) for fluid flow and heat transfer-transport in the wellbore and reservoir are presented in Table 6.1. Note that the conservation law for both mass and energy holds the same format. The differences in equations between the wellbore and the reservoir lie in the definitions of energy flux terms and fluid velocity. For the momentum equation, fluid flow in the reservoir takes Darcy's law and Navier-Stokes type of equation for the wellbore flow where the inertial forces are considered. Furthermore, kinetic energy and gravitational potential energy are included in the wellbore heat equation. In contrast, the heat equation for the reservoir does not account for these terms due to the creeping flow in the porous medium.

Table 6.1. The mass, energy and momentum equations solved in the coupled wellbore-reservoir simulator.

Equation and term	1D Wellbore	3D Reservoir
Mass (MS) conservation Energy (EG) conservation	$\frac{\partial M_i}{\partial t} + \nabla \cdot F_i - q_i{}^{cp} = 0$ (i = *MS* or *EG*)	
Mass density: M_{MS}	$\rho_l^w A$	$\phi\rho_l^r$
Mass flux: F_{MS}	$\rho_l^w A u_l^w$	$\rho_l^r \boldsymbol{u}_l^r$
Energy density: M_{EG}	$\rho_l^w A \left[c_{p,l}^w T^w + \frac{(u_l^w)^2}{2}\right]$	$\left[\phi c_{p,l}^r \rho_l^r + (1-\phi) c_{p,s}^r \rho_s^r\right] T^r$
Energy flux: F_{EG}	$\rho_l^w A u_l^w c_{p,l}^w T^w - \lambda_l \nabla(\mathrm{A} T^w) + \rho_l^w A u_l^w \left[\frac{p_l^w}{\rho_l^w} + \frac{(u_l^w)^2}{2} + gz\cos\theta\right]$	$\rho_l^r c_{p,l}^r \boldsymbol{u}_l^r T^r - [\phi\lambda_l^r + (1-\phi)\lambda_s^r]\nabla T^r$
Momentum	$\nabla(p_l^w \mathrm{A}) = \rho_l^w A g\cos\theta \pm \frac{f\rho_l^w A (u_l^w)^2}{2d} \pm \left\{\frac{\partial}{\partial t}(\rho_l^w A u_l^w) + \nabla[\rho_l^w A (u_l^w)^2]\right\}$	$\boldsymbol{u}_l^r = \frac{k}{\mu_l}(-\nabla p_l^r + \rho_l^r g)$

*The indexes *cp, EG, i, l, MS, r, s and w* represent coupling, energy, equation type, liquid, mass, reservoir, solid and wellbore, respectively.

Regarding the mass and energy coupling between the reservoir and wellbore, two regions are considered: the open-hole and the non-open-hole sections. In the open-hole section, there is mass transfer and energy transfer due to fluid flow (convection) and heat conduction driven by the local temperature gradient. A Peaceman-type equation (Peaceman, 1983) is employed for calculating the source terms in the mass equations for the open-hole section, which is a function of the pressure difference between the reservoir and the wellbore (see Table 6.2). The well index (*WI*) in the Peaceman-type formula (Chen and Zhang, 2009) accounts for the impact of the reservoir grid size, reservoir permeability and wellbore radius, etc. It reflects the well's ability to inject or produce fluid.

$$WI = 2\pi\sqrt{k_{xx}k_{yy}}\Delta z / \ln(r_e/r_{bh}) \tag{6.1}$$

where k_{xx}, k_{yy}, Δz, r_e and r_{bh} are separately reservoir permeability [m^2] in the length direction, reservoir permeability [m^2] in width direction, grid block size [m] in depth direction, wellbore radius [m] and effective wellbore radius [m] which can be calculated by (Chen and Zhang, 2009):

$$r_e = 0.28\frac{\sqrt{\sqrt{k_{xx}/k_{yy}}(\Delta x)^2+\sqrt{k_{yy}/k_{xx}}(\Delta y)^2}}{(k_{xx}/k_{yy})^{1/4}+(k_{yy}/k_{xx})^{1/4}} \tag{6.2}$$

where Δx is the length [m] and Δy is the width [m] of a grid block.

Table 6.2. Comparison of coupling terms at the wellbore-reservoir interface. The heat exchange calculations at the non-open-hole section interface are compared using the numerical and analytical approaches, and the approach without considering wellbore lateral heat transfer.

Region	Coupling term	Numerical approach	Analytical approach	An approach without considering wellbore lateral heat transfer
Non-open-hole	Energy: q_{EG}^{cp}	$2\pi r_{to}U_{to}(T^w - T_{ne}^{fo})$ (Willhite, 1967)	$\frac{2\pi\lambda^{fo}(T^w - T_{fa}^{fo})}{f(t)}$ (Ramey, 1962)	0
Open-hole	Mass: q_{MS}^{cp}	$\rho_l^j \frac{WI}{\mu_l^j}(p_l^w - p_l^r)$ (Peaceman, 1983)		
	Energy: q_{EG}^{cp}	$\rho_l^j \frac{WI}{\mu_l^j}(p_l^w - p_l^r)h_l^j + B\lambda^r\nabla T$		

*1. The indexes *cf*, *cp*, *EG*, *fo*, *fa*, *j*, *l*, *MS*, *ne*, *r*, *to* and *w* refer to cement/formation interface, coupling, energy, formation, far-field, well type, liquid, mass, nearest, reservoir, overall and wellbore, respectively; 2. well type $j = \begin{cases} w, & injection\ well \\ r, & production\ well \end{cases}$; 3. well sign $B = \begin{cases} 1, & injection\ well \\ -1, & production\ well \end{cases}$; 4. $f(t)$ is dimensionless time function. When time is greater than one week, it can be calculated by $f(t) = ln\frac{2\sqrt{\frac{\lambda^{fo}}{\rho^f c_p^{fo}}t}}{r_{cf}} - 0.29$.

As for the fluid flow and heat transfer in the radial direction for the non-open-hole section, mass transfer is not considered and only heat exchange exists between the wellbore and surrounding formation. For the non-open-hole section, three calculation approaches for the heat exchange are shown with numerical, analytical and without considering wellbore lateral heat transfer, see Table 6.2. In the numerical approach, the heat exchange is characterized by the temperature difference between the wellbore (i.e., T^w where subscript *w* means wellbore) and the nearest formation (i.e., T_{ne}^{fo} where superscript *f* and subscript *ne* are formations and nearest node, separately) and an overall heat transfer coefficient (U_{to}). Both formation temperature and temperature at the interface of cement and formation are dynamic. As shown in Eq. (6.3), the overall heat transfer coefficient is a combination of several thermal resistances including those of the tubing, annulus fluid,

casing and cement, which can be referred to in more detail in Willhite (1967) and Xiong et al. (2016).

$$U_{to} = \frac{1}{\frac{r_{to}}{r_{ti}\beta_{ff}} + \frac{r_{to}\ln(r_{to}/r_{ti})}{\lambda_t} + \frac{r_{to}\ln(r_{ins}/r_{to})}{\lambda_{ins}} + \frac{r_{to}}{r_{ins}(\beta_{con}+\beta_{rad})} + \frac{r_{to}\ln(r_{co}/r_{ci})}{\lambda_{cas}} + \frac{r_{to}\ln(r_{cf}/r_{co})}{\lambda_{cem}}} \quad (6.3)$$

where r_{ti}, r_{to}, r_{ins}, r_{ci}, r_{co} and r_{cf} represent the radii of inside tubing, outside tubing, tubing insulation, inside casing, outside casing and cement/formation interface, respectively. λ_{t}, λ_{ins}, λ_{cas} and λ_{cem} are the thermal conductivities of the tubing wall, tubing insulation, casing wall and cement. β_{fft}, β_{con} and β_{rad} are the convective heat transfer coefficient between the fluid film in tubing and the tubing wall, and the convective and radial heat transfer coefficients of fluid inside annulus. Assuming that the far-field formation temperature (T_{fa}^{f} in Table 6.2) is constant, the analytical approach only consider the heat transfer between the wellbore and formation but ignores the heat transfer processes between the tubing-casing-cement-formation regions. The third approach (Table 6.2) for calculating the heat exchange in the non-open-hole section neglects the wellbore lateral heat transfer.

6.2.2 Numerical model settings

Inspired by the GeoSwiss Bern Project (Vidal et al., 2022), a five-spot system containing a 3D multi-layer (i.e., caprock, aquifer and basement) HT-ATES system for reservoir and five 1D wellbores, is employed in this study (see Fig. 6.1a). A 40 m thick aquifer, sandwiched between low-permeable caprock and basement layers, serves as the target zone for thermal energy storage. The whole model, including formation and wellbore system, spans depths from 0 m to 440 m and formation extends horizontally from -250 m to 250 m. The aquifer is located at a depth of 400 m to 440 m. An unstructured mesh consisting of hexahedral elements was created using GMSH software (Geuzaine & Remacle, 2009). The element size of reservoir grids varies from 1 m near the wellbores to 25 m at boundaries (Fig. 6.2a and b). The wellbore system comprises one centrally located main well (red color in Fig. 6.1a) and four supporting wells (green color in Fig. 6.1a), each symmetrically positioned around the main well at an equal distance of 40 m. For heat storage and extraction in the aquifer, the open-hole section of the wellbore

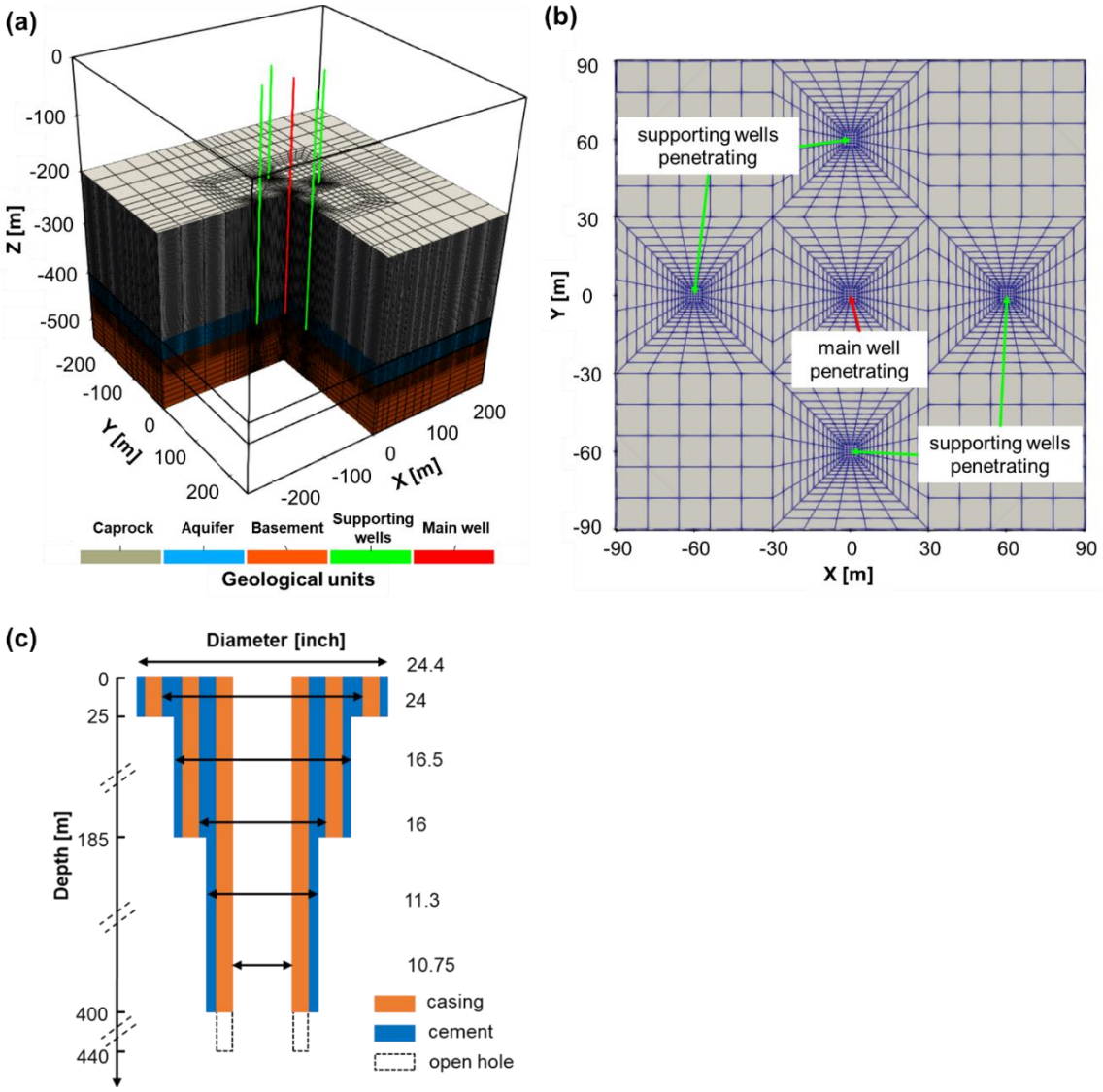

Figure 6.1. Schematic representation of (a) a five-spot system for HT-ATES; (b) the top view of the wellbore placement; (c) the geometrical configuration of the wellbore. Note that the main well and supporting well have the same configuration.

system (located at a depth of 400 m to 440 m) allows fluid flow and heat transfer (including both convection and conduction) with the aquifer. In contrast, the non-open-hole section exchanges heat solely through conduction with the surrounding formations. The geometrical configuration of a typical borehole completion within this wellbore system is illustrated in Fig. 6.1c. The wellbore above the open-hole section is cased to ensure stability, with diameters ranging from 10.75 inches to 24.4 inches. 0.05 m is used as the mesh size of the wellbore to capture the important dynamics in the flow process. Referring to the realistic and representative data in the GeoSwiss Bern Project, the

physical properties of solids (i.e., rock, wellbore cement layer and casing) and fluid are summarized in Tables 6.3 and 6.4, respectively.

Table 6.3. Rock properties of the reservoir and wellbore systems.

Properties	Symbols	Units	Reservoir system			Wellbore system	
			Caprock	Aquifer	Basement	Cement	Casing
Porosity	ϕ	-	0.01	0.25	0.01	-	-
Permeability	k	m^2	10^{-16}	10^{-13}	10^{-16}	-	-
Density	ρ^s	$kg \cdot m^{-3}$	2600	2600	2600	-	-
Specific heat capacity	c_p^s	$J \cdot kg^{-1} \cdot K^{-1}$	850	850	850	-	-
Heat conductivity	λ^s	$W \cdot m^{-1} \cdot K^{-1}$	2	2	2	1.1	45
Roughness	f	m	-	-	-	-	10^{-4}

*The index *s* is solid.

Table 6.4. Fluid properties in the reservoir and wellbore systems (L. Smith & Chapman, 1983).

Properties	Symbols	Units	Value
Bulk modulus	K_l	Pa	$2 \cdot 10^{10}$
Density	ρ_l	$kg \cdot m^{-3}$	$\rho_l = 1000 \cdot e^{\frac{p_l}{K_l}}$
Viscosity	μ_l	Pa·s	$\mu_l = 2.4 \cdot 10^{\left(\frac{248.37}{T_l - 140} - 5\right)}$
Specific heat capacity	$C_{p,l}$	$J \cdot kg^{-1} \cdot K^{-1}$	4000
Heat conductivity	λ_l	$W \cdot m^{-1} \cdot K^{-1}$	0.6

*The index *l* refers to liquid.

For the initial temperature condition, the ground surface temperature is assumed to be 20°C, and the subsurface temperature follows the general geothermal gradient $0.03°C \cdot m^{-1}$. The initial pressure distribution takes the hydrostatic gradient $9.81 \cdot 10^3$ $Pa \cdot m^{-1}$. Regarding the reservoir boundary conditions, a constrained temperature distribution (same as initial) and no fluid flow boundaries are applied at the four lateral sides (including the front, back, left and right sides), while the top (i.e., ground surface) and the bottom of the model are set with closed boundaries for both heat energy and fluid flow. One complete heat storage and extraction cycle takes one year. During the heat storage phase (nine months), 90°C hot fluid is pumped into the reservoir with an injection rate of 25 $L \cdot s^{-1}$ through the main well while four supporting wells produce fluid with the constrained wellhead pressure of 1 bar. In the following three months, the injection and production schemes are reversed for the heat extraction phase. During this period, 50°C liquid (water) is injected with 6.25 $L \cdot s^{-1}$ through each supporting well and fluid can be freely produced from the main well (wellhead pressure 1 bar). Note that there is a considerable compression effect on the fluid density due to pressure variation in the

system, such as pressure build-up between the main wellbore and supporting wellbores. We perform five cycles in this study, taking a total time of five years. The operational time for injecting and producing hot fluid can be influenced by factors such as local climate conditions, heating demand, etc. (Sheldon et al., 2021; Beernink et al., 2024). The nine months for heat storage and three months for heat extraction are chosen just for demonstration purposes.

6.2.3 Performance indicators of the HT-ATES system

The performance of the HT-ATES system is evaluated based on four annual performance indicators: energy recovery efficiency, extracted energy, wellbore lateral heat transfer fraction and reservoir heat loss fraction. Furthermore, wellbore lateral heat transfer is defined in two ways: (1) wellbore lateral heat loss, which occurs when heat transfers from the wellbore to the surrounding formation; (2) wellbore lateral heat gain, which occurs when heat transfers from the formation to the wellbore. Based on preliminary research, the wellbore lateral heat loss to the formation is always higher than the lateral heat gain from the formation. Therefore, we just use the net wellbore (lateral) heat loss to represent the annual lateral heat transfer of the wellbore, for simplicity. The main and supporting wells can be marked by their functions depending on injection or extraction. The definition of relevant parameters are summarized as follows.

The energy recovery efficiency (η) (Doughty et al., 1982) equals to:

$$\eta = \frac{E_{ext}}{E_{inj}} \tag{6.4}$$

where E_{ext} and E_{inj} are the extracted energy and the injected energy, separately.

The extracted energy (E_{ext}) can be calculated by:

$$E_{ext} = \int_0^t c_l \, |Q_{ext}| (\rho_{ext} T_{ext} - \rho_0 T_0) dt \tag{6.5}$$

where t, c_l, ρ_{ext}, Q_{ext}, T_{ext}, ρ_0 and T_0 are time [s], specific heat capacity [$J \cdot kg^{-1} \cdot K^{-1}$] of liquid, liquid density [$kg \cdot m^{-3}$], total extraction flow rate [$m^3 \cdot s^{-1}$] and temperature [K] at extraction wellhead, initial liquid density [$kg \cdot m^{-3}$] and initial liquid temperature [K] in reservoir, separately.

Meanwhile, the injected energy (E_{inj}) is:

$$E_{inj} = \int_0^t c_l \left|Q_{inj}\right|(\rho_{inj}T_{inj} - \rho_0 T_0)dt \tag{6.6}$$

where ρ_{inj}, Q_{inj} and T_{inj} are injection liquid density [kg·m^{-3}], total injection flow rate [m^3·s^{-1}] and injection liquid temperature [K] at wellhead, respectively.

Furthermore, according to the energy consumption types of the injected energy (E_{inj}), it can be divided into the extracted energy (E_{ext}), wellbore lateral heat loss (E_{los_w}) and reservoir heat loss (E_{los_r}):

$$E_{inj} = E_{ext} + E_{los\_w} + E_{los\_r} \tag{6.7}$$

The four terms in Eq. (6.7) are interrelated, meaning that one of these terms can be obtained if the other three are known. According to the heat transfer flux between the wellbore and formation in the non-open-hole section (as shown in Table 6.2), the wellbore lateral heat loss ($E_{los\_w}^{num}$) from numerical approach can be obtained from:

$$E_{los\_w}^{num} = \int_0^t 2\pi r_{to} U_{to}(T^w - T_{ne}^f)\, dt \tag{6.8}$$

where superscript *f* and subscript *ne* are formation and nearest node of the corresponding reservoir grid, separately.

Similarly, the wellbore lateral heat loss ($E_{los\_w}^{ana}$) from the analytical approach is:

$$E_{los\_w}^{ana} = \int_0^t 2\pi\lambda^f \left(T^w - T_{fa}^f\right) dt \tag{6.9}$$

where subscript *fa* represents far-field.

The wellbore lateral heat loss fraction α_{los_w} can be obtained from:

$$\alpha_{los\_w} = \frac{E_{los\_w}}{E_{inj}} \tag{6.10}$$

where E_{los_w} is $E_{los\_w}^{num}$ in the numerical approach or $E_{los\_w}^{ana}$ in the analytical approach.

Thus, the reservoir heat loss fraction α_{los_r} equals to:

$$\alpha_{los\_r} = 1 - \eta - \alpha_{los\_w} \tag{6.11}$$

6.3 Results and discussions

In this part, we first present the behavior of a reference case for the HT-ATES, including the temperature distributions and performance evaluation of the HT-ATES system. Following this, to reveal the impact of wellbore lateral heat loss on HT-ATES performance, we perform a parameter sensitivity analysis of key factors, including wellbore configurations (wellbore diameter, casing thermal conductivity and supporting well number) and operational parameters (injection flow rate and injection temperature at the main well).

6.3.1 Reference case

1) Temperature distributions

Temperature distributions within the aquifer, its surrounding formations and the formations around the wellbore are depicted in Fig. 6.2a at four key times: at the end of the first storage (0.75 years, subplot a1), at the end of the first extraction (1 year, marking the completion of the first full cycle, subplot a2), at the end of the fifth storage (4.75 years, subplot a3) and at the end of the fifth extraction (5 years, marking the completion of the fifth full cycle, subplot a4). Each storage period involves injecting 90°C hot fluid, leading to continuous heating of the aquifer and its overlying and underlying formations (Fig. 6.2a(1) and (3)). During the extraction phase, hot fluid is withdrawn from the main well at the center of the model, resulting in an I-shaped temperature distribution in the aquifer and its adjacent overlying and underlying formations. This pattern becomes more pronounced with an increasing number of complete heat storage and extraction cycles (Fig. 6.2a(2) and (4)). The observed phenomenon occurs because the overlying and underlying formations are heated by conduction from the hot fluid injected into the aquifer. While the hot fluid is produced from the main well during the extraction time, the temperatures in the high-temperature zones of both the aquifer and its surrounding formations decrease. However, the overlying and underlying formations primarily lose heat through conduction, which is slower compared to the convective heat transfer in the

aquifer. Consequently, there is a delayed temperature response in the overlying and underlying formations compared to the aquifer.

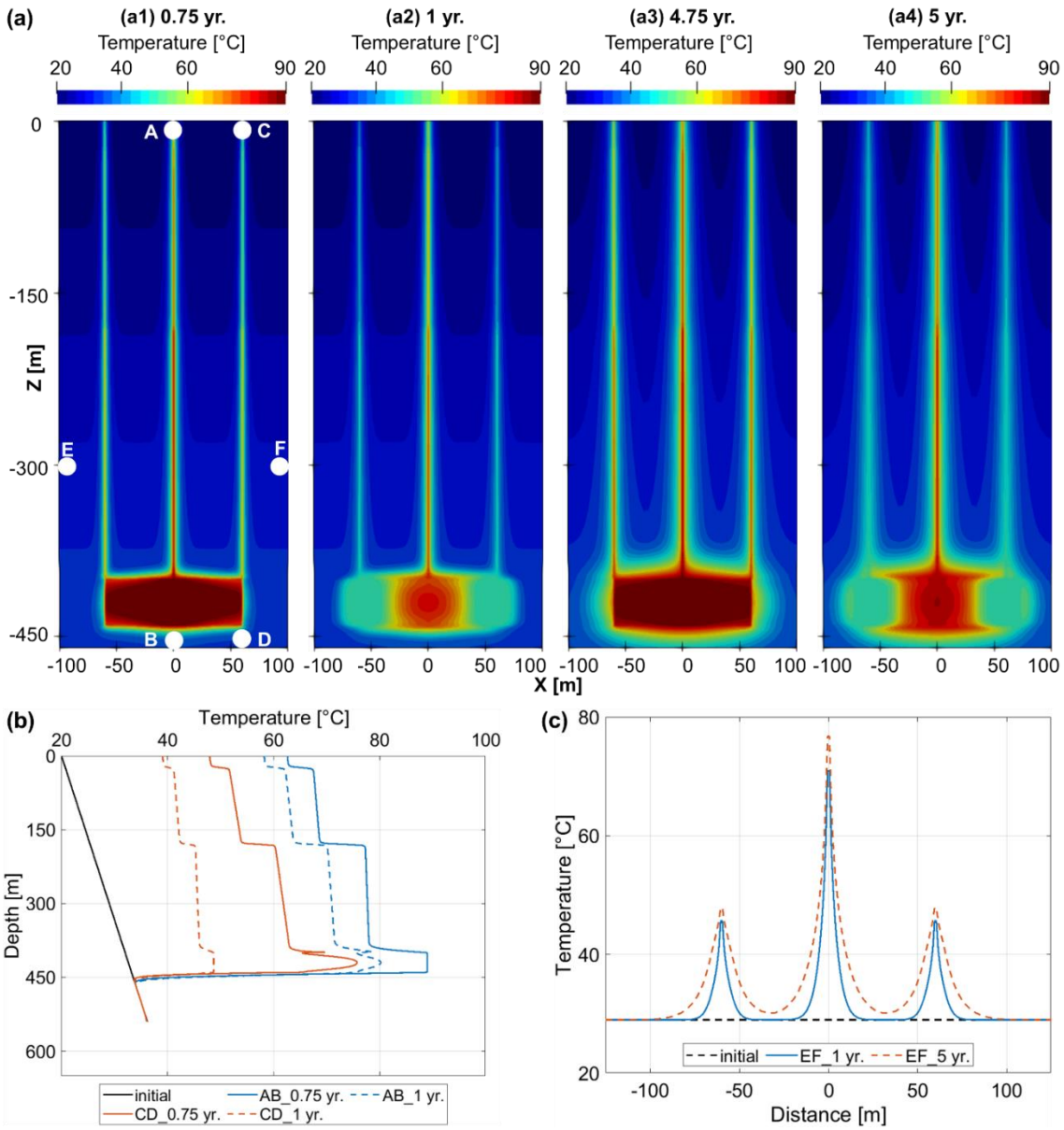

Figure 6.2. Numerical results of the reference case, including the temperature distributions in the aquifers and formations at (a1) 0.75 years; (a2) 1 year; (a3) 4.75 years; (a4) 5 years; (b) vertical temperature profile along lines A-B and C-D across the entire model; and (c) horizontal temperature profile along line E-F at depth of 300 m across the entire model.

Around the non-open-hole section of the wellbores, wellbore lateral heat loss to the surrounding formations causes their temperatures to rise, with the increase becoming more pronounced with depth (Fig. 6.2b). This intensified temperature rise with depth is due to the weak insulation of the wellbore as the number of insulation layers decreases.

Specifically, there are three insulation layers from 0 to 25 m depth, two insulation layers from 25 m to 185 m depth and one insulation layer from 185 m to 400 m depth (Fig. 6.1c) in the non-open-hole section of the wellbores. By comparison, in the open-hole sections (i.e., from 400 m to 440 m depth), the aquifer experiences a greater temperature increase compared to the formations around the non-open-hole sections of the wellbores. This occurs because the convective heat transfers due to fluid flow in the open-hole section, combined with heat conduction, results in more effective heat transfer compared to the pure heat conduction occurring around the non-open-hole sections of the wellbores. Additionally, the horizontal extent of lateral heat propagation (Fig. 6.2c) around the non-open-hole sections of the wellbores expands due to the continuous heating from the wellbore to the surrounding formations. This effect becomes more pronounced as the number of complete heat storage and extraction cycles accumulates over time (Eq. (6.8)).

2) Performance indicators

The fluid temperatures at the wellheads of the main and supporting wells are shown in Fig. 6.3a and b. The temperatures calculated using the analytical approach and the approach that ignores wellbore are higher than those obtained from the numerical approach. For instance, at 0.75 years, the temperature at the supporting wellhead (T_{sw}) is 0.8°C higher using the analytical approach and 4.2°C higher using the approach without considering wellbore lateral heat transfer compared to the temperature obtained using the numerical approach (68.7°C see Fig. 6.3b). These discrepancies separately arise from the steady-state heat transfer between the wellbore and formation in the analytical approach and the neglect of heat exchange between the wellbores and their surrounding formations in the third approach.

To assess the HT-ATES performance of the reference case, we use energy recovery efficiency (Fig. 6.3c), wellbore lateral heat loss fraction (Fig. 6.3d) and reservoir heat loss fraction (Fig. 6.3d) as performance indicators. Since the amount of injected energy remains constant and the extracted energy amount is directly proportional to energy recovery efficiency and injected energy, variations in extracted energy can be inferred from changes in energy recovery efficiency, and thus the extracted energy is disregarded here. The annual energy recovery efficiency (Fig. 6.3c) in the first year, calculated by the

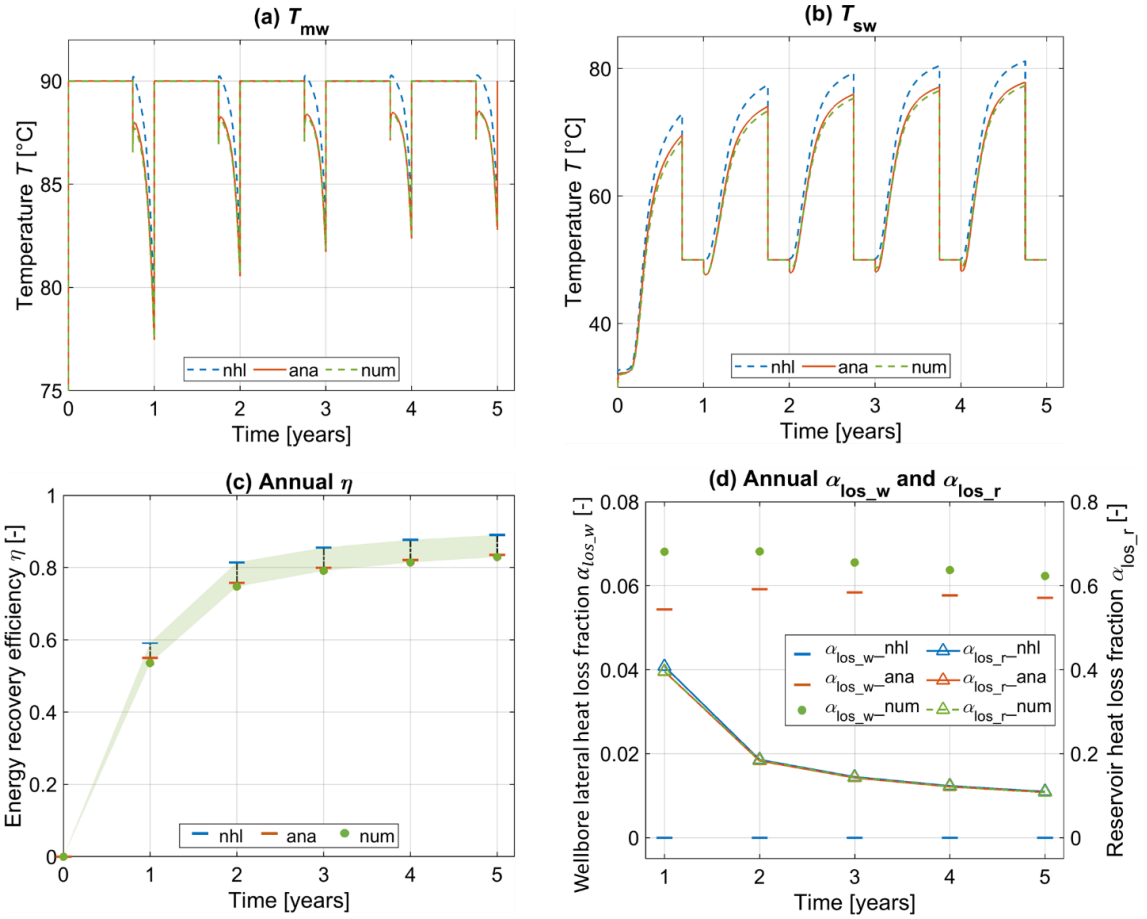

Figure 6.3. Performance indicators of the HT-ATES system: (a) temperature at the main wellhead; (b) temperature at the supporting wellhead; (c) annual energy recovery efficiency; (d) annual wellbore lateral heat loss fraction (left y-axis) and reservoir loss fraction (right y-axis).

numerical approach (53.6%), is lower than that obtained using the analytical approach (55%) and the approach that disregards wellbore (59.2%). The low energy recovery efficiencies in the first year are primarily due to the high reservoir heat loss (Fig. 6.3d), which is driven by the large temperature difference between the injected hot fluid and the initial reservoir temperature. Specifically, the reservoir heat loss fractions calculated by the numerical and analytical approaches, and the approach without considering wellbore lateral heat transfer are 39.59%, 39.57% and 40.8%, respectively. As heat storage and extraction cycles accumulate over time, the reservoir heat loss fraction gradually decreases, reaching approximately 11% by the fifth year. This reduction in heat loss leads to a significant improvement in energy recovery efficiency, which increases by about 30%, surpassing 80% by the fifth year. Fig. 6.3d shows the wellbore lateral heat loss fraction obtained using the numerical approach, which reaches a maximum of 6.8% in the second

year. This is higher than the 5.9% calculated from the analytical approach and the 0% from the approach without considering wellbore lateral heat transfer. The lateral heat loss calculated using the analytical approach is 13% lower than that obtained from the numerical approach. After the second year, wellbore lateral heat loss decreases as the surrounding formations heat up, reducing the temperature difference and consequently, the amount of heat lost as described by Eqs. (6.8) and (6.9). This decline in wellbore lateral heat loss further contributes to the improvement in energy recovery efficiency.

The numerical approach is the most accurate, as it captures complex heat exchange processes between the wellbore and surrounding formations, along with dynamic temperature variations in far-field formations. In contrast, the analytical approach and the approach that neglects wellbore lateral heat transfer tend to overestimate fluid temperature and energy recovery efficiency due to simplifying assumptions. While the analytical approach reduces the running time of one simulation from ~46.5 hours (numerical approach) to ~44.5 hours using 152 CPU cores, this gain comes at the expense of accuracy, particularly in capturing detailed thermal interactions and wellbore lateral heat loss. Although the analytical method can approximate general trends over time, such as improvements in energy recovery and decreases in wellbore lateral heat losses, the numerical approach remains essential for high-precision applications including system optimization and minimizing heat losses, as it can accurately model complex dynamics and provide reliable long-term performance predictions.

6.3.2 Effects of wellbore configurations

1) Wellbore diameter

We evaluate seven wellbore diameter sets of main and supporting wellbores, with inner diameters ranging from 6.75 inches (4 inches smaller than the reference case) to 14.75 inches (4 inches larger than the reference case), with four intermediate inner diameters of 8.75, 11.75, 12.75 and 13.75 inches. The entire wellbore geometry at all depths is adjusted according to the inner diameter variations. All other parameters remain consistent with those of the reference case. The energy recovery efficiency (Fig. 6.4a) decreases as the wellbore diameter increases, while both the wellbore lateral heat loss fraction (Fig. 6.4b)

and reservoir heat loss fraction (Fig. 6.4c) show the opposite trend. When the wellbore inner diameter increases from 6.75 inches to 12.75 inches (range I), the changes in annual energy recovery efficiency and reservoir heat loss fraction are gradual and linear, with only minor variations. In contrast, a further increase in wellbore diameter, from 13.75 inches to 14.75 inches (range II), results in more significant changes, as depicted in Fig. 6.4a and b. The wellbore lateral heat loss fraction, however, changes throughout the entire range of diameter increases (Fig. 6.4b). The diminished differences in the ranges and variations of energy recovery efficiency and wellbore lateral heat loss fraction between the numerical approach and the approach without considering wellbore lateral heat transfer, influenced by changes in wellbore diameter, are summarized from the 1st to the 5th year in Fig. 6.4d. From the 1st to the 5th year, the case with a large inner diameter of 14.75 inches consistently demonstrates low energy recovery efficiency and high wellbore lateral heat loss compared to the other cases, which exhibit only minor and smooth variations.

These trends can be explained as follows. According to Eq. (6.1), with constant reservoir characteristics and grid size, a large wellbore diameter owns a high *WI* value (Fig. 6.4e). This indicates that, for the same injection flow rate, a large wellbore diameter leads to small pressure build-up around the injection area in the aquifer. The combination of less initial fluid production due to reduced pressure build-up, followed by increased production as the system stabilizes and pressure dynamics improve, and the eventual equalization of production rates, leads to a net increase in total fluid production from the supporting wells with large wellbore diameters (see Fig. 6.4f). During the extraction phase, the main well with a larger diameter experiences consistently lower pressure levels than the smaller diameter cases . The pressure increase is slow in the large diameter case due to reduced flow resistance, which results in a weak pressure gradient between the reservoir and the well. As a result, the driving force for fluid movement from the reservoir into the main well is diminished. Because the pressure at the main well is lower, the extraction rate of fluid from the reservoir is significantly reduced. This diminished pressure gradient leads to a substantial decrease in the volume of fluid produced from the main well. The combination of low pressure and a slow pressure response means that, during the extraction phase, the main well with a larger diameter produces considerably

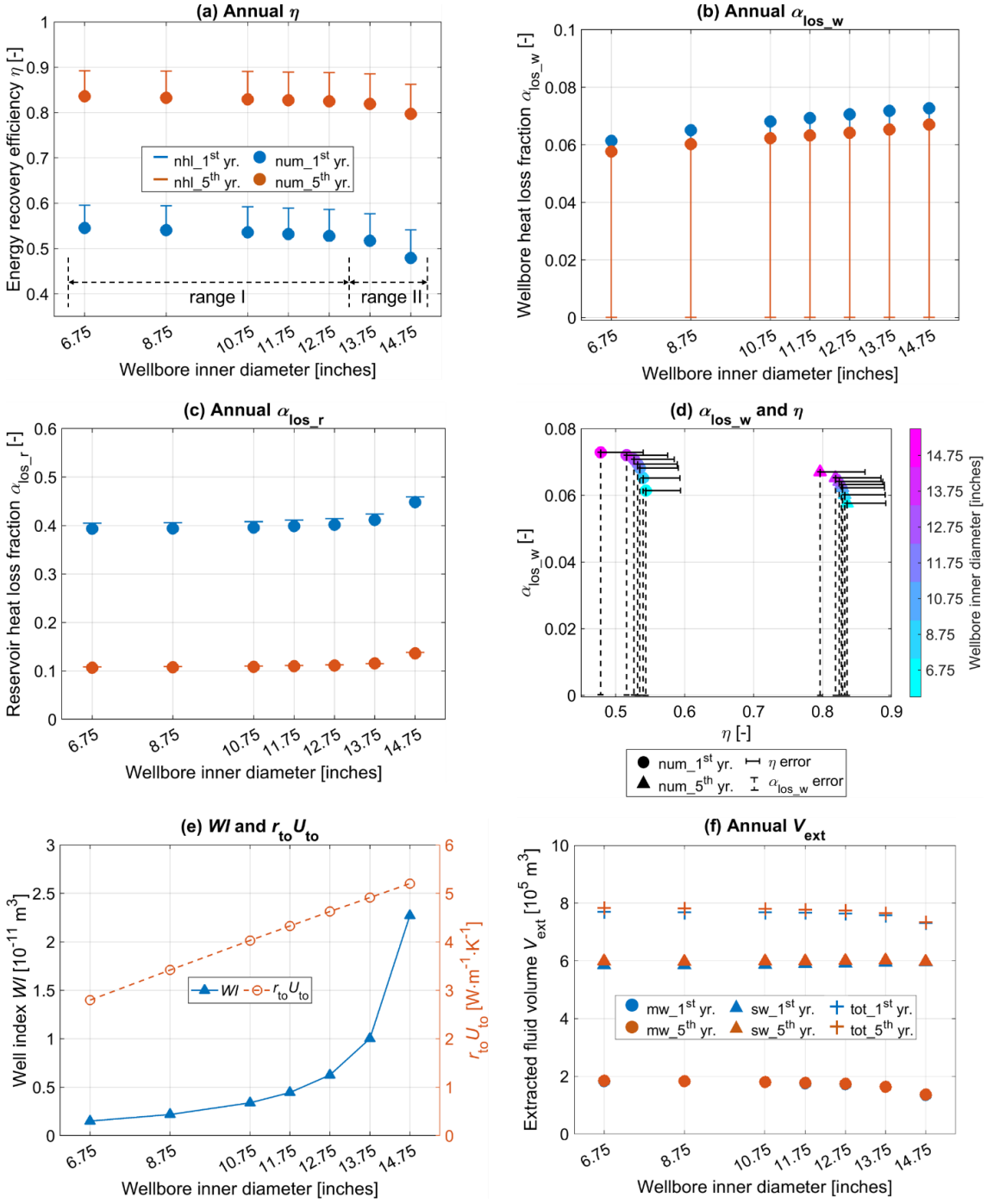

Figure 6.4. Effects of wellbore diameter on annual (a) energy recovery efficiency; (b) wellbore lateral heat loss fraction; (c) reservoir heat loss fraction; (d) wellbore lateral heat loss fraction versus annual energy recovery efficiency from the numerical approach at 1st and 5th year. The horizontal and vertical error bars mean the differences between the numerical approach and the approach without considering wellbore lateral heat transfer in annual energy recovery efficiency and wellbore lateral heat loss fraction, respectively; (e) *WI* in open-hole section and $r_{to}U_{to}$ of non-open-hole section at 200 m depth; (f) annual extracted fluid volumes from the main well, supporting wells, and the total volume, as calculated using the numerical approach. The inner diameter of the wellbore in the reference case is 10.75 inches.

less fluid compared to smaller diameters. Consequently, despite large wellbore diameters leading to great fluid production in the heat storage phase, the associated decrease in heat storage due to low pressures and weak gradients results in a low net annual fluid production when compared to small diameters (Fig. 6.4f). The reduced fluid extraction volumes result in less energy carried by the extracted fluid. As a result, the energy recovery efficiency (Fig. 6.4a) decreases, and there is more heat loss in the reservoir (Fig. 6.4c). Additionally, a large wellbore diameter increases the lateral heat exchange area with the surrounding formations, which linearly increases the values of $r_{to}U_{to}$ in Eq. (6.8) (Fig. 6.4e). Meanwhile, a large wellbore diameter means slow flow and long time to lose heat. Thus, the case with large wellbore diameter result in a high wellbore lateral heat loss fraction (Fig. 6.4b and d), further reducing the energy recovery efficiency. These changes favor the wellbore diameter set case with a 6.75 inches inner diameter, which demonstrates good performance (Fig. 6.4d). However, it is important to consider that small wellbore diameter may generates high wellbore pressure drops thus increasing the energy consumption for pumps. Therefore, it is crucial to balance these factors and optimize the wellbore diameter based on specific geological conditions, design requirements and heating demands of the system.

2) Casing thermal conductivity

In the HT-ATES systems, the thermal conductivity (Eq. (6.3)) and cost of casing materials play a critical role in determining the system's thermal performance, operational longevity and overall efficiency. The casing thermal conductivity (Fig. 6.1c) represents the ability of the casing material to transfer heat between the fluid inside the wellbore and the surrounding formation. Common materials (Pribnow et al., 1995; Anwar et al., 2019; Mohammed et al., 2019; Wiktorski et al., 2019) used for wellbore casings include carbon steel (45~60 $W{\cdot}m^{-1}{\cdot}K^{-1}$), stainless steel (15~30 $W{\cdot}m^{-1}{\cdot}K^{-1}$), PVC (polyvinyl chloride, ~0.19 $W{\cdot}m^{-1}{\cdot}K^{-1}$), HDPE (high-density polyethylene, ~0.48 $W{\cdot}m^{-1}{\cdot}K^{-1}$) and fiberglass (~0.04 $W{\cdot}m^{-1}{\cdot}K^{-1}$). In this example, we consider eight different thermal conductivities (ranging from 0.045~45 $W{\cdot}m^{-1}{\cdot}K^{-1}$) of wellbore casing to assess their impact on the performance of the HT-ATES system. Note that only the wellbore casing thermal

conductivity is varied, while all other parameters remain consistent with the reference case.

The clear distinction in annual energy recovery efficiency, wellbore lateral heat loss fraction and reservoir heat loss fraction, obtained using the numerical approach and the approach that excludes wellbore lateral heat transfer, is displayed in Fig. 6.5a, b and c for different casing thermal conductivity cases. The energy recovery efficiency (Fig. 6.5a) increases as wellbore casing thermal conductivity decreases due to the reduced wellbore lateral heat loss fraction (Fig. 6.5b). The minimum casing thermal conductivity of 0.045 $W \cdot m^{-1} \cdot K^{-1}$ behaves better than other cases by decreasing the annual wellbore lateral heat loss fraction to 3.3% (i.e., removing ~51.4% of that in the reference case) and increasing the annual energy recovery efficiency by 3% than the reference case at the 1st year. From the 1st to the 5th year, the reduced differences in energy recovery efficiency and wellbore lateral heat loss fraction, influenced by changes in casing thermal conductivity, are highlighted when comparing the numerical approach to the approach without considering wellbore lateral heat transfer, as summarized in Fig. 6.5d. The magnitudes of the error bars for energy recovery efficiency and wellbore lateral heat loss fraction between the numerical approach and the approach that excludes wellbore lateral heat transfer increase as the casing thermal conductivity rises. The linear relationship between the variations in energy recovery efficiency and wellbore lateral heat loss fraction with changes suggests that casing thermal conductivity negatively impacts efficiency in a linear manner by changing wellbore lateral heat loss. The changes in annual energy recovery efficiency, wellbore lateral heat loss fraction and reservoir heat loss fraction with wellbore casing thermal conductivity can be identified into three ranges: 0.045~0.1 $W \cdot m^{-1} \cdot K^{-1}$ (i.e., range I); 0.15~0.45 $W \cdot m^{-1} \cdot K^{-1}$ (i.e., range II); 4.5~45 $W \cdot m^{-1} \cdot K^{-1}$ (i.e., range III). The variations within each of the ranges are smooth and small, however, significant differences are observed among them. The explanations are as follows: according to Eq. (6.8), a high wellbore casing thermal conductivity results in an increased U_{to} value (Fig. 6.5e) with three obvious variation ranges (i.e., 0.045~0.1 $W \cdot m^{-1} \cdot K^{-1}$; 0.15~0.45 $W \cdot m^{-1} \cdot K^{-1}$; 4.5~45 $W \cdot m^{-1} \cdot K^{-1}$), which in turn leads to great wellbore lateral heat loss fraction (Fig. 6.5b) and consequently reduces the energy recovery efficiency (Eq. (6.4) and Fig. 6.5a). As shown in Fig. 6.5d, low thermal conductivity materials enhance thermal performance by

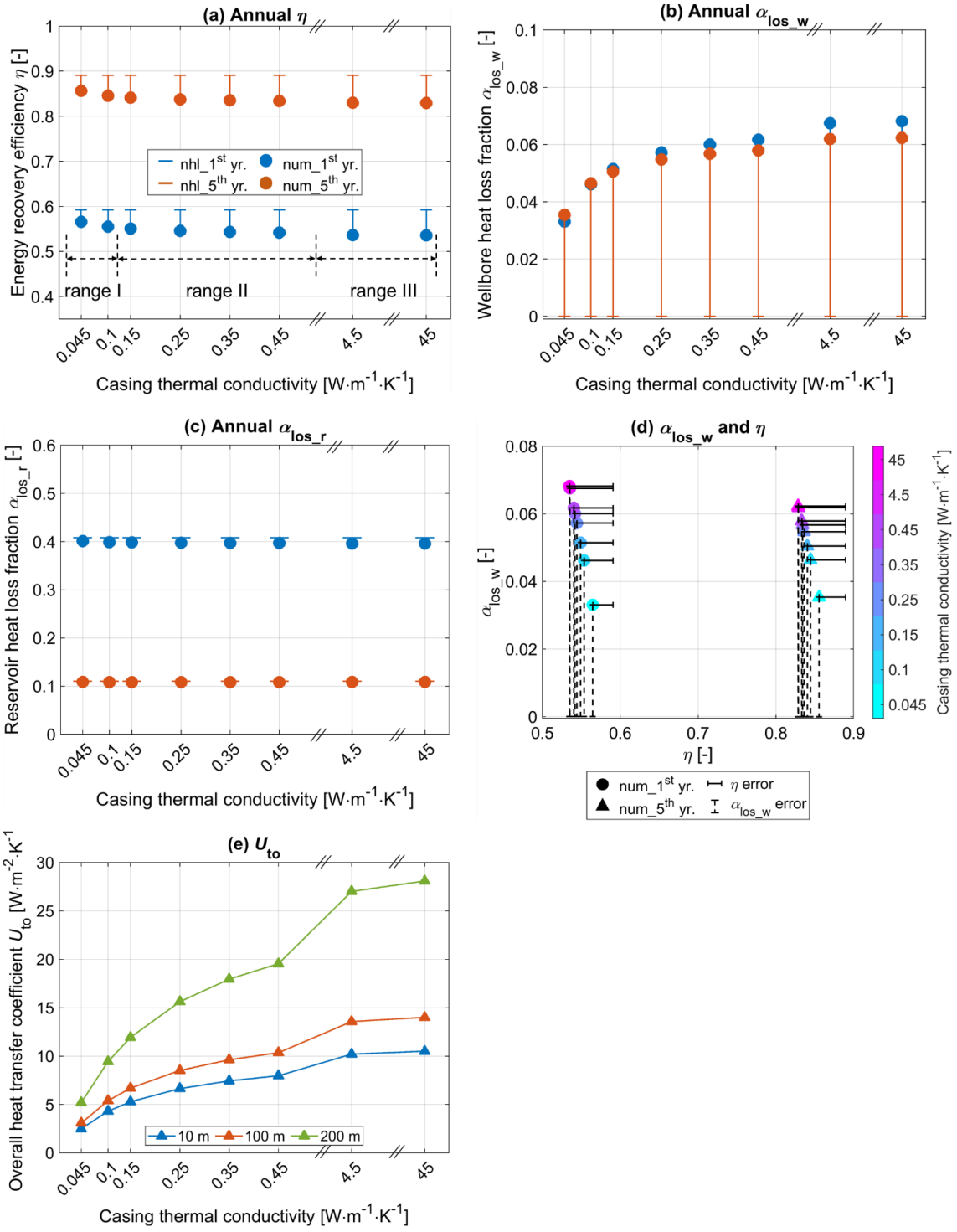

Figure 6.5. Effects of wellbore casing thermal conductivity on the annual (a) energy recovery efficiency; (b) wellbore lateral heat loss fraction; (c) reservoir heat loss fraction; (d) wellbore lateral heat loss fraction versus annual energy recovery efficiency from the numerical approach at 1st and 5th year. The horizontal and vertical error bars mean the differences between the numerical approach and the approach without considering wellbore lateral heat transfer in annual energy recovery efficiency and wellbore lateral heat loss fraction, respectively; (e) U_{to} of non-

open-hole section at 10 m, 100 m and 200 m, separately. The casing thermal conductivity in the reference case is 45 $W \cdot m^{-1} \cdot K^{-1}$.

reducing wellbore lateral heat loss fraction. Although high HT-ATES system performance requires low casing thermal conductivity, the high cost of selecting casing materials with low thermal conductivity must also be considered, necessitating economic analysis and related optimization.

3) Supporting well number

In the following analysis, we investigate the effects of varying the number of supporting well — specifically 1, 2, 3 and 4 — on the HT-ATES system's performance. All other parameters, including the total injection flow rate, are kept consistent with those of the reference case. The resulting annual energy recovery efficiency, wellbore lateral heat loss fraction and reservoir heat loss fraction are shown in Fig. 6.6a, b and c. In the first year, the energy recovery efficiency (Fig. 6.6a) decreases as the supporting well number increases, while the reservoir heat loss fraction (Fig. 6.6c) exhibits the opposite trend. By the fifth year, the case with three supporting wellbores demonstrates the highest energy recovery efficiency and the lowest reservoir heat loss fraction compared to the other cases. Additionally, the annual wellbore lateral heat loss fraction consistently increases with the supporting well number. The reduced differences in the ranges and variations of energy recovery efficiency and wellbore lateral heat loss fraction, influenced by changes in wellbore diameter, are compared between the numerical approach and the approach excluding wellbore lateral heat transfer from the 1st to the 5th year (Fig. 6.6d). The magnitudes of the error bars for energy recovery efficiency and wellbore lateral heat loss fraction between the numerical approach and the approach that excludes wellbore lateral heat transfer increase with the rise of supporting well number. The volume of heat storage space is directly proportional to the number of supporting wells. With few supporting wells, the storage space for fluid is limited and unevenly distributed, whereas with more supporting wells, the storage space is large and more evenly distributed. In the first year, with a constant amount of injected heat, a great number of supporting wells results in more areas contacting the surroundings, reduced flow velocity and increased travel time within the wellbores. As a result, less heat is extracted from the produced fluid, and more heat remains stored in the reservoir, leading to great reservoir heat losses (Fig. 6.6c).

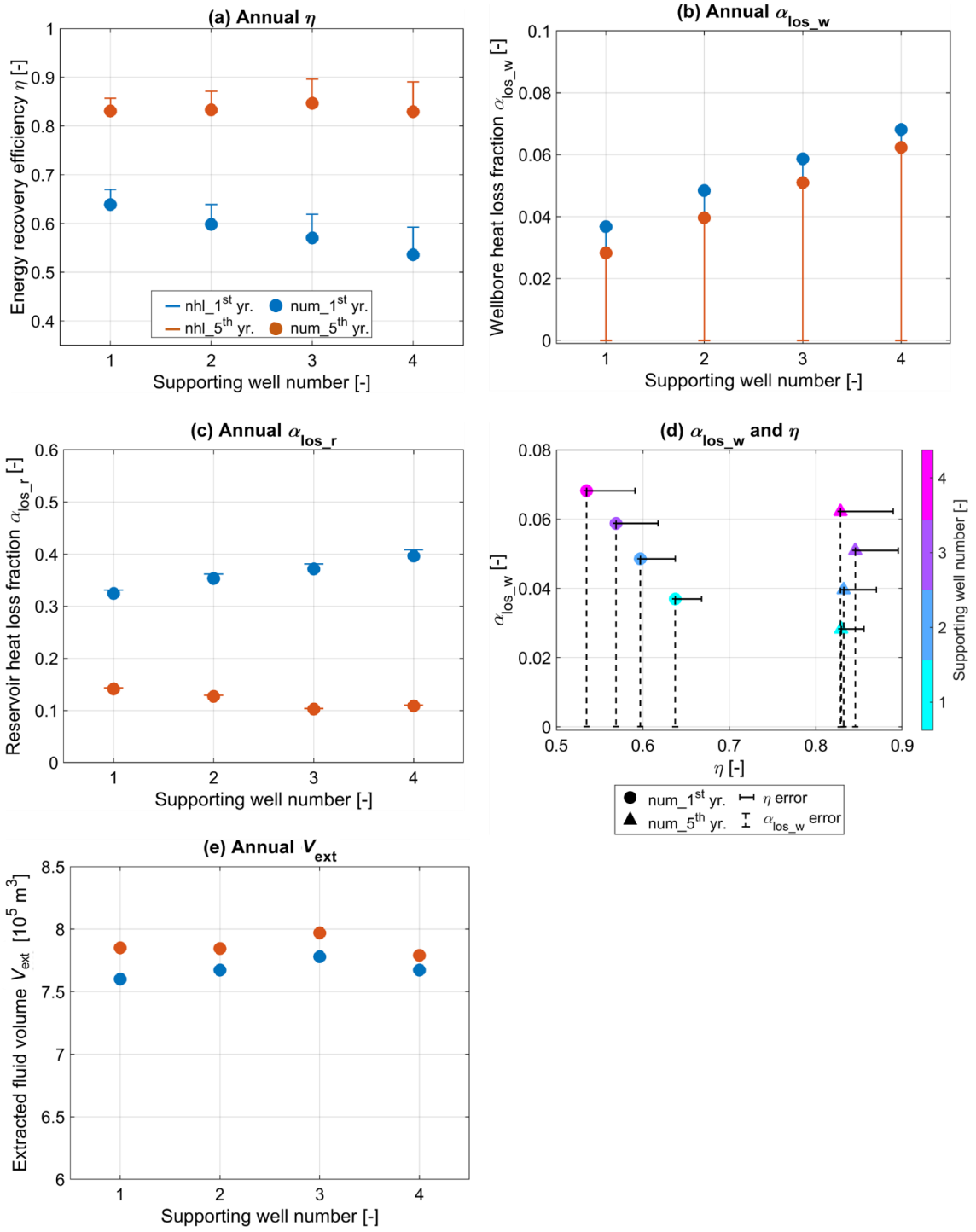

Figure 6.6. Effects of supporting well number on the annual (a) energy recovery efficiency; (b) wellbore lateral heat loss fraction; (c) reservoir heat loss fraction; (d) wellbore lateral heat loss fraction versus annual energy recovery efficiency from the numerical approach at 1st and 5th year. The horizontal and vertical error bars mean the differences between the numerical approach and the approach without considering wellbore lateral heat transfer in annual energy recovery efficiency and wellbore lateral heat loss fraction, respectively; (e) extracted fluid volumes from the main well, supporting wells and the total volume, as calculated using the numerical approach. The supporting well number in the reference case is 4.

Although the case with three supporting wells produces the largest volume of fluid in the first year (Fig. 6.6e), the volume of the thermal fluid accumulation area predominantly influences the energy recovery efficiency (Fig. 6.6a) and reservoir heat loss (Fig. 6.6c), which are negatively and positively correlated with the supporting well number, respectively. By the fifth year, cases with a high supporting well number (such as 3 or 4) achieve more uniform heating of the wellbore area. This results in reduced heat loss in the reservoir (Fig. 6.6c)), high heat production compared to cases with few supporting wells (Fig. 6.6a)) and a large volume of produced fluid (Fig. 6.6e). In the first year, the linear relationship between the variations in energy recovery efficiency and wellbore lateral heat loss fraction with changes in supporting well number implies that supporting well number negatively impacts energy recovery efficiency and positively affects wellbore lateral heat loss fraction in a linear manner (Fig. 6.6d). The case with 3 supporting wells demonstrates best performance in improving energy recovery efficiency to above 0.5 and diminishing wellbore lateral heat loss to less than 0.1 (Fig. 6.6d). This suggests that optimizing the number of supporting well presents an opportunity to enhance the HT-ATES performance while simultaneously reducing drilling costs.

6.3.3 Effects of operational parameters

1) Injection flow rate

In this part, we consider seven different injection flow rates from the main well in the storage period or from all the supporting wells in the extraction period, ranging evenly from 6.25 to 25 $L \cdot s^{-1}$. The annual energy recovery efficiency and reservoir heat loss fraction under varying injection flow rates are illustrated in Fig. 6.7a, b, c and d). The differences in the ranges and variations of energy recovery efficiency, extracted energy and wellbore lateral heat loss fraction between the numerical approach and the approach without considering wellbore lateral heat transfer, influenced by changes in injection flow rate, are summarized from the 1^{st} to the 5^{th} year in Fig. 6.7e and f. As shown in Fig. 6.7a the energy recovery efficiency increases with high injection flow rates, which also boosts the annual extracted energy (Fig. 6.7b). In contrast, both the wellbore lateral heat loss

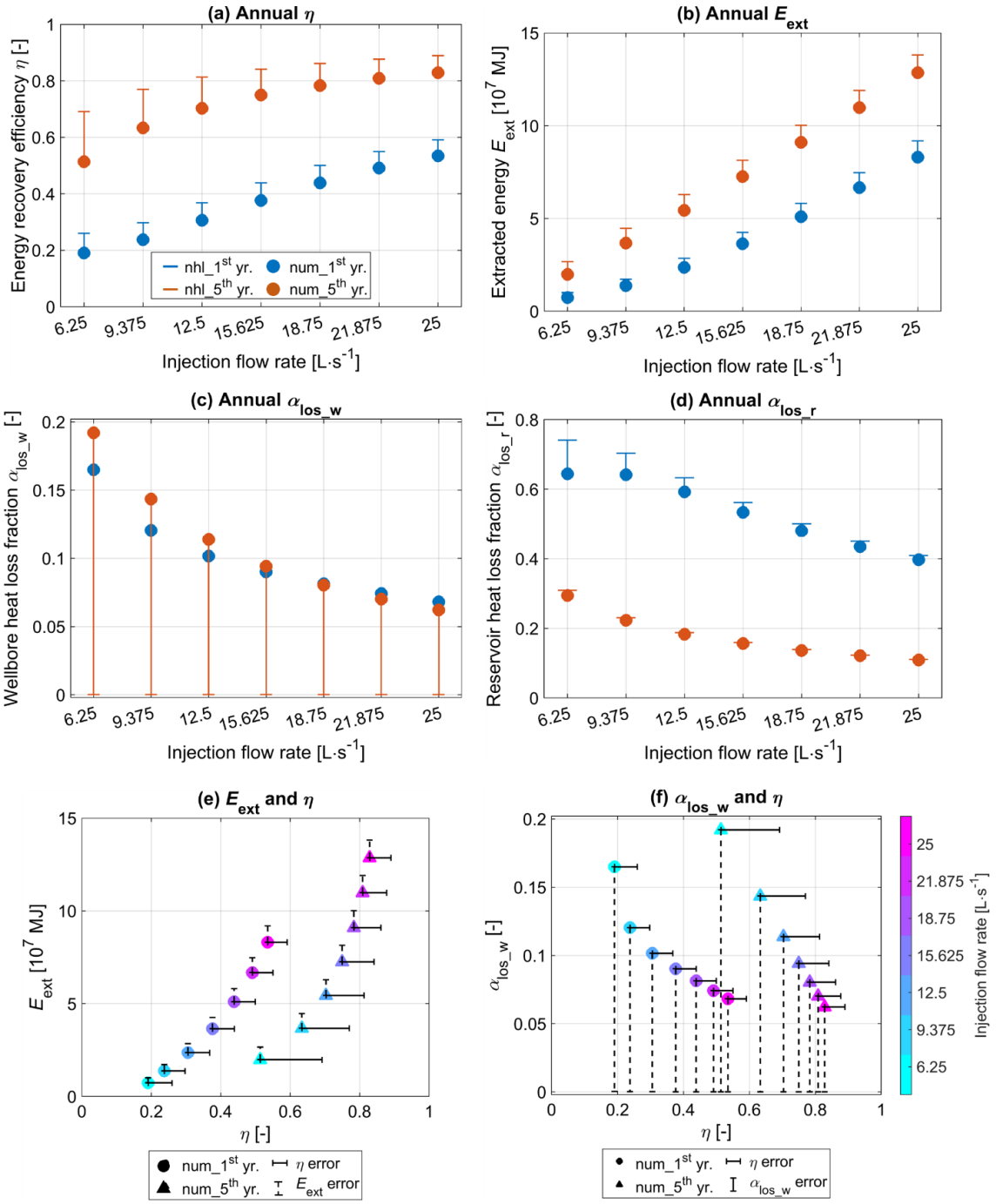

Figure 6.7. The impact of injection flow rate on the annual (a) energy recovery efficiency; (b) extracted energy; (c) wellbore lateral heat loss fraction; (d) reservoir heat loss fraction; (e) extracted energy versus energy recovery efficiency, and (f) wellbore lateral heat loss fraction versus energy recovery efficiency from the numerical approach at 1st and 5th year. The horizontal and vertical error bars in (e) and (f) mean the differences between the numerical approach and the approach without considering wellbore lateral heat transfer. The injection flow rate in the reference case is 25 L·s^{-1}.

fraction (Fig. 6.7c) and the reservoir heat loss fraction (Fig. 6.7d) decrease with increasing injection flow rates. The magnitudes of the error bars for energy recovery efficiency, extracted energy and wellbore lateral heat loss fraction between the numerical approach and the approach that excludes wellbore lateral heat transfer decrease with the rise of injection flow rate (Fig. 6.7e and f).

Without constraining the total injected energy and with a fixed injection fluid temperature, an increase in injection flow rate results in a great amount of heat being injected (E_{inj}) and extracted (E_{ext}) from the reservoir per unit time (Eqs. (6.5) and (6.6); Fig. 6.7b). High injection flow rates also reduce the fluid's residence time in the wellbore, which decreases the period available for heat dissipation. This effect is more pronounced at high injection flow rates where temperature differences are greater, leading to reduced heat loss along the wellbore (Fig. 6.7c). At low injection flow rates, the slow movement of fluid within the reservoir enhances thermal diffusion, which reduces the amount of heat that can be extracted. Conversely, high injection flow rates enable more efficient heat extraction before significant thermal diffusion occurs, thereby minimizing its impact (Fig. 6.7d). Moreover, high injection flow rates facilitate more effective heat exchange between the fluid and the reservoir rock, resulting in reduced total heat losses (including both wellbore and reservoir heat losses) and improved overall system efficiency (Fig. 6.7a). The cases with injection flow rates between 15.625 $L \cdot s^{-1}$ and 25 $L \cdot s^{-1}$ exhibit better performance in improving energy recovery efficiency to above 0.5 and diminishing wellbore lateral heat loss less than 0.1 (Fig. 6.7e and f). Optimizing the injection flow rate is essential for improving the performance of a HT-ATES system. It requires balancing multiple factors, such as energy demand, pumping requirements and key performance indicators. By selecting the appropriate injection flow rate, the system's efficiency can be significantly enhanced, leading to reduced operational costs and a more effective overall system design.

2) Injection temperature at the main well

In this example, we examine seven different injection temperatures at the main well ranging from 90°C to 210°C to evaluate their effects on the system's performance. The injection temperature at supporting well in extraction period is fixed at 50°C. As shown

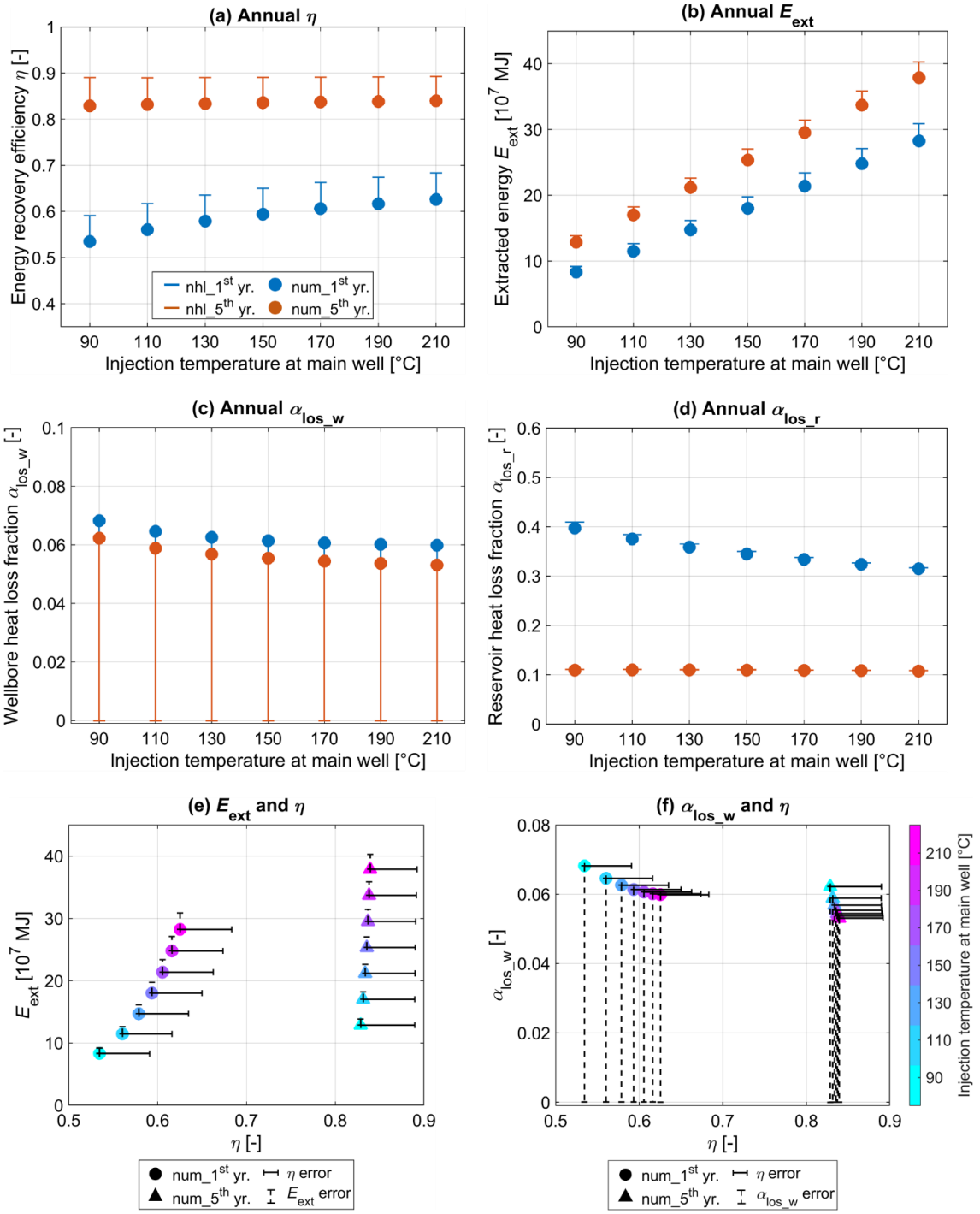

Figure 6.8. The impact of injection temperature at the main well on the annual (a) energy recovery efficiency; (b) extracted energy; (c) wellbore lateral heat loss fraction; (d) reservoir heat loss fraction; (e) extracted energy versus energy recovery efficiency, and (f) wellbore lateral heat loss fraction versus energy recovery efficiency from the numerical approach at 1st and 5th year. The horizontal and vertical error bars in (e) and (f) mean the differences between the numerical approach and the approach without considering wellbore lateral heat transfer. The injection temperature at the main well in the reference case is 90°C.

in Fig. 6.8a, both energy recovery efficiency and extracted energy increase with rising injection temperatures at the main well. Conversely, the wellbore lateral heat loss fraction (Fig. 6.8b) and reservoir heat loss fraction (Fig. 6.8c) decrease as the injection temperature at the main well increases. An increase in injection temperature at the main well amplifies the temperature difference between the injected fluid and the reservoir's in-situ temperature. According to Eqs. (6.5) and (6.6), this results in a great amount of heat being injected and extracted (Fig. 6.8b). Additionally, as indicated by Eq. (6.8), although a high injection temperature at the main well enhances the temperature gradient between the wellbore and surrounding formation, it also accelerates heat transfer, leading to greater net heat loss along the wellbore. Similarly, the rise in injection temperature increases the temperature difference between the injected fluid and the aquifer, resulting in higher net reservoir heat loss. However, both the wellbore lateral heat loss fraction and reservoir heat loss fraction decrease because the increase in injected energy is much more efficient than the increase in conductive heat loss through the wellbore and the reservoir. This results in a great fraction of high-temperature heat being extracted from the reservoir and reduces overall heat losses (including both wellbore and reservoir heat losses), thereby improving the energy recovery efficiency (Fig. 6.8a). The differences in the ranges and variations of energy recovery efficiency, extracted energy and wellbore lateral heat loss fraction between the numerical approach and the approach without considering wellbore lateral heat transfer, influenced by changes in injection temperatures at the main well, are summarized from the 1st to the 5th year in Fig. 6.8e and f. With the rise of injection temperatures at the main well, the magnitudes of the error bars for energy recovery efficiency, extracted energy and wellbore lateral heat loss fraction between the numerical approach and the approach that excludes wellbore lateral heat transfer decrease. Up until the fifth year, there are minor differences in energy recovery efficiency and wellbore lateral heat loss fraction due to the fully heated conditions in the aquifer. The impact of injection temperature on a HT-ATES system's performance is multifaceted, directly affecting heat storage efficiency, heat loss, energy consumption and overall economic benefits. Optimizing the injection temperature can maximize the economic benefits by balancing the efficiency of heat recovery with the costs associated with energy consumption and heat loss, leading to a more profitable operation.

6.4 Conclusions

In this work, we investigated the impact of wellbore lateral heat transfer on the performance of HT-ATES systems. Our study focused on a specific HT-ATES project (the Swiss Bern project (Vidal et al., 2022)) using a five-spot system and numerically evaluated different ATES performance indicators including energy recovery efficiency, extracted energy, wellbore lateral heat loss fraction and reservoir heat loss fraction. We also examined how various wellbore configurations and operational parameters affect the HT-ATES performance, particularly due to the changes of the wellbore lateral heat loss. The key conclusions for this specific project can be listed as follows:

- Based on the reference case, the wellbore lateral heat loss can diminish the energy recovery efficiency of the HT-ATES system by around 7%, which reflects the necessity of considering the wellbore in the ATES performance evaluation rather than ignoring the wellbore.
    - The analytical approach to calculate the wellbore heat loss gives rise to slightly lower values than the numerical one, thus leading to a higher energy recovery efficiency.
- Using a small wellbore diameter can enhance the energy recovery efficiency of ATES, while large wellbore diameters lead to increased wellbore lateral and reservoir heat losses due to low fluid extraction volumes. The small diameter lowers the drilling costs but generates high wellbore pressure drops thus increasing the energy consumption for pumps.
- Wellbore casing materials with low thermal conductivity (e.g., fiberglass), improve the ATES system performance (energy recovery efficiency) by minimizing wellbore lateral heat loss to 3.3%, which is approximately 51.4% less than in the reference case.
- Regarding the number of supporting wells, energy recovery efficiency decreases with more wells in the first storage cycle due to the large space of reservoir heating. However, the case with three supporting wells demonstrates the best performance in the last cycle, mainly affected by the large extracted fluid volume from the warm reservoir condition.

- High flow rates enhance energy recovery efficiency and extracted energy while decreasing both wellbore and reservoir heat losses. This improvement results from the fast injection and production of fluid, which relatively reduces fluid residence time and thermal diffusion.
- High fluid injection temperatures at the main well can increase both wellbore and reservoir heat loss. However, the fractions of the wellbore and reservoir heat loss decrease due to the large amount of energy injected.

In conclusion, this study underscores the significance of wellbore lateral heat loss in the evaluation of the HT-ATES system performance. Our findings indicate that wellbore configurations and operational parameters should be carefully considered for designing an effective HT-ATES system. Although the studied parameters can give an impact on the energy recovery efficiency in a monotonous manner, other relevant factors such as material price, supply energy for hydraulic pump and drilling cost must be considered in order to find the optimal design solution of HT-ATES system.

7 Conclusions and future work

7.1 Major findings of the research

This research presents a comprehensive exploration of geothermal reservoir dynamics, set against the backdrop of an urgent global transition toward sustainable energy sources. Geothermal energy, with its potential to provide continuous, low-emission power, is increasingly recognized as a vital resource for meeting rising energy demands and mitigating climate change. The studies conducted herein focus on three interconnected aspects of geothermal systems: the mechanisms governing temperature distribution, fluid flow dynamics, and energy storage capabilities. By examining these critical components, this research enhances our understanding of geothermal energy potential and identifies key factors that influence the efficiency of resource extraction. Furthermore, it proposes innovative methodologies for improved resource assessment and sustainable utilization, aiming to optimize the management of geothermal resources. Collectively, these studies contribute to advancing geothermal energy as a reliable and sustainable solution for addressing the challenges of global energy consumption and environmental stewardship.

7.1.1 Insights into hydrothermal convection mechanisms

Chapter 3 investigates transport mechanisms of hydrothermal convection in faulted tight sandstones, particularly in the context of the Piesberg Quarry in northwestern Germany. By creating an idealized numerical model, we derived critical parameters and processes responsible for the formation of thermal anomalies in analogous geological environments. This study primarily concentrated on the interactions between various heat transfer mechanisms—conduction, convection, and advection—and their role in shaping fluid flow pathways within faulted tight sandstones.

Our findings reveal that buoyancy-driven convection plays a pivotal role in energy transport within the primary fault, significantly impacting the thermal profile of the reservoir. Specifically, under favorable hydraulic conditions—such as high sandstone

permeability and balanced fault permeability—convective flows in sandstone and advective flows in transfer faults effectively redistribute heat and fluid. This interplay results in elevated reservoir temperatures exceeding 269 °C, as opposed to the maximum temperatures observed under conduction-dominated scenarios (⩽ 250 °C). Additionally, lateral regional flow was shown to interact with convective and advective flows, altering the dominant heat transfer mechanism from conduction to advection in certain scenarios.

The detailed analysis of anisotropic and depth-dependent permeability further emphasizes the influence of local permeability distributions on temperature anomalies. The study concludes that the key determinants of thermal anomalies are the permeability of the main fault and the ratio of horizontal permeabilities between the sandstone and the fault, rather than topographic conditions. This insight underscores the potential for fractured and faulted zones in tight sandstone reservoirs to serve as viable geothermal energy sources in sedimentary basins worldwide.

7.1.2 Advancements in reservoir characterization with nanoparticle tracers

Chapters 4 and 5 introduce a novel approach to geothermal reservoir characterization using temperature-reporting nanoparticle tracers. This methodology addresses the need for precise mapping of temperature distributions within fractured geothermal systems, particularly in light of the complexities posed by geological and thermal heterogeneities.

Our numerical modeling efforts demonstrate that these tracers, which irreversibly convert at specific temperature thresholds, can effectively track temperature changes throughout the reservoir. The study analyzed tracer behavior in both homogeneous and fractured reservoirs, revealing how variations in injection-production configurations significantly influence tracer breakthrough data. The results indicate that the flow paths of injected nanotracers are affected by geological features, such as thermal anomalies and inclined permeable zones, thereby impacting the peak concentrations and arrival times of the tracers.

A key conclusion of this study is that the temperature range within the reservoir can be inferred from the peak concentration curves of the tracers. Specifically, the temperature thresholds at which tracers convert provide upper and lower limits on reservoir

temperatures, allowing for a more accurate assessment of subsurface conditions. Furthermore, the study presents a new analytical method for interpreting tracer data, which can be used to characterize in-situ reservoir temperatures during both exploration and production phases.

7.1.3 Evaluation of high-temperature aquifer thermal energy storage systems performance

Chapter 6 investigates the influence of wellbore lateral heat transfer on the performance of high-temperature aquifer thermal energy storage (HT-ATES) systems. By numerically evaluating the Swiss Bern project, this research highlights the critical role that wellbore configurations and operational parameters play in optimizing energy recovery efficiency.

Our findings indicate that wellbore lateral heat loss significantly affects the energy recovery efficiency of HT-ATES systems, with a reduction of approximately 7% in the reference case. This underscores the importance of incorporating wellbore dynamics into the performance evaluation of thermal energy storage systems. We explored how various configurations—such as wellbore diameter, casing materials, and fluid flow rates—impact energy recovery and heat loss. Notably, smaller wellbore diameters were found to enhance energy recovery efficiency, while low thermal conductivity casing materials effectively reduced heat losses.

The study also examined the effects of multiple supporting wells on system performance, demonstrating that while energy recovery efficiency may decline with additional wells during the initial storage cycle, optimal configurations can lead to enhanced performance in later cycles. Furthermore, high flow rates and injection temperatures were shown to improve energy recovery, although they also increase overall heat loss fractions. These findings highlight the delicate balance between maximizing energy extraction and minimizing thermal losses in HT-ATES systems.

7.1.4 Pathways to sustainable geothermal utilization

Collectively, these studies contribute to a more nuanced understanding of geothermal reservoir temperature characterization and highlight the interplay between geological,

thermal, and operational factors in geothermal energy systems. The insights gained provide pathways for enhancing the assessment and utilization of geothermal resources, underscoring the importance of detailed subsurface characterization in advancing geothermal energy as a sustainable solution to global energy demands. Moving forward, it is essential for future research to build on these findings by exploring the integration of additional factors such as geochemical interactions, geological variability, and the influence of external energy sources on geothermal systems. Field validation of the methodologies proposed in this research, particularly the use of temperature-reporting nanoparticle tracers, will be crucial for demonstrating their applicability in real-world scenarios. As the global energy landscape continues to evolve towards sustainability, the role of geothermal energy becomes increasingly vital. By leveraging the insights gained from this research, we can better harness geothermal resources, ultimately contributing to a decarbonized energy future that is both reliable and resilient.

7.2 Future work

The findings from this thesis underscore the transformative potential of geothermal energy in addressing global energy challenges and mitigating climate change. As we look toward the future, several key areas emerge for further exploration and innovation that can enhance the efficacy of geothermal resource management and utilization.

1) advanced characterization techniques

Future research should prioritize the development and refinement of advanced characterization techniques for geothermal reservoirs. The integration of innovative tools such as machine learning and data analytics can significantly improve our ability to interpret complex datasets from subsurface investigations. These techniques can facilitate the identification of optimal drilling locations and enhance predictions of reservoir behavior by recognizing patterns in geological and thermal data.

2) coupled modeling approaches

Expanding on the numerical modeling efforts presented in this work, future studies should focus on coupled thermo-hydraulic-chemical models that account for the interactions between heat transfer, fluid dynamics, and geochemical processes. This comprehensive approach will enable a deeper understanding of the factors influencing

geothermal reservoir performance, particularly in systems with complex geology or active faulting.

3) understanding geological heterogeneities

Addressing the impact of geological heterogeneities remains crucial for accurate geothermal resource assessment. Future investigations should include field-based studies that explore the spatial variability of geological properties, including fracture patterns and thermal anomalies. This empirical data will complement modeling efforts, enhancing our capacity to predict reservoir behavior under varying conditions.

4) integration of geothermal energy in hybrid systems

As the energy landscape evolves, integrating geothermal energy with other renewable sources presents a promising avenue for future research. Investigating hybrid energy systems that combine geothermal, solar, and wind resources can optimize energy production and increase grid reliability. Additionally, assessing the economic viability and technological compatibility of such integrations will be critical for widespread adoption.

5) development of innovative thermal energy storage solutions

Research into aquifer thermal energy storage systems can be advanced by exploring new materials and configurations that minimize heat loss and maximize energy recovery efficiency. Investigating the application of phase change materials (PCMs) and advanced insulation techniques can enhance the performance of thermal storage systems. Furthermore, integrating these systems with existing infrastructure in urban environments could facilitate the transition to more sustainable energy practices.

6) policy and economic frameworks

Finally, aligning geothermal energy development with supportive policy and economic frameworks is essential. Future work should focus on identifying and addressing regulatory barriers that hinder geothermal project development. Research into the economic implications of geothermal energy, including cost-benefit analyses and financing models, will aid stakeholders in making informed decisions about resource investments.

In conclusion, the path forward for geothermal energy is promising, yet it requires continued research and innovation across multiple fronts. By pursuing these outlined directions, we can unlock the full potential of geothermal resources, contributing

significantly to a sustainable energy future that is resilient, reliable, and environmentally responsible. Collaborative efforts across academia, industry, and government will be essential to navigate the complexities of geothermal energy development and ensure its integration into the global energy portfolio.

References

Achtziger‐Zupančič, P., Loew, S., & Hiller, A. (2017). Factors controlling the permeability distribution in fault vein zones surrounding granitic intrusions (Ore Mountains/Germany). Journal of Geophysical Research: Solid Earth, 122(3), 1876-1899.

Achtziger‐Zupančič, P., Loew, S., & Mariethoz, G. (2017). A new global database to improve predictions of permeability distribution in crystalline rocks at site scale. Journal of Geophysical Research: Solid Earth, 122(5), 3513-3539.

Alaskar, M., Ames, M., Liu, C., Connor, S., Horne, R., Li, K., & Cui, Y. (2011). Smart nanosensors for in-situ temperature measurement in fractured geothermal reservoirs. In Australian Geothermal Energy Conference (p. 2011).

Alaskar, M., Ames, M., Liu, C., Li, K., & Horne, R. (2015). Temperature nanotracers for fractured reservoirs characterization. Journal of Petroleum Science and Engineering, 127, 212-228.

Ames, M., Li, K., & Horne, R. (2015). The utility of threshold reactive tracers for characterizing temperature distributions in geothermal reservoirs. Mathematical Geosciences, 47, 51-62.

Andrews, J. R., Day, J., & Marshall, J. E. A. (1996). A thermal anomaly associated with the Rusey Fault and its implications for fluid movements. PROCEEDINGS-USSHER SOCIETY, 9, 068-071.

Anwar, I., Chojnicki, K., Bettin, G., Taha, M. R., & Stormont, J. C. (2019). Characterization of wellbore casing corrosion product as a permeable porous medium. Journal of Petroleum Science and Engineering, 180, 982-993.

Axelsson, G., Flovenz, O. G., Hauksdottir, S., Hjartarson, A., & Liu, J. (2001). Analysis of tracer test data, and injection-induced cooling, in the Laugaland geothermal field, N-Iceland. Geothermics, 30(6), 697-725.

Aydin, H., Nagabandi, N., Jamal, D., & Temizel, C. (2022, April). A comprehensive review of tracer test applications in geothermal reservoirs. In SPE Western Regional Meeting (p. D021S010R003). SPE.

Bächler, D., Kohl, T., & Rybach, L. (2003). Impact of graben-parallel faults on hydrothermal convection—Rhine Graben case study. Physics and Chemistry of the Earth, Parts A/B/C, 28(9-11), 431-441.

Baillieux, P., Schill, E., Edel, J. B., & Mauri, G. (2013). Localization of temperature anomalies in the Upper Rhine Graben: insights from geophysics and neotectonic activity. International Geology Review, 55(14), 1744-1762.

Baldschuhn, R., Binot, F., Fleig, S., & Kockel, F. (2001). Geotektonischer Atlas von Nordwest-Deutschland und dem deutschen Nordsee-Sektor [Tectonic Atlas of Northwest Germany and the German North Sea Sector]. Geologisches Jahrbuch Reihe A, 153.

Barbier, E. (2002). Geothermal energy technology and current status: an overview. Renewable and sustainable energy reviews, 6(1-2), 3-65.

Beck, A. E., Garven, G., & Stegena, L. (1989). Hydrogeological regimes and their subsurface thermal effects. Geophysical Monograph Series, 47.

Becker, I., Busch, B., Koehrer, B., Adelmann, D., & Hilgers, C. (2019). Reservoir quality evolution of Upper Carboniferous (Westphalian) tight gas sandstones, lower Saxony Basin, NW Germany. Journal of Petroleum Geology, 42(4), 371-392.

Beernink, S., Hartog, N., Vardon, P. J., & Bloemendal, M. (2024). Heat losses in ATES systems: The impact of processes, storage geometry and temperature. Geothermics, 117, 102889.

Blackwell, D. D., Negraru, P. T., & Richards, M. C. (2006). Assessment of the enhanced geothermal system resource base of the United States. Natural Resources Research, 15, 283-308.

Bloemendal, M., & Hartog, N. (2018). Analysis of the impact of storage conditions on the thermal recovery efficiency of low-temperature ATES systems. Geothermics, 71, 306-319.

Brown, C. S., & Falcone, G. (2024). Investigating heat transmission in a wellbore for Low-Temperature, Open-Loop geothermal systems. Thermal Science and Engineering Progress, 48, 102352.

Bruhn, R. L., Parry, W. T., Yonkee, W. A., & Thompson, T. (1994). Fracturing and hydrothermal alteration in normal fault zones. Pure and applied geophysics, 142, 609-644.

Bruns, B., Di Primio, R., Berner, U., & Littke, R. (2013). Petroleum system evolution in the inverted L ower S axony B asin, n orthwest G ermany: a 3 D basin modeling study. Geofluids, 13(2), 246-271.

Busch, B., Becker, I., Koehrer, B., Adelmann, D., & Hilgers, C. (2019). Porosity evolution of two Upper Carboniferous tight-gas-fluvial sandstone reservoirs: Impact of fractures and total cement volumes on reservoir quality. Marine and Petroleum Geology, 100, 376-390.

Cacace, M., & Jacquey, A. B. (2017). Flexible parallel implicit modelling of coupled thermal–hydraulic–mechanical processes in fractured rocks. Solid Earth, 8(5), 921-941.

Chen, Z., & Zhang, Y. (2009). Well flow models for various numerical methods. International Journal of Numerical Analysis & Modeling, 6(3).

Cheng, A. D., Ghassemi, A., & Detournay, E. (2001). Integral equation solution of heat extraction from a fracture in hot dry rock. International Journal for Numerical and Analytical Methods in Geomechanics, 25(13), 1327-1338.

Cheng, P. (1979). Heat transfer in geothermal systems. In Advances in heat transfer (Vol. 14, pp. 1-105). Elsevier.

Cherubini, Y., Cacace, M., Blöcher, G., & Scheck-Wenderoth, M. (2013). Impact of single inclined faults on the fluid flow and heat transport: results from 3-D finite element simulations. Environmental earth sciences, 70, 3603-3618.

Clauser, C., & Villinger, H. (1990). Analysis of conductive and convective heat transfer in a sedimentary basin, demonstrated for the Rheingraben. Geophysical Journal International, 100(3), 393-414.

Cloetingh, S. A. P. L., van Wees, J. D., Ziegler, P. A., Lenkey, L., Beekman, F., Tesauro, M., ... & Worum, G. (2010). Lithosphere tectonics and thermo-mechanical properties: an integrated modelling approach for Enhanced Geothermal Systems exploration in Europe. Earth-Science Reviews, 102(3-4), 159-206.

Dashti, A., Korzani, M. G., Geuzaine, C., Egert, R., & Kohl, T. (2023). Impact of structural uncertainty on tracer test design in faulted geothermal reservoirs. Geothermics, 107, 102607.

David, F. (1990). Sedimentology and basin analysis in Westphalia C and D of the Northwest German Upper Carbon. Sedimentologie und Beckenanalyse im Westfal C und D des Nordwestdeutschen Oberkarbons.

Dean, C., Reimus, P., Newell, D., Diagnostics, C., Observations, E. S., & Alamos, L. (2012). Evaluation of a cation exchanging tracer to interrogate fracture surface area in EGS systems. In Proceedings of the 37th Workshop on Geothermal Reservoir Engineering (Vol. 30).

Dickinson, J. S., Buik, N., Matthews, M. C., & Snijders, A. (2009). Aquifer thermal energy storage: theoretical and operational analysis. Geotechnique, 59(3), 249-260.

Dincer, I. (2002). Thermal energy storage systems as a key technology in energy conservation. International journal of energy research, 26(7), 567-588.

Divine, C. E., & McDonnell, J. J. (2005). The future of applied tracers in hydrogeology. Hydrogeology journal, 13, 255-258.

Doughty, C., Hellström, G., Tsang, C. F., & Claesson, J. (1982). A dimensionless parameter approach to the thermal behavior of an aquifer thermal energy storage system. Water Resources Research, 18(3), 571-587.

DuFrance, W., Vericella, J., Duoss, E., Smith, M., Aines, R., & Roberts, J. (2014). Smart tracers for geothermal reservoir assessment (No. LLNL-CONF-654138). Lawrence Livermore National Lab.(LLNL), Livermore, CA (United States).

Duijff, R., Bloemendal, M., & Bakker, M. (2023). Interaction effects between aquifer thermal energy storage systems. Groundwater, 61(2), 173-182.

Egert, R., Korzani, M. G., Held, S., & Kohl, T. (2020). Implications on large-scale flow of the fractured EGS reservoir Soultz inferred from hydraulic data and tracer experiments. Geothermics, 84, 101749.

Egert, R., Nitschke, F., Gholami Korzani, M., & Kohl, T. (2021). Stochastic 3D Navier‐Stokes flow in self‐affine fracture geometries controlled by anisotropy and channeling. Geophysical Research Letters, 48(9), e2020GL092138.

EIA (2009). Residential Energy Consumption Survey. US Energy Information Administation.

Elie, L., Granier, C., & Rigot, S. (2021). The different types of renewable energy finance: A Bibliometric analysis. Energy Economics, 93, 104997.

Elderfield, H., Wheat, C. G., Mottl, M. J., Monnin, C., & Spiro, B. (1999). Fluid and geochemical transport through oceanic crust: a transect across the eastern flank of the Juan de Fuca Ridge. Earth and Planetary Science Letters, 172(1-2), 151-165.

Emry, E. L., Nyblade, A. A., Horton, A., Hansen, S. E., Julià, J., Aster, R. C., ... & Wilson, T. J. (2020). Prominent thermal anomalies in the mantle transition zone beneath the Transantarctic Mountains. Geology, 48(7), 748-752.

Erkan, K. A. M. İ. L. (2015). Geothermal investigations in western Anatolia using equilibrium temperatures from shallow boreholes. Solid Earth, 6(1), 103-113.

Erol, S., Bayer, P., Akın, T., & Akın, S. (2022). Advanced workflow for multi-well tracer test analysis in a geothermal reservoir. Geothermics, 101, 102375.

EU (2010). In: Union O.J.o.t.E (Ed.), Directive on the Energy Performance of Buildings 153.

Ezekiel, J., Ebigbo, A., Adams, B. M., & Saar, M. O. (2020). Combining natural gas recovery and CO2-based geothermal energy extraction for electric power generation. Applied energy, 269, 115012.

Fairley, J. P. (2009). Modeling fluid flow in a heterogeneous, fault‐controlled hydrothermal system. Geofluids, 9(2), 153-166.

Farrell, N. J. C., Healy, D., & Taylor, C. W. (2014). Anisotropy of permeability in faulted porous sandstones. Journal of Structural Geology, 63, 50-67.

Fournier, R. O. (1966). Estimation of underground temperatures from the silica content of water from hot springs and wet-steam wells. Amer. J. Sci., 264, 685-697.

Fox, D. B., Koch, D. L., & Tester, J. W. (2016). An analytical thermohydraulic model for discretely fractured geothermal reservoirs. Water Resources Research, 52(9), 6792-6817.

Frey, M., Bär, K., Stober, I., Reinecker, J., van der Vaart, J., & Sass, I. (2022). Assessment of deep geothermal research and development in the Upper Rhine Graben. Geothermal Energy, 10(1), 18.

Geuzaine, C., & Remacle, J. F. (2009). Gmsh: A 3-D finite element mesh generator with built-in pre-and post-processing facilities. International journal for numerical methods in engineering, 79(11), 1309-1331.

Guillou-Frottier, L., Carrė, C., Bourgine, B., Bouchot, V., & Genter, A. (2013). Structure of hydrothermal convection in the Upper Rhine Graben as inferred from corrected temperature data and basin-scale numerical models. Journal of Volcanology and Geothermal Research, 256, 29-49.

Guillou-Frottier, L., Duwiquet, H., Launay, G., Taillefer, A., Roche, V., & Link, G. (2020). On the morphology and amplitude of 2D and 3D thermal anomalies induced by buoyancy-driven flow within and around fault zones. Solid Earth, 11(4), 1571-1595.

Guo, C., Zhang, K., Pan, L., Cai, Z., Li, C., & Li, Y. (2017). Numerical investigation of a joint approach to thermal energy storage and compressed air energy storage in aquifers. Applied Energy, 203, 948-958.

Gringarten, A. C., Witherspoon, P. A., & Ohnishi, Y. (1975). Theory of heat extraction from fractured hot dry rock. Journal of Geophysical Research, 80(8), 1120-1124.

Haarmann, E. (1911). Die geologischen Verhältnisse des Piesberg-Sattels bei Osnabrück. Jahrbuch der preußischen geologischen Landesanstalt, 30, 1-58.

Harcouët-Menou, V., Guillou-Frottier, L., Bonneville, A., Adler, P. M., & Mourzenko, V. (2009). Hydrothermal convection in and around mineralized fault zones: insights from

two‐and three‐dimensional numerical modeling applied to the Ashanti belt, Ghana. Geofluids, 9(2), 116-137.

Hasan, A. R., & Kabir, C. S. (1991). Heat transfer during two-phase flow in wellbores: part I—formation temperature. In SPE Annual Technical Conference and Exhibition? (pp. SPE-22866). SPE.

Hawkins, A. J., Becker, M. W., & Tester, J. W. (2018). Inert and adsorptive tracer tests for field measurement of flow‐wetted surface area. Water Resources Research, 54(8), 5341-5358.

Hawkins, A. J., Bender, J. T., Grooms, R. D., Schissel, C. J., & Tester, J. W. (2021). Temperature-responsive smart tracers for field-measurement of inter-well thermal evolution: Heterogeneous kinetics and field demonstration. Geothermics, 92, 102046.

Henry, A., Prasher, R., & Majumdar, A. (2020). Five thermal energy grand challenges for decarbonization. Nature Energy, 5(9), 635-637.

Herzog, A. V., Lipman, T. E., & Kammen, D. M. (2001). Renewable energy sources. Encyclopedia of life support systems (EOLSS). Forerunner Volume-'Perspectives and overview of life support systems and sustainable development, 76.

Hinze, C. (1979). Erläuterungen zu Blatt Nr. 3614 Wallenhorst. Geologische Karte von Niedersachsen, 1(25), 000.

Horne, R. N., & Shinohara, K. (1979). Wellbore heat loss in production and injection wells. Journal of Petroleum Technology, 31(01), 116-118.

Huang, Y., Pang, Z., Kong, Y., & Watanabe, N. (2021). Assessment of the high-temperature aquifer thermal energy storage (HT-ATES) potential in naturally fractured geothermal reservoirs with a stochastic discrete fracture network model. Journal of Hydrology, 603, 127188.

Huenges, E., & Ledru, P. (Eds.). (2011). Geothermal energy systems: exploration, development, and utilization. John Wiley & Sons.

IEA. (2019). Renewables 2019 - Analysis and forecast to 2024. Retrieved from https://iea.blob.core.windows.net/assets/a846e5cf-ca7d-4a1f-a81b-ba1499f2cc07/Renewables_2019.pdf.

Ingebritsen, S. E., & Manning, C. E. (1999). Geological implications of a permeability-depth curve for the continental crust. Geology, 27(12), 1107-1110.

Jäger-Waldau, A. (2007). Photovoltaics and renewable energies in Europe. Renewable and Sustainable Energy Reviews, 11(7), 1414-1437.

Jobmann, M., & Clauser, C. (1994). Heat advection versus conduction at the KTB: possible reasons for vertical variations in heat-flow density. Geophysical Journal International, 119(1), 44-68.

Kallesøe, A. J., Vangkilde-Pedersen, T., & Guglielmetti, L. (2020). HEATSTORE–underground thermal energy storage (UTES)-state of the art, example cases and lessons learned. In Proceedings World Geothermal Congress (p. 1).

Kämmlein, M., Dietl, C., & Stollhofen, H. (2019). The Franconian Basin thermal anomaly: testing its origin by conceptual 2-D models of deep-seated heat sources covered by low thermal conductivity sediments. International Journal of Energy and Environmental Engineering, 10(4), 389-412.

Kana, J. D., Djongyang, N., Raïdandi, D., Nouck, P. N., & Dadjé, A. (2015). A review of geophysical methods for geothermal exploration. Renewable and Sustainable Energy Reviews, 44, 87-95.

Kangas, M. T., & Lund, P. D. (1994). Modeling and simulation of aquifer storage energy systems. Solar energy, 53(3), 237-247.

Kim, J., Lee, Y., Yoon, W. S., Jeon, J. S., Koo, M. H., & Keehm, Y. (2010). Numerical modeling of aquifer thermal energy storage system. Energy, 35(12), 4955-4965.

Kohl, T., Bächler, D., & Rybach, L. (2000, May). Steps towards a comprehensive thermo-hydraulic analysis of the HDR test site Soultz-sous-Forêts. In Proceedings World Geothermal Congress (pp. 2671-2676). Japan: Kyushu-Tohoku.

Kohl, T., & Rybach, L. (1996). Thermal and hydraulic aspects of the KTB drill site. Geophysical Journal International, 124(3), 756-772.

Kong, X. Z., Deuber, C. A., Kittilä, A., Somogyvári, M., Mikutis, G., Bayer, P., ... & Saar, M. O. (2018). Tomographic reservoir imaging with DNA-labeled silica nanotracers: the first field validation. Environmental science & technology, 52(23), 13681-13689.

Korzani, M. G., Nitschke, F., Held, S., & Kohl, T. (2019). The development of a fully coupled wellbore-reservoir simulator for geothermal application. In Geothermal: Green Energy for the Long Run-Geothermal Resources Council 2019 Annual Meeting, GRC 2019 (pp. 927-936). Geothermal Resources Council.

Korzani, M. G., Held, S., & Kohl, T. (2020). Numerical based filtering concept for feasibility evaluation and reservoir performance enhancement of hydrothermal doublet systems. Journal of Petroleum Science and Engineering, 190, 106803.

Kuang, X., & Jiao, J. J. (2014). An integrated permeability‐depth model for Earth's crust. Geophysical Research Letters, 41(21), 7539-7545.

Kühn, M., & Gessner, K. (2009). Testing hypotheses for the Mount Isa Copper mineralisation with numerical simulations. Surveys in geophysics, 30, 253-268.

Lampe, C., & Person, M. (2000). Episodic hydrothermal fluid flow in the Upper Rhinegraben (Germany). Journal of Geochemical Exploration, 69, 37-40.

Lee, K. S., & Lee, K. S. (2013). Underground thermal energy storage (pp. 15-26). Springer London.

Leecaster, K., Ayling, B., Moffitt, G., & Rose, P. (2012, January). Use of safranin T as a reactive tracer for geothermal reservoir characterization. In Proceedings, 37th Workshop on Geothermal Reservoir Engineering.

Li, J., Pei, Y., Jiang, H., Zhao, L., Li, L., Zhou, H., ... & Zhang, Z. (2016, November). Tracer flowback based fracture network characterization in hydraulic fracturing. In Abu Dhabi international petroleum exhibition and conference (p. D021S023R005). SPE.

Li, L., Jiang, H., Li, J., Wu, K., Meng, F., & Chen, Z. (2017). Modeling tracer flowback in tight oil reservoirs with complex fracture networks. Journal of Petroleum Science and Engineering, 157, 1007-1020.

Li, Y., Yu, H., Luo, X., Liu, Y., Zhang, G., Tang, D., & Liu, Y. (2023). Full cycle modeling of inter-seasonal compressed air energy storage in aquifers. Energy, 263, 125987.

Li, Y., Yu, H., Xiao, Y., Liu, Y., Luo, X., Tang, D., ... & Liu, Y. (2023). Numerical verification on the feasibility of compressed carbon dioxide energy storage in two aquifers. Renewable Energy, 207, 743-764.

Li, Y., Yu, H., Tang, D., Zhang, G., & Liu, Y. (2024). Study on the applicability of compressed carbon dioxide energy storage in aquifers under different daily and weekly cycles. Renewable Energy, 222, 119987.

Liewig, N., & Clauer, N. (2000). K-Ar dating of varied microtextural illite in Permian gas reservoirs, northern Germany. Clay Minerals, 35(1), 271-281.

Linstrom, P. J., & Mallard, W. G. (2001). The NIST Chemistry WebBook: A chemical data resource on the internet. Journal of Chemical & Engineering Data, 46(5), 1059-1063.

Livescu, S., Durlofsky, L. J., Aziz, K., & Ginestra, J. C. (2008). Application of a new fully-coupled thermal multiphase wellbore flow model. In SPE Improved Oil Recovery Conference (pp. SPE-113215). SPE.

Livescu, S., Durlofsky, L. J., Aziz, K., & Ginestra, J. C. (2010). A fully-coupled thermal multiphase wellbore flow model for use in reservoir simulation. Journal of Petroleum Science and Engineering, 71(3-4), 138-146.

López, D. L., & Smith, L. (1995). Fluid flow in fault zones: analysis of the interplay of convective circulation and topographically driven groundwater flow. Water resources research, 31(6), 1489-1503.

López, D. L., & Smith, L. (1996). Fluid flow in fault zones: Influence of hydraulic anisotropy and heterogeneity on the fluid flow and heat transfer regime. Water resources research, 32(10), 3227-3235.

Lu, C., Jiang, H., You, C., Wang, Y., Ma, K., & Li, J. (2021). A novel method to determine the thief zones in heavy oil reservoirs based on convolutional neural network. Journal of Petroleum Science and Engineering, 201, 108471.

Lu, S. M. (2018). A global review of enhanced geothermal system (EGS). Renewable and Sustainable Energy Reviews, 81, 2902-2921.

Lucazeau, F. (2019). Analysis and mapping of an updated terrestrial heat flow data set. Geochemistry, Geophysics, Geosystems, 20(8), 4001-4024.

Lund, J. W., Bjelm, L., Bloomquist, G., & Mortensen, A. K. (2008). Characteristics, development and utilization of geothermal resources–a Nordic perspective. Episodes Journal of International Geoscience, 31(1), 140-147.

Magri, F., Littke, R., Rodon, S., & Urai, J. L. (2008). Temperature fields, petroleum maturation and fluid flow in the vicinity of salt domes. In Dynamics of Complex Intracontinental Basins: The Central European Basin System (pp. 323-344). Springer.

Magri, F., Möller, S., Inbar, N., Möller, P., Raggad, M., Rödiger, T., ... & Siebert, C. (2016). 2D and 3D coexisting modes of thermal convection in fractured hydrothermal systems-Implications for transboundary flow in the Lower Yarmouk Gorge. Marine and Petroleum Geology, 78, 750-758.

Malkovsky, V. I., & Magri, F. (2016). Thermal convection of temperature‐dependent viscous fluids within three‐dimensional faulted geothermal systems: Estimation from linear and numerical analyses. Water Resources Research, 52(4), 2855-2867.

Manning, C. E., & Ingebritsen, S. E. (1999). Permeability of the continental crust: Implications of geothermal data and metamorphic systems. Reviews of Geophysics, 37(1), 127-150.

McKenna, J. R., & Blackwell, D. D. (2004). Numerical modeling of transient Basin and Range extensional geothermal systems. Geothermics, 33(4), 457-476.

Moeck, I. S. (2014). Catalog of geothermal play types based on geologic controls. Renewable and sustainable energy reviews, 37, 867-882.

Mohammed, A. I., Oyeneyin, B., Atchison, B., & Njuguna, J. (2019). Casing structural integrity and failure modes in a range of well types-a review. Journal of natural gas science and engineering, 68, 102898.

Muhammed, G., & Tekbiyik-Ersoy, N. (2020). Development of renewable energy in China, USA, and Brazil: A comparative study on renewable energy policies. Sustainability, 12(21), 9136.

Nield, D. A., & Bejan, A. (2017). Convection in porous media (5th edn.). New York: Springer.

Nitschke, F., Held, S., Villalon, I., Neumann, T., & Kohl, T. (2017). Assessment of performance and parameter sensitivity of multicomponent geothermometry applied to a medium enthalpy geothermal system. Geothermal energy, 5, 1-20.

Nottebohm, M., Licha, T., & Sauter, M. (2012). Tracer design for tracking thermal fronts in geothermal reservoirs. Geothermics, 43, 37-44.

O'brien, J. J., & Lerche, I. (1988). Impact of heat flux anomalies around salt diapirs and salt sheets in the Gulf Coast on hydrocarbon maturity: models and observations.

Olasolo, P., Juárez, M. C., Morales, M. P., & Liarte, I. A. (2016). Enhanced geothermal systems (EGS): A review. Renewable and Sustainable Energy Reviews, 56, 133-144.

Oldenburg, C. M., & Pan, L. (2013). Porous media compressed-air energy storage (PM-CAES): Theory and simulation of the coupled wellbore–reservoir system. Transport in porous media, 97, 201-221.

Paksoy, H. O., Gürbüz, Z., Turgut, B., Dikici, D., & Evliya, H. (2004). Aquifer thermal storage (ATES) for air-conditioning of a supermarket in Turkey. Renewable Energy, 29(12), 1991-1996.

Pan, L., Oldenburg, C. M. (2014). T2Well—an integrated wellbore–reservoir simulator. Computers & Geosciences, 65, 46-55.

Panja, P., McLennan, J., & Green, S. (2021). Influence of permeability anisotropy and layering on geothermal battery energy storage. Geothermics, 90, 101998.

Parry, W. T. (1998). Fault-fluid compositions from fluid-inclusion observations and solubilities of fracture-sealing minerals. Tectonophysics, 290(1-2), 1-26.

Peaceman, D. W. (1983). Interpretation of well-block pressures in numerical reservoir simulation with nonsquare grid blocks and anisotropic permeability. Society of Petroleum Engineers Journal, 23(03), 531-543.

Permann, C. J., Gaston, D. R., Andrš, D., Carlsen, R. W., Kong, F., Lindsay, A. D., ... & Martineau, R. C. (2020). MOOSE: Enabling massively parallel multiphysics simulation. SoftwareX, 11, 100430.

Plummer, M. A., Palmer, C. D., Hull, L. C., & Mattson, E. D. (2010). Sensitivity of a reactive-tracer based estimate of thermal breakthrough in an EGS to properties of the reservoir and tracer (No. INL/CON-10-17688). Idaho National Lab.(INL), Idaho Falls, ID (United States).

Plummer, M. A., Palmer, C. D., Mattson, E. D., & Hull, L. C. (2011). A reactive tracer analysis method for monitoring thermal drawdown in geothermal reservoirs. In Proceedings, 36th Workshop on Geothermal Reservoir Engineering.

Pollack, A., Cladouhos, T. T., Swyer, M. W., Siler, D., Mukerji, T., & Horne, R. N. (2021). Stochastic inversion of gravity, magnetic, tracer, lithology, and fault data for geologically realistic structural models: Patua Geothermal Field case study. Geothermics, 95, 102129.

Pribnow, D. F., & Sass, J. H. (1995). Determination of thermal conductivity for deep boreholes. Journal of Geophysical Research: Solid Earth, 100(B6), 9981-9994.

Przybycin, A. M., Scheck-Wenderoth, M., & Schneider, M. (2017). The origin of deep geothermal anomalies in the German Molasse Basin: results from 3D numerical models of coupled fluid flow and heat transport. Geothermal Energy, 5, 1-28.

Puddu, M., Mikutis, G., Stark, W. J., & Grass, R. N. (2015). Submicrometer-Sized Thermometer Particles Exploiting Selective Nucleic Acid Stability. Small (Weinheim an der Bergstrasse, Germany), 12(4), 452-456.

Qiao, Y., Andersen, P. Ø., Evje, S., & Standnes, D. C. (2018). A mixture theory approach to model co-and counter-current two-phase flow in porous media accounting for viscous coupling. Advances in water resources, 112, 170-188.

Ramey Jr, H. J. (1962). Wellbore heat transmission. Journal of Petroleum Technology, 14(04), 427-435.

Redden, G., Stone, M., Wright, K. E., Mattson, E., Palmer, C. D., Rollins, H., ... & Hull, L. C. (2010, February). Tracers for characterizing enhanced geothermal systems. In Proc. of Thirty-Fifth Workshop on Geothermal Reservoir Engineering, Stanford University.

Robinson, B. A. (1985). Tracer and Geochemistry Analysis–Experiment 2059 (No. LA-UR-16-23930-32). Los Alamos National Laboratory (LANL), Los Alamos, NM (United States).

Robinson, B. A., & Tester, J. W. (1984). Dispersed fluid flow in fractured reservoirs: An analysis of tracer ‐ determined residence time distributions. Journal of Geophysical Research: Solid Earth, 89(B12), 10374-10384.

Robinson, B. A., Tester, J. W., & Brown, L. F. (1988). Reservoir sizing using inert and chemically reacting tracers. SPE Formation Evaluation, 3(01), 227-234.

Rose, P. E. (1994). The application of rhodamine WT as a geothermal tracer. Geothermal Resources Council Transactions, 18, 237-240.

Rudolph, B., Berson, J., Held, S., Nitschke, F., Wenzel, F., Kohl, T., & Schimmel, T. (2020). Development of thermo-reporting nanoparticles for accurate sensing of geothermal reservoir conditions. Scientific reports, 10(1), 11422.

Saar, M. O., & Manga, M. (2004). Depth dependence of permeability in the Oregon Cascades inferred from hydrogeologic, thermal, seismic, and magmatic modeling constraints. Journal of Geophysical Research: Solid Earth, 109(B4).

Sanjuan, B., Millot, R., Asmundsson, R., Brach, M. I. C. H. E. L., & Giroud, N. (2014). Use of two new Na/Li geothermometric relationships for geothermal fluids in volcanic environments. Chemical Geology, 389, 60-81.

Sanjuan, B., Pinault, J. L., Rose, P., Gérard, A., Brach, M., Braibant, G., ... & Touzelet, S. (2006). Tracer testing of the geothermal heat exchanger at Soultz-sous-Forêts (France) between 2000 and 2005. Geothermics, 35(5-6), 622-653.

Satter, A. (1965). Heat losses during flow of steam down a wellbore. Journal of Petroleum Technology, 17(07), 845-851.

Schilling, O., Sheldon, H. A., Reid, L. B., & Corbel, S. (2013). Hydrothermal models of the Perth metropolitan area, Western Australia: implications for geothermal energy. Hydrogeology Journal, 21(3), 605.

Schultz, R. A., Okubo, C. H., & Wilkins, S. J. (2006). Displacement-length scaling relations for faults on the terrestrial planets. Journal of Structural Geology, 28(12), 2182-2193.

Schüppler, S., Fleuchaus, P., & Blum, P. (2019). Techno-economic and environmental analysis of an Aquifer Thermal Energy Storage (ATES) in Germany. Geothermal Energy, 7, 1-24.

Scibek, J. (2020). Multidisciplinary database of permeability of fault zones and surrounding protolith rocks at world-wide sites. Scientific Data, 7(1), 95.

Senglaub, Y., Littke, R., & Brix, M. R. (2006). Numerical modelling of burial and temperature history as an approach for an alternative interpretation of the Bramsche anomaly, Lower Saxony Basin. International Journal of Earth Sciences, 95, 204-224.

Shan, C., & Pruess, K. (2005). An analytical solution for slug tracer tests in fractured reservoirs. Water resources research, 41(8).

Sharmin, T., Khan, N. R., Akram, M. S., & Ehsan, M. M. (2023). A state-of-the-art review on geothermal energy extraction, utilization, and improvement strategies: conventional, hybridized, and enhanced geothermal systems. International Journal of Thermofluids, 18, 100323.

Sheldon, H. A., Florio, B., Trefry, M. G., Reid, L. B., Ricard, L. P., & Ghori, K. A. R. (2012). The potential for convection and implications for geothermal energy in the Perth Basin, Western Australia. Hydrogeology Journal, 7(20), 1251-1268.

Sheldon, H. A., Wilkins, A., & Green, C. P. (2021). Recovery efficiency in high-temperature aquifer thermal energy storage systems. Geothermics, 96, 102173.

Shipton, Z. K., Soden, A. M., Kirkpatrick, J. D., Bright, A. M., & Lunn, R. J. (2006). How thick is a fault? Fault displacement-thickness scaling revisited.

Smith, L., & Chapman, D. S. (1983). On the thermal effects of groundwater flow: 1. Regional scale systems. Journal of Geophysical Research: Solid Earth, 88(B1), 593-608.

Sommer, W., Valstar, J., van Gaans, P., Grotenhuis, T., & Rijnaarts, H. (2013). The impact of aquifer heterogeneity on the performance of aquifer thermal energy storage. Water Resources Research, 49(12), 8128-8138.

Stemmle, R., Blum, P., Schüppler, S., Fleuchaus, P., Limoges, M., Bayer, P., & Menberg, K. (2021). Environmental impacts of aquifer thermal energy storage (ATES). Renewable and Sustainable Energy Reviews, 151, 111560.

Tang, Y., Ma, T., Chen, P., & Ranjith, P. G. (2020). An analytical model for heat extraction through multi-link fractures of the enhanced geothermal system. Geomechanics and Geophysics for Geo-Energy and Geo-Resources, 6, 1-11.

Tester, J. W., Brown, D. W., & Potter, R. M. (1989). Hot Dry Rock geothermal energy---A new energy agenda for the twenty-first century (No. LA-11514-MS). Los Alamos National Lab.(LANL), Los Alamos, NM (United States).

Tester, J. W., Robinson, B. A., & Ferguson, J. (1987). The theory and selection of chemically reactive tracers for reservoir thermal capacity production (No. SGP-TR-109-31). Chemical Engineering Department, Massachusetts Institute of Technology, Cambridge, Mass.

Torabi, A., & Berg, S. S. (2011). Scaling of fault attributes: A review. Marine and petroleum geology, 28(8), 1444-1460.

Tsang, C. F. (1978). Aquifer thermal energy storage. Institute of gas technology symposium on advanced technologies for Storing Energy, Chicago, ILL.

United Nations. Framework Convention on Climate Change. (2015). Adoption of the Paris agreement.

Ürge-Vorsatz, D., Cabeza, L. F., Serrano, S., Barreneche, C., & Petrichenko, K. (2015). Heating and cooling energy trends and drivers in buildings. Renewable and Sustainable Energy Reviews, 41, 85-98.

Usman, O., Akadiri, S. S., & Adeshola, I. (2020). Role of renewable energy and globalization on ecological footprint in the USA: implications for environmental sustainability. Environmental Science and Pollution Research, 27(24), 30681-30693.

van der Roest, E., Beernink, S., Hartog, N., van der Hoek, J. P., & Bloemendal, M. (2021). Towards sustainable heat supply with decentralized multi-energy systems by integration of subsurface seasonal heat storage. Energies, 14(23), 7958.

van Lopik, J. H., Hartog, N., & Schotting, R. J. (2022). Using multiple partially-penetrating wells (MPPWs) to improve the performance of high-temperature ATES systems: Well operation, storage conditions and aquifer heterogeneity. Geothermics, 105, 102537.

Vidal, R., Olivella, S., Saaltink, M. W., & Diaz-Maurin, F. (2022). Heat storage efficiency, ground surface uplift and thermo-hydro-mechanical phenomena for high-temperature aquifer thermal energy storage. Geothermal Energy, 10(1), 23.

Vitorge, E., Szenknect, S., Martins, J. M. F., Barthès, V., & Gaudet, J. P. (2014). Comparison of three labeled silica nanoparticles used as tracers in transport experiments in porous media. Part II: transport experiments and modeling. Environmental pollution, 184, 613-619.

Watanabe, N., Blöcher, G., Cacace, M., Held, S., & Kohl, T. (2017). Geoenergy modeling III. Cham: Springer International Publishing.

Wiktorski, E., Cobbah, C., Sui, D., & Khalifeh, M. (2019). Experimental study of temperature effects on wellbore material properties to enhance temperature profile modeling for production wells. Journal of Petroleum Science and Engineering, 176, 689-701.

Wilkins, A., Green, C. P., & Ennis-King, J. (2021). An open-source multiphysics simulation code for coupled problems in porous media. Computers & Geosciences, 154, 104820.

Will, P., Lüders, V., Wemmer, K., & Gilg, H. A. (2016). Pyrophyllite formation in the thermal aureole of a hydrothermal system in the Lower Saxony Basin, Germany. Geofluids, 16(2), 349-363.

Willhite, G. P. (1967). Over-all heat transfer coefficients in steam and hot water injection wells. Journal of Petroleum Technology, 19(05), 607-615.

Williams, M. D., Reimus, P., Vermeul, V. R., Rose, P., Dean, C. A., Watson, T. B., ... & Brauser, E. (2013). Development of models to simulate tracer tests for characterization of Enhanced Geothermal Systems (No. PNNL-22486). Pacific Northwest National Lab.(PNNL), Richland, WA (United States).

Williams, M. D., Vermeul, V. R., Reimus, P. W., Newell, D., & Watson, T. B. (2010). Development of models to simulate tracer behavior in enhanced geothermal systems (No. PNNL-19523). Pacific Northwest National Lab.(PNNL), Richland, WA (United States).

Wisian, K. W., & Blackwell, D. D. (2004). Numerical modeling of Basin and Range geothermal systems. Geothermics, 33(6), 713-741.

Wu, Y. S., & Pruess, K. (1990). An analytical solution for wellbore heat transmission in layered formations. SPE Reservoir Engineering, 5(04), 531-538.

Wuestefeld, P., Hilgers, C., Koehrer, B., Hoehne, M., Steindorf, P., Schurk, K., ... & Bertier, P. (2014, February). Reservoir heterogeneity in Upper Carboniferous tight gas sandstones: Lessons learned from an analog study. In SPE/EAGE European Unconventional Resources Conference and Exhibition (p. D011S004R002). SPE.

Wüstefeld, P., Hilse, U., Koehrer, B., Adelmann, D., & Hilgers, C. (2017). Critical evaluation of an Upper Carboniferous tight gas sandstone reservoir analog: Diagenesis and petrophysical aspects. Marine and Petroleum Geology, 86, 689-710.

Wüstefeld, P., Hilse, U., Lüders, V., Wemmer, K., Koehrer, B., & Hilgers, C. (2017). Kilometer-scale fault-related thermal anomalies in tight gas sandstones. Marine and Petroleum Geology, 86, 288-303.

Xiong, W., Bahonar, M., & Chen, Z. (2016). Development of a thermal wellbore simulator with focus on improving heat-loss calculations for steam-assisted-gravity-drainage steam injection. SPE Reservoir Evaluation & Engineering, 19(02), 305-315.

Xu, T., Liang, X., Xia, Y., Jiang, Z., & Gherardi, F. (2022). Performance evaluation of the Habanero enhanced geothermal system, Australia: Optimization based on tracer and induced micro-seismicity data. Renewable Energy, 181, 1197-1208.

Yan, G., Andersen, P. Ø., Qiao, Y., Hatzignatiou, D. G., Nitschke, F., Spitzmüller, L., & Kohl, T. (2024). Numerical modeling of temperature-reporting nanoparticle tracer for

fractured geothermal reservoir characterization. Geoenergy Science and Engineering, 237, 212787.

Yan, G., Busch, B., Egert, R., Esmaeilpour, M., Stricker, K., & Kohl, T. (2023). Transport mechanisms of hydrothermal convection in faulted tight sandstones. Solid Earth, 14(3), 293-310.

You, J., Rahnema, H., & McMillan, M. D. (2016). Numerical modeling of unsteady-state wellbore heat transmission. Journal of natural gas science and engineering, 34, 1062-1076.

Ystroem, L. H., Nitschke, F., Held, S., & Kohl, T. (2020). A multicomponent geothermometer for high-temperature basalt settings. Geothermal energy, 8, 1-21.

Zhang, D., Wang, J., Lin, Y., Si, Y., Huang, C., Yang, J., ... & Li, W. (2017). Present situation and future prospect of renewable energy in China. Renewable and Sustainable Energy Reviews, 76, 865-871.

Zhang, Y., Pan, L., Pruess, K., & Finsterle, S. (2011). A time-convolution approach for modeling heat exchange between a wellbore and surrounding formation. Geothermics, 40(4), 261-266.

Zwingmann, H., Clauer, N., & Gaupp, R. (1998). Timing of fluid flow in a sandstone reservoir of the north German Rotliegend (Permian) by K-Ar dating of related hydrothermal illite. Geological Society, London, Special Publications, 144(1), 91-106.

Zwingmann, H., Clauer, N., & Gaupp, R. (1999). Structure-related geochemical (REE) and isotopic (K-Ar, Rb-Sr, δ18O) characteristics of clay minerals from Rotliegend sandstone reservoirs (Permian, northern Germany). Geochimica et Cosmochimica Acta, 63(18), 2805-2823.

Acknowledgements

First, I would like to express my great gratitude to my supervisor Prof. Thomas Kohl for providing me the opportunity to conduct this research in his group. Thanks for your support and constructive suggestions during the planning and development of this research work. I will always remember your optimistic and energetic nature. Furthermore, I would like to thank Jun. Prof. Dr. Haibing Shao for being my co-supervisor during this thesis. You have been a great help to me with all your advice, generous patience and encouragement.

I specially thank Dr. Yangyang Qiao and Assoc. Prof. Dr. Pål Østebø Andersen (University of Stavanger, Norway) for always backing me up. I am very grateful for your time with me for the scientific discussions. I want to express my gratitude to our Geothermal Energy and Reservoir Technology group. I truly appreciated the engaging conversations and discussions during lunch, coffee and beer breaks. Also, I would like to thank Silke for all her support with the administration of KIT.

Last but not least, I thank my family members for their love and support throughout my life's journey, especially my grandparents, parents, wife and daughter, for cheering me up and supporting me.

This work was partly supported by the German Federal Ministry for Economic Affairs and Climate Action (BMWK) and the Project Management Jülich (PtJ) under the grant agreement number 03EE4033A associated with the VESTA project. This study is part of "Geoenergy" in the program "MTET—Materials and Technologies for the Energy Transition" of the Helmholtz Association. The support from the program is gratefully acknowledged. I was funded by the China Scholarship Council (Grant No. 201709370076). I acknowledge support by the state of Baden-Württemberg through bwHPC. This work was performed on the HoreKa supercomputer funded by the Ministry of Science, Research and the Arts Baden-Württemberg and by the Federal Ministry of Education and Research.